Computational Designing of Main Group Based Low Dimensional Ferromagnetic Half-Metallic Materials for Spintronics Applications

Ph.D. Thesis

by

GARGEE BHATTACHARYYA

DISCIPLINE OF METALLURGY ENGINEERING AND MATERIALS SCIENCE

INDIAN INSTITUTE OF TECHNOLOGY INDORE

NOVEMBER 2019

Computational Designing of Main Group Based Low Dimensional Ferromagnetic Half-Metallic Materials for Spintronics Applications

A THESIS

Submitted in partial fulfillment of the

requirements for the award of degree

of

DOCTOR OF PHILOSOPHY

by

GARGEE BHATTACHARYYA

DISCIPLINE OF METALLURGY ENGINEERING AND MATERIALS SCIENCE

INDIAN INSTITUTE OF TECHNOLOGY INDORE

NOVEMBER 2019

INDIAN INSTITUTE OF TECHNOLOGY INDORE

CANDIDATE'S DECLARATION

I hereby certify that the work which is being presented in the thesis entitled **Computational Designing of Main Group Based Low Dimensional Ferromagnetic Half-Metallic Materials for Spintronics Applications** in the partial fulfillment of the requirements for the award of the degree of **DOCTOR OF PHILOSOPHY** and submitted in the **DISCIPLINE OF METALLURGY ENGINEERING AND MATERIALS SCIENCE, INDIAN INSTITUTE OF TECHNOLOGY INDORE**, is an authentic record of my own work carried out during the time period from March 2015 to November 2019 under the supervision of **Dr. BISWARUP PATHAK**, Associate Professor, Discipline of Chemistry, and **Dr. SOMADITYA SEN**, Associate Professor, Discipline of Physics, IIT Indore.

The matter presented in this thesis has not been submitted by me for the award of any other degree of this or any other institute.

Gargee Bhattacharyya **13.11.2019**

Signature of the student with date

(GARGEE BHATTACHARYYA)

This is to certify that the above statement made by the candidate is correct to the best of my knowledge.

Signature of Thesis Supervisor #1 with date

(Dr. BISWARUP PATHAK)

Signature of Thesis Supervisor #2 with date

(Dr. SOMADITYA SEN)

GARGEE BHATTACHARYYA has successfully given her Ph.D. Oral Examination held on **26.05.2020**

Signature of Chairperson (OEB)
Date: 26.05.2020

Signature of External Examiner
Date: 26.05.2020

Signature(s) of Thesis Supervisor(s)
Date: 26.05.2020

Dr. P. R. Sagdeo
Signature of PSPC Member #1
Date:

Signature of PSPC Member #2
Date: May 26, 2020

Signature of Convener, DPGC
Date: 26.05.2020

Signature of Head of Discipline
Date: 26/05/2020

Head
Discipline of Metallurgy Engineering and
Materials Science (MEMS)
Indian Institute of Technology Indore
INDORE-453 552 INDIA

Acknowledgements

It is my great pleasure to acknowledge all those individuals who have supported me over the last four years for the completion of my thesis. First and foremost I would like to express my respect and gratitude to my supervisor, ***Dr. Biswarup Pathak*** *for his continuous guidance and support throughout my work. His suggestions and dedication has an incredible influence on better understanding of my work and me. I am significantly obliged for his inspiration to thrive for excellence in all ups and downs.*

I am thankful to my co-supervisor ***Dr. Somaditya Sen*** *for his inspiration, guidance and helpful suggestions to achieve my goal during my work.*

I would like to thank my PSPC members, Dr. Sanjay Kumar Singh and Dr. Pankaj Ramesh Sagdeo for their guidance and valuable suggestions during my work.

I am very much thankful to Prof. Pradeep Mathur, Director, IIT Indore for his endless motivations, and providing all the facilities at the institute.

I would like to express my gratitude to IIT Indore for providing laboratory, computational facilities, and financial support during my work.

I would also like to show appreciation to Ministry of Human Resource Development (MHRD) for fellowship.

I would also like to thank Dr. Parasharam M. Shirage, Dr. Rupesh Devan, Dr. Vinod Kumar, Dr. Mrigendra Dubey, Dr. Dhirendra Kumar Rai, Dr. Abhijit Ghosh, Dr. Srimanta Pakhira, Dr. I.A. Palani, Dr. Krushna Mavani, Dr. Preeti Bhobe, Dr. M. Mobin Shaikh and Dr. Vipul Singh for their guidance and help during various activities in the department.

I extend my deep appreciations to my group members Dr. Arup Mahata, Dr. Indrani Choudhuri, Dr. Kuber Singh Rawat, Dr. Priyanka Garg, Mr. Sourabh Kumar, Ms. Preeti Bhauriyal, Mr. Chiranjit Mondal, Mr. Akhil S Nair, Mr. Shyama Charan Mandal, Mr. Rameshwar Lal Kumawat, Mr.Sandeep Das, Mr. Arunendu Das, Mr. Surya Sekhar Manna, Mr. Sumit Kumar, Ms. Twinkle Dabur, Mr. Mahendra Patel, Dr. Surajit Nandi, Mr. Amitabha Das, Mr. Sameer Kumar Nayak and Mr. Hariom Saini for their generous help and co-operation to make my work successful.

I would also like to thank my friends Dr. Arun Kumar Yadav, Dr. Nasima Khatun, Dr. Tulika Srivastava, Dr. Nasir Khan, Dr. Gaurav Bajpai, Dr. Saurabh Tiwari and Dr. Anita Verma from Dr. Somaditya Sen's lab for their help and suggestions at various times.

I would also like to express my gratitude Mr. Dhiraj Vijayvargiya, Mr. Yogendra Singh, Ms. Sarita Batra, Mr. Manish Kushwaha, Ms. Vinita Kothari, Mr. Rameshwar Dauhare, Ms. Shagufta Rahim, Mr. Brajesh Dwivedi, Ms. Rinki Kukreja, Mr. Tapesh Parihar, Mr. Kailash Jamra, Mr. Roshan Bhatia, Ms. Divya Bangar and Mr. Sunny Namdev for their technical support. I would also like to thank Ms. Anjali Bandiwadekar, Mr. Rajesh Kumar, Mr. Lala Ram Ahirwar and other library staffs and other non-technical stuff for their constant help, whenever required.

I would also like to show my gratefulness to Ms. Monika Gupta, IIT Indore, for her encouragement, help and moral support.

I would personally like to extend my sincere thanks to my friends during various times of my PhD period, Dr. Nasima Khatun and Ms. Nabanita Ghosh who were always there whenever required and never let me down during these PhD days. Here, it is specially to be mentioned that, it has been a wonderful experience to have many friends Dr. Arpita Tawani, Dr. Pritpal Kaur Sandhu, Dr. Arpan Bhattacharya, Dr. Mriganka Das, Dr.

Vikash Mishra, Dr. Novina Malviya, Dr. Ashish Shukla, Dr. Amitesh Kumar, Ms. Swati Rajput, Ms. Ruksana Pervin, Mr. Sayan Chaudhuri, Mr. Mithun Kr. Majee, Mr. Ruhul Amin, Mr. Kushal Mazumder, Mr. Monojit Pusty and Mr. Alfa Sharma at IIT Indore during my PhD who really helped me in many aspects.

I feel extremely grateful express my respect, love and gratitude to all the teachers and professors from Bethune Collegiate School, Seacom Engineering College and Jadavpur University. I would like to specially mention about Anita Di, Purabi Di, Bharati Di, Mitali Di, Tara Di, Swati Di, Nandita Di, Shabari Di, Tanuka Di, Gitasri Di, Dhriti Di, Swaswati Di, Sarbashree Di, Mita Di, Manju Di, Karabi Di, Priti Di and Kajoli Di from my school and Dr. Chayanika Bose madam from Jadavpur University for their kind love and right advise to choose the right path in life. I could never achieve anything without their guidance, blessings, and support.

Most importantly, none of this would have been possible without the support of my family and I express my unfathomable love and gratitude to my lovable mother Mrs. Geeta Bhattacharyya, father Dr. Shyamal Chandra Bhattacharyya and brother Mr. Debabrata Bhattacharyya, and other family members for their love and support.

There are many people who have directly or indirectly contributed in making this journey successful, I wish I could thank them all, but time and space compel me to stop here. I thank all for being a part of my life.

GARGEE BHATTACHARYYA

Dedicated to
My Family
And
All Well-Wishers

Abstract

Continuous reduction in transistors size has become a mandatory approach to keep pace with the rapidly increasing complex integrated circuits (IC). However, this continuous downscaling of the transistor has approached to a limit as the charge based semiconductor device started facing several problems namely short channel effects (SCE) which degrades the performance of the device. Therefore, several novel approaches have been explored by the researchers to prevail these barricades. Spintronics is one of these emerging technologies which can overcome this problem. Magnetic random-access memory (MRAM) and spin-transfer torque random-access memory (STT-RAM) are those two new technologies which could revolutionize in quantum computing and memory industry. Both of these MRAM as well as STT-RAM consist of magnetic tunnel junction (MTJ), which works on the principle of spintronics. MTJ consists of one insulating layer sandwiched between two ferromagnetic layers. The tunneling current in MTJ depends on the relative orientation of magnetizations of the two ferromagnetic layers. Half-metallic materials play a very crucial role in MTJ since it can provide 100% spin-polarized current.

Transition metal-free ferromagnetism and half-metallicity in atomically thin 2D materials have drawn considerable attention among the researchers due to its potential application in spintronics. Main-group based materials play a very crucial role in this context due to their longer spin-relaxation time. In recent times, several van der Waals layered materials have gained lot of attention for their interesting magnetic properties and easily exfoliation properties. However, many cases the Curie temperature for these materials is much lower than even room temperature. Therefore, more efforts need to be devoted to achieve robust ferromagnetism, half-metallicity along with high Curie temperature in two dimensional as well as one dimensional material.

The contents of each chapter included in the thesis are discussed briefly as follows:

1. Introduction

In this chapter, a brief overview of the recent trends in the memory device, new emerging technologies in memory application and role of spintronics in these emerging technologies have been discussed. However, we have mainly focused on low dimensional (2D and 1D) main group based materials for spintronics applications. The basic working principle of spintronics device has also been discussed to explain the potential applicability of ferromagnetism and half-metallicity in low dimensional materials. Besides, classification of different spintronics materials, recent advancement in designing these materials for spintronics application has also been addressed. Further to this, the advantage of low dimensional material over the bulk materials has been discussed. Magnetic properties, calculation of Curie temperature and strain sustainability of the half-metallicity have also been discussed. In addition to that, introduction of molecular spintronics and its significance has also been discussed.

The last part of this chapter presents the basics of density functional theory (DFT) which has been used to model all our systems. We have discussed spin-polarized density functional theory since all the magnetic calculations are done using spin-based DFT. Theoretical insights, as well as a comparative analysis of different functional (GGA-PBE, PBE+U, PBEsol and HSE06), has also been discussed in this section. Furthermore, in this section, we have discussed the basic theory of phonon dispersion and *ab initio* molecular dynamics (AIMD) simulation which are used to investigate the stability of the system. We have also included the basic theory for calculating Curie temperature using mean-field theory and Monte Carlo simulation. Designing of molecular spintronics device is also discussed in this section. Furthermore, spin-resolved transport calculation and current-voltage ($I-V$) characteristics calculations using non-equilibrium Green's function (NEGF) has been discussed in this section.

2. Ferromagnetism in Magnesium Chloride Monolayer with an Unusually Large Spin-up Gap

In this chapter, we report a novel main group based ferromagnetic half-metallic material ($Mg_{0.89}\delta_{0.11}Cl_2$) with an unusually large spin-up gap (6.135 eV) for its possible application in the domain of spintronics. Modelling of this half-metallic material is done by defect engineering in pure $MgCl_2$ monolayer system. Such defect engineering creates holes in the pure $MgCl_2$ monolayer system, which in turn introduces magnetism in $MgCl_2$ based system. Interestingly, all our defect induced systems exhibits half-metallic properties. Among all these systems, $Mg_{0.89}\delta_{0.11}Cl_2$ combines the two most important properties (large spin-up gap and Dirac like dispersion in its bandstructure) which can prevent the spin current leakage and provide scattering less spin-transport in nano-spintronics device. Alkaline earth halides based $MgCl_2$ was chosen for our study because it is geologically abundant among all the other alkaline earth halides, posses a van der Waals layered structure and has an extremely wide insulating gap of 6.01 eV. Moreover, monolayer and multilayer $MgCl_2$ thin films have been experimentally synthesized on various transition metal single crystal surfaces, such as Pd (111) and (100), Pt (111) and (100)-hex and Rh (1l1), by using molecular beam epitaxy (MBE) and low energy electron diffraction (LEED) method. Our calculated exfoliation energy (0.16 J/m^2) indicates that $MgCl_2$ can be easily exfoliated from its layered bulk phase. The electronic and magnetic properties explore that the magnetism and half-metallicity in $Mg_{0.89}\delta_{0.11}Cl_2$ originate from the Cl 3*p* orbitals. The detailed orbital resolved bandstructure also confirms that the Cl 3*p* orbitals are the main contributor towards half-metallicity. Moreover, $Mg_{0.89}\delta_{0.11}Cl_2$ system explores a ferromagnetic ground state with the Curie temperature of 250 K. Stability analysis of $Mg_{0.89}\delta_{0.11}Cl_2$ indicate that our system is stable at 300 K. The calculated magnetic anisotropy energy (MAE) in $Mg_{0.89}\delta_{0.11}Cl_2$ is found to be 452.84 μeV/Mg vacancy, which indicates the high energy is required for spin-fluctuation, thus signifies the robustness of spin orientation. Furthermore, such system sustains its half-metallic character even after application of external strain as well as the electric field. Therefore, such system is very promising for scattering less spin transport for next-generation in spintronics devices.

3. Defect Induced Ferromagnetism and Half-Metallicity in CaI_2 Based Monolayer for Spintronics Applications

In this chapter, another van der Waals layered halide material CaI_2 was chosen for investigating its possible spintronics application. Similar to $MgCl_2$ monolayer, CaI_2 monolayer can also be exfoliated easily since it has exfoliation energy of 0.15 J/m^2. This CaI_2 is also posses insulating property with much a gap of 3.85 eV. Magnetism and half-metallicity in CaI_2 monolayer are induced via hole doping. Creation of single or pattern Ca vacancy effectively introduces holes in the system. Our thorough study shows that only single Ca vacancy induced system exhibits half-metallic property with a spin-up gap of 3.84 eV. All the other pattern vacancy induced CaI_2 based systems are found to be metallic in nature. Spin-polarized partial density of states, as well as orbital resolved band structure, show that the half-metallic property originates from the iodine *p* orbital. Further investigation of $Ca_{0.89}\delta_{0.11}I_2$ system reveals that it has a ferromagnetic ground state with Curie temperature of 238 K. Moreover, our system has very high magnetic anisotropy energy (MAE) of 14.11 meV/Ca Vacancy. Thus, such system is very robust to external spin fluctuation. Stability analysis indicates that only single Ca vacancy induced system is thermally stable at 300 K. Formation energy calculations indicate that this point defect is favourable under I-rich environment. Therefore, such material with high spin-up gap and MAE can be promising for spintronics device.

4. High Curie Temperature and Half-Metallicity in an Atomically Thin Main Group-Based Boron Phosphide System: Long Range Ferromagnetism

Transitional metal-free magnetism and half-metallicity is a very attractive topic in spintronics domain since such materials have weak spin-orbit coupling due to p-electron system which is very important for spintronics device applications. Moreover, weak spin-orbit coupling provides long spin relaxation time, which can provide long-range magnetic order. In this chapter, we have chosen atomically thin boron phosphide (BP) monolayer for possible spintronics application. Here, we have considered BP monolayer because it has a graphene-like hexagonal arrangement, moderate direct band gap of 0.91 eV, high carrier mobility and high mechanical strength. Moreover, BP films have been experimentally synthesized on an aluminum nitride (0001)/sapphire substrate by chemical vapour deposition (CVD) technique. Here, we have considered Be and Mg doped BP monolayer to introduce magnetism and half-metallicity using state-of-the-art density functional theory (DFT) calculation. Be and Mg are incorporated by substituting both B and P atom in the BP monolayer. Interestingly Be and Mg doping at P-site exhibits magnetism and half-metallicity. Such doping induces hole in the system which is a very useful approach for introducing magnetism in a non-magnetic system. Effect of doping concentration on half-metallicity in Be^P@BP and Mg^P@BP was also investigated by considering a series of doping concentrations. Surprisingly we have found that Mg^P@BP system exhibits its half-metallic characteristic for all the doping concentrations. We have also tried doping second and third row main group elements X (X= Li, Na, C, N, Al, Si, S) both at B and P-sites for possible spintronics application. All these systems are found to be non-magnetic except Li^P@BP, Na^B@BP and Na^P@BP systems. However, we have observed our best result in Mg^P@BP system compared to all other magnetic systems (Li^P@BP, Na^B@BP and Na^P@BP) and thus we have carried out our detailed further investigation for Mg^P@BP system. This strong half-metallicity originates from Mg-B3 unit rather than single Mg atom. Partial density of states indicates that in-plane 2*p* orbitals ($2p_x$ and $2p_y$) of B provide the primary contribution towards the half-metallicity in Mg^P@BP system. The effects of magnetic coupling between the two neighbouring magnetic centers are very vital to their overall effects on the magnetic properties of the system. Therefore, we have considered the effect of magnetic coupling with different spatial separation of magnetic centers and found that Mg^P@BP system has a long-range (12.94 Å) ferromagnetic ordering. Furthermore, we have found that Mg^P@BP system has a ferromagnetic ground state with high Curie temperature (494 K). The stability of Mg^P@BP system is investigated from energetic (formation and binding energy), dynamic (phonon dispersion), thermal (molecular dynamics simulation) and mechanical (stress vs strain) stability analysis. Our calculation proves that Mg^P@BP system energetically, dynamically, thermally and mechanically stable. Thus, such system with robust half-metallicity and high Curie temperature (494 K) is very promising for high-temperature spintronics application.

5. Porphyrin Nanoribbon Based Spin Filtering Device

In this chapter, we have modelled spin-filtering device based on a metal-free C=C embedded porphyrin nanoribbon/array structure for the first time. Porphyrin molecules and its derivatives have been considered as a potential candidate for molecular devices due to their unique electronic structures and interesting properties such as long-range electron tunnelling. Porphyrin based one-dimensional array has also been experimentally realized by several researchers. Therefore, these previous reports open up a new possibility to realize a 1-D nanostructure assembling C=C embedded porphyrin unit via a bottom-up approach since C=C embedded porphyrin unit has already been experimentally synthesized. Motivated by these reports, we have investigated porphyrin nanostructure containing two centrally coordinated hetero atoms (carbon-boron) due to the novelty of such porphyrin unit. Substitution of single carbon with boron among the two centrally coordinated carbons (-C=C-) may induce magnetism due to hole doping. Since nanoribbons have dangling bonds at their edges which provide active sites for chemical bonding; we have considered hydrogen (H) and fluorine (F) for functionalization of our porphyrin array structures. Besides, the unique electronic (metallic/semiconducting/insulating) properties and magnetic properties (ferromagnetic/antiferromagnetic/half-metallic) of the nanoribbons are associated with their edge states; thus edge modification can drastically control electronic and magnetic properties of the nanoribbons. We have considered two different types of nanoribbons (namely along a and along b) based on the orientation of C=C with the periodic diection. Hence, four types of nanoribbons have been considered for our study. It has been observed that undoped hydrogen (H) and fluorine (F) functionalized porphyrin arrays do not exhibit any magnetic properties. On the other hand, B-doping in all four porphyrin nanoribbons/arrays ($B@(C=C)_a^H-PA$, $B@(C=C)_a^F-PA$, $B@(C=C)_b^H-PA$ and $B@(C=C)_b^F-PA$) exhibit magnetism with magnetic moments of 0.4126 μB, 1.00 μB, 1.00 μB and 1.00 μB, respectively. Here, 'PA' represents porphyrin arrays, H/F denotes type of functionalization, and a/b indicates periodicity directions respectively. Among these magnetic systems, $B@(C=C)_a^F-PA$ system exhibits best half-metallic property with a spin-down gap of 0.37 eV. This half-metallic property is also sustained with the increment of its length (n=1, 2 and 3). Additionally, this porphyrin unit $B@(C=C)_a^F-PA$ exhibits itinerant magnetism which is verified from the density of states and spin density distributions. Stability of this porphyrin unit $B@(C=C)_a^F-PA$ is investigated from energetic (formation energy), dynamic (phonon dispersion), thermal (molecular dynamics simulation) and mechanical (stress vs strain) studies which indicate that our system is stable. We have also tried Al doping in C=C embedded porphyrin unit; however, B doping shows the best property and therefore $B@(C=C)_a^F - PA$ unit has been placed between two Au (111) electrodes for modelling our molecular spintronics device. Further, spin-resolved electron transport properties have been analyzed from the transmission function and current-voltage $(I-V)$ characteristics using non-equilibrium Green's function (NEGF) within DFT approach. Our calculated spin filtering efficiency (SFE) for our spintronics device is found as high as 98% which indicate that such system is very promising for metal-free novel spin-filtering device.

6. Conclusions

The conclusions of the thesis can be described as follows:

i) The s-block element based alkaline earth halide based monolayers show ferromagnetism half-metallicity with large spin-gap.

ii) The s-block elements based alkaline earth iodide based monolayers show strong half-metallicity with high magnetic anisotropy energy. This indicates that such system can prohibit spin fluctuation.

iii) Similarly, the p-block phosphorous based boron phosphide monolayers also show promising results for spintronics applications (such as long-range ferromagnetism, half-metallicity and high Curie temperature).

iv) Porphyrin nanoribbon/array containing main group element-based materials can exhibit long-range itinerant magnetism, half-metallicity and high spin-filtering efficiency (SFE) and thus, possible to design high spin-filtering based device.

List of Publications

1) **Bhattacharyya G.**, Mahata A., Choudhuri I**.**, Pathak B. (2017), Semiconducting state in borophene: role of defects., J. Phys. D: Appl. Phys., 50, 405103. (DOI: 10.1088/1361-6463/aa81b8) (Impact Factor: **2.829**)

2) **Bhattacharyya G.,** Choudhuri I., Pathak B. (2018), High Curie temperature and half-metallicity in an atomically thin main group-based boron phosphide system: long range ferromagnetism, Phys. Chem. Chem. Phys., 20, 22877-22889. (DOI: 10.1039/C8CP03440K) (Impact Factor: **3.567**)

3) **Bhattacharyya G.,** Choudhuri I., Bhauriyal P., Garg P., Pathak B. (2018), Ferromagnetism in magnesium chloride monolayer with an unusually large spin-up gap, Nanoscale, 10, 22280-22292. (DOI: 10.1039/C8NR07429A) (Impact Factor: **6.970**)

4) **Bhattacharyya G.,** Garg P., Bhauriyal P., Pathak B. (2019), Density Functional Theory Study of Defect Induced Ferromagnetism and Half-Metallicity in CaI_2 Based Monolayer for Spintronics Applications, ACS Appl. Nano Mater., 10, 6152-6161. (DOI: 10.1021/acsanm.9b00967) (**Cover Art Article**)

5) **Bhattacharyya G.,** Kumawat L. R., Pathak B. (2019), Porphyrin Nanoribbon Based Spin Filtering Device, (under review)

6) Choudhuri I., **Bhattacharyya G.**, Kumar S., Pathak B. (2016), Metal-free half-metallicity in a high energy phase C-doped gh-C_3N_4 system: a high curie temperature planar system, J. Mater. Chem. C, 4, 11530-11539. (DOI: 10.1039/C6TC04163A) (Impact Factor: **6.641**)

7) Bhauriyal P., Rawat K. S., **Bhattacharyya G.**, Garg P., Pathak B. (2018), First-Principles Study of Magnesium Peroxide Nucleation for Mg-Air Battery, Chem. Asian J., 13, 3198-3203. (DOI: 10.1002/asia.201801057) (Impact Factor: **3.698**)

8) Garg P., **Bhattacharyya G.,** Bhauriyal P., Pathak B. (2019), Enhanced Lewis Acid-Base Adducts in Doped Stanene: Sensing and Photocatalysis. Appl. Surf. Sci., 478, 946-958. (DOI: 10.1016/j.apsusc.2019.02.048) (Impact Factor: **5.155**)

9) Bhauriyal P., **Bhattacharyya G.,** Rawat K. S., Pathak B. (2019), Graphene/hBN Heterostructure as High Capacity Cathode with High Voltage for Next Generation Aluminium Batteries, J. Phys. Chem. C, 7, 3959-3967. (DOI: 10.1021/acs.jpcc.8b10550) (Impact Factor: **4.309**)

10) Garg P., Rawat K. S., **Bhattacharyya G.,** Kumar S., Pathak B. (2019), Hexagonal CuCl Monolayer for Overall Water Splitting: A DFT Study, ACS Appl. Nano Mater., 2, 4238−4246. (DOI: 10.1021/acsanm.9b00699)

Table of Contents

1. List of Figures **xxii**

2. List of Tables **xxxix**

3. Acronyms **xIii**

Chapter 1: Introduction

1.1. Introduction 3
1.2. Recent Trends in Memory Devices 4
  1.2.1. Conventional MOSFET Device 5
  1.2.2. Problems of Conventional MOSFET Device 6
  1.2.3. New approaches for Memory Device 6
    1.2.3.1. Innovation in the Design of Charge Based Device 6
    1.2.3.2. Introduction of New Emerging Technology 7
1.3. Origin of Spintronics 8
1.4. History of Spintronics 10
1.5. Spintronics Materials 12
  1.5.1. Classification Based on Intrinsic (Electronic) Property 12
    1.5.1.1.Magnetic Metals 12
      1.5.1.1.1. Ferromagnetic Metals 12
      1.5.1.1.2. Half-metallic Ferromagnet 13
    1.5.1.2. Topological Insulator 13
      1.5.1.2.1. Inorganic Topological Insulator 14
      1.5.1.2.2. Organometallic Topological Insulator 15
      1.5.1.2.3. Topological Crystalline Insulator 15
    1.5.1.3. Magnetic Semiconductor 16
  1.5.2. Classification Based on Intrinsic (Magnetic) Property 16
    1.5.2.1. Diamagnetic Materials 17

- 1.5.2.2. Paramagnetic Materials 18
- 1.5.2.3. Ferromagnetic Materials 18
- 1.5.2.4. Ferrimagnetic Materials 19
- 1.5.2.5. Antiferromagnetic Materials 19
- 1.5.3. Classification Based on Extrinsic (Materials) Property 20
  - 1.5.3.1. Metal Embedded Spintronics Materials 20
  - 1.5.3.2. Metal Free Spintronics Materials 20
- 1.6. Importance of Half-Metallic Materials 21
- 1.7. Role of Dimensionality on Spintronics 22
- 1.8. Molecular Spintronics 24
- 1.9. Theory 25
  - 1.9.1. The Many-Body Problem 25
    - 1.9.1.1. The Born-Oppenheimer Approximation 27
    - 1.9.1.2. Hartree-Fock Theory 28
  - 1.9.2. Density Functional Theory (DFT) 29
    - 1.9.2.1. The Hohenberg-Kohn Theorems 30
    - 1.9.2.2. Kohn-Sham Equations 31
    - 1.9.2.3. Exchange-correlation Functional 33
    - 1.9.2.4. Local Density Approximation (LDA) 33
    - 1.9.2.5. Generalized Gradient Approximation (GGA) 34
    - 1.9.2.6. DFT+U/GGA+U Method 35
    - 1.9.2.7. Hybrid Functional 36
    - 1.9.2.8. Projector Augmented Wave (PAW) Method 37
    - 1.9.2.9. Dispersion in Density Functional Theory 38

1.9.3. Other Computational Tools

- 1.9.3.1. *Ab initio* Molecular Dynamics 39
- 1.9.3.2. Bader Charge Analysis 40
- 1.9.3.3. Phonon dispersion 41
- 1.9.4. Magnetic Calculations 41
  - 1.9.4.1. Magnetic Anisotropy Energy (MAE) 41
  - 1.9.4.2. Mean Field Theory (MFT) Method 43

1.9.4.3. Monte Carlo Simulation (MC Simulation) 44
1.9.4.4. Calculation of Curie temperature for itinerant magnetism 44
1.9.5. Spin-Transport Calculation 45
1.10. References 46

Chapter 2: Ferromagnetism in Magnesium Chloride Monolayer with an Unusually Large Spin-up Gap

2.1. Introduction 65
2.2. Computational Methods 67
2.3. Results and Discussion 69
2.3.1. Cleavage energy of monolayer$MgCl_2$ from bulk 69
2.3.2. Incorporation of magnetism in $MgCl_2$ monolayer 70
2.3.3. Energetic stability and experimental realization 75
2.3.4. Dynamic and thermal stability 76
2.3.5. Magnetic properties of $Mg_{0.89}\delta_{0.11}Cl_2$ 79
2.3.6. Effect of strain on magnetism and half-metallicity of $Mg_{0.89}\delta_{0.11}Cl_2$ 85
2.3.7. Effect of external electric field on magnetism and half-metallicity of $Mg_{0.89}\delta_{0.11}Cl_2$ 91
2.4. Conclusion 94
2.5. References 95

Chapter 3: Defect Induced Ferromagnetism and Half-Metallicity in CaI_2 Based Monolayer for Spintronics Applications

3.1. Introduction 109
3.2. Computational Methods 111
3.3. Results and Discussion 113
3.3.1. Cleavage Energy of Monolayer CaI_2 from Bulk 113
3.3.2. Introduction of Magnetism in CaI_2 Monolayer 116
3.3.3. Analysis of Oxidation State of Ca in CaI_3 122

3.3.4. Magnetic Properties of $Ca_{0.89}\delta_{0.11}I_2$ Monolayer 123
3.3.5. Effect of Strain on Magnetism and Half-Metallicity in $Ca_{0.89}\delta_{0.11}I_2$ 129
3.3.6. Energetic stability and experimental realization of $Ca_{0.89}\delta_{0.11}I_2$ 136
3.3.7. Dynamic, and Thermal Stability of $Ca_{0.89}\delta_{0.11}I_2$ 137
3.4. Conclusion 140
3.5. References 141

Chapter 4: High Curie Temperature and Half-Metallicity in an Atomically Thin Main Group-Based Boron Phosphide System: Long Range Ferromagnetism

4.1. Introduction 151
4.2. Computational Methods 154
4.3. Results and Discussion 156
4.3.1. BP ML and Be- and Mg@BP 156
4.3.2. Magnetic properties of Be^P@BP and Mg^P@BP 165
4.3.3. Energetic Stability 175
4.3.4. Dynamic Stability 178
4.3.5. Thermal Stability 180
4.3.6. Mechanical stability and mechanical properties of Mg^P@BP (6.25%) 181
4.4. Conclusions 183
4.5. References 184

Chapter 5: Porphyrin Nanoribbon Based Spin Filtering Device

5.1. Introduction 199
5.2. Computational Methods 201
5.3. Results and Discussion 207
5.3.1. C=C embedded porphyrin MLs/PAs 207
5.3.2. Introduction of magnetism and half-metallicity in C=C embedded PA 209
5.3.3. Energetic stability of B and Al-doped C=C embedded PA

215
5.3.4. Dynamic and thermal stability of B doped C=C embedded PA 216
5.3.5. Possibility of an experiential realization of B doped C=C embedded PA 218
5.3.6. Introduction of magnetism in B doped C=C embedded PA 219
5.3.7. Effect of strain on magnetism and half-metallicity in B doped C=C embedded PA 222
5.3.8. Spin transport in B doped C=C embedded PA 225
5.3.9. Spin filtering efficiency (SFE) 227
5.4. Conclusions 228
5.5. References 229

Chapter 6: Scope for Future Work

6.1. Scope for future work 239

List of Figures

Chapter 1

Figure 1.1 Schematic representation of basic MOSFET (n-type) with its terminals source, drain, substrate and gate. **5**

Figure 1.2 Schematic representation of SRAM, DRAM and Flash memory. **8**

Figure 1.3 (a) Schematic representation of Magnetic Tunnel Junction (MTJ), Density of states (DOS) of (b) non-magnetic metal, (c) Ferromagnet, and (d) Half-Metal. **9**

Figure 1.4 Schematic representation of the band structure of topological insulator. The Fermi level lies within the bulk band gap. **14**

Figure 1.5 (a) - (e) Schematic representation of spin orientation in diamagnetic, paramagnetic, ferromagnetic, ferrimagnetic and anitiferromagnetic materials. **17**

Figure 1.6 Carbon based low dimensional (2D graphene, 1D carbon nanotube and graphene nanoribbon and 0D fullerene) materials. **23**

Chapter 2

Figure 2.1 Crystal structure of bulk $MgCl_2$: (a) top view and side view, (b) supercell geometry (3 × 3 × 1) of bulk $MgCl_2$ with an introduced fracture to simulate the exfoliation procedure. (c) Cleavage energy Ecl (J m^{-2}) as a function of the separation between two fractured parts. **70**

Figure 2.2 (a) Optimized structure (top/side view), (b) total electron density (isosurface value: 0.08 e $\mathrm{Å}^{-3}$), (c) phonon dispersion plot, (d) spin polarized total density of states (TDOS) of the $MgCl_2$ monolayer. Here, the black dashed box indicates the unit cell of $MgCl_2$ system. The Fermi level is shifted to zero and indicated by a navy blue dashed line. **71**

Figure 2.3 Optimized structures, spin polarized density of states along with magnified spin-polarised TDOS around the Fermi levels showing half-metallic gap (Δ, in the inset figures) and band structures of (a) $Mg_{0.89}\delta_{0.11}Cl_2$, (b) $Mg_{0.78}\delta_{0.22}Cl_2$, (c) $Mg_{0.67}\delta_{0.33}Cl_2$ systems. The Fermi level is set to zero and indicated by the blue dashed line. **72**

Figure 2.4 (a) Optimized structure, (b) spin polarized density of states and (c) band structures (showing coexistence of half-metallicity and Dirac cone) in $Mg_{0.89}\delta_{0.11}Cl_2$ system, (d)–(f) orbital resolved band structure of $Mg_{0.89}\delta_{0.11}Cl_2$. The radii of the red, green and violet circles are proportional to the Cl p_x, Cl p_y and Cl p_z character, (g) band structure (showing only spin-down channel) of $Mg_{0.89}\delta_{0.11}Cl_2$ system using PBEsol and (h) expanded view of band structure of $Mg_{0.89}\delta_{0.11}Cl_2$ using PBEsol showing gapless Dirac cone in $Mg_{0.89}\delta_{0.11}Cl_2$ system. The Fermi level is set to zero and indicated by the blue dashed line. **74**

Figure 2.5 (a) Optimized structure after phonon soft mode relaxation, (b) phonon dispersion plot after phonon soft mode relaxation and (c) total energy fluctuation of AIMD simulation of $Mg_{0.89}\delta_{0.11}Cl_2$ system. **77**

Figure 2.6 Spin density distribution (top/side view) [isosurface value 0.0046 e $Å^{-3}$] and partial density of states (PDOS) plot of Mg and Cl atoms in $Mg_{0.89}\delta_{0.11}Cl_2$, $Mg_{0.78}\delta_{0.22}Cl_2$, and $Mg_{0.67}\delta_{0.33}Cl_2$ systems. **79**

Figure 2.7 (a) Optimized structure of $Mg_{0.89}\delta_{0.11}Cl_2$ with Cl atoms denoted by blue (up) and green (down) circles. (b) Electron localization function of $Mg_{0.89}\delta_{0.11}Cl_2$ (ELF; maximum saturation level = 0.72 e $Å^{-3}$, minimum saturation level = 0.0 $Å^{-3}$). (c) Optimized structure of $Mg_{0.67}\delta_{0.33}Cl_2$ ($MgCl_3$) with unit cell in the black dotted line, and (d) corresponding electron localization function (ELF; maximum saturation level = 0.1 e $Å^{-3}$, minimum saturation level = 0.0 $Å^{-3}$). **80**

Figure 2.8 PDOS plot of Cl in (a) $Mg_{0.89}\delta_{0.11}Cl_2$ (b) $Mg_{0.67}\delta_{0.33}Cl_2$ ($MgCl_3$) and (c) $MgCl_2$ systems. The Fermi level is set to zero and indicated by the blue dashed line. **82**

Figure 2.9 (a)–(b) Optimized FM and AFM configurations of $Mg_{0.89}\delta_{0.11}Cl_2$, where each Cl atom is considered as a magnetic center, (c)–(e) optimized FM, AFM-I and AFM-II configurations and corresponding TDOS plots of $Mg_{0.89}\delta_{0.11}Cl_2$, where six Cl atom is considered as a magnetic center, (f) variation of magnetic moment (μB) of $Mg_{0.89}\delta_{0.11}Cl_2$ as a **83**

function of temperature, and (g) mean susceptibility of $Mg_{0.89}\delta_{0.11}Cl_2$ as a function of temperature.

Figure 2.10 (a)-(d) Spin density distribution and TDOS plot of $Mg_{0.89}\delta_{0.11}Cl_2$ under the application of biaxial tensile strain from 1% to 4% along with magnified spin-polarised TDOS around the Fermi showing half-metallic gap [Δ, in the inset figure]. **87**

Figure 2.11 (a)-(d) Spin density distribution and TDOS plot of $Mg_{0.89}\delta_{0.11}Cl_2$ under the application of uniaxial tensile strain from 1% to 4% along with magnified spin-polarised TDOS around the Fermi showing half-metallic gap [Δ, in the inset figure]. **88**

Figure 2.12 (a)-(d) Spin density distribution and TDOS plot of $Mg_{0.89}\delta_{0.11}Cl_2$ under the application of uniaxial compressive strain from 1% to 4% along with magnified spin-polarised TDOS around the Fermi showing half-metallic gap [Δ, in the inset figure]. **89**

Figure 2.13 (a)-(d) Spin density distribution and TDOS plot of $Mg_{0.89}\delta_{0.11}Cl_2$ under the application of biaxial compressive strain from 1% to 4% along with magnified spin-polarized TDOS around the Fermi showing half-metallic gap [Δ, in the inset figure]. **90**

Figure 2.14 Variation of Spin-up gap in $Mg_{0.89}\delta_{0.11}Cl_2$ with (a) application of Strain (1% to 4%), (b) application of transverse electric field (0.0 VÅ^{-1} to 1.0 VÅ^{-1}). **91**

Figure 2.15 (a)-(e) Spin density distribution and TDOS plot of $Mg_{0.89}\delta_{0.11}Cl_2$ under the application of transverse electric field ranging from 0.0 to 1.0 VÅ^{-1}. **92**

Figure 2.16 (Spin density distribution, spin-polarized density of states and bandstructure with the application of (a) 0.1 VÅ^{-1} (b) 0.2 VÅ^{-1} and (c) 0.3 VÅ^{-1} transverse electric field. **93**

Figure 2.17 Optimized structure and spin-polarized density of states of $Mg_{0.96}\delta_{0.04}Cl_2$ and $Mg_{0.92}\delta_{0.08}Cl_2$ systems. **94**

Chapter 3

Figure 3.1 Crystal structure of bulk CaI_2 (top and side views; d_0 denotes the interlayer spacing), (b) unit cell geometry of bulk CaI_2 with induced fracture (d is the distance between two fractured parts) to simulate the exfoliation procedure, (c) spin-polarized density of states of bulk CaI_2, where the Fermi level is set to zero and indicated by the blue dashed line, and (d) cleavage energy, E_{cl} (J/m^2), as a function of the separation between two fractured parts. **114**

Figure 3.2 Total density of states (TDOS) plot of CaI_2 system using (a)-(f) PBE+U (U=0, 1, 2, 3, 4, 5) and (g) HSE06 calculations. **115**

Figure 3.3 (a) Optimized structure (top and side views; the red dashed box indicates the unit cell of the CaI_2 system), (b) total electron density (isosurface value, 0.07 e Å^{-3}), (c) electron localization function (maximum saturation level 0.4 e Å^{-3}; minimum saturation level 0.0 Å^{-3}), (d) spin polarized total density of states (TDOS), (e) band structure, and (f) phonon dispersion plot of the CaI_2 monolayer. The Fermi level is shifted to zero and indicated by a navy blue dashed line. **116**

Figure 3.4 Optimized structures, spin density distribution, and spin polarized density of states (inset, magnified spin-polarized TDOS around the Fermi level) of (a) $Ca_{0.89}\delta_{0.11}I_2$, (b) $Ca_{0.78}\delta_{0.22}I_2$, (c) $Ca_{0.67}\delta_{0.33}I_2$ (CaI_3) systems. The Fermi level is set to zero and indicated by the blue dashed line. **118**

Figure 3.5 (a) Spin polarized band structure and density of states of $Ca_{0.89}\delta_{0.11}I_2$ system, (b) spin polarized band structure covering all the equivalent high symmetry points of the Brillouin zone and density of states of $Ca_{0.89}\delta_{0.11}I_2$ system. (c) Orbital resolved band structure of $Ca_{0.89}\delta_{0.11}I_2$ system, where size of the red, green, and blue dots in the lines are proportional to the I p_x, I p_y and I p_z orbital contribution (spin-down), respectively. The cyan line indicates the spin-up character. Partial density of states (PDOS) of (d) CaI_2 and (e) $Ca_{0.89}\delta_{0.11}I_2$ systems. The Fermi level is set to zero and indicated by the blue dashed line. **119**

Figure 3.6 Spin density distribution and spin polarized density of states of (a) $Ca_{0.94}\delta_{0.06}I_2$, and (b) $Ca_{0.96}\delta_{0.04}I_2$ systems. The Fermi level is set to zero and indicated by the blue dashed line. **120**

Figure 3.7 Partial density of states (PDOS) plot of Ca and I atoms of (a) CaI_2, (b) semiconducting $Ca_{0.96}\delta_{0.04}I_2$, (c) metallic $Ca_{0.78}\delta_{0.22}I_2$ and (d) metallic $Ca_{0.67}\delta_{0.33}I_2$ systems. The Fermi level is set to zero and indicated by the blue dashed line. **121**

Figure 3.8 (a, b) Optimized structures of $Ca_{0.89}\delta_{0.11}I_2$ in FM and AFM configurations considering a single iodine (I) as the magnetic center, (c-e) optimized **124**

structures of $Ca_{0.89}\delta_{0.11}I_2$ in FM, AFM-I, and AFM-II configurations in 2 × 2 × 1 supercell and their corresponding TDOS plot. The Fermi level is set to zero and indicated by the blue dashed line. (f) Variation of magnetic moment as a function of temperature.

Figure 3.9 Graphical representation of spin-up gap of the half-metallic system $Ca_{0.89}\delta_{0.11}I_2$ under the application of 1% to 5% biaxial compressive, biaxial tensile, uniaxial compressive, and uniaxial tensile strain. **130**

Figure 3.10 (a)-(e) Spin density distribution and TDOS plot of $Ca_{0.89}\delta_{0.11}I_2$ under the application of biaxial compressive strain from 1% to 5% along with magnified spin-polarized TDOS around the Fermi for the three half-metallic systems. **131**

Figure 3.11 (a)-(e) Spin density distribution and TDOS plot of $Ca_{0.89}\delta_{0.11}I_2$ under the application of biaxial tensile strain from 1% to 5% along with magnified spin-polarized TDOS around the Fermi for the systems **132**

Figure 3.12 (a)-(e) Spin density distribution and TDOS plot of $Ca_{0.89}\delta_{0.11}I_2$ under the application of uniaxial compressive strain from 1% to 5% along with magnified spin-polarized TDOS around the Fermi for the two half-metallic systems. **133**

Figure 3.13 (a)-(e) Spin density distribution and TDOS plot of $Ca_{0.89}\delta_{0.11}I_2$ under the application of uniaxial tensile strain from 1% to 5% along with magnified spin-polarized TDOS around the Fermi for the two half-metallic systems. **134**

Figure 3.14 Optimized structure and spin density distribution **134**

(SDD) of $Ca_{0.89}\delta_{0.11}I_2$ system under 2% biaxial compressive strain with (a) FM, (b) AFM-I and (c) AFM-II configurations in 2 × 2 × 1 supercell.

Figure 3.15 Optimized structure and spin density distribution (SDD) of $Ca_{0.89}\delta_{0.11}I_2$ system under 2% biaxial tensile strain with (a) FM, (b) AFM-I and (c) AFM-II configurations in 2 × 2 × 1 supercell. **135**

Figure 3.16 Optimized structure and spin density distribution (SDD) of $Ca_{0.89}\delta_{0.11}I_2$ system under 2% uniaxial compressive strain with (a) FM, (b) AFM-I and (c) AFM-II configurations in 2 × 2 × 1 supercell. **135**

Figure 3.17 Optimized structure and spin density distribution (SDD) of $Ca_{0.89}\delta_{0.11}I_2$ system under 2% uniaxial tensile strain with (a) FM, (b) AFM-I and (c) AFM-II configurations in 2 × 2 × 1 supercell. **135**

Figure 3.18 (a) Phonon dispersion plot of $Ca_{0.89}\delta_{0.11}I_2$ system, and (b) total energy fluctuation of AIMD simulation of $Ca_{0.89}\delta_{0.11}I_2$ system. **137**

Figure 3.19 Displacement eigenvectors (indicated by blue arrows) corresponding to the soft phonon mode with imaginary frequencies of (a) 25.40*i* cm^{-1}, (b) 21.74*i* cm^{-1} (c) 16.80*i* cm^{-1} (d) 2.15*i* cm^{-1} and (e) 0.98*i* cm^{-1} of $Ca_{0.89}\delta_{0.11}I_2$ system. The violet and green atoms respectively denote I and Ca. **138**

Figure 3.20 (a) Soft mode relaxed optimized structure and (b) phonon dispersion plot of soft mode relaxed $Ca_{0.89}\delta_{0.11}I_2$ (structure-2) system. **139**

Figure 3.21 Displacement eigenvectors (indicated by blue arrows) corresponding to the soft phonon mode with imaginary frequencies of (a) 0.29*i* cm^{-1}, (b) 0.37*i* cm^{-1} (c) 0.45*i* cm^{-1} and (d) 20.13*i* cm^{-1} of **139**

$Ca_{0.89}\delta_{0.11}I_2$ (structure-2) system. The violet and green atoms respectively denote I and Ca.

Chapter 4

Figure 4.1 (a) Optimized structure (top/side view), (b) total electron density (isosurface value: 0.08 e $Å^{-3}$), (c) electron localization function (ELF; maximum saturation level 0.17 e $Å^{-3}$, minimum saturation level 0.0 $Å^{-3}$), (d) spin polarized total/partial density of states (TDOS/PDOS) of the BP monolayer. Here, the red dashed box indicates the unit cell of the system. The Fermi level is shifted to zero and is indicated by a navy blue dashed line. **157**

Figure 4.2 Spin Density Distribution of (a) BP monolayer with single B-vacancy, (isosurface value: 0.002337 e $Å^{-3}$) (b) Be^B@BP system (isosurface value: 5.0 e-8 $Å^{-3}$) and (c) Mg^B@BP (isosurface value: 1.0 e-8 $Å^{-3}$). **158**

Figure 4.3 Optimized structures (top/side view) and spin polarized density of states of 6.25% doped (a) Be^B@BP, (b) Mg^B@BP, (c) Be^P@BP and (d) Mg^P@BP systems. The Fermi level is set to zero and is indicated by a blue dashed line. The doped Be and Mg atoms are denoted by violet and orange colors. Red dotted circles show the doped Be/Mg atoms in the systems. **159**

Figure 4.4 Optimized structures (top/side view) and spin polarized density of states of (a) 4.00%, (b) 2.78%, (c) 2.04% Be^P@BP and (d) 4.00%, (e) 2.78%, (f) 2.04% Mg^P@BP systems. The Fermi level is set to zero and indicated by a blue dashed **160**

line. Red dotted circles show the doped Be/Mg atoms of the system.

Figure 4.5 Optimized structure and TDOS of (a) Li^{B}@BP with 6.25% doping concentration. The Fermi level is shifted to zero and indicated by a blue dashed line. B, P and Li atoms are indicated by green, gray and pink color respectively. Doped Li atom is indicated by red circle. **161**

Figure 4.6 Optimized structure and TDOS of (a) C^{B}@BP (b) C^{P}@BP with 6.25% doping concentration. The Fermi level is shifted to zero and indicated by a blue dashed line. B, P and C atoms are indicated by green, gray and brown color respectively. Doped C atom is indicated by red circle. **162**

Figure 4.7 Optimized structure and TDOS of (a) N^{B}@BP (b) N^{P}@BP with 6.25% doping concentration. The Fermi level is shifted to zero and indicated by a blue dashed line. B, P and N atoms are indicated by green, gray and bluish silver color respectively. Doped N atom is indicated by red circle. **162**

Figure 4.8 Optimized structure and TDOS of (a) Al^{B}@BP (b) Al^{P}@BP with 6.25% doping concentration. The Fermi level is shifted to zero and indicated by a blue dashed line. B, P and Al atoms are indicated by green, gray and light blue color respectively. Doped Al atom is indicated by red circle. **163**

Figure 4.9 Optimized structure and TDOS of (a) Si^{B}@BP (b) Si^{P}@BP with 6.25% doping concentration. The Fermi level is shifted to zero and indicated by a blue dashed line. B, P and Si atoms are indicated **164**

by green, gray and dark blue color respectively. Doped Si atom is indicated by red circle.

Figure 4.10 Optimized structure and TDOS of (a) S^B@BP (b) S^P@BP with 6.25% doping concentration. The Fermi level is shifted to zero and indicated by a blue dashed line. B, P and S atoms are indicated by green, gray and yellow color respectively. Doped S atom is indicated by red circle. **164**

Figure 4.11 Optimized structures (top view), spin density distributions (isosurface value: 0.00244284 e Å^{-3}) and spin polarized densities of states of the (a) Li^P@BP (6.25%) (b) Na^B@BP (6.25%) (c) Na^P@BP (6.25%) systems. The doped Li and Na atoms are denoted by dark pink and red colors. Red dotted circles show the doped Li/Na atoms in the systems. **165**

Figure 4.12 Schematic of the presence of residual spin in the Mg^P@BP (6.25%) system due to Mg doping in the BP monolayer. **166**

Figure 4.13 (a) Spin density distribution (isosurface value: 0.001191 e Å^{-3}), (b) electronic structure (band structure, DOS), (c)–(e) PDOS plots of the Mg, B and P atoms of Mg^P@BP (6.25%). **166**

Figure 4.14 TDOS plot of (Mg-B3) unit in Mg^P@BP system. The Fermi level is shifted to zero and indicated by a blue dashed line. **167**

Figure 4.15 (a) Spin density distribution (SDD) (isosurface value: 0.0005 e Å^{-3}), (b) TDOS plot, (c)-(e) PDOS plots of Be, B and P atoms of Be^P@BP (6.25%). The Fermi level is shifted to zero and indicated by a blue dashed line. **168**

Figure 4.16 Spin density distributions of the Mg^P@BP ground states at distances of (a) 12.94 Å between two Mg–B3 magnetic units [FM coupling, (isosurface value: 0.0010 e $Å^{-3}$)] and (b) 9.74 Å between two Mg–B3 magnetic units [AFM coupling, (isosurface value: 0.0011 e $Å^{-3}$)]. **171**

Figure 4.17 Spin density distribution (SDD) (isosurface value: 0.0012 e $Å^{-3}$) of (a) FM and (b) AFM configuration of Mg^P@BP system in a larger (10 × 5 × 1) BP supercell. **172**

Figure 4.18 Optimized structures, Spin Density Distribution (isosurface value: 0.0012 e $Å^{-3}$), and TDOS of (a) FM, (b) AFM-I and (c) AFM-II configuration of Mg^P@BP (6.25%) in 8 × 8 × 1 BP supercell. The Fermi level is indicated by the blue dashed line. **172**

Figure 4.19 (a) Sustainability of the half-metallicity of Mg^P@BP under application of biaxial strain (1% to 3%). The Fermi level is indicated by a blue dashed line. (b) Variation of the total magnetic moment (μB) per formula unit of Mg^P@BP (6.25% doping) as a function of temperature. **174**

Figure 4.20 Electron localization function (ELF; maximum saturation level 1.0 e $Å^{-3}$, minimum saturation level 0.0 $Å^{-3}$) of (a) Be^P@BP (6.25%) and (b) Mg^P@BP (6.25%). **177**

Figure 4.21 (a) Phonon dispersion plot of Mg^P@BP (6.25%) after 2nd soft mode relaxation, (b) - (c) optimized structures (Mg^P@BP (6.25%)) corresponding to the maximum Mg vibration due to lattice dynamical instability and (d) – (e) TDOS plots of the two structures. The Fermi level is shifted to **178**

zero and is indicated by a blue dashed line.

Figure 4.22 (a) Optimized structure and phonon dispersion plot of Mg^P@BP (6.25%), (b) Optimized structure and phonon dispersion plot of Mg^P@BP (6.25%) after 1st soft mode relaxation. **179**

Figure 4.23 Displacement eigenvectors (indicated by blue arrows) corresponding to the soft phonon mode with imaginary frequencies of (a) $0.038i$ cm^{-1}, (b) $0.052i$ cm^{-1} and (c) $0.11i$ cm^{-1} of Mg^P@BP (6.25%). The light orange, pink and green atoms respectively denote Mg, B and P. **180**

Figure 4.24 Total energy fluctuations of the AIMD simulation of Mg^P@BP (6.25%) at (a) 300 K, (b) 500 K. (c) Tensile strain vs. stress plot for Mg^P@BP (6.25%). (d) Strain energy vs. applied strain plot for MgP@BP (6.25%). **181**

Chapter 5

Figure 5.1 Schematic illustration of the proposed molecular nanoscale devices containing: (a) $[(C=C)_a^F - PA_n\ (n=1)]$, (b) $[B@(C=C)_a^F - PA_n\ (n=1)]$, and (c) $[B@(C=C)_a^F - PA_n\ (n=2)]$ units. **206**

Figure 5.2 (a) Top view of C=C embedded porphyrin monolayer with unit cell showing in the red dotted line, (b) Electron localization function (ELF; maximum saturation level 0.8 e $Å^{-3}$, minimum saturation level 0.0 $Å^{-3}$), (c)-(e) Spin-polarized density of states and bandstructure of C=C embedded porphyrin monolayer calculated by GGA-PBE, (f) Spin-polarized density of states of C=C embedded porphyrin monolayer calculated **207**

by HSE06.

Figure 5.3 Optimized structures and spin-polarized density of states of (a) $(C=C)_a^H-PA$, (b) $(C=C)_a^F-PA$, (c) $(C=C)_b^H-PA$ and (d) $(C=C)_b^F-PA$ systems. The Fermi level is set to zero and is indicated by a blue dashed line. The C, N, H and F atoms are denoted by brown, blue, white and light gray colours. **208**

Figure 5.4 Optimized structures and spin-polarized density of states of (a) $B@(C=C)_a^H-PA$ and (b) $B@(C=C)_a^F-PA$ systems along with the magnified spin-polarized density of states (in the inset) around the Fermi level. The Fermi level is set to zero and is indicated by a blue dashed line. The B, C, N, H and F atoms are denoted by green, brown, blue, white and light gray colours. **210**

Figure 5.5 Optimized structures and spin-polarized density of states along with the magnified spin-polarized density of states (in the inset) around the Fermi level of (a) $B@(C=C)_b^H-PA$ and (b) $B@(C=C)_b^F-PA$ systems. The Fermi level is set to zero and is indicated by a blue dashed line. The B, C, N, H and F atoms are denoted by green, brown, blue, white and light gray colours. **211**

Figure 5.6 Spin density distribution of (a) $B@(C=C)_a^H-PA$, (b) $B@(C=C)_a^F-PA$, (c) $B@(C=C)_b^H-PA$ and (d) $B@(C=C)_b^F-PA$ systems. **212**

Figure 5.7 Total and partial density of states of (a) $(C=C)_a^H-PA$, (b) $B@(C=C)_a^H-PA$ and (c) **212**

magnified partial density of states of $B@(C=C)_a^H-PA$ system. Total and partial density of states of (d) $(C=C)_a^F-PA$, (e) $B@(C=C)_a^F-PA$ and (f) magnified partial density of states of $B@(C=C)_a^F-PA$ system. The Fermi level is set to zero and is indicated by a blue dashed line.

Figure 5.8 Optimized structures, spin polarized density of states and magnified spin polarized density of states (third panel) of (a) $Al@(C=C)_a^H-PA$, (b) $Al@(C=C)_a^F-PA$, (c) $Al@(C=C)_b^H-PA$ and (d) $Al@(C=C)_b^F-PA$ systems. The Fermi level is set to zero and is indicated by a blue dashed line. The Al, C, N, H and F atoms are denoted by sky blue, brown, blue, white and light gray colors. **213**

Figure 5.9 Spin density distribution of (a) $Al@(C=C)_a^H-PA$, (b) $Al@(C=C)_a^F-PA$, (c) $Al@(C=C)_b^H-PA$ and (d) $Al@(C=C)_b^F-PA$ systems. **214**

Figure 5.10 Optimized structures, spin polarized density of states and magnified spin polarized density of states (third panel) of (a) $(B-B)_a^H-PA$, (b) $(B-B)_a^F-PA$, (c) $(B-B)_b^H-PA$ and (d) $(B-B)_b^F-PA$ systems. The Fermi level is set to zero and is indicated by a blue dashed line. The B, C, N, H and F atoms are denoted by green, brown, blue, white and light gray colours. **214**

Figure 5.11 Spin density distribution of (a) $(B-B)_a^H-PA$, (b) $(B-B)_a^F-PA$, (c) $(B-B)_b^H-PA$ and (d) $(B-B)_b^F-PA$ systems. **215**

Figure 5.12 Optimized structures and spin polarized density of **215**

states of (a) B doped, (b) Al doped, and (c) two B doped C=C embedded porphyrin monolayer systems (unit cell is shown in the red dotted line).

Figure 5.13 (a) Optimized structures, (b) phonon dispersion plot and (c) total energy fluctuation of AIMD simulations of $B@(C=C)_a^F-PA$ system. Displacement eigenvectors (indicated by blue arrows) corresponding to the soft phonon mode with imaginary frequencies of (d) 0.15 cm^{-1}, (e) 1.29 cm^{-1} and (f) 30.72 cm^{-1} of $B@(C=C)_a^F-PA$ system. **217**

Figure 5.14 Optimized structure and phonon dispersion plot of $(C=C)_a^F-PA$ system. **218**

Figure 5.15 (a)-(c) Spin density distribution (SDD) of $B@(C=C)_a^F-PA_n$ system (where n=1, 2, 3 respectively) and (d)-(f) total density of states of $B@(C=C)_a^F-PA_n$ system (where n=1, 2, 3 respectively). **219**

Figure 5.16 Variation of magnetic moments in $B@(C=C)_a^F-PA$ with increasing smearing factor (σ). **222**

Figure 5.17 (a)-(e) Optimized structure, spin density distribution and TDOS plot of $B@(C=C)_a^F-PA$ under the application of uniaxial tensile strain from 1% to 5%. **224**

Figure 5.18 (a)-(e) Optimized structure, spin density distribution and TDOS plot of $B@(C=C)_a^F-PA$ under the application of uniaxial compressive strain from 1% to 5%. **225**

Figure 5.19 (a) The metal-molecule-metal nanodevice consisting C=C embedded porphyrin and its spin-polarized current-voltage pattern with applied bias **226**

voltages up to 0.5 V, (b)-(c) The metal-molecule-metal nanodevices consisting B doped C=C embedded porphyrin $B@(C=C)_a^F - PA_n$ with increasing length (n=1, and 2) and their spin-polarized $I-V$ curves for the corresponding device.

Figure 5.20 A comparison of the transmission spectra for the system $(C=C)_a^F - PA$ computed at different bias voltages ranging from 0.3 to 0.4 V. **227**

Figure 5.21 Spin filtering efficiency as function of the bias voltage for all the nanoscale devices. **228**

List of Tables

Chapter 2

Table 2.1	Summary of magnetic moments/vacancy (μB), nature of the material and spin-up band gap (eV) for with different Mg-vacancy concentrations	**73**
Table 2.2	Summary of formation energy/vacancy (E_F) under Mg-rich and Cl-rich environments for with different Mg-vacancy concentrations	**75**
Table 2.3	Bond distance and Bader charge analysis of pure $MgCl_2$, $Mg_{0.67}\delta_{0.33}Cl_2$ ($MgCl_3$) and $Mg_{0.89}\delta_{0.11}Cl_2$	**81**
Table 2.4	Summary of magnetic anisotropy energies in μeV/vacancy and the easy axis for $Mg_{0.89}\delta_{0.11}Cl_2$	**85**
Table 2.5	Modulation of Spin-Up Gap (eV) and Half-Metallic Gap (eV) in $Mg_{0.89}\delta_{0.11}Cl_2$ system with % of applied Strain along Biaxial-tensile and Biaxial-compressive direction	**86**
Table 2.6	Modulation of Spin-Up Gap (eV) and Half-Metallic Gap (eV) in $Mg_{0.89}\delta_{0.11}Cl_2$ system with % of applied Strain along Uniaxial-tensile and Uniaxial-compressive direction	**86**
Table 2.7	Bader charge analysis of $Mg_{0.89}\delta_{0.11}Cl_2$ system with and without application of electric field	**93**

Chapter 3

Table 3.1	Variation of band gap calculated using HSE06 and PBE+U (U=0, 1, 2, 3, 4, 5) calculations	**115**
Table 3.2	Bader charge analysis and bond distance of pure CaI_2, $Ca_{0.89}\delta_{0.11}I_2$, $Ca_{0.78}\delta_{0.22}I_2$ and $Ca_{0.67}\delta_{0.33}I_2$	**122**

Table 3.3 Summary of magnetic anisotropy energies in meV/vacancy and the easy axis for $Ca_{0.89}\delta_{0.11}I_2$ **125**

Table 3.4 Modulation of spin-up gap (eV) in $Ca_{0.89}\delta_{0.11}I_2$ system and nature of the system with % of applied strain along biaxial-tensile and biaxial-compressive direction **129**

Table 3.5 Modulation of spin-up gap (eV) in $Ca_{0.89}\delta_{0.11}I_2$ system and nature of the system with % of applied Strain along uniaxial-tensile and uniaxial-compressive direction **130**

Table 3.6 Relative energy difference of magnetic ground states (FM, AFM-I and AFM-II) under 2% biaxial and uniaxial strain **133**

Table 3.7 Summary of formation energy/vacancy (E_F) under Ca-rich and I-rich environments and nature of the material for with different Ca-vacancy concentrations **136**

Chapter 4

Table 4.1 Bader charge analysis of pure BP and Mg^P@BP **157**

Table 4.2 Magnetic moments per dopant (μB), nature of the system and spin gaps (eV) for the Be^P@BP and Mg^P@BP systems with different doping concentrations **159**

Table 4.3 Optimized spatial separations between two dopants (Å), optimized structures, relative energies (eV), exchange energies (meV) and magnetic ground states of the Mg^P@BP systems **169**

Table 4.4 Optimized spatial separation between two dopants (Å), Optimized structure, Exchange energy (meV) and Magnetic ground state of **170**

Be^P@BP systems

Table 4.5 Summary of Magnetic Anisotropy Energies in μeV/dopant and the EA for Mg^P@BP (6.25%) **173**

Table 4.6 Formation energies per dopant (E_F) and binding energies per dopant (E_B) for the Be^P@BP and Mg^P@BP systems with different doping concentrations **175**

Table 4.7 Formation energy/dopant (E_F), binding energy/dopant (E_B), magnetic moments/dopant (μB) and band gap (eV) for Be^B@BP and Mg^B@BP systems **176**

Chapter 5

Table 5.1 Formation energies per dopant (E_F), magnetic moments per dopant (μB), nature of the system and spin gap (eV) for the B and Al doped C=C embedded PA **216**

Table 5.2 Bader charge analysis of pure $(C=C)_a^F-PA$ and B doped $B@(C=C)_a^F-PA$ **221**

Table 5.3 Summary of magnetic anisotropy energies in μeV/vacancy and the easy axis for $B@(C=C)_a^F-PA$ system **221**

Table 5.4 Modulation of spin-up gap (eV) in and nature of the $B@(C=C)_a^F-PA$ system with % of applied strain along uniaxial-tensile and uniaxial-compressive direction **225**

Acronyms

IC	Integrated Circuit
CMOS	Complementary Metal-Oxide-Semiconductor (field effect transistor)
SRAM	Static Random-Access Memory
DRAM	Dynamic Random-Access Memory
FG	Floating Gate
NMOS	*n*-channel Metal-Oxide-Semiconductor (field effect transistor)
PMOS	*p*-channel Metal-Oxide-Semiconductor (field effect transistor)
MOSFET	Metal-Oxide-Semiconductor Field Effect Transistor
SCE	Short Channel Effects
DIBL	Drain Induced Barrier Lowering
DMDG	Dual Material Double Gate
TMDG	Triple Material Double Gate
NVM	Non Volatile Memory
MRAM	Magnetic Random-Access Memory
STT-RAM	Spin-Transfer Torque Random-Access Memory
FeRAM	Ferroelectric Random-Access Memory
PCM	Phase Change Memory
RRAM	Resistive Random-Access Memory
MTJ	Magnetic Tunnel Junction
GMR	Giant magneto-resistance
CIP	Current-in-plane
CPP	Current-perpendicular-to-the-plane
TMR	Tunnel magneto-resistance
TI	Topological Insulator
DOS	Density of states
OTI	Organometallic Topological Insulators

TCI	Topological Crystalline Insulators
DMS	Diluted Magnetic Semiconductors
HSC	Half Semiconductors
SGS	Spin Gapless Semiconductors
BMS	Bipolar Magnetic Semiconductors
AAFMS	Asymmetric Antiferromagnetic Semiconductors
FM	Ferromagnetic
AFM	Antiferromagnetic
2D	Two-dimensional
VB	Valence band
CB	Conduction band
DFT	Density functional theory
LDA	Local density approximation
GGA	Generalized Gradient Approximation
PBE	Perdew-Burke-Ernzerhof
PAW	Projector augmented wave
LSDA	Local spin-density approximation
B3LYP	Becke, three-parameter, Lee-Yang-Parr
HSE	Heyd-Scuseria-Ernzerhof
NEGF	Non-equilibrium Green’s function
VASP	Vienna Ab initio Simulation Package
AIMD	Ab initio molecular dynamics
VESTA	Visualization of Electronic and STructural analysis
DFPT	Density functional perturbation theory
PDOS	Projected density of states
SDD	Spin density difference
MAE	Magnetic anisotropy energy
MFT	Mean field theory

Chapter 1

Introduction

1.1. Introduction

With the advancement of human civilization, a rapid progression in the field of high-performance computing, communication, and real time automation has become the driving forces for the escalating requirements of a high-performance electronic device. Therefore, the complexity of the integrated circuit (IC) has amplified day by day in order to accommodate more number of components/devices in a single chip *[1]*. The demand for developing more complex IC, has led to miniaturization of minimum feature size (also called channel length) of the device *[2]*. Following this concept, an exponential increment of the number of transistors on a silicon chip has been observed in the late 1960s *[3]*. Gordon Moore, the co-founder of Intel Corporation, observed this trend thoroughly and anticipated in 1965 that the number of transistors in a single chip would double every year. This prediction has stated as Moore's law *[4]*. Later on, he modified this law that number of transistors in a single chip would double every two years *[3]*. Moore's prediction was found to be true for many decades and it has become a guideline to every semiconductor company *[2]*. At present-day most of the industry state that Moore's law doubling period is approximately 18 months *[3]*. In addition to the requirement of continuous increment of number of transistors obeying Moore's law, minimal power consumption in transistor operation has also become the significant criterion in the electronic industry *[2]*. In 1965, the semiconductor industry has produced chips with about 50 components/transistors having minimum feature size of approximately 50 mm *[5]*. However, at present-day, leading chips generally incorporate several billion transistors having minimum feature size of approximately 10 nm *[5]*. Thus, semiconductor industry has approached a new era of scaling to satisfy this demand. The first generation transistor scaling (geometrical scaling) was observed in 70s, 80s, and 90s *[2]*. This is called classic/traditional scaling *[5]*. The traditional scaling was productively used in the industry until early 2000s with minimum feature size of 130 nm *[5]*. By the 130-nm generation, gate oxide thickness has scaled down to 1.2 nm, and therefore, electron tunneling through this thin gate oxide can potentially contribute a significant amount to the total device leakage current *[5]*. Hence, researchers have to find out new method of scaling since we have reached the limits of scaling device using traditional method. This new scaling approach was called as equivalent scaling, where materials and structural limitations were investigated *[2]*. The main features of this approach are use of strained silicon, high-k/metal gate, use of other semiconductor materials and FinFET technology *[2]*. Moreover, in order to maintain the future growth of electronic industry, several new materials, new device concepts, and new technologies have to come up to replace the standard silicon CMOS (complementary metal-oxide-semiconductor) technology. Such new concepts are graphene based nanoelectronic devices, phase change materials and spintronics.

1.2. Recent Trends in Memory Devices

The present day's computing system is dreadfully dependent on the performance of the memory subsystem. This memory subsystem consists of volatile and non-volatile memory. Volatile memory consists of static random-access memory (SRAM) and dynamic random-access memory (DRAM) while the non-volatile memory consists of flash memory which serves as cache, main memory, and storage memory such as solid-state drive; respectively *[6]*. Conventional memory technologies are primarily based on the charge storage mechanism. For example, these charges are stored at the storage nodes of the cross-coupled inverter in case of SRAM, similarly charges are stored at the cell capacitor in case of DRAM and at the floating gate (FG) of the transistor in case of flash memory *[6]*. Most of the logic circuits, microprocessors as well as static RAMs are put together using CMOS technology *[7]*. The Inverter used in SRAM is also based on CMOS technology which is built using both NMOS (*n*-channel metal-oxide-semiconductor) and PMOS (*p*-channel metal-oxide-semiconductor) transistor *[7]*.

1.2.1. Conventional MOSFET Device

The conventional MOSFET (metal-oxide-semiconductor field-effect transistor) is made up of four-terminals namely source (S), gate (G), drain (D), and body/substrate (B) terminals. However, mostly the substrate of the MOS device is connected with the source terminal, thus making it a three-terminal device *[7]*. The MOSFET device is absolutely symmetrical with respect to its source and drain terminals. The source and the drain terminal can be distinguished from the direction of the current flow which in turn depends on the supply voltage. The basic structure of a MOSFET device is shown in Fig. 1.1.

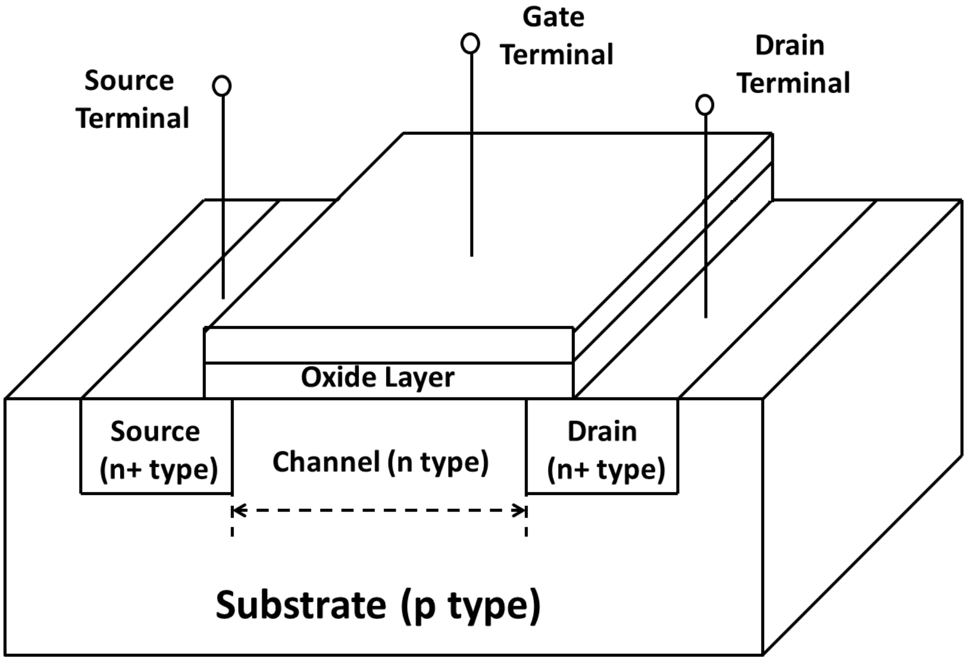

Figure 1.1: Schematic representation of basic MOSFET (n-type) with its terminals source, drain, substrate, and gate.

Depending on the type of the conducting channel, MOSFET can be categorized into two types that are p-channel and n-channel MOSFET (sometimes also referred to as p-type and n-type). The source and the drain of an n-channel MOSFET are doped heavily with n+ type and the substrate is built with p-type material *[7]*. Similar way, for a p-channel MOSFET, the source and the drain are doped with heavily p+ type doped material and the substrate is built with n-type material *[7]*. For both the cases the gate electrode is made up with metal. The basic difference between these two types of MOSFET is that electrons are the majority carriers for n-channel MOSFET while holes are the majority carriers for p-channel MOSFET *[7]*.

1.2.2. Problems of Conventional MOSFET Device

Conventional charge based device has started facing several challenges with downscaling up to 10-nm and beyond. These are mainly referred to as short channel effects (SCE) *[7-8]*. Due to these numerous SCE, the charge sharing between the drain and the source electrode increases, thus the gate electrode loses its control over the charge in the channel and the drain current which results in the increment of off-state leakage current and degradation of device performance *[8-10]*. These various SCEs are referred as threshold voltage reduction, drain induced barrier lowering (DIBL), mobility reduction, carrier velocity saturation, hot electron effects, impact ionization near drain electrode, channel length modulation and punch-through *[11-14]*. Therefore, quite a lot of unconventional structures based on gate technology, gate oxide and channel materials have been explored by the researchers to prevail these barricades *[8-9, 15-17]*.

1.2.3. New approaches for Memory Device

1.2.3.1. Innovation in the Design of Charge Based Device

The first innovation was introduced on Intel’s 90-nm technology in 2003 using strained silicon transistor *[5-18]*. In 2007, high-k metal gate transistor was first introduced in Intel’s 45-nm technology to improve the transistor gate dielectric *[5, 19]*. In this 45-nm technology, high-k dielectric material (hafnium-based) was used as gate-oxide replacing the traditional SiO_2 to reduce the gate oxide leakage current as well as improves the transistor drive current *[5, 19]*. In addition to that, various alternative MOSFET with unconventional gate electrode such as dual material double gate (DMDG), triple material double gate (TMDG), tri-gate and gate all around MOSFET have also been introduced during this time to provide better electrostatic control of the channel region *[20-27]*. Further to this, Intel has introduced FinFET (tri-gate) transistor in 2011, as a next major innovation, on its new 22-nm technology *[5, 28]*. As the gate length of traditional planar MOSFET (metal-oxide-semiconductor field-effect transistor) has reached below 32 nm, off-state leakage has become a serious problem. Thus, a 3D FinFET MOSFET structure was introduced by the researchers to solve this issue as the gate electrode of FinFET has better electrostatic control of the transistor channel *[5]*.

1.2.3.2. Introduction of New Emerging Technology

It has been a long time since DRAM, SRAM and Flash are used as dominant solid-state memory technologies. The DRAM is constructed with one transistor and one capacitor and SRAM is constructed with six transistors using CMOS technology (Fig. 1.2a-b) *[29]*. Flash memory works with FG component which is placed in between the control gate and the source-drain area and isolated by an insulating oxide layer (Fig. 1.2c) *[29]*. The increasing demand for reducing the feature size of microelectronic products leads to several limitations in MOS-based memory device SRAM and DRAM which has already been discussed in section 1.2.2. This scaling trend also requires the effective oxide thickness (EOT) of Flash memory to be reduced *[29]*. However, very thin oxide suffers from many reliability issues such as reduction of operating voltage and stress induced leakage current (SILC) *[29]*.

Therefore, some other new storage conceptions have been suggested in search of ideal memory devices or ‘unified memory’ which can satisfy concurrently three requirements such as high speed, high density and non-volatility *[29]*. Among these emerging nonvolatile memories five types of non-volatile memory (NVM) technology have become very captivating. These are categorized as magnetic random-access memory (MRAM), ferroelectric random-access memory (FeRAM), spin-transfer torque random-access memory (STT-RAM), resistive random-access memory (RRAM) and phase-change memory (PCM) which can combine the density of DRAM, the speed of SRAM, and non-volatility of Flash memory *[29]*.

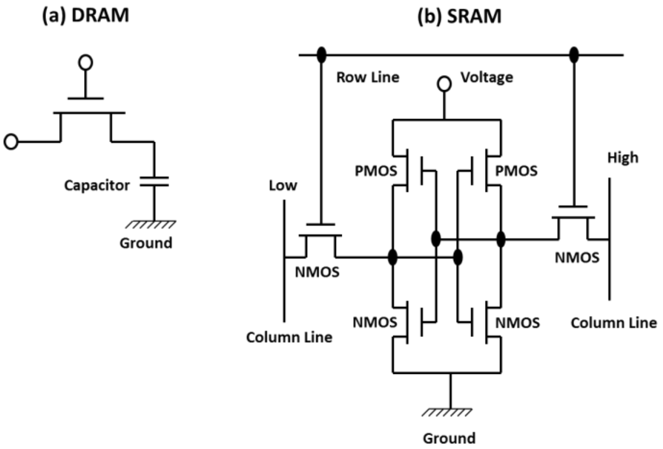
(a) DRAM
Capacitor
Ground
(b) SRAM
Row Line
Voltage
PMOS
PMOS
Low
High
NMOS
NMOS
NMOS
NMOS
Column Line
Column Line
Ground
(c) FLASH
Floating Gate
Ground

Figure 1.2: Schematic representation of SRAM, DRAM and Flash memory.

As a consequence, the memory industry has expected a massive change over a couple of years with more complex, and reliable technologies to replace the dominant Flash memory *[29]*. Researchers have predicted that RRAM, MRAM, and STT-RAM are the most promising emerging technologies revolutionizing the memory hierarchy *[6, 29]*. Moreover, according to published report from Yole Development, Emerging Non-volatile Memory Technologies, Industry Trends and Market Analysis, STT-RAM is expected to replace SRAM in SoC (System on Chip) applications from 2015 reducing cell size by 50% *[29]*. Both of these MRAM as well as STT-RAM consist of magnetic tunnel junction (MTJ) (Fig. 1.3) which works on principle of spintronics.

1.3. Origin of Spintronics

Spintronics is a novel spin-based electronics technology where the spin of the electron carries the information instead of the charge of the electron *[30]*. Spintronics involves active generation, detection, manipulation and transport of spin in spintronic material as well as device *[30]*. The spin dependent effects in the spintronics material arise from the interaction of the spin of the carrier with the magnetic properties of the material *[30]*.

The conventional approach of spin is based on the alignment of a spin (termed as "up" or "down") relative to a reference which may be an applied magnetic field or orientation of magnetization in the ferromagnetic film *[30]*. The official beginning of this new era is considered with the discovery of the giant magnetoresistive (GMR) effect in 1988 *[30]*. GMR effect was independently discovered by two research groups from University of Paris-Sud, France (group of Albert Fert) and Forschungszentrum Jülich, Germany (group of Peter Grünberg) in 1988 *[31-32]*. Later, in 2007, both of them have jointly received Nobel Prize in Physics for the practical significance of this discovery. GMR has significant applications in magnetic field sensors which are used in hard disk drives, microelectromechanical systems (MEMS), MRAM and many other devices *[33]*.

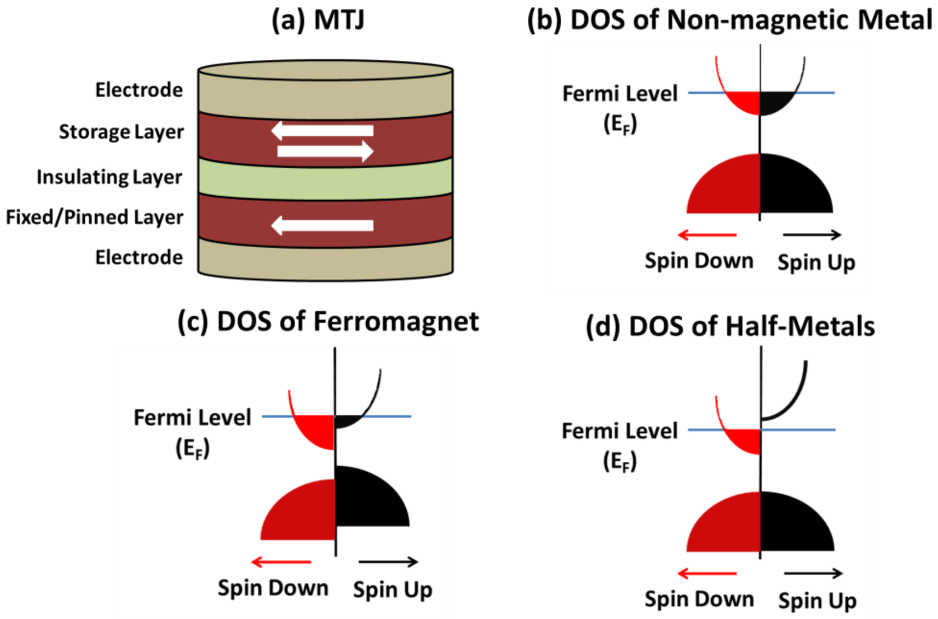
(a) MTJ
Electrode
Storage Layer
Insulating Layer
Fixed/Pinned Layer
Electrode
(b) DOS of Non-magnetic Metal
Fermi Level
(E_F)
Spin Down
Spin Up
(c) DOS of Ferromagnet
Fermi Level
(E_F)
Spin Down
Spin Up
(d) DOS of Half-Metals
Fermi Level
(E_F)
Spin Down
Spin Up

Figure 1.3: (a) Schematic representation of Magnetic Tunnel Junction (MTJ), Density of states (DOS) of (b) non-magnetic metal, (c) Ferromagnet, and (d) Half-Metal.

The term 'magnetoresistance' refers to the tendency of a material (preferably ferromagnetic) to change its electrical resistance with the application of an external magnetic field *[34]*. Numerically magnetoresistance can be defined as

$$\delta_H = \frac{R_H - R_0}{R_0} \tag{1.1}$$

where R_H and R_0 corresponds to the resistance of the sample under the application of the magnetic field and without any magnetic field, respectively *[35]*. Giant magnetoresistance refers to a very high value of δ_H which exceeds the value of anisotropic magnetoresistance *[35-36]*. Typical GMR device consists of two ferromagnetic slabs and one non-magnetic layer in between them. The thickness (t) of these ferromagnetic slabs and the mean free path of electrons with up and down spin channel influences on the GMR effect. When this thickness (t) value lies in between the mean free path of these two spin up and down channel, relative orientation of the magnetic moments in these two ferromagnetic slabs determines the spin scattering *[35-38]*. This scattering is weakest when the spins are aligned parallel and strongest when the magnetic moments have aligned anti-parallel. Since electrical resistance of a material is significantly affected by scattering of electrons, thus it has a strong dependence on the magnetic orientation of the atoms in the crystal. The theory of direction of current in GMR device was developed in few years after the invention of GMR effect. In 1989, Camley and Barnaś have calculated the current-in-plane (CIP) in GMR geometry using classical approximations, which flows along the layers *[39]*, while Levy and co-workers calculated the same using quantum formalism *[40]*. The theory of current perpendicular to the plane (CPP) in GMR geometry was proposed by Verlet and Fert in the year of 1993 *[41]*. Among these two, CPP geometry provides greater magnetoresistance ratio δ_H, thus has a better application regarding device sensitivity *[42]*.

1.4. History of Spintronics

Although the invention of GMR is considered as the origin of spintronics, ‘spin’ property in an elementary particle electron was discovered by German physicists Otto Stern and Walter Gerlach in 1922 *[43]*. In the original Stern-Gerlach experiment, a beam of silver atoms gets deflected in a spatially varying magnetic field, which indicates these particles have non-zero magnetic moment although electrically neutral silver atoms were considered for this experiment. In case of silver atom, all the inner electrons are paired, so that their spin and orbital angular momenta cancel out. The net spin is observed due to the outermost unpaired electron. Thus, this result proves that particles have an intrinsic angular momentum which is nearly analogous to the angular momentum of a 'classically spinning object' which can take only quantized values. Spin-sensitive tunneling transport was demonstrated for the first time from superconducting aluminum to ferromagnetic films by Meservey and Tedrow *[44]*. In 1975, for the first time, tunnel magnetoresistance (TMR) effect in a Fe/Ge/Co junction was discovered experimentally by Julliere, where he observed an increase in resistance when the magnetic layers were switched from parallel to anti-parallel configuration *[45]*. In 1988, GMR effect was jointly discovered by Albert Fert and Peter Grünberg which won the Nobel Prize in Physics in the year 2007 *[31-32]*.

At present day, magnetic random-access memory (MRAM) has become important for practical spintronics device applications. Primarily MRAM was based on the GMR effect; however, with the advancements of TMR technology, MRAM devices made a transition to TMR based structures as produced by Freescale Semiconductor and IBM *[46]*. Moreover, TMR based advanced technology has also led the memory industry to switch towards TMR-based read heads *[47]*. Lately, spin-transfer torque-MRAM (STT-MRAM) has gained lot of attention due to its new technique to control magnetization switching *[48-49]*. This STT-MRAM controls magnetization by electrical current, thus providing better scaling capabilities, and requires less switching energy. Later on, spin-transfer torque-magnetic tunnel junction (STT-MTJ) technology has received lot of researcher's attention for building logic configurations combining non-volatile memories and logic circuits *[50-51]*. In 1990, another new idea of spin field-effect transistor (spinFET) was introduced by Dutta and Das which is composed of two ferromagnetic terminals separated by non-magnetic materials *[52]*. These inventions have become very popular in spintronics industry which ignites the requirement of new spintronics materials for spintronics devices.

1.5. Spintronics Materials

1.5.1. Classification Based on Intrinsic (Electronic) Property

Spintronic materials have huge applications in modern-day spintronics devices. The fundamentally spintronic device consists of three parts namely spin source, spin drain and the channel region *[53]*. Based on the intrinsic electronic property and the density of states spintronics materials can be classified into three types *[53]*.

(1) Magnetic Metals
(2) Topological Insulator
(3) Magnetic Semiconductor

Based on the application in the spintronics device, these materials can be divided into two parts. Magnetic metals and topological insulators (TI) can be used in spin source and the spin drain while the magnetic semiconductors can be used in the channel region *[53]*.

1.5.1.1. Magnetic Metals

Magnetic metals are used mainly for the spin injection phenomenon in the spintronics device. Magnetic materials can be classified into two parts as follows:

(1) Ferromagnetic Metals
(2) Half-Metallic Ferromagnet

1.5.1.1.1. Ferromagnetic Metals

Ferromagnetic metals are the oldest spintronic materials that are used to construct magnetic tunnel junctions (MTJ) and spin-valves. Typical example of ferromagnetic metals includes Fe, Ni, Co and their alloys *[53]*. These materials are very abundant in nature, very cheap and easy to handle. They can provide spin-polarization of the carriers; however, 100%

spin-polarization cannot be achieved from these types of materials. The density of states (DOS) plot indicates (Fig. 1.3) that both the up-spin as well as down spin have contribution at the Fermi energy level.

1.5.1.1.2. Half-metallic Ferromagnet (HMF)

Half-metallic ferromagnetic are those types of materials in which on spin-channel has metallic nature while the other has semiconducting/insulating nature. The density of states (DOS) plot of the half-metallic ferromagnetic is shown in Fig. 1.3. These materials can provide 100% spin-polarization of carriers, thus can be very efficient for spin generation and injection. In 1983, Groot and Mueller proposed about half-metallic ferromagnet for the first time *[54]*. Half-metallic gap and of a half-metallic ferromagnet should be large enough to prevent the spin-flip transition efficiently due to the thermally agitation and to preserve the half-metallic nature of the materials. Moreover, the Curie temperature of the half-metallic ferromagnet should be more than room temperature for the practical application. Examples of HMF are CrO_2 *[55]* and Fe_3O_4 *[56]*.

1.5.1.2. Topological Insulators (TI)

Topological Insulators are a special type of materials with bulk band gap like original insulator originated due to strong spin-orbit coupling (SOC) and topologically protected conducting surface states (Fig. 1.4). Most importantly, these metallic conducting states are protected by time-reversal symmetry *[57]*. These new types of quantum state of matter can produce Quantum spin Hall (QSH) effect *[58]*. These new states consist of two counter-propagating, dissipationless spin currents (both spin-up and spin-down electrons) and therefore the total charge current in such material vanishes in the ground state and a pure spin current is realized, which is a very important goal in the domain of spintronics *[58]*. The topological insulator can be identified by a few rules such as SOC, an odd number of band inversions (BIs) between the conduction band (CB) and the valence band (VB) by increasing the average nuclear charge, and a change of sign of the symmetry of the molecular orbitals *[58]*. In addition to their fundamental interest, these materials could be useful for applications ranging from spintronics to quantum computation. Topological insulators can be categorized into three classes as follows:

(1) Inorganic Topological Insulator

(2) Organometallic Topological Insulator (OTI)

(3) Topological Crystalline Insulator (TCI)

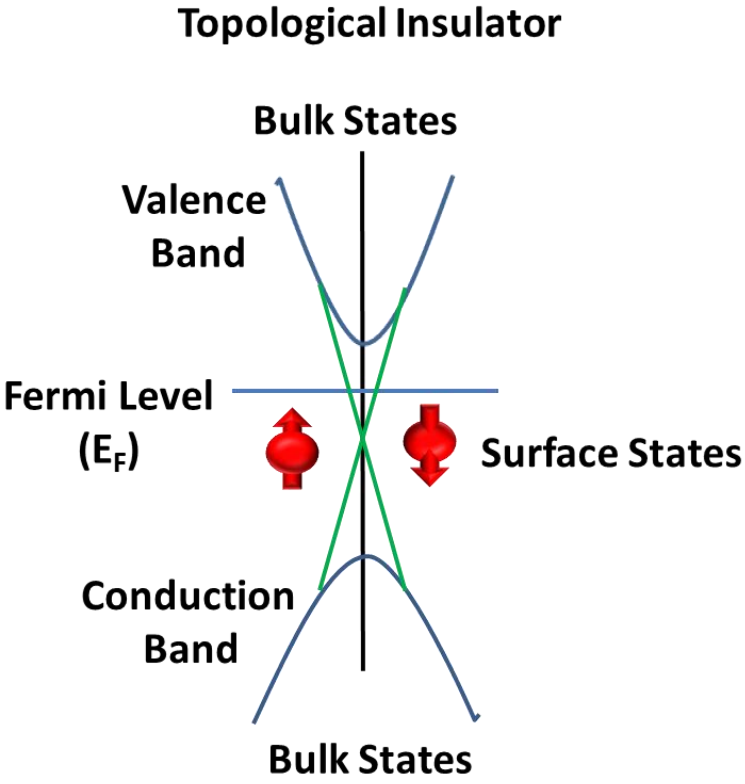

Figure 1.4: Schematic representation of the band structure of topological insulator. The Fermi level lies within the bulk band gap.

1.5.1.2.1. Inorganic Topological Insulators

Conventional topological insulators are mostly lies in the category of inorganic topological insulator. There are two large families of TIs presently known, the HgTe family and the Bi_2Se_3 family *[58]*. These topological materials have been predicted theoretically and also experimentally observed *[59]*. Typical example of such system includes HgTe quantum wells, BiSb alloys, Bi_2Te_3 and Bi_2Se_3 crystals *[60]*. The existence of edge states in HgTe/CdTe quantum wells was demonstrated from transport experiments *[60]*. Similarly, experiments on $Bi_{1-x}Sbx$, Bi_2Se_3, Bi_2Te_3, and Sb_2Te_3 establish them as 3D topological insulators by directly probing the topology of their surface states *[60]*. Several new TIs have been predicted by theory, however, only a few have been realized experimentally. This is due to the lack of high-quality samples with well-defined charge carriers and control over disorder and defects.

1.5.1.2.2. Organometallic Topological Insulators (OTI)

Organometallic topological insulators are composed of a covalent organic framework in which metal atoms are embedded in this framework. Liu and co-workers first proposed this new concept of TIs *[61]*. They have designed two organometallic lattices, namely 2D triphenyl-lead [$Pb(C_6H_5)_3$] lattice and triphenyl-bismuth [$Bi(C_6 H_5)_3$] lattice, where a metal atom was bonded with three benzene rings with 3-fold rotational symmetry *[61]*. The lattices of these types of TIs are found to be slightly bulked due to the sp^3 hybridization of Pb and Bi atoms. The Dirac point in 2D [$Pb(C_6H_5)_3$] system is found to be located exactly at the Fermi level. Magnetic transition metal incorporation in this type of covalent organic framework can lead to formation of TIs with spin-polarized Dirac cones, which are promising for realizing the quantum anomalous Hall effect. An example of this type of system is 2D triphenylmanganese [$Mn(C_6H_5)_3$] lattice *[62]*.

1.5.1.2.3. Topological Crystalline Insulators (TCI)

Topological Crystalline Insulators (TCIs) are another new class of topological materials, which are different from conventional TIs. The metallic surface states in such TCIs are protected by the crystal symmetry, for example, mirror symmetry, rather than time-reversal symmetry in conventional TIs *[53]*. Therefore, the occurrence of topological states does not require spin-orbit (SO) interaction. This type of material was first reported by Fu and co-workers *[63]*. However, TCIs only have gapless modes in high-symmetry directions or planes, and they are vulnerable to certain disorders *[53]*. Theoretically bulk SnTe was first proposed as TCI based on first-principles calculations *[64]*. The metallic surface states of SnTe with Dirac cones on high symmetry crystal surfaces [such as (001), (110), and (111)] are topologically protected by reflection symmetry of the crystal. This was verified later by a subsequent experiment *[65]*.

1.5.1.3. Magnetic Semiconductors

Magnetic semiconductors are those materials that can combine the properties and advantages of both magnets and semiconductors. The basic spintronic device consists of three regions namely: spin source, central region and spin drain *[53]*. Although magnetic semiconductors can be used as spin source or spin drain for spin generation, injection, and detection, however, mostly they are used in the central region in the spintronics device while half-metals and topological insulators are used as spin source and spin drain *[53]*. Generally, magnetic semiconductors can be divided into two main categories: diluted magnetic semiconductors (DMSs) and intrinsic magnetic semiconductors. Additionally, intrinsic magnetic semiconductors can be subdivided into four types based on different electronic and magnetic properties, such as half semiconductors (HSCs), spin gapless semiconductors (SGSs), bipolar magnetic semiconductors (BMSs), and asymmetric antiferromagnetic semiconductors (AAFMSs). Divisions of magnetic materials are given below:

(1) Diluted Magnetic Semiconductor
(2) Intrinsic Magnetic Semiconductor
    (i) Half-semiconductors (HSCs)
    (ii) Spin Gapless Semiconductors (SGSs)
    (iii) Bipolar Magnetic Semiconductors (BMSs)
    (iv) Asymmetric Antiferromagnetic Semiconductors (AAFMSs)

1.5.2. Classification Based on Intrinsic (Magnetic) Property

The origination of magnetism deals with the orbital and spin motions of electrons and the mutual interactions between the electrons based on their spin *[66]*. Magnetic materials are classified according to their response towards external magnetic fields which is also related to the interactions among their internal spin states. All matter is magnetic to varying degrees. It’s the collective long-range interaction between atomic magnetic moments, which differentiate between these materials. Fundamentally, based on the behavior of magnetic materials, they can be classified into the five major groups as follows:

1.5.2.1. Diamagnetic Materials:

Diamagnetism is a fundamental property of all matter and usually it is very weak *[66]*. Diamagnetic materials have no net magnetic moment without any applied magnetic field because diamagnetic materials are composed of atoms with no net magnetic moment due to completely filled orbital shells or absence of any unpaired electrons. However, under the influence of an applied magnetic field, it produces a magnetization (M) in the direction opposite to that of the applied field. The schematic representations of the spin orientation in diamagnetic material are presented in Fig. 1.5a.

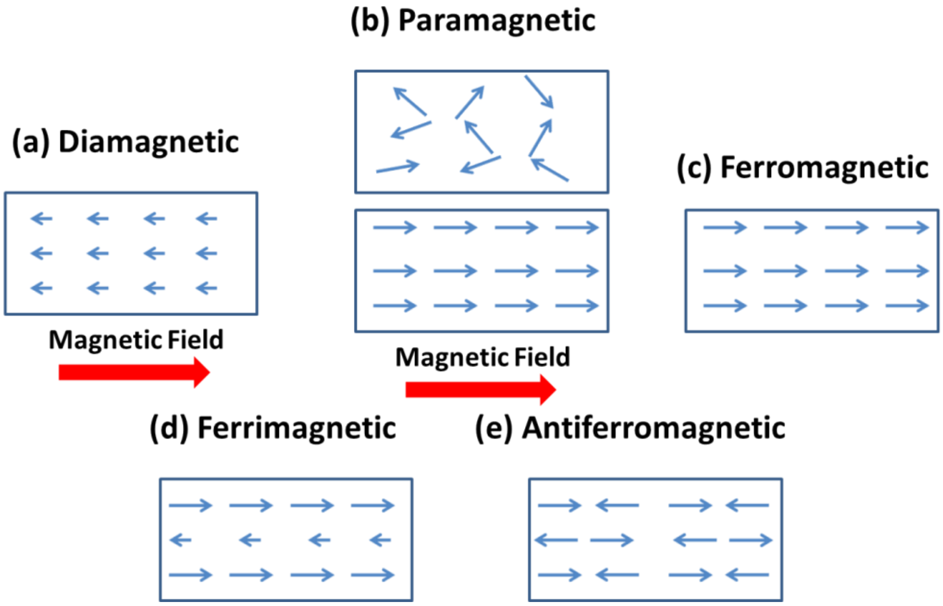

Figure 1.5: (a)-(e) Schematic representation of spin orientation in diamagnetic, paramagnetic, ferromagnetic, ferrimagnetic and anitiferromagnetic materials.

1.5.2.2. Paramagnetic Materials:

Paramagnetic materials are those materials with non-interacting localized electrons, which indicate that each atom has a magnetic moment randomly oriented as a result of thermal agitation *[66]*. Paramagnetism in a material arises from atoms, molecules, and lattice defects, possessing an odd number of electrons or unpaired electrons causing a nonzero total spin. Application of external magnetic field can create an alignment of these randomly oriented magnetic moments and thus a low magnetization is observed in the direction same as the applied field *[66]*. However, this alignment can be destroyed with the increment of temperature because it enhances the thermal agitation which can destroy the magnetic orientation. The schematic representations of the spin orientation in paramagnetic material are depicted in Fig. 1.5b.

1.5.2.3. Ferromagnetic Materials:

Ferromagnetic materials are those materials where atoms are arranged in a lattice and the atomic magnetic moments align parallel to each other due to self-interaction, resulting in spontaneous magnetic moment. This magnetic alignment can be observed even at zero applied magnetic fields *[66]*. Ferromagnetism was initially postulated by Weiss in the year of 1907 by a classical theory that assumed the presence of a molecular field within the ferromagnetic material *[66]*. Later, ferromagnetism was explained by quantum mechanics using the Heisenberg model in terms of the exchange interaction between neighboring moments *[66]*. Below a critical temperature, the magnetic alignment in ferromagnetic materials remained unaltered while above that critical temperature, thermal agitation becomes so much that it destroys these alignments turning this material into paramagnetic. This critical temperature is called the Curie temperature of the material. Above Curie temperature (T_C), the thermal agitation becomes so great that the material turns into paramagnetic *[66]*. In the strict definition, a material can be defined as ferromagnetic only if all of its magnetic ions are aligned in the same direction and add a positive contribution to the net magnetization *[66]*. We have shown the schematic representations of the spin orientation in a ferromagnetic material in Fig. 1.5c.

1.5.2.4. Ferrimagnetic Materials:

In ferrimagnetic materials, the atoms are arranged in a lattice, however, all the atomic magnetic moments are not aligned parallel to each other. As some of the magnetic ions are aligned anti-parallel, it is subtracted from the net magnetization and the material exhibits ferrimagnetism *[66]*. Fig. 1.5d depicts the schematic representations of a ferrimagnetic material along with their spin orientation. Generally, ferrimagnetism is observed only in compounds with complex crystal structures. The exchange interaction in these materials leads to parallel alignment in one sublattice while anti-parallel alignment in another sublattice. However, the magnetic moment in sublattice 1 and sublattice 2 do not completely cancel out each other, rather the magnetic moment associated with sublattice 1 is larger than sublattice 2 in ferromagnetic materials *[66]*. Therefore, ferrimagnetic materials generally have lower saturation magnetizations. However, the magnetic behaviors in ferrimagnetic and ferromagnetic materials also have very similarities.

1.5.2.5. Antiferromagnetic Materials:

Antiferromagnetic materials also have similar feature like ferrimagnetic materials. They also form magnetic domain where two sublattices exist with opposite spin alignments *[66]*. Antiferromagnetic materials can be identified as the extreme case where spins in the sublattices cancel out completely each other’s contribution exhibiting zero net magnetization (Fig. 1.5e) *[66]*. All these alignments in antiferromagnetic materials can be observed at temperatures below the Néel temperature (T_N). Above this temperature the aniferromagnetic materials become paramagnetic in nature *[66]*.

1.5.3. Classification Based on Extrinsic (Materials) Property

Based on the constitute materials, spintronics materials can be categorized into two main sections as described in the following subsections.

1.5.3.1. Metal Embedded Spintronics Materials

Conventionally transition metal based systems were considered for spintronics applications for long time because transition metals have partially filled *d* or *f* orbitals which are responsible for their magnetic character. Since main group based systems generally do not exhibit any magnetism, transition metal incorporation in main group based system can introduce magnetism in those materials. For example, (Ga, Mn)As and (In, Mn)As have been used as spintronics materials in the past years *[67-69]*. Transition metal incorporated two-dimensional (2D) metals have also attracted lot of attention in recent past for their interesting electronic and magnetic properties. Both theories as well as experimental investigations prove that that transition metals incorporation can successfully induce magnetism in the main group based 2D systems which are non-magnetic in nature *[70-71]*. Moreover, after the successful synthesization of 2D graphene and graphene-like nanosheets, researchers have started paying attention to designing novel magnetic materials by doping transition metal into graphene, graphitic carbon nitride (gt-C_3N_4) and graphene-like similar 2D materials *[70, 72-75]*.

1.5.3.2. Metal Free Spintronics Materials

Metal free spintronics materials are another important class because they can provide very long spin-relaxation time. Metal free systems are mostly composed of main group based elements which are mainly *s* or *p*-electron-based systems. Such systems have very weak spin-orbit coupling which is the main reason for longer spin-relaxation time compared to metal based systems. However, most of the main group based 2D materials are nonmagnetic, which limits their application for magnetic devices. Therefore, researchers have thought of several effective methods such as application of electric field, surface adsorption, edge modification, strain engineering, defect engineering and substitutional doping to induce magnetism into non-magnetic materials *[76]*. Introduction of magnetism in atomically patterned graphene nanoribbons has already been predicted theoretically as well as experimentally and these reports also showed a pathway to the advancement of next-generation metal-free spintronics materials *[77-80]*. However, it is found to be very difficult to synthesize such patterned structures and there is a high chance of formation of random functionalization of host structure. Therefore, researchers have tried several ways to induce magnetism in metal-free two dimensional systems. Researchers have used electron or hole doping in graphene and graphene-like 2D materials for the introduction of magnetism in such systems *[81-83]*.

1.6. Importance of Half-Metallic Materials

Among all the magnetic materials, half-metals have become very important because of its 100% spin-polarization. Until now, many efforts have been dedicated to design half-metallic compounds. Traditionally, several three dimensional (3D) materials such as in transition metal oxides, double perovskites, and Heusler alloys have been established as half-metallic materials *[84]*. Half-metallicity can be validated experimentally by measuring the degree of spin polarization around the Fermi level via point contact Andreev reflection *[85]*, spin-resolved photoelectron spectroscopy *[86]*, spin-polarized electron tunneling *[87]*.

Generally, half-metallicity can be achieved only when the two conditions occur simultaneously, one is metallicity in one spin channel and semiconducting/insulating in another spin channel and the other is the integer spin magnetization per unit cell *[76]*. However, general rules regarding the compositions or structures to design half-metals have not been found yet. Therefore, first-principles calculations based on density functional theory have become a powerful tool to explore the possibility of half-metallicity in diverse structures with different compositions. Moreover, experimental modelling of such materials needs many trials which are very costly. Hence, computational modelling is very crucial before experimental investigation.

Half-metallic materials can be very much beneficial for several spintronics devices, particularly for GMR device with non-magnetic materials sandwiched between ferromagnetic/half-metallic slabs. In GMR, the value of magnetoresistance (MR) is defined as the relative change in resistance (or conductance G) between parallel (↑↑) and antiparallel (↑↓) configurations as follows:

$$MR = \frac{R\ (\uparrow\downarrow) - R\ (\uparrow\uparrow)}{R\ (\uparrow\uparrow)} \tag{1.2}$$

$$= \frac{G\ (\uparrow\uparrow) - G\ (\uparrow\downarrow)}{G\ (\uparrow\downarrow)} \tag{1.3}$$

According to the equation described above, it is assumed the spins do not change direction while passing through the layers in GMR. Now, this magnetoresistance (MR) can be described by the Jullière formula as below *[88]*.

$$MR = \frac{2P^2}{1-P^2} \tag{1.4}$$

where ‘P’ denotes the spin polarization at the Fermi level (E_F) of the ferromagnetic/half-metallic layer.

$$P = \frac{DOS_{\uparrow}(E_F) - DOS_{\downarrow}(E_F)}{DOS_{\uparrow}(E_F) + DOS_{\downarrow}(E_F)} \tag{1.5}$$

In the case of ferromagnetic materials $P < 0$, however, for half-metals $P = 1$, and thus, infinite MR can be observed in GMR device consists of half-metals as predicted by R. A. de Groot and co-workers *[89]*. Therefore, numerous applications have been implemented based on half-metallic materials. In industry, these materials have a huge prospective in magnetic random access memory (MRAM) device.

1.7. Role of Dimensionality on Spintronics

At the beginning of spintronics, researchers have mostly investigated three-dimensional half-metallic materials (transition metal oxides, double perovskites, and Heusler alloys) for spintronics applications *[84]*. With the increment of data processing speed and integration density in the semiconductor industry, need for low dimensional half-metallic materials has been drastically enhanced.

Low-dimensional materials generally refer to those systems where materials are confined in only two, one or zero dimensions (Fig. 1.6). The successful synthesis of two-dimensional (2D) graphene introduces a new horizon to low dimensional materials. After that several 2D and 1D (e.g. nanotube, nanoribbon) and 0D systems (e.g. nanoclusters, quantum dots) have been investigated for many applications.

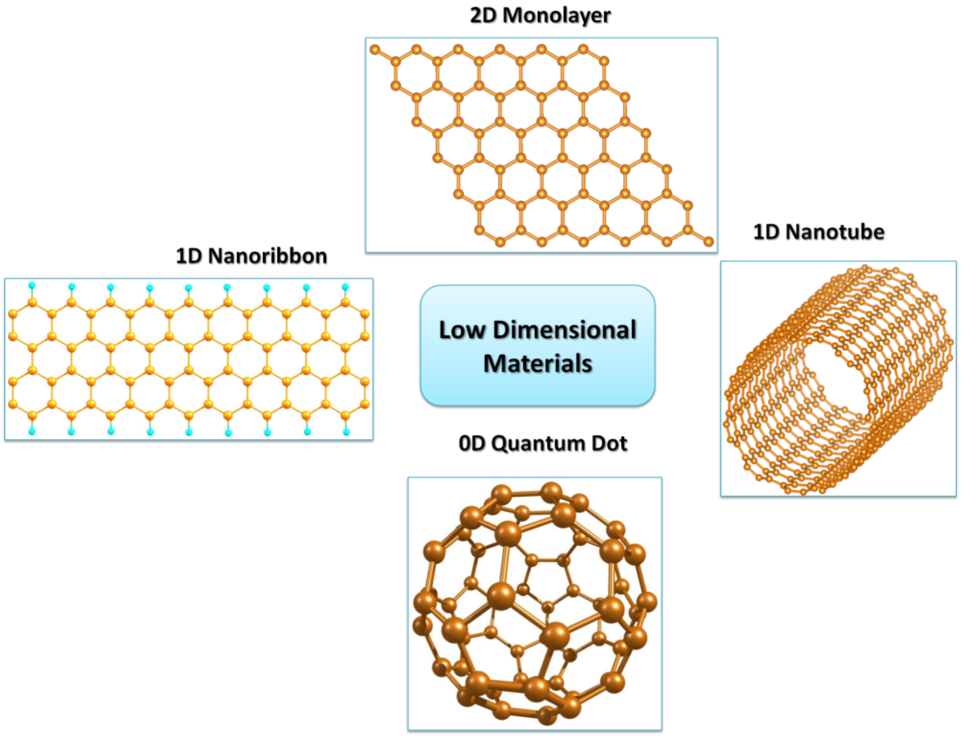

Figure 1.6: Carbon based low dimensional (2D graphene, 1D carbon nanotube and graphene nanoribbon and 0D fullerene) materials.

Although, achieving ferromagnetism and half-metallicity in low-dimension materials is very difficult, researchers have investigated several low dimensional materials such as single-layer graphene, graphitic carbon nitride, hexagonal boron nitride (h-BN), silicon carbide (SiC), transition metal di-chalcogenides, transition metal di-halides, transition metal tri-halides, silicene and their nanoribbons, and nanotubes structures for spintronics applications *[90-91]*.

1.8. Molecular Spintronics

Molecular spintronics is an interdisciplinary domain where organic spintronics, molecular magnetism, molecular electronics and quantum computing merge together to provide a new advanced technology *[92]*. Traditionally bulk and 2D materials have been used for spintronics application. However, there is a constant search for new materials in the domain of spintronics. The conventional electronics industry has already experienced a performance improvement over the past half-century due to miniaturization of their 'top-down' manufactured components *[93]*. There is another interesting approach, namely 'bottom-up' fabrication of molecular components by which miniaturization can be possible without compromising the performance of the device *[93]*. In 1974, Arieh Aviram and Mark A. Ratner proposed for the first time that a molecule could act as a rectifier *[93]*, and in mid-1990 charge transport through single molecule was measured *[93]*. Molecular spintronics proposes to use molecules to perform spintronic functions and spin-related transport in molecular magnetic devices for conventional applications and beyond *[92]*. The fundamental motivation in molecular spintronics has begun due to their long spin lifetime and weak spin scattering mechanisms, which made them the ideal materials to store and manipulate the spin information *[94]*. Molecular spintronics device is generally composed of a molecule sandwiched between two electrodes (electrode-molecule-electrode). Researchers have already reported several molecule-based spintronics devices such as single-molecule-magnet (SMM), and spin-valve which are very important for next-generation spintronics *[92, 93]*. Therefore, molecular spintronics is a fascinating playground for scientists to investigate spins related phenomena, which may be used in next-generation memory industry.

1.9. Theory

We have concisely described the fundamental theories and computational techniques used in our works in this part of the thesis. Density functional theory (DFT) is one of the most powerful and popular tool for computations of the quantum state of atoms, molecules and solids. It's been past 30 years, since DFT has been used as dominant method for quantum mechanical simulations of periodic systems. Nowadays it is routinely applied for investigation of structural, electronic, magnetic properties, stability analysis of two dimensional and one dimensional materials.

1.9.1. The Many-Body Problem

Solid-state materials consist of numerous atoms which have built up with a few hundreds of self-interacting electrons and nuclei. These basic interactions that occur between the electrons-electron, electron-nuclei or nuclei-nuclei are due to electrostatic or Coulomb interaction. Quantum mechanically these electrons should be described by time-independent non-relativistic Schrödinger equation. Since the electrons in any solid state materials move at speeds much less than the speed of light, non-relativistic Schrödinger equation is used. In 1926, Schrödinger proposed the most important equation to describe any quantum particle, based on the concepts of the uncertainty principle, wave-particle duality and energy quantization according to the given equation:

$$\left[-\frac{\hbar^2\nabla^2}{2m_e} + \mathrm{v}(r)\right]\Psi(r) = \mathrm{E}\Psi(r) \tag{1.6}$$

Here, in this above equation (1.6), $\Psi(r)$ is denoted as the wave function of electron, $V\ (r)$ as the potential energy of that electron and E is the total energy of the electron/particle. The parameter m_e and r denote the mass and position of the electron respectively. In addition, $\hbar$ denotes $\frac{h}{2\Pi}$, where h is the Plank constant. Most commonly this equation can be written as

$$H\Psi(r) = \mathrm{E}\Psi(r) \tag{1.7}$$

This Hamiltonian of this above equation can only be solved for the single electron system. For any multi-electron systems this equation becomes,

$$\mathrm{H}\Psi(r_1, r_2 \ldots, r_N) = \mathrm{E}\Psi(r_1, r_2 \ldots, r_N) \tag{1.8}$$

Here N in equation (1.8) is the number of electrons. It is practically impossible to solve Schrödinger equation. Density functional theory (DFT) is a clever way to solve the Schrödinger equation for such multi-electron system which is found in any practical solid-state material. It is a rigorous, way of approaching any interacting problem, by mapping it exactly to a much easier-to-solve non-interacting problem. To achieve that aim, the complex many-body wave function, which is the solution of the Schrodinger equation, is solved from the density which only depends on the spatial coordinates. The energy is just a function of this function, (i.e., a density functional). Most commonly, using this methodology, the ground-state electronic structure problem is solved. This formulation which describes any real system by an effective one-body system, was given by Kohn, Hohenberg, and Sham in the 1960's. For many-electron system, the Hamiltonian operator (H) can be written as follows:

$$\mathrm{H} = \mathrm{T_e} + \mathrm{T_n} + \mathrm{V_{ee}} + \mathrm{V_{nn}} + \mathrm{V_{ne}} \tag{1.9}$$

Here, $\mathrm{T_e}$ denotes the kinetic energy of the electrons, $\mathrm{T_n}$ represents the kinetic energy of the nucleus, $\mathrm{V_{ee}}$, $\mathrm{V_{nn}}$, and $\mathrm{V_{ne}}$ are the potential energy derived from the electrons-electrons, nucleus-nucleus and electron-nucleus interactions; respectively. Therefore, the Hamiltonian can be written as:

$$H = -\frac{h^2}{2m_e}\sum_i \nabla_i^2 - \sum_I \frac{h^2}{2M_I}\nabla_I^2 + \frac{1}{2}\sum_{i\neq j}\frac{e^2}{|\boldsymbol{r}_i - \boldsymbol{r}_j|} + \frac{1}{2}\sum_{I\neq J}\frac{Z_I Z_J e^2}{|\boldsymbol{R}_I - \boldsymbol{R}_J|} - \sum_{i,I}\frac{Z_I e^2}{|\boldsymbol{r}_i - \boldsymbol{R}_I|} \tag{1.10}$$

In the above equation (1.10), m_e and $\boldsymbol{r}_i$ are the mass and position of the electron respectively. The parameters M_I, R_I and Z_I in (1.10) define mass, position and nuclear charges of nuclei respectively. The kinetic energy of electrons and nuclei are represented by first and second terms in the equation (1.10), respectively. The remaining terms in the equation (1.10) denote the potential energy which originates due to electron-electron repulsion, nuclei-nuclei repulsion and electron-nuclei attraction, respectively. However, solving the Schrödinger equation with this Hamiltonian is nearly impossible for any many-body system. Therefore, some approximation needs to be considered to solve this issue. For this purpose, Born-Oppenheimer (BO) approximation has been introduced in the year of 1927 by Max Born and J. Robert Oppenheimer *[95]*.

1.9.1.1. The Born-Oppenheimer Approximation

The Born-Oppenheimer (BO) Approximation is an approximation that has been used in the field of quantum chemistry, molecular physics and solid state physics for long time. With this approximation, the atomic nuclei and the electrons are treated separately. Atoms in any system consist of two parts, one is electronic part and another is nuclear part. BO approximation considers a large difference in the time's scales of the motion of nuclei and electron corresponding to the large difference in their mass (nucleus is 1836 times heavier than that of the electron). Hence, the kinetic energy of the nuclei can be neglected compared to the kinetic energy of electron. According to BO approximation, the wavefunction of any molecule can be expressed as product of electronic and nuclear part as follows:

$$\Psi_{Total} = \Psi_{Electronic}\Psi_{Nucler} \qquad (1.11)$$

Therefore, this method enables us to separate the Hamiltonian operator into electronic and nuclear terms, in which cross-terms between electrons and nuclei are neglected, thus, the smaller and decoupled systems can be solved more efficiently. Finally considering this BO approximation, the Hamiltonian of the electron can be expressed as follows:

$$H = -\frac{h^2}{2m_e}\sum_i \nabla_i^2 + \frac{1}{2}\sum_{i\neq j}\frac{e^2}{|\boldsymbol{r}_i - \boldsymbol{r}_j|} - \sum_{i,I}\frac{Z_I e^2}{|\boldsymbol{r}_i - \boldsymbol{R}_I|} \qquad (1.12)$$

After applying the BO approximation, the solution of equation (1.7) still remains very complex for any many-body system. Hence, some more approximation is needed to find the solution of equation (1.7). This is done by Hartree-Fock theory which imagines a many-body system as non-interacting electrons in some effective potential, chosen somehow to mimic the actual electronic system. Since the electrons are non-interacting, their coordinates can decouple, and their wave function can be expressed simply as the product of one-electron wave functions. For this reason, we need to solve a much simpler 3D equation with only three coordinates, even with many N electrons system, as opposed to a 3N-coordinate Schrödinger equation.

1.9.1.2 Hartree-Fock Theory

The Hartree–Fock theory is a self-consistent field (SCF) method by which it approximates an exact N-body wave function to an N non-interacting electronic system by a single Slater determinant. This theory is based on the variational principle. Hartree-Fock theory based on an ansatz for the Ψ that it an antisymmetric product of functions (ϕ_i) each of which depends on the coordinates of a single electron:

$$\Psi_{HF} = \frac{1}{\sqrt{N!}} det[\phi_1 \phi_2 \phi_3 \dots \phi_N] \qquad (1.13)$$

where 'det' is the matrix determinant in the equation (1.13). Expression of Hartree-Fock energy can be found by substituting this Ψ_{HF} into the Schrödinger equation:

$$\begin{aligned} \mathrm{E}_{HF} = & \int \phi_i^*(r) \left(-\frac{1}{2} \sum_i^N \nabla_i^2 + V_{ext} \right) \phi_i(r)\, dr \\ & + \frac{1}{2} \sum_{i,j}^N \int \frac{\phi_i^*(r_1)\phi_i(r_1)\phi_j^*(r_2)\phi_j(r_2)}{|r_i - r_j|} dr_1 dr_2 \\ & - \frac{1}{2} \sum_{i,j}^N \int \frac{\phi_i^*(r_1)\phi_j(r_1)\phi_i(r_2)\phi_j^*(r_2)}{|r_i - r_j|} dr_1 dr_2 \end{aligned} \qquad (1.14)$$

Here, the second term corresponds to the classical Coulomb interaction and the third term corresponds to the exchange energy. The parameter V_{ext} in the first term indicates the electron-nuclei attraction as follows:

$$V_{ext} = \sum_{i,I} \frac{Z_I e^2}{|\boldsymbol{r}_i - \boldsymbol{R}_I|} \tag{1.15}$$

The ground state orbitals can be determined by applying the variational theorem to the Hartree-Fock energy as expressed in the equation (1.14) with the condition that the orbitals are orthonormal. Therefore, the Hartree-Fock equations can be found as:

$$\left[-\frac{1}{2}\nabla^2 + V_{ext}(r) + \int \frac{\rho(r')}{|r-r'|} dr'\right] \phi_i(r) + \int v_X(r,r')\, \phi_i(r') dr' = \varepsilon_i \phi_i(r) \tag{1.16}$$

where $\int \frac{\rho(r')}{|r-r'|} dr'$ term denotes Hartree potential and $v_X(r,r')$ denotes the non-local exchange potential such that

$$\int v_X(r,r')\, \phi_i(r') dr' = -\sum_j^N \int \frac{\phi_j(r)\phi_j^*(r')}{|r-r'|} \phi_i(r') dr' \tag{1.17}$$

The Hartree-Fock equations above in (1.16) describe a fictitious system of non-interacting electrons under the influence of a mean field potential consisting of the classical Coulomb potential and a non-local exchange potential.

However, accurate solutions need a very flexible description of the wavefunction's spatial variation; thus, a large basis set is required. Therefore, it becomes computationally very costly for practical calculations. Moreover, the calculated energy of any system using HF theory is always higher than that of the real energy of the system. This may be due to the consideration of the average electronic field in which some amount of the electron-electron correlations is omitted. Therefore, direct solution of the Schrödinger equation is not feasible for systems in condensed matter science. This has become a major motivation for the development some new approach that can solve this issue and it has been found that the use of density functional theory can solve this problem.

1.9.2. Density Functional Theory (DFT)

Density functional theory (DFT) is a quantum-mechanical approach, which is used extensively nowadays to investigate the electronic structure and properties of many-body systems. According to DFT, to compute the total energy of any many-body system, 3N dimensional wavefunction need to not be solved. The ground state energy can be determined by the diagonal elements of the first order density matrix i.e, the charge density. Therefore, this theory is the derived from of the N-particle Schrödinger equation and ground state can be expressed in terms of the density distribution of the single particle wave function. At the first time, Thomas-Fermi proposed the first version of DFT with the relation between an external potential $v(r)$ and the density distribution $\rho(r)$, where interacting electrons are moving in an external potential $v(r)$:

$$\rho(r) = \gamma\left(\mu - v_{eff}(r)\right)^{3/2} \tag{1.18}$$

$$v_{eff}(r) = v(r) + \int \frac{\rho(r')}{|r-r'|} dr' \tag{1.19}$$

where $\gamma = \frac{1}{3\pi^2}\left(\frac{2m}{\hbar^2}\right)^{3/2}$ and μ is the r dependent chemical potential. This model was predicted for ideal free electron gaseous molecules which are the examples of the non-interacting system. Later on, P. Hohenberg and W. Kohn proposed two theorems which are very crucial for the DFT calculations *[96-97]*.

1.9.2.1. The Hohenberg-Kohn Theorems

Hohenberg and Kohn theorems started from Thomas-Fermi theory and establish the connection between the electron density with the many-electron Schrödinger equation. These two theorems as proposed by P. Hohenberg and W. Kohn are described below:

Theorem 1: The first theorem states that the ground state density $n(\boldsymbol{r})$ of a bound system of interacting electrons moving under the influence of the external potential of $V_{ext}(\boldsymbol{r})$ determines this potential uniquely. Therefore, the ground state properties of many electron systems can be estimated from the electron density $n(\boldsymbol{r})$ of the interacting electrons under the influence of the external potential of $V_{ext}(\boldsymbol{r})$. The ground-state energy of Schrödinger's equation is the functional of the electron density $n_0(\boldsymbol{r})$. In mathematics, functional refers to mapping from space X to real numbers.

Thus, in a simple way it can be stated that a functional assigns a number to a function.

Theorem 2: The second theorem states that electronics ground state can be calculated by variational principle as follows:

$$E_{GS} = min_{\psi}\langle\psi|H|\psi\rangle \tag{1.20}$$

where E_{GS} denotes the ground state energy, H and ψ denote Hamiltonian and ground state wave function respectively. According to this theorem total energy functional can be expressed in terms of electron density $n(\boldsymbol{r})$ and external potential $V_{ext}(\boldsymbol{r})$ as follows:

$$E[\rho(\boldsymbol{r})] = E_{HK}[\rho(\boldsymbol{r})] + \int V_{ext}(\boldsymbol{r})\rho(\boldsymbol{r})d\boldsymbol{r} \geq E_{GS} \tag{1.21}$$

where, $E_{HK}[\rho(\boldsymbol{r})]$ denotes the internal and kinetic energies of the all interacting particles of the systems. Therefore, ground state energy of any system can be obtained only if the functional of the electron density, which actually minimizes the energy of the system, become the true ground state density $n_0(\boldsymbol{r})$.

1.9.2.2. The Kohn-Sham Equations

Kohn-Sham equations are also self-consistent equation which has the same structure as obtained in the Hartree-Fock equation (Eqn 1.16). However, here the non-local exchange potential is replaced by the local exchange-correlation potential V_{xc}. Energy functional in the Schrödinger equation contains three terms: the kinetic energy term, the interaction with the external potential and the electron-electron interaction and it can be written according to the given equation:

$$E[\rho] = T[\rho] + V_{ext}[\rho] + V_{ee}[\rho] \tag{1.22}$$

Kohn and Sham introduced a fictitious system of N non-interacting electrons to be described by a single determinant wavefunction in N orbitals ϕ_i. In this system kinetic energy and electron density can be expressed as:

$$T_s[\rho] = -\frac{1}{2}\sum_i^N\langle\phi_i|\nabla^2|\phi_i\rangle \tag{1.23}$$

The suffix in the equation (1.23) represents that this is not original kinetic energy of the system rather it is the kinetic energy of non-interacting electrons which reproduce the ground state density

$$\rho(r) = \sum_i^N |\phi_i|^2 \tag{1.24}$$

The interaction with the external potential can be expressed as:

$$V_{ext}[\rho] = \int V_{ext}(\boldsymbol{r})\rho(\boldsymbol{r})d\boldsymbol{r} \tag{1.25}$$

The electron-electron interaction is the classical Coulomb interaction or Hartree energy:

$$V_{ee}[\rho] \;\cong\; V_H[\rho] = \frac{1}{2}\iint \frac{\rho(r_1)\rho(r_2)}{|r_1 - r_2|} dr_1 dr_2 \tag{1.26}$$

Therefore, this energy functional can be rewritten as follows:

$$E[\rho] = T_s[\rho] + V_{ext}[\rho] + V_H[\rho] + E_{xc}[\rho] \tag{1.27}$$

Here new term E_{xc} is introduced in the equation which represents the error due to non-interacting kinetic energy and the error due to treating electron-electron interaction classically.

$$E_{xc}[\rho] = (T[\rho] - T_s[\rho]) + (V_{ee}[\rho] - V_H[\rho]) \tag{1.28}$$

Therefore, the Schrödinger equation can be rewritten as:

$$\left[-\frac{1}{2}\nabla^2 + V_{ext}(r) + \frac{1}{2}\iint \frac{\rho(r_1)\rho(r_2)}{|r_1 - r_2|} dr_1 dr_2 + v_{xc}(r)\right]\phi_i(r) = \varepsilon_i \phi_i(r) \tag{1.29}$$

Here, a local multiplicative potential is introduced which is the functional derivative of the exchange-correlation energy with respect to density

$$v_{xc}(r) = \frac{\delta E_{xc}[\rho]}{\delta \rho} \tag{1.30}$$

Therefore, the Kohn-Sham equation can be written as follows:

$$\left[-\frac{1}{2}\nabla^2 + V_{KS}(r)\right]\phi_i(r) = \varepsilon_i \phi_i(r) \tag{1.31}$$

where $V_{KS}(r)$ can be defined as follows:

$$V_{KS}(r) = V_{ext}(r) + V_H(r) + V_{xc}(r) \tag{1.32}$$

This Kohn-Sham equation is used extensively both in molecular as well as solid state problems *[98]*.

1.9.2.3. Exchange-correlation Functional

The exchange-correlation term in the Kohn-Sham equation (equation 1.27) is can be separated into exchange and correlations contributions, which are as follows:

$$E_{xc}(\rho) = E_x(\rho) + E_c(\rho) \tag{1.33}$$

$$=> E_{xc}\big(n(\boldsymbol{r})\big) = E_x\big(n(\boldsymbol{r})\big) + E_c\big(n(\boldsymbol{r})\big) \tag{1.34}$$

The Dirac form is used for exchange contributions

$$E_x(\rho) = -C\rho^{1/3} \tag{1.35}$$

Where C is a free constant and can be expressed as $C = -\frac{3}{4}\left(\frac{3}{\pi}\right)^{1/3}$, determined for the homogeneous gas. Functional for correlation energy is solved by numerical quantum Monte Carlo simulation. The result is fitted by a number of analytic forms and it is found that all of these yield similar results which are collectively referred as LDA functionals.

1.9.2.4. Local Density Approximation (LDA)

In the Local Density Approximation (LDA), the exchange-correlation functional can be expressed as follows *[99-100]*,

$$E_{xc}^{LDA} = \int d^3r\, n(\boldsymbol{r})\, \varepsilon_{xc}^{hom}(n(\boldsymbol{r})) \tag{1.36}$$

Where, $\varepsilon_{xc}^{hom}(n(\boldsymbol{r}))$ is the average exchange-correlation energy of homogeneous gas as considered in the approximation with the electron density $n(\boldsymbol{r})$.

Compared to the Hartree-Fock method, LDA approximation gives better results and it has been used widely for determination of the stable ground state properties of the solid state materials. This LDA approximation gives best result for the system with slowly varying charge density. It can also give considerably appropriate result where the charge density varies rapidly. However, LDA has some limitations in the calculation of thermodynamic and electronic properties when the charge density varies very quickly. For instance, it overestimates cohesive energy, adsorption energy and bulk moduli over experimental values while underestimates lattice contacts and band gap of semiconductor and insulator over experimental values *[101]*.

To perform the magnetic calculation for magnetic materials, spin-polarized DFT needs to be introduced. Moreover, magnetism in any materials has a large influence on the competition between exchange energy and kinetic energy. Hence, exchange-correlation functional also needs to be modified considering the effect of spin-resolved arrangements of electrons. Considering this effect, the LDA functional becomes local spin-density approximation (LSDA) *[102]*,

$$E_{xc}^{LDA}[n_{\uparrow}, n_{\downarrow}] = \int \mathcal{E}_{xc}(n_{\uparrow}, n_{\downarrow})n(\boldsymbol{r})d^3r \tag{1.37}$$

However, researchers have found some drawback in both LDA and LSDA method that it assumes an almost constant electron density everywhere resulting overestimation of exchange-correlation energy *[102]*. Terkura and co-workers also observed that LSDA is not good enough to estimate the magnetic properties of metal, oxide and insulator properly *[100]*. Therefore, some corrections need to be included in the exchange-correlation functional which is referred to as generalized gradient approximations (GGA).

1.9.2.5. Generalized Gradient Approximation (GGA)

Instead of using the electron density, Generalized Gradient Approximation (GGA) method uses the gradient of electron density for the calculation of the exact exchange energy *[103]*. Thus, the exchange-correlation function can be expressed as follows:

$$E_{xc}^{GGA} = \int d^3r\, n(\boldsymbol{r})\, \mathcal{E}_{xc}^{GGA}\big(n(\boldsymbol{r}), \nabla n(\boldsymbol{r})\big) \tag{1.38}$$

The GGA is a more efficient method that works well for the systems with rapidly varying electron density. It has been observed that GGA provides accurate results while calculating the lattice parameters, total energies, and adsorption energies, etc. The regularly used GGA method has been developed by Perdew, Burke and Ernzerhof (PBE). The exchange energy of PBE approximation can be expressed as:

$$E_{x}^{PBE} = \int d^3r\, n(\boldsymbol{r})\, \mathcal{E}_{x}^{PBE}\big(n(\boldsymbol{r}), s(\boldsymbol{r})\big) \tag{1.39}$$

The PBE exchange energy density depends on the parameter $s(\boldsymbol{r})$ which is the product of LDA exchange and enhancement factor F_x^{PBE} .

$$\varepsilon_x^{PBE}\big(n(\boldsymbol{r}), s(\boldsymbol{r})\big) = \varepsilon_x^{LDA}\big(n(\boldsymbol{r})\big) * F_x^{PBE}\ \big(s(\boldsymbol{r})\big) \tag{1.40}$$

The spin-polarized counterpart of the GGA exchange-correlation functional can be expressed with the following form:

$$E_{xc}^{GGA}[n_\uparrow, n_\downarrow] = \int \varepsilon_{xc}\ (n_\uparrow, n_\downarrow \vec{\nabla}_{n_\uparrow}, \overrightarrow{\nabla}_{n_\downarrow}) n(\vec{r}) d^3 r \tag{1.41}$$

Several other GGA approximations are also used extensively such as Perdew-Wang 91 (PW91), revised PBE (RPBE), and Perdew-Burke-Ernzerhof for solids (PBEsol), etc. *[103,104-106]*.

However, both of these LSDA and GGA methods are failed produce accurate results for the systems with strongly correlated electrons. This type of strong correlation generally observed in the partially filled *d* and *f* orbitals. In such case, Hubbard potential ‘U’ is introduced to describe the strongly correlated electrons in the partially filled *d* and *f* subshells. This method is named as GGA+U method *[107-110]*.

1.9.2.6. DFT+U/GGA+U Method

The basic concept behind DFT+U is to consider the strong on-site Coulomb interaction of localized electrons with an additional Hubbard-like term, which is not accurately described by LDA or GGA. Although these on-site Coulomb interactions are particularly strong for localized *d* and *f* electrons, however, it can be also important for *p* localized orbitals. Generally, the strength of the on-site interactions are described by U (on site Coulomb) and J (on site exchange) parameters. Even though these U and J parameters can be extracted from ab initio calculations, usually these are obtained semi-empirically. Within GGA+U approach, the total energy of the system can be represented as follows:

$$E = E_{LDA/GGA} + \sum_I \left[\frac{U^I}{2} \sum_{m,\sigma \neq m'\sigma'} n_m^{I\sigma} n_{m'}^{I\sigma'} - \frac{U^I}{2} n^I (n^I - 1)\right] \tag{1.42}$$

where, $n_m^{I\sigma} = n_{mm}^{I\sigma}$, $n^I = \sum_{m,\sigma} n_m^{I\sigma}$, and the index m labels the localized states of the same atomic site I. The second term and the third term in the equation (1.42) denotes the Hubbard term and double-counting terms respectively. This GGA+U method improves excited-state properties of such as energy gaps, and ground-state magnetic properties such as magnetic moments and interatomic exchange parameters. It is very important to choose proper 'U' values for any particular system as it directly affects the computational results.

1.9.2.7. Hybrid Functional

Hybrid functional provides better approximations to the exchange and correlation energy compared to standard density functional LDA and GGA. Thus, the hybrid functional improves the total energy of any system. In LDA and GGA, the Coulomb term does not cancel with its exchange term, leading to the self-interaction error. Hybrid functional incorporates Hartree-Fock exchange term with the LDA/GGA functional to reduce the self-interaction term which leads to more accurate description of total energy *[111]*. Therefore, Hybrid functional is a combination of Hartree-Fock (HF), Generalized Gradient Approximation (GGA) and Local Spin-Density Approximation (LSDA).

Here most frequently used hybrid functionals are given below:

a) **B3LYP:** It has been found that the B3LYP functional can predict successfully a wide range of molecular properties. However, it cannot accurately predict the properties of periodic systems, due to the failure to attain the exact homogeneous electron gas limit and semiempirical construction of the functional *[112]*. The B3LYP (Becke, 3-parameter, Lee-Yang-Parr) exchange-correlation functional can be expressed as:

$$E_{xc}^{B3LYP} = E_x^{LDA} + a_0(E_x^{HF} - E_x^{LDA}) + a_x(E_x^{GGA} - E_x^{LDA}) \\ + E_c^{LDA} + a_c(E_c^{GGA} - E_c^{LDA}) \tag{1.43}$$

where, $a_0 = 0.20$, $a_x = 0.72$, and $a_c = 0.81$. E_x^{GGA} and E_c^{GGA} are Becke 88 exchange functional within GGA and correction functional of Lee, Yang and Parr for B3LYP. E_c^{LDA} is the VWN LDA to the correlation functional.

b) **PBE0:** The PBE0 functional was first developed by mixing 75% GGA PBE exchange with 25% HF exchange by Adamo and Barone

[113]. The exchange-correlation functional for PBE0 can be expressed as follows:

$$E_{xc}^{PBE0} = \frac{1}{4}E_x^{HF} + \frac{3}{4}E_x^{PBE} + E_c^{PBE} \tag{1.44}$$

The first and second term in the equation (1.44) denotes HF exchange and exchange from GGA-PBE functional. The third term E_c^{PBE} is the PBE correlation functional.

c) **HSE:** This HSE functional was first developed by Heyd, Scuseria, and Ernzerh which uses an error function screened Coulomb potential to calculate the exchange energy to improve the GGA-PBE functional, HSE functional proved to be very efficient particularly for metallic systems. Most commonly this functional is used to predict the band gap of semiconductors as it predicts band gap values close to the experimental values *[114]*. The exchange correlation energy for HSE functional can be expressed as:

$$E_{XC}^{PBEh} = aE_X^{HF,SR}(\omega) + (1-a)E_X^{PBE,SR}(\omega) + E_X^{PBE,LR}(\omega) + E_c^{PBE} \tag{1.45}$$

where, a is the mixing parameter and ω is the adjustable parameter for controlling the short-ranginess of the interaction. Most commonly a = 1/4 and ω= 0.2 is taken which is referred to as **HSE06** functional.

1.9.2.8. Projector Augmented Wave (PAW) Method

The Projector Augmented Wave (PAW) Method is a technique that is used to describe the interaction between ion and core electrons during *ab initio* electronic structure calculations. It is a combination of the ultra-soft pseudopotential and linear augmented-plane-wave methods which can perform with greater computational efficiency. Atomic wavefunctions are mutually orthogonal since all the atomic wavefunctions are eigenstates of the atomic Hamiltonian. Generally, the core electrons are almost unaffected by the chemical environment of an atom. Thus, valence states wavefunctions must oscillate rapidly near the core region to maintain the orthogonality of wavefunctions. The large kinetic energy generated due to the fast oscillation of valence wavefunctions in the core region is balanced by large potential energy due to the strong Coulomb attraction. Generally the valence electrons are described by plane wave basis set. However, it is computationally difficult to represent the rapidly varying valence wavefunction near the core region by plane waves. The PAW method solves this problem transforming these rapidly oscillating wavefunctions near the core region into smooth wavefunctions which are more computationally convenient *[115]*.

The linear transformation operator (T), transforms the all electron wave function, Ψ_n to a pseudo wave function, $\widetilde{\Psi}_n$ as follows

$$|\Psi_n\rangle = T|\widetilde{\Psi}_n\rangle \tag{1.46}$$

Around each atom, both of these $|\Psi_n\rangle$ and $|\widetilde{\Psi}_n\rangle$ can be expanded as linear combination of partial waves for each augmentation regions,

$$|\Psi_n\rangle = \sum_i c_i |\phi_i\rangle \tag{1.47}$$

$$|\widetilde{\Psi}_n\rangle = \sum_i c_i |\tilde{\phi}_i\rangle \tag{1.48}$$

The transformation operator, T is written as

$$T = 1 + \sum_i (|\phi_n\rangle - |\tilde{\phi}_n\rangle) \langle \tilde{p}_i| \tag{1.49}$$

Here $\langle \tilde{p}_i|$ is the set of projection function which can be initiated from different practical schemes. In my thesis work, the PAW method has been used as implemented in the Vienna *ab-initio* simulation package (VASP) *[116]*.

1.9.2.9. Dispersion in Density Functional Theory

The above discussed local and semilocal density functionals are unable to describe correctly van der Waals interactions which mostly occurs due to dynamical correlations between fluctuating charge distributions. Therefore, another method is introduced to incorporate the dispersion interactions adding a correction term with the conventional Kohn-Sham DFT energy. In general, Grimme's method is used for dispersion energy correction. Grimme's DFT-D_3 has been used in my thesis work. Total energy in DFT-D_3 can be given by *[117]*

$$E_{DFT-D_3} = E_{KS-DFT} - E_{disp} \tag{1.50}$$

Where E_{KS-DFT} is the self-consistent Kohn-Sham energy and the E_{disp} is the dispersion correction term which is the sum of the two-body and three-body energies

$$E_{disp} = E^{(2)} + E^{(3)} \tag{1.51}$$

$$E^{(2)} = \sum_{AB} \sum_{n=6,8,10....} S_n \frac{C_n^{AB}}{R_{AB}^n} f_{damp}(R_{AB}) \tag{1.52}$$

The equation (1.52) provides most important parameter two-body energy, which is summation of all atom pairs, where C_n^{AB} represents averaged nth-order dispersion coefficient for pairs AB atom pairs, and R_{AB} is the intra-nuclear distance between A and B. Here, S_n denotes the adjusted correction for the repulsion. For avoiding double-counting effect of correlation, a damping function $f_{damp}(R_{AB})$ is used as an intermediate distance. By applying the concept of short-range damping analogy as a pair wise term, nonadditive energy contribution (three body contribution) can be expressed as *[117]*

$$E^{(3)} = \sum_{ABC} f_{d,(3)}(r_{ABC}) E^{ABC} \tag{1.53}$$

In the equation (1.53), provides summation of all over atoms triples ABC in the system and r_{ABC} is the geometrically averaged radii used as a damping function. The parameter E^{ABC} is the nonadditive dispersion term (also called as Axilrod-Teller-Muto or triple dipole) derived from the third-order perturbation theory for three atoms ABC. Since the dispersion correction mainly related to the atomic forces, some structural change is observed generally during optimization of the system with respect to the non-correction based optimization.

1.9.3. Other Computational Tools

1.9.3.1. *Ab initio* Molecular Dynamics

The effect of temperature on the structure and dynamic behavior of the system is investigated by *ab initio* molecular dynamics (AIMD) simulation. AIMD simulation is more accurate than the MD simulation as it is based on the quantum Schrodinger equation rather than Newton's equation which is used in the classical MD simulation *[118]*. Moreover, AIMD uses real physical potential while MD relies on semiempirical effective potentials which approximate quantum effects. However, the only drawback of AIMD simulation compared to MD simulation is its huge computational cost, which limits its application to a few hundreds of atoms. Common thermal ensemble used in AIMD simulations are microcanonical ensemble (NVE), canonical ensemble (NVT), isobaric-isothermal ensemble (NPT) and grand canonical ensemble (μVT). In a microcanonical ensemble (NVE), the system is isolated, total energy is constant and all the microstate has equal probability. In canonical ensemble (NVT), the system can exchange energy via a heat bath, the temperature is constant and probability of any state *i* is given by

$$p_i = \frac{e^{-E_i/K_BT}}{\sum_i e^{-E_i/K_BT}} \tag{1.54}$$

In NPT ensemble both the pressure and the temperature are constant.

In this thesis work, AIMD simulation was done using canonical ensemble (NVT) at different temperature with a time step of 1 femto second. During the AIMD simulation, the temperature can be controlled using different types of thermostat models such as Berendsen thermostart, Anderson thermostat and Nosé-Hoover thermostat. In our calculation, Nosé-Hoover thermostat model is used for temperature controlling *[119]*.

1.9.3.2. Bader Charge Analysis

We have used Bader charge analysis in our thesis work to investigate the partial charge transfer mechanism inside our system. This method was developed by Richard Bader, from McMaster University, which provides an intuitive way of dividing molecules or solid state materials or crystals into atoms. This analysis based on the electronic charge density which can be visualized by VESTA (Visualization of Electronic and STructural Analysis) software package *[120]*. This division of atoms in the system is done by zero flux surfaces which is a two-dimensional (2D) surface on which the charge density is a minimum perpendicular to the surface. Both in molecular systems and solid state materials, the charge density reach a minimum between atoms and this is a natural place thus separating atoms from each other. The charge inside the Bader volume generally gives a good approximation to the total electronic charge of an atom.

In this thesis work, a fast algorithm is used on the charge density grid for Bader charge analysis which was developed by Henkelman and coworkers *[121]*. This program read the charge densities from the CHGCAR (VASP format) to produce total charge associated with each atom as output.

1.9.3.3. Phonon Dispersion

Phonon Dispersion calculation is carried out to investigate the dynamic stability of any system. The term ‘phonon’ defines a collective vibration of periodic atoms in molecules as well as in condensed matter, which represents an excited state in the quantum mechanical quantization of the vibrational modes of elastic structures of interacting particles. In static model, the atoms are arranged in a crystal periodically without any movement. Lattice dynamics deals with the concept that periodically arranged atoms in the crystal lattice are capable of motion due to thermal excitation. In practical case, all the atoms vibrate to some extend due to thermal agitation. The vibration of an atom is a superposition of vibrations of atoms around their equilibrium sites due to the interaction with neighbor atoms. This collective vibration of atoms in the crystal lattice forms a wave having allowed wavelength and amplitude. Comparing with light ‘quanta’ photon (which also has wave nature), quantum of lattice vibrational waves is named as ‘phonon’.

Phonon frequency calculation is done by density functional perturbation theory (DFPT) *[122]* as implemented in VASP. Phonon dispersion is plotted by the Phonopy package *[123]*, which gives the dispersion of the phonon frequencies along the high symmetry points of the Brillion zone in reciprocal space.

1.9.4. Magnetic Calculations

1.9.4.1. Magnetic Anisotropy Energy (MAE)

Magnetic anisotropy energy (MAE) provides an idea about the preferable orientation of spin with respect to magnetic field direction. This MAE is an important parameter for magnetic materials to determine the low-temperature magnetic orientation with respect to the lattice structure, which is directly related to the thermal stability regarding magnetic data storage. Without any external magnetic field these spin have no preference. This orientation of spins responds to the applied magnetic field. There exists an axis called easy axis (EA) of magnetization along which spins in a magnetic material tend to align very easily when an external magnetic field is applied along that direction. Similar way, there also exists another axis namely hard axis (HA) of magnetization along which spins in a magnetic material do not tend to align very easily when an external magnetic field is applied along that direction.

Here, in my thesis work, the magnetic anisotropy energy (MAE) is calculated using the torque approach *[124-126]*. For this, non-collinear self-consistent calculations (including spin-orbit coupling) has been carried out along <001>, <010>, <100>, <110> and <111> directions, considering them as magnetization axis directions, respectively. Considering the origination of MAE from the perpendicular and in plane contribution of spin orbit coupling (SOC), MAE can be expressed in terms of angular momentum operators Lx, L_y or L_z. In this case, contribution of different spins orientations can be expressed by the second-order perturbation equation *[126]*

$$MAE = \xi^2 \sum_{o,u} \frac{|<o|L_z|u>|^2 - |<o|L_x|u>|^2}{E_u - E_o} \qquad (1.55)$$

In the above equation (1.55), o and u represent the occupied and unoccupied electronic states, respectively. The two parameters E_o and E_u represent their respective band energies. The parameter ξ denotes the strength of the SOC. Therefore, the system should have a high value of ξ for acquiring high MAE value which has potential for practical spintronics application. Fundamentally, the interaction between the occupied and unoccupied orbitals in a system determines the preferred spin orientation of the electron. From our first principle simulation, the MAE is calculated by using the following equation:

$$MAE = E_{HA} - E_{EA} \tag{1.56}$$

where E_{EA} denotes the energy of the system along easy axis when an external magnetic field is applied and E_{HA} is the energy of the system along hard axis under application of magnetic field.

1.9.4.2. Mean Field Theory (MFT) Method

Mean Field Theory has been used in this thesis work for calculating the Curie temperature of all our the two-dimensional (2D) systems. Previously, this method has been used by Li and coworkers for the Curie temperature calculation *[127]*. In this approach, all the magnetic interactions are replaced with one body interaction with an average or effective interaction *[128]*. As a result, this method reduces any multi-body problem into an effective one-body problem. The partition function used in this method can be written as follows,

$$\mathrm{Z} = \sum_{m=-M,-M+2,.....M-2,M} e^{\gamma J' m<M>/k_B T} \tag{1.57}$$

Here in the equation (1.57), the 'J' is the exchange parameter, 'γ' is the coordination number, 'm' is the ensemble average magnetic moment, and "M" is the calculated magnetic moment for our system per unit cell.

Therefore, the average spin of each magnet becomes,

$$<\mathrm{m}> = \frac{1}{Z}\sum_{m=-M,-M+2,.....M-2,M} m \times e^{\gamma J' m<M>/k_B T} \tag{1.58}$$

Considering P = $\frac{\gamma J'}{k_B T}$, the above equation (Equation 1.58) can be deductible easily when the parameter 'P' varies along with the static solution <m>. At the critical point,

$$\mathrm{P} = \mathrm{P_c} = \frac{\gamma J'}{k_B T_c} \tag{1.59}$$

At this critical point, a phase transition occurs in the system between ferromagnetic to paramagnetic state which is known as the Curie temperature of the system.

1.9.4.3. Monte Carlo Simulations (MC Simulation)

Monte Carlo simulation is used in this thesis work to calculate the Curie temperature of the system. Since it is reported that mean-field theory (MFT) generally overestimates the value of Curie temperature while the Monte Carlo (MC) simulation gives more reliable results, Curie temperature of the systems was calculated by Monte Carlo simulation *[129-131]*. It generates a subset of configurations or samples, chosen from a random algorithm from a configuration space. This is done using a probability distribution or weight function. Observables are computed as averages over the samples *[132]*. Let us denote one configuration of the magnet in a particular assignment of spin values as the follows,

$$S_1 = +1;\ S_2 = -1;\ S_3 = +1; \dots\dots\dots\dots\dots\dots\dots..S_{Ns} = +1 \qquad (1.60)$$

Here, the spin configuration is set as either "up" or "down". The average value of an observable can be calculated by weighting each configuration with the Boltzmann factor using statistical mechanics. In this way, the average magnetization at some fixed temperature T can be calculated as,

$$<M> = \frac{\sum_{Config} M e^{-E/k_BT}}{\sum_{Config} e^{-E/k_BT}} \qquad (1.61)$$

At the critical point, a noticeable fluctuation of the magnetic moment is observed, which is known as the Curie temperature (T_c) of the system.

1.9.4.4. Calculations of Curie temperature for itinerant magnetism

Itinerant magnetism deals with strong interaction between conduction electrons in a magnetic system *[133]*. This was modelled by Stoner criterion *[134]*, in which a large density of states $\rho(E_F)$ arise at Fermi level (E_F) and large coupling constant I is observed, which can predict the long-range magnetic order below the ordering temperature. The strength of magnetism (i.e how "strong" or "weak" the magnetism is) is determined by the difference between the magnitude of the spin-up and spin-down ($n_\uparrow - n_\downarrow$) density. Since, Monte Carlo simulation based on local magnetism model is not appropriate for itinerant magnetic system *[135]*, Curie temperature for such system can be calculated by gradually increasing the Gauss smearing factor (σ) to investigate the effect of temperature (K_BT) on magnetic moment of the system. Gauss smearing factor is related to the temperature by the following equation:

$$\sigma = K_B T \tag{1.62}$$

As the smearing factor increases, the temperature also increases, which enhances the thermal excitation and thus eventually weaken the magnetic moments. Finally, at a certain temperature magnetic moment becomes zero, results in the Curie transition.

1.9.5. Spin-Transport Calculation

Spin-polarized transport is calculated for our spin-filtering device using the SIESTA (Spanish Initiative for Electronic Simulations with Thousands of Atoms) code *[136-139]*. The transmission function and $I - V$ characteristics curves are computed by combining the non-equilibrium Green's function (NEGF) and DFT approach, as implemented in TranSIESTA module of SIESTA code *[136]*. The transmission function defines the possibility of an electron to be transmitted from left electrode to right electrode through the central scattering region with specific energy (E). This transmission function can be calculated from the given equation:

$$T(E,V) = tr[\Gamma_R(E,V)\mathcal{G}_C(E,V)\Gamma_L(E,V){\mathcal{G}_c}^{\dagger}(E,V)] \tag{1.63}$$

where $\mathcal{G}_{\mathrm{C}}$ is the Green's function of the central scattering region and is the coupling matrix of left and right electrodes. Further, the integration of transmission function provides the electric current as follows *[136]*:

$$I(V_b) = \frac{2e}{h}\int_{\mu_R}^{\mu_L} T(E,V_b)\,[f(E-\mu_L) - f(E-\mu_R)]dE \tag{1.64}$$

Where $T(E,V_b)$ is to represent the transmission spectrum of the electrons entering at energy (E) from Left (L) to Right (R) electrode in presence of an applied finite bias voltage V_b, $f\left(E - \mu_{\mathrm{L,R}}\right)$ is showing the Fermi-Dirac distribution of electrons in the L and R electrodes and $\mu_{\mathrm{L,R}}$ the chemical potential where $\mu_{\mathrm{L/R}} = E_F \pm V_b/2$ are moved correspondingly up and down according to the Fermi energy E_F *[137-139]*.

1.10. References

[1] The International Technology Roadmap for Semiconductors (ITRS) Report, 2011.

[2] The International Technology Roadmap for Semiconductors (ITRS) Report, 2015.

[3] Golio M. (2015), Fifty Years of Moore’s Law, Proceedings of the IEEE, 103, 1932-1937 (DOI: 10.1109/JPROC.2015.2473896)

[4] Moore G. E. (1998), Cramming more components onto integrated circuits, Proceedings of the IEEE, 86, 82-85 (DOI: 10.1109/JPROC.1998.658762)

[5] Bohr M. T., Young I. A. (2017), CMOS Scaling Trends and Beyond, IEEE Micro, 37, 20-29 (DOI: 10.1109/MM.2017.4241347)

[6] Yu S., Chen P. Y. (2016), Emerging Memory Technologies: Recent Trends and Prospects, IEEE Solid-State Circuits Magazine, 8, 43-56 (DOI: 10.1109/MSSC.2016.2546199)

[7] Kang S. M., Leblebici Y. (2003), CMOS Digital Integrated Circuits Analysis & Design, Tata McGraw-Hill Education, 3rd Edition.

[8] Shee S., Bhattacharyya G., Sarkar S. K. (2014), Quantum Analytical Modeling for Device Parameters and I –V Characteristics of Nanoscale Dual-Material Double-Gate Silicon-on-Nothing MOSFET, IEEE Trans. Electron Device, 61, 2697-2704 (DOI: 10.1109/TED.2014.2332400)

[9] Bhattacharyya G., Shee S., Sarkar S. K. (2015), Comprehensive Quantum Mechanical Modelling of Short Channel SON MOSFET with Spatial Composition Grading of Binary Metal Alloy Gate Electrode, Superlattice. Microst., 83, 676-689 (DOI: 10.1016/j.spmi.2015.04.004)

[10] Jagadesh Kumar M., Orouji A. A. (2005), Two-Dimensional Analytical Threshold Voltage Model of Nanoscale Fully Depleted SOI

MOSFET With Electrically Induced S/D Extensions, IEEE Trans. Electron Device, 52, 1568-1575 (DOI: 10.1109/TED.2005.850624)

[11] Chaudhry A., Kumar M. J. (2004), Controlling Short-Channel Effects in Deep-Submicron SOI MOSFETs for Improved Reliability: A Review, IEEE Trans. Device Mater. Reliab., 4, 99-109 (DOI: 10.1109/TDMR.2004.824359)

[12] Xie Q., Xu J., Taur Y. (2012), Review and Critique of Analytic Models of MOSFET Short-Channel Effects in Subthreshold, IEEE Trans. Electron Device, 59, 1569-1579 (DOI: 10.1109/TED.2012.2191556)

[13] Khanna V.K. (2016), Short-Channel Effects in MOSFETs In: Integrated Nanoelectronics, NanoScience and Technology, Springer, New Delhi, ISBN: 978-81-322-3623-8 (DOI: 10.1007/978-81-322-3625-2_5)

[14] De S., Das D., Sarkar C. K. (2014), Remedies of Short Channel Effects in Conventional Mosfet, LAP Lambert Academic Publishing, ISBN-10: 3659566268

[15] Xu N., Ho B., Andrieu F., Smith L., Nguyen B.-Y., Weber O., Poiroux T., Faynot O., King Liu T.-J. (2012), Carrier-Mobility Enhancement via Strain Engineering in Future Thin-Body MOSFETs, IEEE Electron Device Lett., 33, 318-320 (DOI: 10.1109/LED.2011.2179113)

[16] Hou Y.-T., Li M.-F., Low T., Kwong D.-L. (2004), Metal Gate Work Function Engineering on Gate Leakage of MOSFETs, IEEE Trans. Electron Device, 51, 1783- 1789 (DOI: 10.1109/TED.2004.836544)

[17] Mukherjee S., Bandyopadhyay D., Dutta P. K., Sarkar S. K. (2016), Quantum analytical modeling and simulation of CNT on insulator (COI) and CNT on nothing (CON) FET: a comparative analysis, J Theor. Appl. Phys., 10, 91-97 (DOI: 10.1007/s40094-015-0205-5)

[18] Ghani T. *et al.* (2003), A 90nm High Volume Manufacturing Logic Technology Featuring Novel 45nm Gate Length Strained Silicon CMOS Transistors, IEEE Int'l Electron Devices Meeting Technical Digest, 978–980 (DOI: 10.1109/IEDM.2003.1269442)

[19] Mistry K. *et al.* (2007), A 45nm Logic Technology with High-k 1 Metal Gate Transistors, Strained Silicon, 9 Cu Interconnect Layers, 193nm Dry Patterning, and 100% Pb-free Packaging, IEEE Int'l Electron Devices Meeting Technical Digest, 247–250 (DOI: 10.1109/IEDM.2007.4418914)

[20] Venkateshwar Reddy G., Jagadesh Kumar M. (2005), A New Dual-Material Double-Gate (DMDG) Nanoscale SOI MOSFET-Two-Dimensional Analytical Modeling and Simulation, IEEE Trans. Nanotechnol., 4, 260-268 (DOI: 10.1109/TNANO.2004.837845)

[21] Gupta S. K., Baidya A., Baishya S. (2012), Simulation and Analysis of Gate Engineered Triple Metal Double Gate (TM-DG) MOSFET for Diminished Short Channel Effects, International Journal of Advanced Science and Technology, 38, 15-24

[22] Jagar S., Singh N., Mehta S. S., Agrawal N., Samudra G., Balasubramanian N. (2004), A FinFET and Tri-gate MOSFET's channel structure patterning and its influence on the device performance, Thin Solid Films, 462-463, 1-5 (DOI: 10.1016/j.tsf.2004.05.120)

[23] Hamid H. A. E., Iñíguez B., Guitart J. R. (2007), Analytical Model of the Threshold Voltage and Subthreshold Swing of Undoped Cylindrical Gate-All-Around-Based MOSFETs, IEEE Trans. Electron Device, 54, 572-579 (DOI: 10.1109/TED.2006.890595)

[24] Wu Y. S., Su P. (2009), Analytical Quantum-Confinement Model for Short-Channel Gate-All-Around MOSFETs Under Subthreshold Region, IEEE Trans. Electron Device, 56, 2720-2725 (DOI: 10.1109/TED.2009.2030714)

[25] Jiménez D., Iñíguez B., Suñé J., Marsal L. F., Pallarès J., Roig J., Flores D. (2004), Continuous Analytic I–V Model for Surrounding-Gate MOSFETs, IEEE Electron Device Lett., 25, 571-573 (DOI: 10.1109/LED.2004.831902)

[26] Srivastava V. M., Yadav K. S., Singh G. (2011), Design and performance analysis of cylindrical surrounding double-gate MOSFET for RF switch, Microelectron. J., 42, 1124-1135 (DOI: 10.1016/j.mejo.2011.07.003)

[27] Pradhan K. P., Kumar M. R., Mohapatra S. K., Sahu P. K. (2015), Analytical modeling of threshold voltage for Cylindrical Gate All Around (CGAA) MOSFET using center potential, Ain Shams Eng. J., 6, 1171-1177 (DOI: 10.1016/j.asej.2015.04.009)

[28] Auth A.C. *et al.* (2012), A 22nm High Performance and Low-Power CMOS Technology Featuring Fully-Depleted Tri-gate Transistors, Self-Aligned Contacts and High Density MIM Capacitors, Proc. Symp. VLSI Technology, 131-132 (DOI: 10.1109/VLSIT.2012.6242496)

[29] Meena J. S., Sze S. M., Chand U., Tseng T. Y. (2014), Overview of emerging nonvolatile memory technologies, Nanoscale Res. Lett., 9, 526 (1-33) (DOI: 10.1186/1556-276X-9-526)

[30] Wolf S. A., Awschalom D. D., Buhrman R. A., Daughton J. M., von Molnàr S., Roukes M. L., Chtchelkanova A. Y., Treger D. M. (2001), Spintronics: A Spin-Based Electronics Vision for the Future, Science, 294, 1488-1495 (DOI: 10.1126/science.1065389)

[31] Baibich M. N., Broto J. M., Fert A., Nguyen Van Dau F., Petroff F. (1988), Giant Magnetoresistance of (001) Fe/ (001) Cr Magnetic Superlattices, Phys. Rev. Lett., 61, 2472-2475 (DOI: 10.1103/PhysRevLett.61.2472)

[32] Barnas J., Fuss A., Camley R. E., Grunberg P., Zinn W. (1990), Novel magnetoresistance effect in layered magnetic structures: Theory and experiment, Phys. Rev. B, 42, 8110-8120 (DOI: 10.1103/PhysRevB.42.8110)

[33] Reig C., Cardoso S., Mukhopadhyay S. C. (2013), Giant Magnetoresistance (GMR) Sensors, Springer, ISBN 978-3-642-37172-1 (DOI: 10.1007/978-3-642-37172-1)

[34] Coleman R. V., Isin A. (1966), Magnetoresistance in Iron Single Crystals, J. Appl. Phys., 37, 1028-1029 (DOI: 10.1063/1.1708320)

[35] Hirota E., Sakakima H., Inomata K. (2002), Giant Magneto-Resistance Devices, Springer, p-30, ISBN 978-3-540-41819-1 (DOI: 10.1007/978-3-662-04777-4)

[36] Chappert C., Fert A., Nguyen Van Dau F. (2007), The emergence of spin electronics in data storage, Nat. Mat., 6, 813-823 (DOI: 10.1038/nmat2024)

[37] Binasch G., Grunberg P., Saurenbach F., Zinn W. (1989), Enhanced magnetoresistance in layered magnetic structures with antiferromagnetic interlayer exchange, Phys. Rev. B, 39, 4828-4830 (DOI: 10.1103/PhysRevB.39.4828)

[38] Baibich M. N., Broto J. M., Fert A., Nguyen Van Dau F., Petroff F. (1988), Giant Magnetoresistance of (001) Fe/ (001) Cr Magnetic Superlattices, Phys. Rev. Lett., 61, 2472-2475 (DOI: 10.1103/PhysRevLett.61.2472)

[39] Camley R. E., Barnaś J. (1989), Theory of giant magnetoresistance effects in magnetic layered structures with antiferromagnetic coupling, Phys. Rev. Lett., 63, 664-667 (DOI: 10.1103/PhysRevLett.63.664)

[40] Levy P. M., Zhang S., Fert A. (1990), Electrical conductivity of magnetic multilayered structures, Phys. Rev. Lett., 65, 1643-1646 (DOI: 10.1103/PhysRevLett.65.1643)

[41] Nagasaka K. (2009), CPP-GMR technology for magnetic read heads of future high-density recording systems, J. Magn. Magn. Mater, 321, 508-511 (DOI: 10.1016/j.jmmm.2008.05.040)

[42] Buschow K. H. J. (2005), Concise encyclopedia of magnetic and superconducting materials, 2nd ed., Elsevier, ISBN 9780080445861

[43] Gerlach W., Stern O. (1922), The experimental proof of the directional quantization in the magnetic field, Magazine for Physics, 9, 349-352 (DOI: 10.1007/BF01326983)

[44], Tedrow P. M., Meservey R. (1973), Spin Polarization of Electrons Tunneling from Films of Fe, Co, Ni, and Gd, Phys. Rev. B, 7, 318-326 (DOI: 10.1103/PhysRevB.7.318)

[45] Julliere M. (1975), Tunneling between Ferromagnetic Films, Phys. Lett. A, 54, 225-226 (DOI: 10.1016/0375-9601(75)90174-7)

[46] Mathon J., Umerski A. (1999), Theory of Tunneling Magnetoresistance in a Junction with a Nonmagnetic Metallic Interlayer, Phys. Rev. B, 60, 1117-1121 (DOI: 10.1103/PhysRevB.60.1117)

[47] Shinjo T. (2009), Nanomagnetism and Spintronics, Elsevier Science, ISBN: 978-0-444-53114-8 (DOI: 10.1016/C2009-0-18006-6)

[48] Slonczewski J. C. (1996), Current-Driven Excitation of Magnetic Multilayers, J. Magn. Magn. Mater, 159, L1–L7 (DOI: 10.1016/0304-8853(96)00062-5)

[49] Berger L. (1996), Emission of Spin Waves by a Magnetic Multilayer Traversed by a Current, Phys. Rev. B, 54, 9353-9358 (DOI: 10.1103/PhysRevB.54.9353)

[50] Ohno H., Endoh T., Hanyu T., Kasai N., Ikeda S. (2010), Magnetic Tunnel Junction for Nonvolatile CMOS Logic, 2010 IEEE International Electron Devices Meeting (IEDM), 9.4.1-9.4.4 (DOI: 10.1109/IEDM.2010.5703329)

[51] Natsui M., Suzuki D., Sakimura N., Nebashi R., Tsuji Y., Morioka A., Sugibayashi T., Miura S., Honjo H., Kinoshita K., Ikeda S., Endoh T., Ohno H., Hanyu T. (2013), Nonvolatile Logic-in-Memory Array Processor in 90nm MTJ/MOS Achieving 75% Leakage Reduction Using Cycle-Based Power Gating, 2013 IEEE International Solid-State Circuits Conference, 194-195 (DOI: 10.1109/ISSCC.2013.6487696)

[52] Datta S., Das B. (1990), Electronic Analog of the Electro-Optic Modulator, Appl. Phys. Lett., 56, 665-667 (DOI: doi.org/10.1063/1.102730)

[53] Li X., Yang J. (2016), First-principles design of spintronics materials, Nat. Sci. Rev., 3, 365-381 (DOI: 10.1093/nsr/nww026)

[54] de Groot R. A., Mueller F. M., van Engen P. G., Buschow K. H. J. (1983), New class of materials: Half-Metallic Ferromagnets, Phys. Rev. Lett, 50, 2024-2027 (DOI: 10.1103/PhysRevLett.50.2024)

[55] Schwarz K. (1986), CrO_2 predicted as a half-metallic ferromagnet, J Phys. F: Met. Phys., 16, L211–5 (DOI: 10.1088/0305-4608/16/9/002)

[56] Dedkov Y. S., Rüdiger U., Güntherodt G. (2002), Evidence for the half-metallic ferromagnetic state of Fe_3O_4 by spin-resolved photoelectron spectroscopy, Phys. Rev. B, 65, 064417 (1-5) (DOI: 10.1103/PhysRevB.65.064417)

[57] Kane C. L., Mele E. J. (2005), Z_2 topological order and the quantum spin Hall effect, Phys. Rev. Lett., 95, 146802 (1-4) (DOI: 10.1103/PhysRevLett.95.146802)

[58] Mühler L., Zhang H., Chadov S., Yan B., Casper F., Kübler J., Zhang S. C., Felser C. (2012), Topological insulators from a chemist's perspective, Angew. Chem. Int. Ed., 51, 1–5 (DOI: 10.1002/anie.201202480)

[59] Qi X. L., Zhang S. C. (2011), Topological insulators and superconductors, Rev. Mod. Phys., 83, 1057-1110 (DOI: 10.1103/RevModPhys.83.1057)

[60] Hasan M. Z., Kane C. L. (2010), Colloquium: topological insulators, Rev. Mod. Phys., 82, 3045-3067 (DOI: 10.1103/RevModPhys.82.3045)

[61] Wang Z. F., Liu Z., Liu F. (2013), Organic topological insulators in organometallic lattices, Nat. Commun., 4, 1471 (1-5) (DOI: 10.1038/ncomms2451)

[62] Wang Z. F., Liu Z., Liu F. (2013), Quantum anomalous Hall effect in 2D organic topological insulators, Phys. Rev. Lett., 110, 196801 (1-5) (DOI: 10.1103/PhysRevLett.110.196801)

[63] Fu L. (2011), Topological crystalline insulators, Phys. Rev. Lett., 106, 106802 (1-4) (DOI: 10.1103/PhysRevLett.106.106802)

[64] Hsieh T. H., Lin H., Liu J., Duan W., Bansil A., Fu L. (2012), Topological crystalline insulators in the SnTe material class, Nat. Commun., 3, 982 (1-6) (DOI: 10.1038/ncomms1969)

[65] Tanaka Y., Ren Z., Sato T., Nakayama K., Souma S., Takahashi T., Segawa K., Ando Y. (2012), Experimental realization of a topological crystalline insulator in SnTe, Nat. Phys., 8, 800-803 (DOI: 10.1038/nphys2442)

[66] Özgür Ü., Alivov Y., Morkoc H., (2009), Microwave ferrites, part 1: fundamental properties, J. Mater. Sci. Mater. Electron., 20, 789-834 (DOI: 10.1007/s10854-009-9923-2)

[67] Edmonds K. W., Bogusławski P., Wang K. Y., Campion R. P., Novikov S. N., Farley N. R. S., Gallagher B. L., Foxon C. T., Sawicki M., Dietl T., Buongiorno Nardelli M., Bernholc J. (2004), Mn Interstitial Diffusion in (Ga, Mn)As, Phys. Rev. Lett., 92, 037201 (1-4) (DOI: 10.1103/PhysRevLett.92.037201)

[68] Jungwirth T., Wang K. Y., Mašek J., Edmonds K. W., König J., Sinova J., Polini M., Goncharuk N. A., MacDonald A. H., Sawicki M., Rushforth A. W., Campion R. P., Zhao L. X., Foxon C. T., Gallagher B. L. (2005), Prospects for high temperature ferromagnetism in (Ga,Mn)As semiconductors, Phys. Rev. B, 72, 165204 (1-13) (DOI: 10.1103/PhysRevB.72.165204)

[69] Blattner A. J., Lensch J., Wessels B. W. (2001), Growth and Characterization of OMVPE Grown (In,Mn)As Diluted Magnetic Semiconductor, J. Electron. Mater., 30, 1408-1411 (DOI: 10.1007/s11664-001-0192-y)

[70] Ghosh D., Periyasamy G., Pati S. K. (2014), Transition Metal Embedded Two-Dimensional C_3N_4–Graphene Nanocomposite: A Multifunctional Material, J. Phys. Chem. C , 118, 15487-15494 (DOI: 10.1021/jp503367v)

[71] Nasir Baig R. B., Verma S., Varma R. S., Nadagouda M. N. (2016), Magnetic Fe@g‑C_3N_4: A Photoactive Catalyst for the Hydrogenation of Alkenes and Alkynes, ACS Sustainable Chem. Eng., 4, 1661-1664 (DOI: 10.1021/acssuschemeng.5b01610)

[72] Wu M., Cao C., Jiang J. Z. (2010), Electronic structure of substitutionally Mn-doped graphene, New J. Phys., 12, 063020 (11pp) (DOI: 10.1088/1367-2630/12/6/063020)

[73] Choudhuri I., Garg P., Pathak B. (2016), TM@gt-C_3N_3 monolayers: high-temperature ferromagnetism and high anisotropy, J. Mater. Chem. C, 4, 8253-8262 (DOI: 10.1039/C6TC03030K)

[74] He J., Zhou P., Jiao N., Ma S. Y., Zhang K. W., Wang R. Z., Sun L. Z. (2013), Magnetic Exchange Coupling and Anisotropy of 3d Transition Metal Nanowires on Graphyne, Sci. Rep., 4, 04014 (DOI: 10.1038/srep04014)

[75] Ma D.W., Wang Q., Yan X., Zhang X., C. He, Zhou D., Tang Y., Lu Y., Yang Z. (2016), 3d transition metal embedded C_2N monolayers as promising single-atom catalysts: A first-principles study, Carbon, 105, 463-473 (DOI: 10.1016/j.carbon.2016.04.059)

[76] Li X., Yang J. (2017), Low-dimensional half-metallic materials: theoretical simulations and design, WIREs Comput. Mol. Sci., 7, e1314 (DOI: 10.1002/wcms.1314)

[77] Felser C., Fecher G.H., Balke B. (2007), Spintronics: A challenge for materials science and solid-state chemistry, Angew. Chem., Int. Ed., 46, 668-699 (DOI: 10.1002/anie.200601815)

[78] Ruffieux P., Wang S., Yang B., Sánchez-Sánchez C., Liu J., Dienel T., Talirz L., Shinde P., Pignedoli C. A., Passerone D., Dumslaff T., Feng X., Müllen K., Fasel R. (2016), On-surface synthesis of graphene nanoribbons with zigzag edge topology, Nature, 531, 489-492 (DOI: 10.1038/nature17151)

[79] Son Y.W., Cohen M. L., Louie S. G. (2006), Half-metallic graphene nanoribbons, Nature (London), 2006, 444, 347-349 (DOI: 10.1038/nature05180)

[80] Kan E., Li Z., Yang J., Hou J. G. (2008), Half-metallicity in edge-modified zigzag graphene nanoribbons, J. Am. Chem. Soc, 130**,** 4224-4225 (DOI: 10.1021/ja710407t)

[81] Choudhuri I., Bhattacharyya G., Kumar S., Pathak B. (2016), Metal-free half-metallicity in a high energy phase C-doped gh-C_3N_4 system: a high Curie temperature planar system, J. Mater. Chem. C, 4, 11530-11539 (DOI: 10.1039/C6TC04163A)

[82] Choudhuri I.**,** Pathak B. (2017), Ferromagnetism and half-metallicity in atomically thin holey nitrogenated graphene based system, ChemPhysChem, 18, 1-12 (DOI: 10.1002/cphc.201700633)

[83] Du A., Sanvito S., Smith S. C. (2012), First-principles prediction of metal-free magnetism and intrinsic half-metallicity in graphitic carbon nitride, Phys. Rev. Lett., 108, 197207 (DOI: 10.1103/PhysRevLett.108.197207)

[84] Li X., Yang J. L. (2016), First-principles design of spintronics materials, Natl. Sci. Rev., 3, 365-381 (DOI: 10.1093/nsr/nww026)

[85] Soulen Jr R. J., Byers J. M., Osofsky M. S., Nadgorny B., Ambrose T., Cheng S. F., Broussard P. R., Tanaka C. T., Nowak J., Moodera J. S., Barry A., Coey J. M. D. (1998), Measuring the spin polarization of a metal with a superconducting point contact, Science, 282, 85-88 (DOI: 10.1126/science.282.5386.85)

[86] Dedkov Y. S, Rüdiger U., Güntherodt G. (2002), Evidence for the half-metallic ferromagnetic state of Fe_3O_4 by spin-resolved photoelectron spectroscopy, Phys. Rev. B, 65, 064417 (DOI: 10.1103/PhysRevB.65.064417)

[87] Meservey R., Tedrow P. M. (1994), Spin-polarized electron tunneling, Phys. Rep., 238, 173-243 (DOI: 10.1016/0370-1573(94)90105-8)

[88] Julliere M. (1975), Tunneling between ferromagnetic films, Phys. Lett. A, 54, 225-226 (DOI: 10.1016/0375-9601(75)90174-7)

[89] de Groot R. A., Mueller F. M., van Engen P. G., Buschow K. H. J. (1983), New class of materials: Half-Metallic Ferromagnets, Phys. Rev. Lett, 50, 2024-2027 (DOI: 10.1103/PhysRevLett.50.2024)

[90] Choudhuri I., Bhauriyal P., Pathak B. (2019), Recent Advances in Graphene-like 2D Materials for Spintronics Applications, Chem. Mater., 31, 8260-8285 (DOI: 10.1021/acs.chemmater.9b02243)

[91] Li X., Dong B., Sun X., Wang H., Yang T., Yu G., Vitto Han Z. (2019), Perspectives on exfoliated two-dimensional spintronics, J. Semicond. 40, 081508 (DOI: 10.1088/1674-4926/40/8/081508)

[92] Cornia A., Seneor P. (2017), The molecular way, Nat. Mat., 16, 505-506 (DOI: nmat4900)

[93] Venkataraman L. (2015), Molecular electronics under the microscope, Nature Chemistry (Editorial), 7, 181 (DOI: 10.1038/nchem.2200)

[94] Gobbi M., Novak M. A., Barco E. D. (2019), Molecular spintronics, J. Appl. Phys., 125, 240401 (DOI: https://doi.org/10.1063/1.5113900)

[95] Born M., Oppenheimer J. (1927), Zur quantentheorie der molekeln, J. Ann. Physik, 84, 457 (DOI: 10.1002/andp.19273892002)

[96] Hohenberg P., Kohn W. (1964), Inhomogeneous electron gas, Phys. Rev. B, 136, B864-B871 (DOI: 10.1103/PhysRev.136.B864)

[97] Kohn W., Sham L. J. (1965), Self-consistent equations including exchange and correlation effects, Phys. Rev., 140, A1133-A1138 (DOI: 10.1103/PhysRev.140.A1133)

[98] Xia B. Y., Wu H. B., Wang X., Lou X. W. (2013), Index facets and enhanced electrocatalytic properties, Angew. Chem. Int. Ed., 52, 12337-12340 (DOI: 10.1002/anie.201307518)

[99] Martin, R. M. (2012), Electronic structure: basic theory and practical methods, Cambridge University press, ISBN: 9780511805769 (DOI: 10.1017/CBO9780511805769)

[100] Ceperley D. M., Alder B. (1980), Ground State of the Electron Gas by a Stochastic Method, Phys. Rev. Lett., 45, 566-569 (DOI: 10.1103/PhysRevLett.45.566)

[101] van de Walle A., Ceder G. (1999), Correcting over binding in local-density-approximation calculations, Phys. Rev. B, 59, 14992-15001 (DOI: 10.1103/PhysRevB.59.14992)

[102] Oliver G. L., Perdew J. P. (1979), Spin-density gradient expansion for the kinetic energy, Phys. Rev. A., 20, 397-403 (DOI: 10.1103/PhysRevA.20.397)

[103] Perdew J. P., Burke K., Ernzerhof M. (1996), Generalized gradient approximation made simple, Phys. Rev. Lett., 77, 3865-3868 (DOI: 10.1103/PhysRevLett.77.3865)

[104] Perdew J. P., Wang Y. (1992), Accurate and simple analytic representation of the electron-gas correlation energy, Phys. Rev. B, 45, 13244-13249 (DOI: 10.1103/PhysRevB.45.13244)

[105] Perdew J. P., Ruzsinszky A., Csonka G. I., Vydrov O. A., Scuseria G. E., Constantin L. A., Zhou X., Burke K. (2008), Restoring the density-gradient expansion for exchange in solids and surfaces, Phys. Rev. Lett., 100, 136406 (1-4) (DOI: 10.1103/PhysRevLett.100.136406)

[106] Vanderbilt D. **(**1990), Soft self-consistent pseudopotentials in a generalized eigenvalue formalism, Phys. Rev. B, 41, 7892-7895 (DOI: 10.1103/PhysRevB.41.7892)

[107] Panchmatia P. M., Sanyal B., Oppeneer P. M. (2008), GGA + U modeling of structural, electronic, and magnetic properties of iron porphyrin-type molecules, Chem. Phys., 343, 47-60 (DOI: 10.1016/j.chemphys.2007.10.030)

[108] Bernien M., Miguel J., Weis C., Ali Md. E., Kurde J., Krumme B., Panchmatia P. M., Sanyal B., Piantek M., Srivastava P., Baberschke K., Oppeneer P. M., Eriksson O., Kuch W., Wende H. (2009), Tailoring the nature of magnetic coupling of Fe-porphyrin molecules to ferromagnetic substrates, Phys. Rev. Lett., 102, 047202 (1-4) (DOI: 10.1103/PhysRevLett.102.047202)

[109] Shick A. B., Kudrnovsky J., Drchal V. (2004), Coulomb correlation effects on the electronic structure of III-V diluted magnetic semiconductors, Phys. Rev. B, 69, 125207 (1-5) (DOI: 10.1103/PhysRevB.69.125207)

[110] Anisimov V. I., Zaanen J., Andersen O. K. (1991), Band theory and Mott insulators: Hubbard U instead of Stoner I, Phys. Rev. B, 44, 943-954 (DOI: 10.1103/PhysRevB.44.943)

[111] Perdew J. P., Ernzerhof M., Burke K. J. (1996), Rationale for mixing exact exchange with density functional approximations, J. Chem. Phys., 105, 9982-9985 (DOI: 10.1063/1.472933)

[112] Paier J., Marsman M., Kresse G. (2007), Why does the B3LYP hybrid functional fail for metals?, J. Chem. Phys., 127, 024103 (1-10) (DOI: https://doi.org/10.1063/1.2747249)

[113] Adamo C., Barone V. (1998), Toward chemical accuracy in the computation of NMR shieldings: the PBE0 model, Chem. Phys. Lett., 298, 113-119 (DOI: 10.1016/S0009-2614(98)01201-9)

[114] Heyd J., Scuseria G. E., Ernzerhof M. (2003), Hybrid functionals based on a screened Coulomb potential, J. Chem. Phys., 118, 8207 (DOI:10.1063/1.1564060)

[115] Blochl P. E. (1994), Projector augmented-wave method, Phys. Rev. B, 50, 17953-17979 (DOI: 10.1103/PhysRevB.50.17953)

[116] Kresse G., Joubert D. (1999), From ultrasoft pseudopotentials to the projector augmented-wave method, Phys. Rev. B, 59, 1758-1775 (DOI: 10.1103/PhysRevB.59.17580)

[117] Grimme S., Antony J., Ehrlich S., Krieg H. (2010), A consistent and accurate ab initio parametrization of density functional dispersion correction (DFT-D) for the 94 elements H-Pu, J. Chem. Phys. 132, 154104 (1-18) (DOI: https://doi.org/10.1063/1.3382344)

[118] Paquet E., Viktor H. L. (2018), Computational Methods for Ab Initio Molecular Dynamics, Advances in Chemistry, 2018, 14 pages (DOI: https://doi.org/10.1155/2018/9839641)

[119] Nosé S. (1984), A unified formulation of the constant temperature molecular dynamics methods, J. Chem. Phys., 81, 511-519 (DOI: 10.1063/1.447334)

[120] Momma K., Izumi F. (2011), VESTA3 for three-dimensional visualization of crystal, volumetric and morphology data, J. Appl. Crystallogr., 44, 1272−1276 (DOI:10.1107/S0021889811038970)

[121] Bader, R. F. W. (1994), Atoms in molecules: a quantum theory; Oxford University Press: USA.

[122] Baroni S., Giannozzi P., Testa A. (1987), Green's-function approach to linear response in solids, Phys. Rev. Lett., 58, 1861-1864 (DOI: 10.1103/PhysRevLett.58.1861)

[123] Togo A., Oba F., Tanaka I. (2008), First-principles calculations of the ferroelastic transition between rutile-type and $CaCl_2$-type SiO_2 at high pressures, Phys. Rev. B: Condens. Matter., 78, 134106 (1-9) (DOI: 10.1103/PhysRevB.78.134106)

[124] Pick Š. (1999), Magnetic anisotropy calculation: implementation of the torque method into the recursion-technique scheme, Solid State Commun., 111, 15-18 (DOI: 10.1016/S0038-1098(99)00170-2)

[125] Hu J., Wu R. (2013), Control of the magnetism and magnetic anisotropy of a single-molecule magnet with an electric field, Phys. Rev. Lett., 110, 097202 (1-5) (DOI: 10.1103/PhysRevLett.110.097202)

[126] Wang D. S., Wu R. Q., Freeman A. J. (1993), First-principles theory of surface magneto crystalline anisotropy and the diatomic-pair model,

Phys. Rev. B: Condens. Matter Mater. Phys., 1993, 47, 14932-14947 (DOI: 10.1103/PhysRevB.47.14932)

[127] Li X., Wu X., J. Yang. (2014), Room-temperature half-metallicity in La(Mn,Zn)AsO alloy via elment substitutions, J. Am. Chem. Soc., 136, 5664-5669 (DOI: 10.1021/ja412317s)

[128] Chaikin P. M., Lubensky T. C. (2007), Principles of condensed matter physics (4th print ed.), Cambridge: Cambridge University Press, ISBN 978-0-521-79450-3.

[129] Hu L., Wu X., Yang J. (2016), Mn_2C Monolayer: A 2D Antiferromagnetic Metal with High Néel Temperature and Large Spin–Orbit Coupling, Nanoscale, 8, 12939-12945 (DOI: 10.1039/C6NR02417C)

[130] Kan M., Adhikari S., Sun Q. (2014), Ferromagnetism in MnX_2 (X = S, Se) Monolayers, Phys. Chem. Chem. Phys., 16, 4990-4994 (DOI: 10.1039/c3cp55146f)

[131] Zhang L., Zhang S. F., Ji W. X., Zhang C. W., Li P., Wang P. J., Li S. S., Yan S. S. (2018), Discovery of a Novel Spin-Polarized Nodal Ring in a Two-Dimensional HK Lattice, Nanoscale, 10, 20748- 20753 (DOI: 10.1039/C8NR05383A)

[132] Kroese D. P., Brereton T., Taimre T., Botev Z. I. (2014), Why the Monte Carlo method is so important today, Comput. Stat., 6, 386-392 (DOI: 10.1002/wics.1314)

[133] Santiago J. M., Huang C. L., Morosan E. (2017), Itinerant magnetic metals, J. Phys. Condens. Matter., 29, 373002 (21pp) (DOI: 10.1088/1361-648X/aa7889)

[134] Stoner E. C. (1939), Collective electron ferromagnetism, Proc. R. Soc. Lond. A, 165, 372–414 (DOI: 10.1098/rspa.1939.0003)

[135] Zhang S. H., Liu B. G. (2018), Hole-doping-induced half-metallic ferromagnetism in a highly-air-stable $PdSe_2$ monolayer under uniaxial stress, J. Mater. Chem. C, 6, 6792-6798 (DOI: 10.1039/c8tc01450g)

[136] Brandbyge M., Mozos J. L., Ordejón P., Taylor J., Stokbro K. (2002), Density-Functional Method for Nonequilibrium Electron Transport, Phys. Rev. B, 65, 165401 (1-17) (DOI: 10.1103/PhysRevB.65.165401)

[137] Kumawat R. L., Pathak B. (2019), Individual Identification of DNA Nucleobases on Atomically Thin Black Phosphorene Nanoribbons: van der Waals Corrected Density Functional Theory Calculations, J. Phys. Chem. C, 123, 36, 22377-22383 (DOI: 10.1021/acs.jpcc.9b06239)

[138] Kumawat R. L., Garg P., Kumar S., Pathak B. (2019), Electronic Transport through DNA Nucleotides in Atomically Thin Phosphorene Electrodes for Rapid DNA Sequencing, ACS Appl. Mater. Interfaces, 11, 1, 219-225 (DOI: 10.1021/acsami.8b17239)

[139] Kumar S., Kumawat R. L., Pathak B. (2019), Spin-Polarized Current in Ferromagnetic Half-Metallic Transition-Metal Iodide Nanowires, J. Phys. Chem. C, 123, 25, 15717-15723 (DOI: 10.1021/acs.jpcc.9b02464)

Chapter 2

Ferromagnetism in Magnesium Chloride Monolayer with an Unusually Large Spin-up Gap

2.1. Introduction

Contemporary developments in nanoscience and nanotechnology have created the opportunity to use the electron spin instead of electron charge while developing next generation device. Scientists the world over have been envisioned spintronics devices as a new forthcoming technology replacing the conventional electronic devices in recent times *[1, 2]*. Fundamental concept in spintronic research for practical applications is to develop materials with well-arranged spin structure and 100% spin polarization *[3]*. Half-metals are remarkable materials with one conducting spin channel and one insulating/semiconducting spin channel, and are considered ideal for spintronic applications *[4]*. In the contemporary research, much interest has been focused on developing low dimensional ferromagnetic half-metals to assist the fabrication of spintronics device at nanoscale.

After the first successful exfoliation of graphene, researchers have devoted much effort to develop 2D crystals for spintronics applications. However, intrinsic robust magnetic order in a single 2D layer was absent until 2017, when two independent experiments showed magnetic order in $Cr_2Ge_2Te_6$ *[5]* and CrI_3 *[6]* at low temperature in the monolayer. Layered chromium triiodide *[6-8]* has attracted interest as a potential candidate for two-dimensional magnets after the synthesis of its monolayer, which was established as the thinnest intrinsic FM material with a Curie temperature (T_C) of 45 K *[6]*. This discovery opens up the prospect of accomplishing intrinsic spin ordering in 2D materials. Consequently, tremendous attention in developing 2D layered magnetic materials has been recently observed *[9-12]*.

Inspired by the discovery of thinnest 2D layered magnet CrI_3 in 2017 *[6]*, we have started investigating the layered CrI_2 crystal *[13]* and found that CrI_3 single layer can be obtained by creating a particular pattern of Cr vacancies in the CrI_2 monolayer. This idea motivated us to fabricate a magnetic monolayer similar to CrI_3 by creating patterned vacancy in similar di-halide structures.

Most of the layered 2D magnetic crystals reported to date are transition metal halides *[6-8]*, or transition-metal trichalcogenides *[3, 12, 14-16]*. It has been also reported earlier *[17,18]* that researchers have preferred investigations into the main group based system over TM based ones due to their longer spin relaxation time, which is a prerequisite for using any magnetic materials in spintronics and data storage application.

Although several alkaline earth halides *[19]* possess similar layered crystalline structures as CrI_2 *[13, 19, 20]*, these materials have not been explored for magnetism and spintronics application to date. Many of these halides are geologically abundant and have great application value. Amongst them, bulk $MgCl_2$ is most common in nature, can be extracted from brine or seawater *[19]*, and utilized for dust control, ice control and hydrogen storage. Monolayer and multilayer $MgCl_2$ thin films have been grown on various transition metal single crystal surfaces, such as Pd (111) and (100), Pt (111) and (100)-hex and Rh (1 l 1), by H. Fairbrother and co-workers using molecular beam epitaxy (MBE) and low energy electron diffraction (LEED) method *[21-22]*. Motivated by these findings, we have investigated the $MgCl_2$ monolayer for possible spintronics application.

Due to absence of intrinsic spin ordering in metal–free materials, magnetism was achieved by several approaches, such as phase incorporation due to vacancies *[23]*, adatom defect *[24-26]*, and substitutional doping *[27]*. However, these approaches show the introduction of local magnetism centered in a single atom in a main group based system. Creating a patterned Mg vacancy in $MgCl_2$ monolayer can explore new monolayers similar to that of CrI_3, where the magnetic moment would be distributed over the Cl atoms. Hence, analyzing the magnetic ground state (ferromagnetism or anti-ferromagnetism) in such system is an intriguing research area. These holes in $MgCl_2$ monolayer can be produced experimentally using heavy ion bombardment or beam treatment *[28-29]*. Magnetic interactions in such systems are different than in the previously studied transition metal based system. Hence, in this report we will explore the effect of hole density on magnetism and the type of magnetic exchange interactions in Mg vacancy induced $MgCl_2$ monolayer.

2.2. Computational Methods

We have performed spin-polarized density functional theory (DFT) calculations for all our structures as implemented in the Vienna Ab initio Simulation Package (VASP) *[30]*. All our calculations have been carried out within the Perdew-Burke-Ernzerhof (PBE) functional using generalized gradient approximation (GGA) *[31-32]* to describe correctly the electron–electron exchange and correlation energies of delocalized s and p electrons. Projected augmented wave (PAW) method *[33]* is employed using a plane wave cut-off energy of 320 eV to treat interactions between ion cores and valence electrons. Since the van der Waals interactions play a very decisive role for the layered systems, we have adopted van der Waals corrected density functional theory (DFT-D3) proposed by Grimme to overcome the deficiencies of DFT in treating dispersion interactions and correcting potential energy and interatomic forces *[34]*. $MgCl_2$ monolayer and defect induced various phases of $MgCl_2$ structures are modeled using (3×3×1) hexagonal supercell containing 27 atoms. We have used gamma-centered k-point grid of 9 × 9 × 1 is used to sample the first Brillouin zone of $MgCl_2$ monolayer for geometry optimization and 15×15×1 is used for spin-polarized electronic properties (Density of States) calculations. A 20 Å vacuum is employed along the z-direction for avoiding interactions between their periodic images. We have accomplished self-consistency with the convergence tolerance set to 10^{-6} eV and 10−3 eV.$Å^{-1}$ for total energy and force calculations respectively.

We have done bader charge analysis *[35-37]* using the Henkelman programme *[38]* with a near-grid algorithm refine-edge method to comprehend the charge transfer process. Moreover, we have calculated defect formation (E_F) energies under two different experimental conditions (Mg-rich environment and Cl-rich environment) to estimate the stability of various phases of $MgCl_2$ systems. Defect formation energy under Mg-rich environment can be calculated from the following equation *[39-40]*

$$E_F = E_{def-phase} - \left(E_{MgCl2} - N \times \mu_{Mg-max}\right) \quad (2.1)$$

Where $E_{def-phase}$ is total energy of the Mg vacancy induced phases of $MgCl_2$ monolayer, E_{MgCl2} is the total energy of pure $MgCl_2$ system, μ_{Mg-max} is the chemical potential of Mg under Mg-rich environment and N is the number vacancy created in the $MgCl_2$ supercell. Under Mg-rich environment, μ_{Mg-max} = $E_{Mg(Bulk)}$, where $E_{Mg(Bulk)}$ is the single atom energy of Mg atom from its respective bulk structure *[41]*. Defect formation energy under Cl-rich environment can be calculated from the following equation *[39-40]*

$$E_F = E_{def-phase} - \left(E_{MgCl2} - N \times \mu_{Mg-min}\right) \quad (2.2)$$

Where μ_{Mg-min} is the chemical potential of Mg under Cl-rich environment which can be calculated as

$$\mu_{Mg-min} = \left(E_{MgCl2-unit} - 2 \times \mu_{Cl-max}\right) \quad (2.3)$$

Here, $E_{MgCl2-unit}$ is the total energy of the $MgCl_2$ unit cell containing one Mg and two Cl atoms and μ_{Cl-max} is the chemical potential of Cl, which is single Cl atom energy from gaseous phase.

Furthermore, to predict the magnetic ground state of in defect induced phases of $MgCl_2$ monolayer, we have calculated the exchange energy *[39]* (E_{ex}) per unit cell and magnetic anisotropic energy *[39]* of $Mg_{0.89}\delta_{0.11}Cl_2$. The exchange energy per supercell (E_{ex}) is calculated using the following equation where E_{FM} and E_{AFM} denotes the energies of ferromagnetic and antiferromagnetic states.

$$E_{ex} = E_{AFM} - E_{FM} \quad (2.4)$$

Similarly, magnetic anisotropic energy (MAE) *[42]* per unitcell is calculated incorporating spin-orbit coupling (SOC) effect using the following equation (2.5) where E_{HA} is the energy of the system (along hard axis) with application of magnetic field along magnetizing direction (100), (010), (110), (111) and (001). E_{EA} is the energy of the system in present of a magnetic easy axis, which is an energetically favorable direction for spontaneous magnetization. We have also tried two out of plane direction (001) and (111) magnetizing direction.

$$MAE = E_{HA} - E_{EA} \tag{2.5}$$

The spin density distribution (SDD) *[39]* is plotted to understand the nature of electron spin density on the unpaired electron in Mg vacancy induced phases of $MgCl_2$ monolayer. The SDD is calculated using the following equation

$$\rho_{SD} = \rho_{up} - \rho_{down} \tag{2.6}$$

Here, ρ_{up} and ρ_{down} are the up and down electron spin density, respectively. In the SDD, the wave functions (up spins and down spins) for different lobes are indicated by yellow and blue colors respectively. The direct mapping of the electron spin density is measured by the neutron diffraction in electron spin resonance (ESR) spectroscopy *[39]*.

2.3. Results and Discussion:

2.3.1. Cleavage energy of monolayer$MgCl_2$ from bulk

It is important to calculate the cleavage energy to scrutinize the feasibility of exfoliating a monolayer from the $MgCl_2$ bulk structure prior to the actual study of $MgCl_2$ monolayer. Bulk magnesium chloride ($MgCl_2$) possesses a rhombohedral layered $CdCl_2$-type structure (named as α-$MgCl_2$) *[43]*. The optimized lattice constants of bulk α-$MgCl_2$ are a = b = 3.64 Å and c = 17.67 Å (Fig. 2.1), which match earlier theoretical (a = b = 3.65 Å, and c = 17.78 Å) and experimental (a = b = 3.635 Å, and c = 17.61 Å) reports *[43]*. We have performed spin-polarized density functional theory (DFT) calculations for all our structures as implemented in the Vienna Ab initio Simulation Package (VASP) *[30]*. We have implemented a fracture in the bulk and then systematically increased the distance between the two fractured parts and measured the variation in total energy. This is a very well-known, effective and widely approved method to calculate cleavage energy *[3, 14, 44-45]*. We have also added van der Waals (vdW) correction terms in our calculations *[34]*. The calculated cleavage energy for $MgCl_2$ is 0.16 J m^{-2}, which falls in the range of previously reported values for rhombohedral $CrCl_3$ (0.10 J m^{-2}), $CrBr_3$ (0.14 J m^{-2}) and CrI_3 (0.16 J m^{-2}) structures *[44]*. This cleavage energy is even smaller than that of graphite (0.36 J m^{-2}), *[44]* which demonstrates that a 2D $MgCl_2$ monolayer can be cleaved easily from the layered bulk phase.

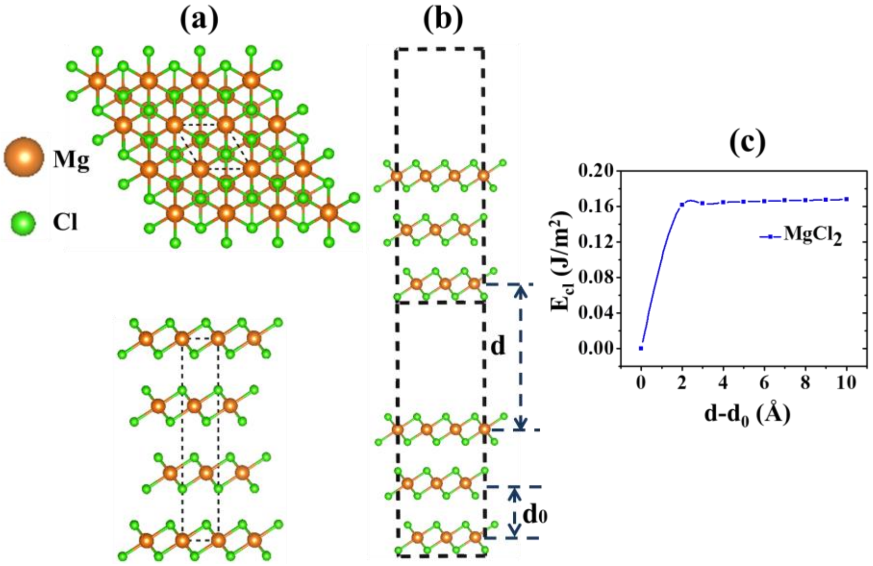

Figure 2.1: Crystal structure of bulk $MgCl_2$: (a) top view and side view, (b) supercell geometry (3 × 3 × 1) of bulk $MgCl_2$ with an introduced fracture to simulate the exfoliation procedure. (c) Cleavage energy Ecl (J m^{-2}) as a function of the separation between two fractured parts.

2.3.2. Incorporation of magnetism in $MgCl_2$ monolayer

In this work, we have considered a three atom hexagonal unit cell (Fig. 2.2a) of $MgCl_2$ monolayer (ML). Our optimized lattice parameters (a = b = 3.64 Å) match the previous published theoretical (3.67 Å, 3.621 Å) *[19, 46]* and experimental (3.641 Å) data for $MgCl_2$ monolayer *[46]*. The calculated Mg–Cl bond distance is found to be 2.52 Å, which is also consistent (2.52 Å) with a previous theoretical report *[46]*. The total electron density distribution of $MgCl_2$ monolayer (Fig. 2.2b) shows that the electrons are highly localized around Cl atoms. Phonon dispersion plot of monolayer $MgCl_2$ (Fig. 2.2c) indicates that $MgCl_2$ is dynamically stable, which is also consistent with an earlier theoretical report *[46]*. Our calculated band gap (~6.01 eV) of the monolayer also matches previously published results (5.98 eV, 6.00 eV) *[19, 46]*. These results indicate that our level of theory is correct enough to proceed with further calculations.

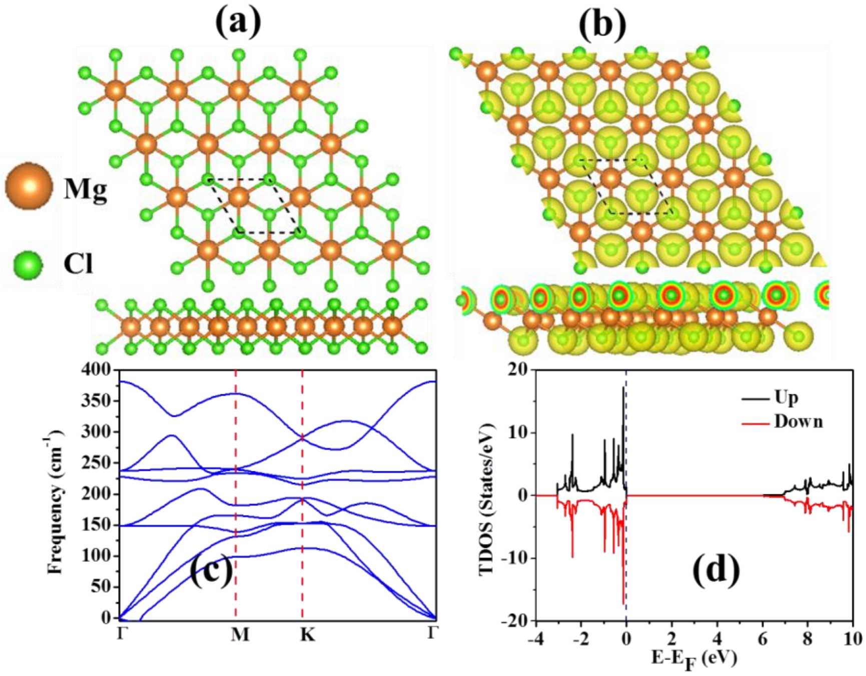

Figure 2.2: (a) Optimized structure (top/side view), (b) total electron density (isosurface value: 0.08 e Å^{-3}), (c) phonon dispersion plot, (d) spin polarized total density of states (TDOS) of the $MgCl_2$ monolayer. Here, the black dashed box indicates the unit cell of $MgCl_2$ system. The Fermi level is shifted to zero and indicated by a navy blue dashed line.

To induce magnetic ordering in the $MgCl_2$ monolayer, it is essential to have spontaneous spin moments in the sheet, which can be created by a hole doping strategy. First, we considered a 3 × 3 × 1 supercell of $MgCl_2$ monolayer (with 9 Mg and 18 Cl atoms) to create $Mg_{0.89}\delta_{0.11}Cl_2$, $Mg_{0.78}\delta_{0.22}Cl_2$ and $Mg_{0.67}\delta_{0.33}Cl_2$ by removing one, two and three Mg atoms, respectively (Fig. 2.3). Here 'δ' refers the Mg vacancy in the $MgCl_2$ monolayer. These systems are found to be magnetic with a magnetic moment of 2.00μB per Mg vacancy. Since Mg has two 3s electrons in its outermost shell, the removal of a single Mg atom creates two holes in the system, which induce magnetism. Therefore, these systems exhibit total magnetic moment of 2.00μB, 4.00μB and 6.00μB, respectively, and an apparent asymmetric spin density from the spin-polarized density of states.

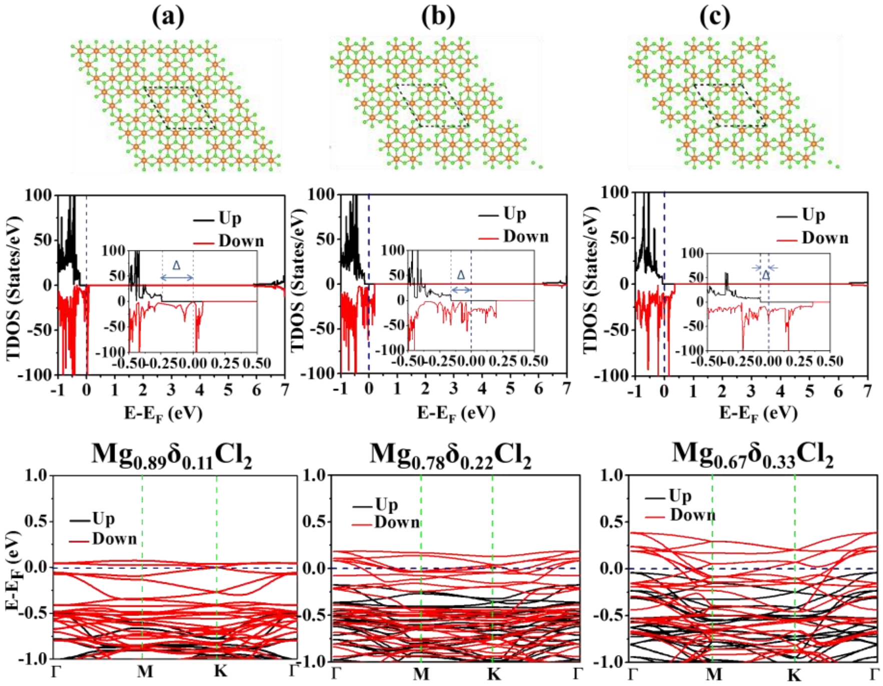

Figure 2.3: Optimized structures, spin polarized density of states along with magnified spin-polarised TDOS around the Fermi levels showing half-metallic gap (Δ, in the inset figures) and band structures of (a) $Mg_{0.89}\delta_{0.11}Cl_2$, (b) $Mg_{0.78}\delta_{0.22}Cl_2$, (c) $Mg_{0.67}\delta_{0.33}Cl_2$ systems. The Fermi level is set to zero and indicated by the blue dashed line.

Interestingly, these systems show half-metallic character (Fig. 2.3) as observed from electronic properties (TDOS and band structure plots). These half-metallic systems ($Mg_{0.89}\delta_{0.11}Cl_2$, $Mg_{0.78}\delta_{0.22}Cl_2$ and $Mg_{0.67}\delta_{0.33}Cl_2$) exhibit insulating spin-up channel (majority) and metallic spin-down (minority) channel. Creation of holes introduces p-type character in the system shifting the Fermi level lower inside the valance band. As we increase the hole doping density, the relative energy between spin polarized and non-spin polarized state increases gradually (0.16 eV, 0.21 eV and 0.32 eV), and thus the splitting between majority spin states and minority spin states increases. Therefore, the minority spin level crosses the Fermi level introducing half-metallicity in the system. The spin up state gap of a defected Mg systems increases (6.135 eV, 6.301 eV and 6.431 eV) with increasing vacancy concentration (Table 2.1). Magnified TDOS plots around the Fermi levels (inset figures, Fig. 2.3) show the half-metallic gap *[47]* decreases (0.242 eV, 0.157 eV and 0.065 eV) with increasing vacancy concentration.

Table 2.1: Summary of magnetic moments/vacancy (μB), nature of the material and spin-up band gap (eV) for with different Mg-vacancy concentrations

Mg Vacancy in $MgCl_2$	**Magnetic moment /vacancy(μB)**	**Nature**	**Spin-Up Gap (eV)**	**Half-Metallic Gap (eV)**
$Mg_{0.89}\delta_{0.11}Cl_2$	2.00	Half-Metallic	6.135	0.242
$Mg_{0.78}\delta_{0.22}Cl_2$	2.00	Half-Metallic	6.301	0.157
$Mg_{0.67}\delta_{0.33}Cl_2$	2.00	Half-Metallic	6.431	0.065

Ferromagnetism and half-metallicity has been explored in some pristine transitional metal based di-halide (MX_2) *[48]*, di-chlorides (MCl_2) *[49]*, tri-halide (MX_3) *[50]*, and tri-chlorides (MCl_3) *[47]* earlier; however, in our work we are predicting Mg-based robust ferromagnetic half-metallic layered material with wide spin-up gap up to 6.431 eV for the first time, which is an interesting and rare finding among the *p*-orbital based magnetic systems. Achieving half-metallicity for all these ranges of vacancy concentrations in a main group based system is noteworthy. Interestingly, the band structure plot of $Mg_{0.89}\delta_{0.11}Cl_2$ exhibits an unusual feature similar to a half-metallic Dirac cone *[51-52]* near the high symmetry K point (Fig. 2.4), where the $Mg_{0.89}\delta_{0.11}Cl_2$ system shows Dirac point in one spin channel (with Fermi level exactly touching the Dirac point) and a gap in the other spin channel *[51-52]*.

A half-metal with a Dirac cone in one conduction channel has massless electrons and hence high electron mobility in one spin channel *[52]*. However, several theoretical attempts for achieving half-metallicity in graphene have altered its Dirac cones *[52]*. Therefore, it's remarkable to have a Dirac cone at the Fermi level and half-metallicity simultaneously in the new $MgCl_2$ based material. To investigate the origin of Dirac cone, we have further explored the orbital resolved band structure (Fig. 2.4d–f). It reveals that the Dirac cone in $Mg_{0.89}\delta_{0.11}Cl_2$ system originates from the Cl p_x, p_y and p_z orbitals, similar to that in Be_3C_2 (p_z orbital of Beryllium and Carbon) *[53]*. Further exploration of the band structure using GGA-PBE calculation shows that our system has a very small ~1 meV gap in the spin-down channel.

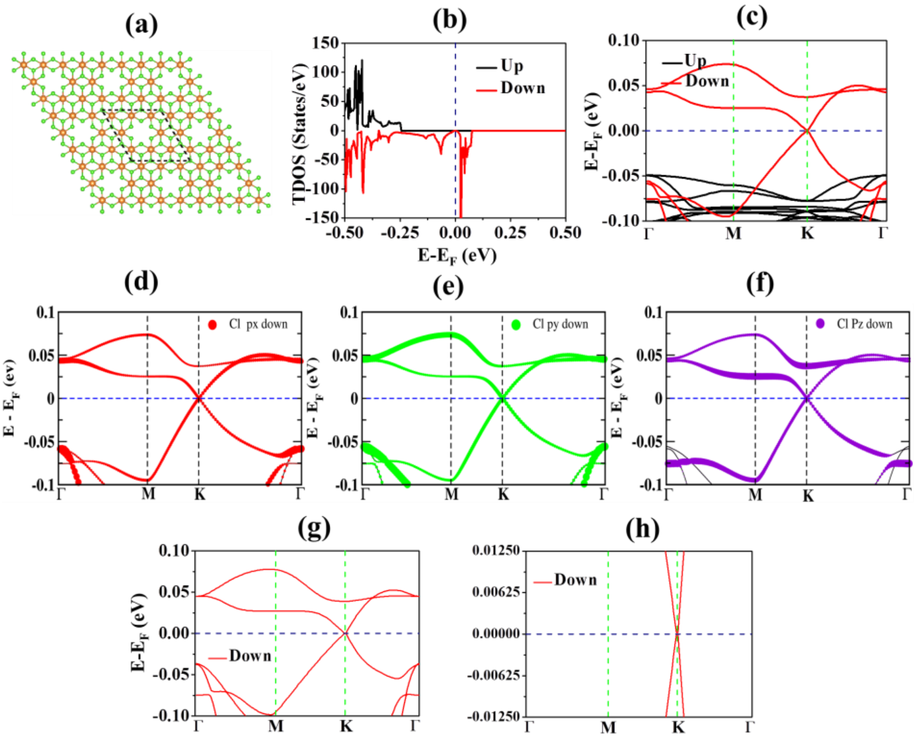

Figure 2.4: (a) Optimized structure, (b) spin polarized density of states and (c) band structures (showing coexistence of half-metallicity and Dirac cone) in $Mg_{0.89}\delta_{0.11}Cl_2$ system, (d)–(f) orbital resolved band structure of $Mg_{0.89}\delta_{0.11}Cl_2$. The radii of the red, green and violet circles are proportional to the Cl p_x, Cl p_y and Cl p_z character, (g) band structure (showing only spin-down channel) of $Mg_{0.89}\delta_{0.11}Cl_2$ system using PBEsol and (h) expanded view of band structure of $Mg_{0.89}\delta_{0.11}Cl_2$ using PBEsol showing gapless Dirac cone in $Mg_{0.89}\delta_{0.11}Cl_2$ system. The Fermi level is set to zero and indicated by the blue dashed line.

GGA-PBE functions tend to overcompensate and underbind, thus overestimating the lattice constants *[54]*, and therefore producing error while estimating band gap. Therefore, we have further studied the band structure using PBEsol and found that a gapless Dirac cone exists at Fermi energy near the K point, which confirms the co-existence of half-metallicity and a Dirac cone in our system. Therefore, these fascinating systems are further investigated to clarify their profound properties.

2.3.3. Energetic stability and experimental realization

We have calculated the vacancy formation energies of $Mg_{0.89}\delta_{0.11}Cl_2$, $Mg_{0.78}\delta_{0.22}Cl_2$ and $Mg_{0.67}\delta_{0.33}Cl_2$ phases under different experimental growth conditions, which are tabulated in Table 2.2.

Table 2.2: Summary of formation energy/vacancy (E_F) under Mg-rich and Cl-rich environments for with different Mg-vacancy concentrations

Mg Vacancy in $MgCl_2$	**Formation energy (eV/Vacancy)**	
	Under Mg-rich environment	**Under Cl-rich environment**
$Mg_{0.89}\delta_{0.11}Cl_2$	7.99	2.16
$Mg_{0.78}\delta_{0.22}Cl_2$	7.96	2.13
$Mg_{0.67}\delta_{0.33}Cl_2$	7.89	2.05

The calculated results show that the formation energies of the Mg vacancy induced phases under Mg-rich environment range from 7.99–7.89 eV per vacancy while formation energies under Cl-rich environment range from 2.16–2.05 eV per vacancy. Hence, the creation of Mg vacancy is favorable under a Cl-rich environment. Since, achieving lower defect concentration by heavy ion bombardment or beam treatment is experimentally more feasible than creating patterned vacancy, we have mainly discussed $Mg_{0.89}\delta_{0.11}Cl_2$ system in the following sections. We have further analysed more deeply the possibility of synthesizing $Mg_{0.89}\delta_{0.11}Cl_2$ system. It has been reported earlier that a significant density of Mg vacancies were observed in ultrathin (001) MgO deposited by dc (direct current) magnetron sputtering *[55]*. The bond length of Mg–O in MgO monolayer *[56]* is 2.01 Å, which is shorter than the bond length of Mg–Cl (2.52 Å) in $MgCl_2$ monolayer *[46]*. Since bond strength is inversely proportional to the bond length, we assume that creation of Mg vacancy in $MgCl_2$ monolayer can also be experimentally realizable. Furthermore, the concentration of various defects can be controlled by regulating the synthesis process or deliberately induced via irradiation by high energy particles, including by electron beam, ion beam, high energy laser, or chemical etching *[57]*. Electron beam irradiation can generate knock-on damage or ionization damage during extended irradiation. To generate a point defect, the electron beam energy should be higher than the knock-on damage threshold *[55]* for the system. To compare our results with previously reported systems, we considered single S and Mo vacancy in MoS_2 vacancy system. Formation energy of a neutral S vacancy in MoS_2 under a S-rich environment and a Mo vacancy under Mo-rich environment are theoretically calculated as 2.35 eV and 8.02 eV *[58]*. Although Mo vacancy in MoS_2 was not seen experimentally, S vacancy has been achieved *[59]*. A S line vacancy in MoS_2 monolayer has been experimentally synthesized even though the predicted value of formation energy was large (5–6 eV per vacancy) *[58]*. Hence, we can predict that the synthesis of $Mg_{0.89}\delta_{0.11}Cl_2$ system is practically achievable.

2.3.4. Dynamic and thermal stability

Dynamic stability of $Mg_{0.89}\delta_{0.11}Cl_2$ system is analyzed from phonon frequency calculations and phonon dispersion plot. The phonon frequency calculations are performed using the density functional perturbation theory (DFPT) *[60]* as implemented in VASP and phonon dispersion calculations are carried out using the Phonopy code *[61]*. Phonon dispersion plot of $Mg_{0.89}\delta_{0.11}Cl_2$ system exhibits imaginary frequency of 41.96*i* cm^{-1} (Fig. 2.5b) after relaxation of phonon soft mode (Fig. 2.5a), which is the highest of four exhibited imaginary frequencies (0.38*i*, 0.49*i*, 0.56*i*, 41.96*i* cm^{-1}). The modes corresponding to the frequencies 0.38*i*, 0.49*i* and 0.56*i* cm^{-1} are very small and hence, can be considered as numerical noise. Analysis of the highest imaginary frequency (41.96*i* cm^{-1}) reveals that these instabilities are arising from the slight vibrational motion of Cl atoms which may be stabilized using a proper substrate *[62-64]*.

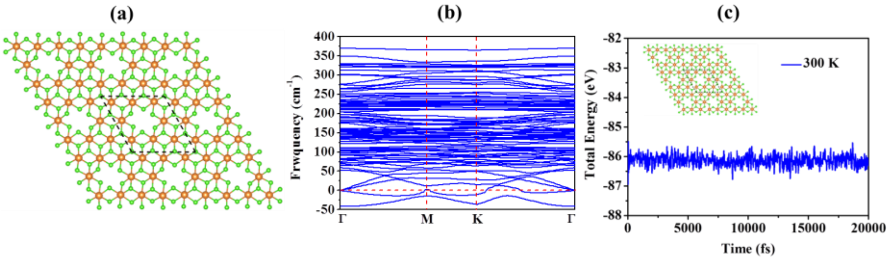

Figure 2.5: (a) Optimized structure after phonon soft mode relaxation, (b) phonon dispersion plot after phonon soft mode relaxation and (c) total energy fluctuation of AIMD simulation of Mg$_{0.89}\delta_{0.11}$Cl$_2$ system.

Phonon dispersion can be modified significantly by a substrate *[62]*, and the modification of phonon dispersion depends on the absorption process of the materials, i.e. physisorption or chemisorption. Significant softening was reported for the in plane optical modes (LO and LA) by ~100 cm^{-1} around Γ and for the out-of-plane optical (ZO) branch by ~160 cm^{-1} due to interaction of Ni (111) with graphene *[62]*. This softening of in-plane optical modes (LO and LA) was explained by the Ni (111) substrate induced lattice expansion of 1.48% *[62]*. The effect of hybridization of π bands of graphene with d bands of Ni plays an important role in removing Kohn anomalies in the highest optical branch at Γ and K point *[62]*.

Moreover, another interesting report *[63]* shows that a borophene sheet with higher hole density (20%) binds more strongly with Ag (111) substrate, which indicates the stability of defected monolayer on metal substrate. Similarly, another group *[64]* reported that formation energies of boron monolayers on Cu (111) surface are reduced by about 0.2 eV per atom, indicating that the Cu substrate can stabilize boron sheets. Therefore, we deduce that our system can also be stable on proper substrate.

Throughout these calculations, we have considered harmonic approximation for calculation of lattice dynamics. In harmonic approximations, vibrations in the crystal are not dependent of the interatomic distance, which implies that the vibrational energy does not depend on the volume. However, in practical condition, the equilibrium lattice parameter is dependent of temperature. When the temperature increases, the thermally induced displacements become large, and therefore expanding the Hamiltonian function only to a second order cannot be appropriate anymore. Since temperature effect is not included in the harmonic approximation, effect of variation of lattice parameters due to anharmonic effects cannot be included in this calculation. Anharmonic effects have been previously included by SCAILD method *[65-67]*. At room temperature (300 K), the imaginary modes (~100.068 cm^{-1}) in β-Ni–Ti were observed to completely vanish *[66]*. Since our calculations are performed at 0 K, we believe that our system $Mg_{0.89}\delta_{0.11}Cl_2$ may be stable at a higher temperature.

Recently, many halide based main group systems have been experimentally synthesized, although their imaginary mode is significantly larger than or comparable to that observed in our $Mg_{0.89}\delta_{0.11}Cl_2$ system. For example, the synthesized methylammonium lead triiodide ($CH_3NH_3PbI_3$) has large-amplitude anharmonic zone edge rotational instabilities of the PbI_6 octahedra with imaginary phonon eigenvector [40 meV (~322.62i cm^{-1})] *[68]*. Formamidinium lead triiodide ($HC(NH_2)_2PbI_3$) [>100i cm^{-1}] *[69]* and Caesium-based $CsPbBr_3$ [>25i cm^{-1}] *[69]* systems with high imaginary phonon modes have also been synthesized. Another halide based system $CsPbI_3$ has also been synthesized experimentally *[70]* with high imaginary phonon modes [>30i cm^{-1}] *[71]*. Therefore, we believe that our system can also be stable on proper substrate.

Thermal stability of $Mg_{0.89}\delta_{0.11}Cl_2$ system (Fig. 2.5c) is analysed from AIMD simulations *[72]* using an NVT ensemble at 300 K with a time step of 1 fs (femto second) for 20 ps (pico second). Room temperature AIMD simulation shows no possibility of inter-conversion or structural distortion from the optimized $Mg_{0.89}\delta_{0.11}Cl_2$ system. Thus, it can be concluded that the $Mg_{0.89}\delta_{0.11}Cl_2$ system is thermally stable in room temperature.

2.3.5. Magnetic properties of $Mg_{0.89}\delta_{0.11}Cl_2$

Before getting into magnetic properties of $Mg_{0.89}\delta_{0.11}Cl_2$, first we have investigated the origin of magnetism in all the defect induced $MgCl_2$ phases. Moreover, electron distribution and bonding analysis is also included in this section. To analyze the origin of magnetism, we have observed the spin density distribution (SDD) and the partial density of states of the Mg vacancy induced systems. Magnetism is observed to originate from the p orbitals of Cl atoms (Fig. 2.6), which were bonded with the Mg atom before the creation of hole. Partial density plot (Fig. 2.6) also reveals that p orbitals of Cl atoms are the origin of half-metallicity in these systems.

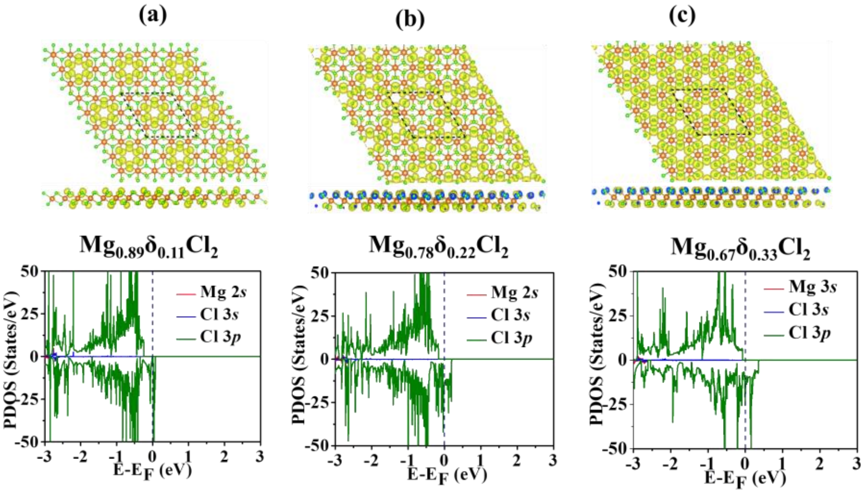

Figure 2.6: Spin density distribution (top/side view) [isosurface value 0.0046 e Å^{-3}] and partial density of states (PDOS) plot of Mg and Cl atoms in $Mg_{0.89}\delta_{0.11}Cl_2$, $Mg_{0.78}\delta_{0.22}Cl_2$, and $Mg_{0.67}\delta_{0.33}Cl_2$ systems.

Excitingly, we have observed a pattern similar to CrI_3 in our $Mg_{0.67}\delta_{0.33}Cl_2$ phase. This periodic system can be made up of a unit cell containing two Mg and six Cl atoms (Fig. 2.7c) similar to the CrI_3 monolayer. Hence, $Mg_{0.67}\delta_{0.33}Cl_2$ system can also be termed as $MgCl_3$, much like CrI_3.

Electron distribution and bonding analysis of $Mg_{0.89}\delta_{0.11}Cl_2$ and $Mg_{0.67}\delta_{0.33}Cl_2$ ($MgCl_3$) can be found from the ELF (Electron localization function), which shows that the electrons are centered towards Cl atoms (Fig. 2.7).

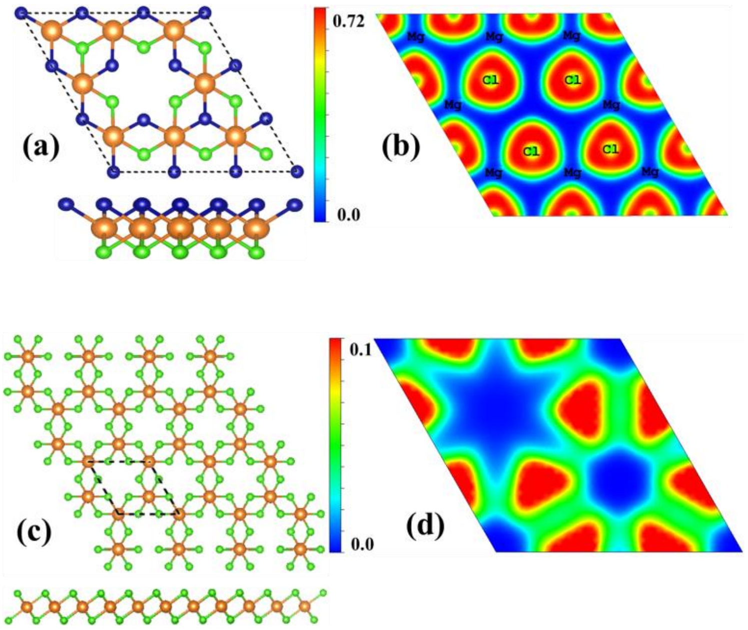

Figure 2.7: (a) Optimized structure of $Mg_{0.89}\delta_{0.11}Cl_2$ with Cl atoms denoted by blue (up) and green (down) circles. (b) Electron localization function of $Mg_{0.89}\delta_{0.11}Cl_2$ (ELF; maximum saturation level = 0.72 e $Å^{-3}$, minimum saturation level = 0.0 $Å^{-3}$). (c) Optimized structure of $Mg_{0.67}\delta_{0.33}Cl_2$ ($MgCl_3$) with unit cell in the black dotted line, and (d) corresponding electron localization function (ELF; maximum saturation level = 0.1 e $Å^{-3}$, minimum saturation level = 0.0 $Å^{-3}$).

Fig. 2.7b indicates the Cl atoms on the top surface (blue atoms in Fig. 2.7a) since we have taken ELF plot from the 001 plane. The contour of electron localization function (ELF) plot for both the $Mg_{0.89}\delta_{0.11}Cl_2$ and $Mg_{0.67}\delta_{0.33}Cl_2$ ($MgCl_3$) systems shows that there is strong ionic bonding between Mg–Cl, similar to that in $MgCl_2$ *[19]*. To comprehend whether the oxidation state of Mg in $Mg_{0.67}\delta_{0.33}Cl_2$ ($MgCl_3$) has been altered, we have investigated Mg–Cl bond distance and Bader charge analysis. The bond distance between Mg and Cl atoms has become shorter (~2.49 Å) in $Mg_{0.67}\delta_{0.33}Cl_2$ ($MgCl_3$) and thus, orbital overlapping between Mg and Cl atoms has increased, compared to $MgCl_2$ (~2.52 Å) monolayer. Bader charge analysis (Table 2.3) shows that in both cases, Mg holds +1.6 charge that indicates a +2 oxidation state in both molecules. Bader charge analysis of $Mg_{0.89}\delta_{0.11}Cl_2$ unveils that Cl atoms surrounding the hole hold −0.58

charge (Table 2.3), similar to that of Cl (−0.55) in $Mg_{0.67}\delta_{0.33}Cl_2$ ($MgCl_3$). Moreover, the other Cl atoms hold −0.82 charge, similar like those of Cl (−0.83) in $MgCl_2$. The bond distance between Mg–Cl surrounding the hole has become shorter (2.47 Å), which is consistent with the Mg–Cl bond distance (2.49 Å) in $Mg_{0.67}\delta_{0.33}Cl_2$ ($MgCl_3$). Bond distance of other Mg–Cl (2.51 Å) are found in similar range (2.52 Å) as in case of pure $MgCl_2$. Thus, all the magnetic systems under study are a combination of $MgCl_2$ and $Mg_{0.67}\delta_{0.33}Cl_2$ ($MgCl_3$) phases.

Table 2.3: Bond distance and Bader charge analysis of pure $MgCl_2$, $Mg_{0.67}\delta_{0.33}Cl_2$ ($MgCl_3$) and $Mg_{0.89}\delta_{0.11}Cl_2$

System		**Bond-distance (Å)**	**Net effective charge**
$MgCl_2$	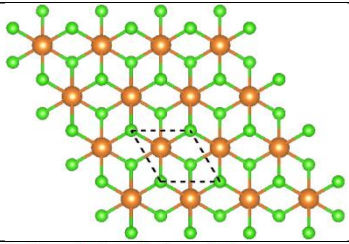	Mg-Cl ~ 2.52 Å	Mg~ +1.66, Cl ~ -0.83
$Mg_{0.67}\delta_{0.33}Cl_2$ **($MgCl_3$)**	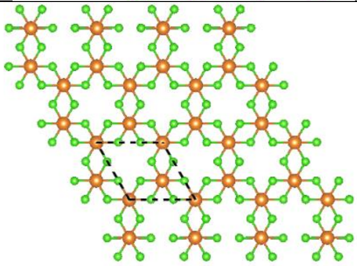	Mg-Cl ~ 2.49 Å	Mg ~ +1.65 , Cl ~ -0.55
$Mg_{0.89}\delta_{0.11}Cl_2$	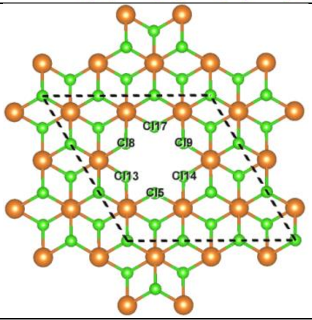	Mg-Cl ~ 2.47 Å (Cl_5, Cl_8, Cl_9, Cl_{13}, Cl_{14}, Cl_{17}) Mg-Cl ~ 2.51 Å	Mg ~ +1.66 Cl ~ -0.58 (Cl_5, Cl_8, Cl_9, Cl_{13}, Cl_{14}, Cl_{17}) Other Cl ~ -0.82

We find that half-metallicity occurs due to the presence of unsaturated Cl atoms, which in turn arises due to the creation of Mg vacancy in $MgCl_2$ monolayer. Fig. 2.8 shows the PDOS plot of Mg-defected $MgCl_2$ monolayer structures, where the Cl p-orbitals appear at the Fermi energy. This further indicates that they are destabilized due to an

Mg-vacancy. Besides, the magnetic moment of the system comes from Cl-atoms, which further supports that they are unsaturated. The creation of Mg vacancy introduces a large spin-up gap in these systems as the pure $MgCl_2$ monolayer has an insulating band gap of 6.01 eV.

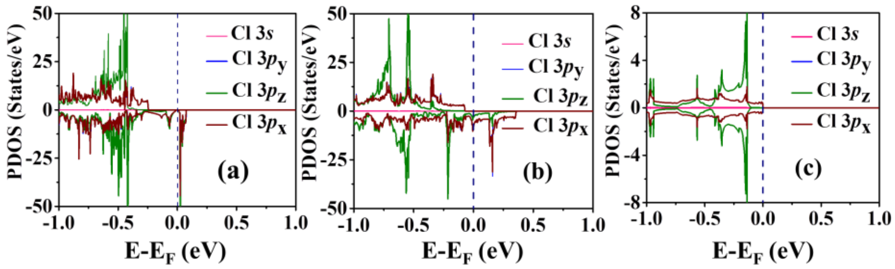

$Mg_{0.89}\delta_{0.11}Cl_2$

$Mg_{0.67}\delta_{0.33}Cl_2$ ($MgCl_3$)

$MgCl_2$

Figure 2.8: PDOS plot of Cl in (a) $Mg_{0.89}\delta_{0.11}Cl_2$ (b) $Mg_{0.67}\delta_{0.33}Cl_2$ ($MgCl_3$) and (c) $MgCl_2$ systems. The Fermi level is set to zero and indicated by the blue dashed line.

The effect of magnetic coupling between the magnetic centers is very crucial for their overall effect on the magnetic properties of the system. Magnetism in Mg vacancy induced systems originates from the p orbitals of Cl atoms, and is not localized on any particular single atom. This distributed spin density combined with the strong overlap between p orbitals may result in faster spin-down electronic hopping, which is very interesting among the non-magnetic materials based spintronic devices. Spin density distribution over the whole sheet was observed earlier in a 2D intrinsic magnet *[6]*. Perfectly symmetric spin density distribution was observed in $MgCl_3$, which has a similar structure to that in CrI_3. However, $MgCl_3$ has an antiferromagnetic ground state. Thus, we have mainly focused on the lower defect concentration based $Mg_{0.89}\delta_{0.11}Cl_2$ system.

To find the magnetic ground state of the half-metallic $Mg_{0.89}\delta_{0.11}Cl_2$ system, we have first considered each Cl as a magnetic center and checked the ground state magnetic configuration between FM and AFM (Fig. 2.9a and b). We have found that the FM configuration is energetically more favourable with exchange energy of 71.28 meV. Consequently, we have considered the six Cl atoms as a single magnetic center contributing a magnetic moment of 2.00μB.

Considering the spin density distribution (Fig. 2.9), it can be predicted that ferromagnetism is established in our $Mg_{0.89}\delta_{0.11}Cl_2$ system due to the interaction among partially filled p orbitals of Cl atoms. The effect of magnetic coupling between the two neighbouring vacancy is crucial for their overall effect on the magnetic properties of the system. Hence, we have further considered 2 × 2 × 1 supercell of single Mg vacancy induced system ($Mg_{0.89}\delta_{0.11}Cl_2$), where six Cl atoms are considered as a single magnetic center, to investigate the magnetic ground state between FM, AFM-I and AFM-II magnetic configurations (Fig. 2.9c–e). We have found that FM configuration is more stable by 25.96 meV and 23.30 meV exchange energies than AFM-I and AFM-II configurations, respectively. The TDOS plots of these AFM indicate that these systems are semiconducting.

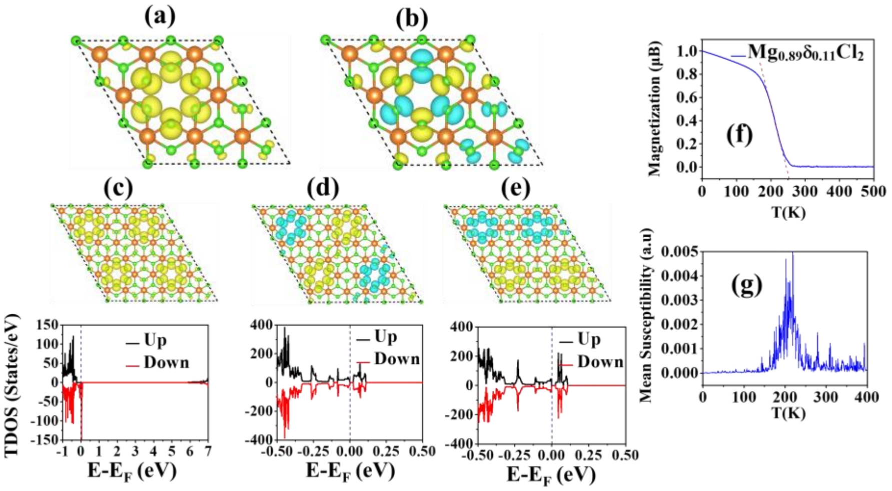

Figure 2.9: (a)–(b) Optimized FM and AFM configurations of $Mg_{0.89}\delta_{0.11}Cl_2$, where each Cl atom is considered as a magnetic center, (c)–(e) optimized FM, AFM-I and AFM-II configurations and corresponding TDOS plots of $Mg_{0.89}\delta_{0.11}Cl_2$, where six Cl atom is considered as a magnetic center, (f) variation of magnetic moment (μB) of $Mg_{0.89}\delta_{0.11}Cl_2$ as a function of temperature, and (g) mean susceptibility of $Mg_{0.89}\delta_{0.11}Cl_2$ as a function of temperature.

Curie temperature (T_C) of a material determines the possibility of its application in spintronic device. Hence, we have adopted the mean field theory (MFT) for estimating the Curie temperatures (T_C) of $Mg_{0.89}\delta_{0.11}Cl_2$ systems. Curie temperature of $Mg_{0.89}\delta_{0.11}Cl_2$ system is found to be 270.42 K from our MFT calculations *[73-75]*. It is well-known that Curie temperature predicted by MFT is overestimated and Monte Carlo (MC) simulation gives more reliable result *[75, 76]*. Thus, we have also calculated the Curie temperature (T_C) of $Mg_{0.89}\delta_{0.11}Cl_2$ using Monte Carlo (MC) simulation *[77]* based on the Heisenberg Model of $H = -\sum_{i,j} J_{i,j} S_i S_j$, where, $J_{i,j}$ is the nearest-neighbor exchange parameter and S_i and S_j represent the total magnetic moments per unit formula. A supercell of 40 × 40 × 1 with periodic boundary condition is constructed for the MC simulation of $Mg_{0.89}\delta_{0.11}Cl_2$. We have plotted the magnetic moment (μB) vs. temperature (K) (Fig. 2.9f) and magnetic susceptibility vs. temperature (K) (Fig. 2.9g) for $Mg_{0.89}\delta_{0.11}Cl_2$. These two plots indicate the transition temperature, where a system undergoes transition from the ferromagnetic to the paramagnetic phase. Therefore, the Curie temperature of our system is found to be 250 K. Although the Curie temperature of our system is below room temperature (300 K), it is higher than those of earlier reported $CrBr_3$ (32.5 K) and CrI_3 (45 K) systems *[6, 7]*. Therefore, our system ($Mg_{0.89}\delta_{0.11}Cl_2$) can be suitable for low temperature spintronic devices.

Furthermore, we have calculated magnetic anisotropy energy (MAE) using non-collinear magnetic calculation with spin–orbit coupling (SOC) for half-metallic $Mg_{0.89}\delta_{0.11}Cl_2$ monolayer. Magnetic anisotropic energy (MAE) is a significant parameter of magnetic materials for determining magnetic orientation at low temperature with respect to the lattice structure, which is directly related to the thermal stability of magnetic data storage *[78]*. It designates the energy required to flip a spin between the two states and thus, relates to the blocking temperature below which magnetic anisotropy can inhibit spin fluctuation. The magnetic easy axis (EA) of $Mg_{0.89}\delta_{0.11}Cl_2$ is found in the (100) direction. We have found high MAE (452.84 μeV per vacancy) for $Mg_{0.89}\delta_{0.11}Cl_2$. These data are tabulated in Table 2.4. $Mg_{0.89}\delta_{0.11}Cl_2$ possesses a comparatively larger MAE values than the previously reported CrF_3 (119.0 μeV per Cr atom) *[8]*, $CrCl_3$ (31.5

μeV per Cr atom) *[8]*, $CrBr_3$ (185.0 μeV per Cr atom) *[8]* and a slightly smaller value than CrI_3 (685.5 μeV per Cr atom) *[8]*.

Table 2.4: Summary of magnetic anisotropy energies in μeV/vacancy and the easy axis for $Mg_{0.89}\delta_{0.11}Cl_2$

$Mg_{0.89}\delta_{0.11}Cl_2$	**Easy Axis (100)**	**(001)-(100)**	**(010)-(100)**	**(110)-(100)**	**(111)-(100)**
	0	452.84 μeV	17.59 μeV	21.01 μeV	160.48 μeV

The large MAE value indicates that our material ($Mg_{0.89}\delta_{0.11}Cl_2$) is good for spintronics and magnetoelectronics applications.

2.3.6. Effect of strain on magnetism and half-metallicity of $Mg_{0.89}\delta_{0.11}Cl_2$

Strain is significant in tuning the geometrical properties, and thus magnetic properties, of the magnetic materials. During synthesis, 2D material undergoes structural strain that changes its lattice parameter since it is fabricated over a substrate. Lattice parameter plays a crucial role in determining the fundamental gap in a material. Therefore, it is necessary to consider the effect of strain on the half-metallicity of magnetic materials as it impacts their practical application. We have investigated the effect of strain on magnetism and half-metallicity in $Mg_{0.89}\delta_{0.11}Cl_2$ system, applying both biaxial and uniaxial tensile and compressive strain ranging from 1% to 4%, to examine the modulation of spin-up gap and half-metallic gap in the $Mg_{0.89}\delta_{0.11}Cl_2$ system. Interestingly, all strained systems sustain robust halfmetallic character. We have found that the spin-up gap and half-metallic gap in our half-metallic $Mg_{0.89}\delta_{0.11}Cl_2$ system can be modulated via external strain, which is tabulated in Table 2.5 and 2.6. Table 2.5 and 2.6 show that the spin-up gap decreases for all cases except in the case of biaxial compressive, where the spin-up gap increases as we increase strain. The highest spin-up gap (6.208 eV) is observed under 4% compressive strain. Therefore, the width of spin-up gap can be modulated by strain

Table 2.5: Modulation of Spin-Up Gap (eV) and Half-Metallic Gap (eV) in $Mg_{0.89}\delta_{0.11}Cl_2$ system with % of applied Strain along Biaxial-tensile and Biaxial-compressive direction

% of applied Strain	**Biaxial-tensile**		**Biaxial-compressive**	
	Spin-Up Gap (eV)	**Half-Metallic Gap (eV)**	**Spin-Up Gap (eV)**	**Half-Metallic Gap (eV)**
1%	6.085	0.255	6.165	0.188
2%	6.023	0.283	6.186	0.176
3%	5.956	0.302	6.206	0.167
4%	5.836	0.272	6.208	0.155

Table 2.6: Modulation of Spin-Up Gap (eV) and Half-Metallic Gap (eV) in $Mg_{0.89}\delta_{0.11}Cl_2$ system with % of applied Strain along Uniaxial-tensile and Uniaxial-compressive direction

% of applied Strain	**Uniaxial-tensile**		**Uniaxial-compressive**	
	Spin-Up Gap (eV)	**Half-Metallic Gap (eV)**	**Spin-Up Gap (eV)**	**Half-Metallic Gap (eV)**
1%	6.096	0.233	6.133	0.217
2%	6.043	0.227	6.131	0.173
3%	5.995	0.220	6.118	0.150
4%	5.940	0.220	6.103	0.127

and the details of corresponding TDOS are shown in Fig. 2.10–2.13.

Half-metallic gap is determined as the minimum between the lowest energy of majority spin conduction bands and the absolute value of the highest energy of the majority spin valence bands *[47, 49, 79-80]*. We have also observed a variation in half-metallic gap with external strain, which is included in the Table 1.5 and 1.6. Maximum half-metallic gap (0.302 eV) is perceived at 3% biaxial-tensile strain. The details of TDOS showing the half-metallic gaps are included in the inset figures (Fig. 2.10-2.13). In our system, the large spin-up gap is the more interesting result than half-metallic gap. Recently, transitional metal based 2D intrinsic half-metals with unusually large spin-up gap *[81]* have already attracted substantial attention since it can suppress spin-leakage at very small device lengths.

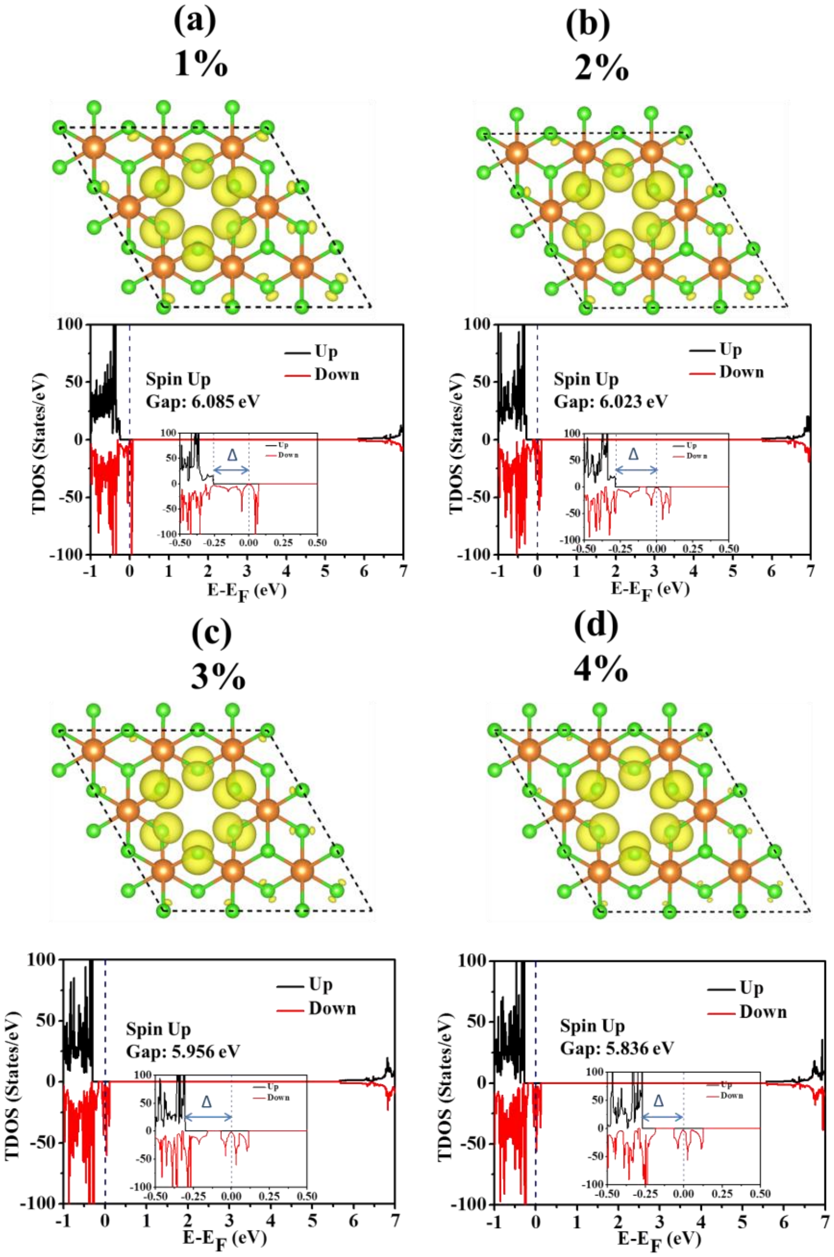

Figure 2.10: (a)-(d) Spin density distribution and TDOS plot of $Mg_{0.89}\delta_{0.11}Cl_2$ under the application of biaxial tensile strain from 1% to 4% along with magnified spin-polarised TDOS around the Fermi showing half-metallic gap [Δ, in the inset figure].

Therefore, we have mainly focused on the unusually large spin-up gap in our $Mg_{0.89}\delta_{0.11}Cl_2$ system and plotted variation of the spin-up gap with the application of strain (Fig. 2.14a). Furthermore, we have also observed the existence of the half-metallic Dirac cone in $Mg_{0.89}\delta_{0.11}Cl_2$ system, even under the application of 1% to 2% biaxial tensile strain (inset figure, Fig. 2.10) and under application of 1% to 2% uniaxial tensile strain (inset figure, Fig. 2.11). Thus, our system sustains its interesting magnetic properties under external strain.

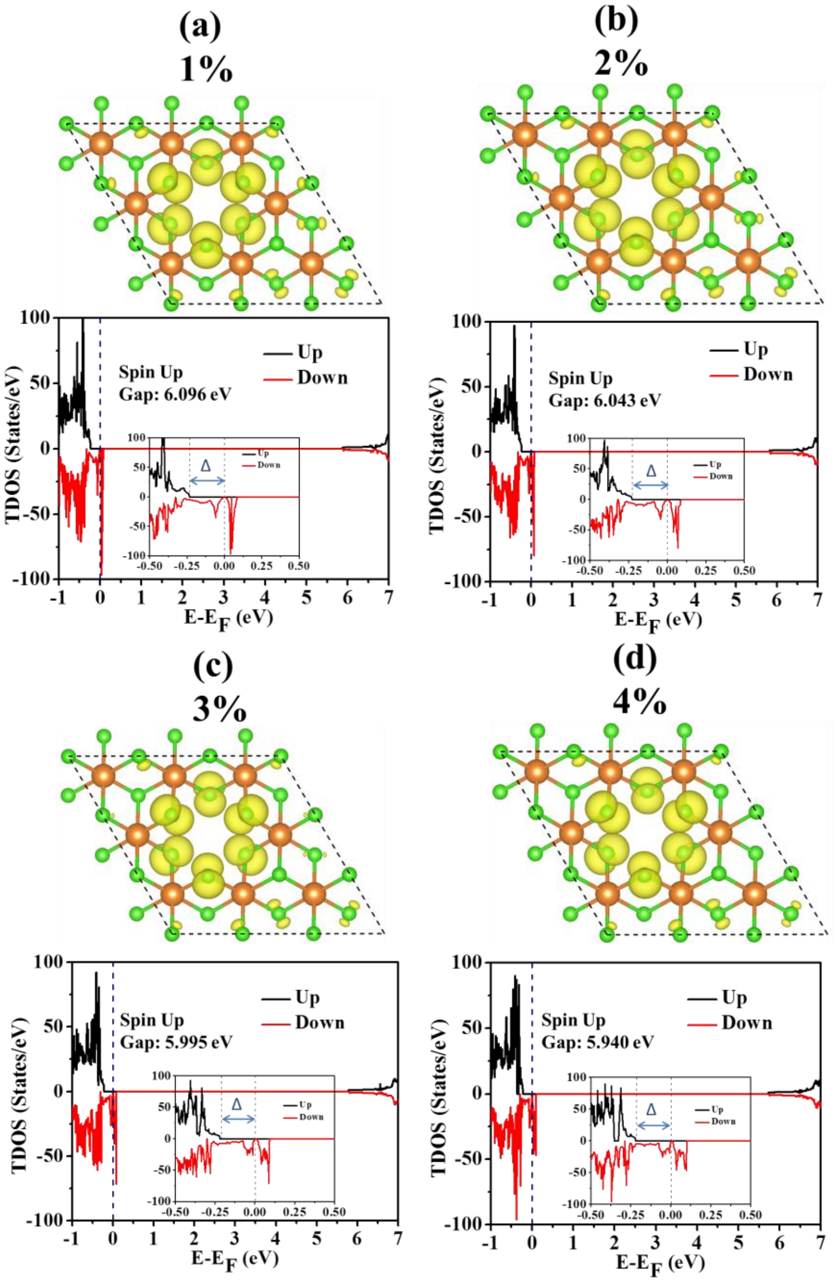

Figure 2.11: (a)-(d) Spin density distribution and TDOS plot of $Mg_{0.89}\delta_{0.11}Cl_2$ under the application of uniaxial tensile strain from 1% to 4% along with magnified spin-polarised TDOS around the Fermi showing half-metallic gap [Δ, in the inset figure].

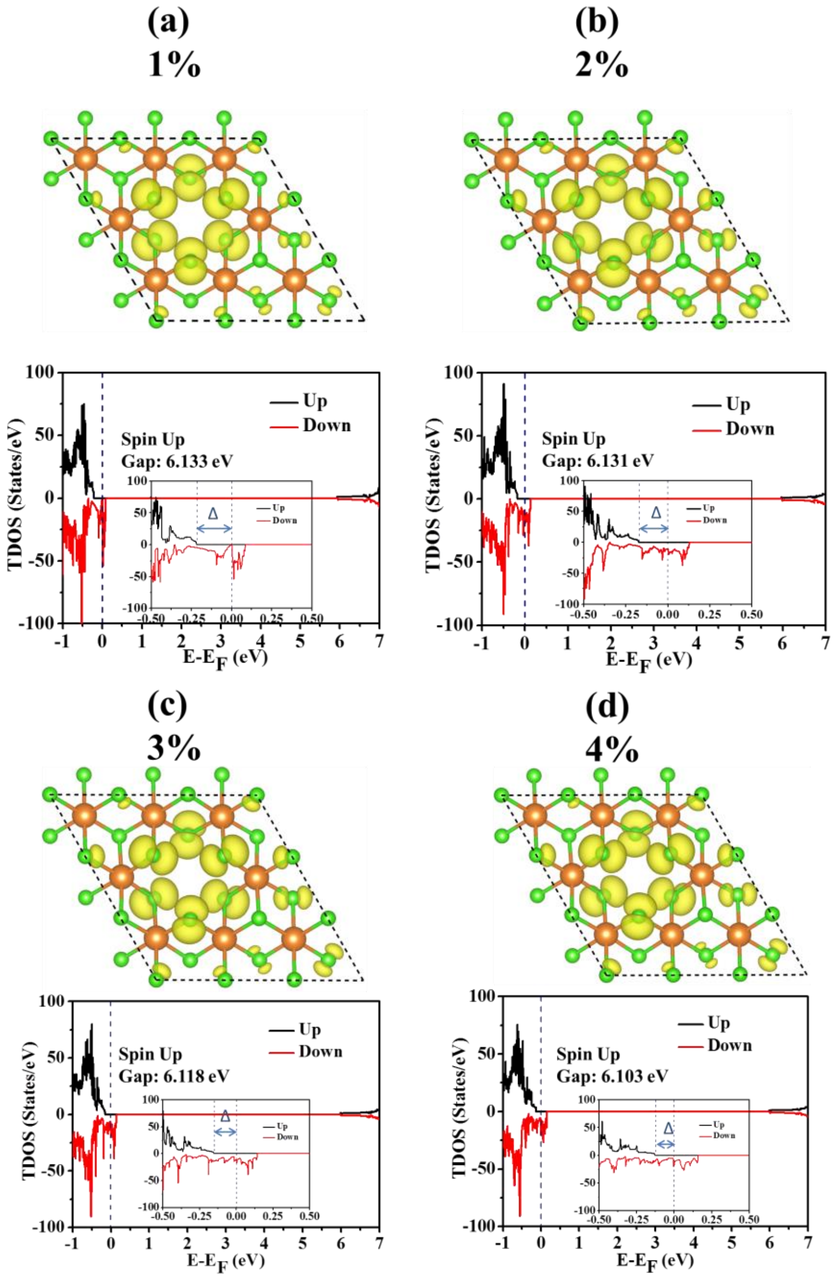

Figure 2.12: (a)-(d) Spin density distribution and TDOS plot of $Mg_{0.89}\delta_{0.11}Cl_2$ under the application of uniaxial compressive strain from 1% to 4% along with magnified spin-polarised TDOS around the Fermi showing half-metallic gap [Δ, in the inset figure].

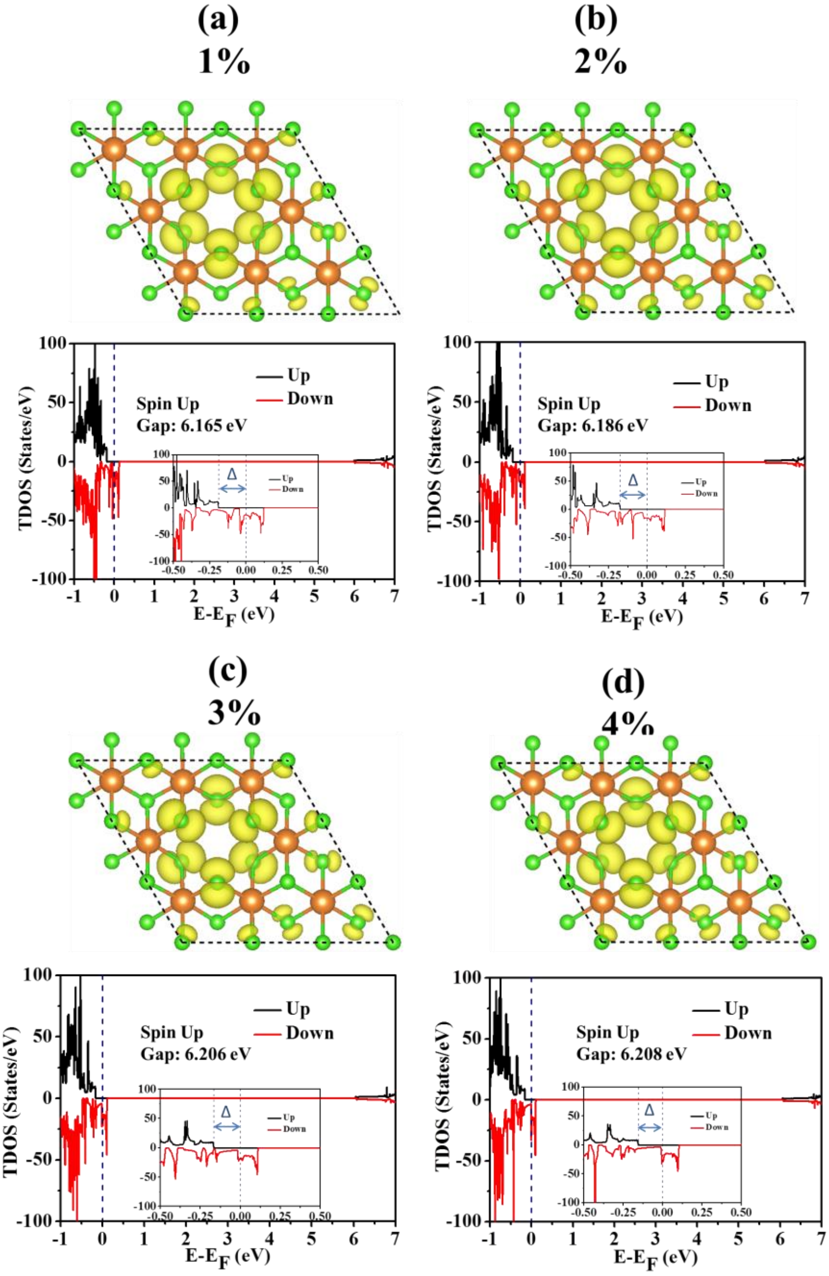

Figure 2.13: (a)-(d) Spin density distribution and TDOS plot of $Mg_{0.89}\delta_{0.11}Cl_2$ under the application of biaxial compressive strain from 1% to 4% along with magnified spin-polarized TDOS around the Fermi showing half-metallic gap [Δ, in the inset figure].

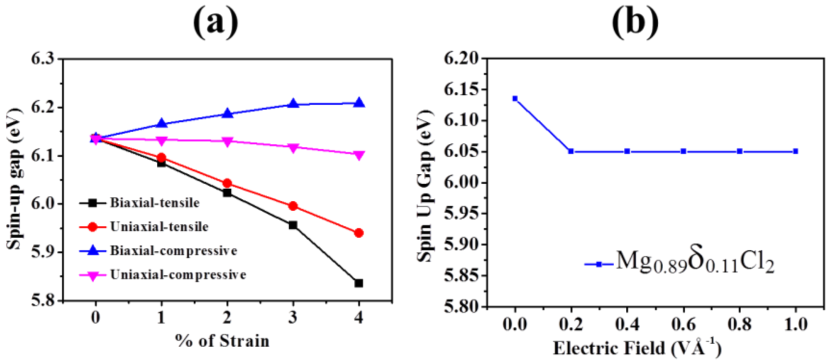

Figure 2.14: Variation of Spin-up gap in $Mg_{0.89}\delta_{0.11}Cl_2$ with (a) application of Strain (1% to 4%), (b) application of transverse electric field (0.0 VÅ^{-1} to 1.0 VÅ^{-1}).

2.3.7. Effect of external electric field on magnetism and half-metallicity of $Mg_{0.89}\delta_{0.11}Cl_2$

Modulation of the fundamental band gap by applying transverse electric field in bilayer structures has drawn interest of researchers since it can be an effective approach for their potential application in spintronics devices *[82-85]*. This electric field is equivalent to the gate voltage applied in field-effect transistors during their practical applications. Band gap engineering in layered monolayer materials via application of transverse electric field was also reported earlier *[86-87]*. Therefore, we have investigated the influence of transverse electric field (0.0–1.0 V Å^{-1}) on magnetic and half-metallic properties of $Mg_{0.89}\delta_{0.11}Cl_2$ monolayer for its potential application in spintronic device. We observe that $Mg_{0.89}\delta_{0.11}Cl_2$ monolayer sustains its half-metallicity under the application of external electric field. The evolution of density of states with different applied electric fields (0.2, 0.4, 0.6, 0.8 and 1.0 V Å^{-1}) is shown in Fig. 2.15. We have observed a transition of spin-up gap in half-metallic $Mg_{0.89}\delta_{0.11}Cl_2$ monolayer from 6.135 eV to 6.05 eV with the corresponding applied electric field of 0.0 V Å^{-1} to 0.1 V Å^{-1}. However, on increasing the value of transverse electric field further up to 1.0 V Å^{-1}, the spin-up gap remains constant at a value 6.05 eV. The evolution of spin-up gap with increasing electric field strength is plotted in Fig. 2.14b. To understand the phenomenon, we have further explored the spin polarized band structure of $Mg_{0.89}\delta_{0.11}Cl_2$ under an electric field of 0.1 V $Å^{-1}$, 0.2 V $Å^{-1}$, and 0.3 V $Å^{-1}$.

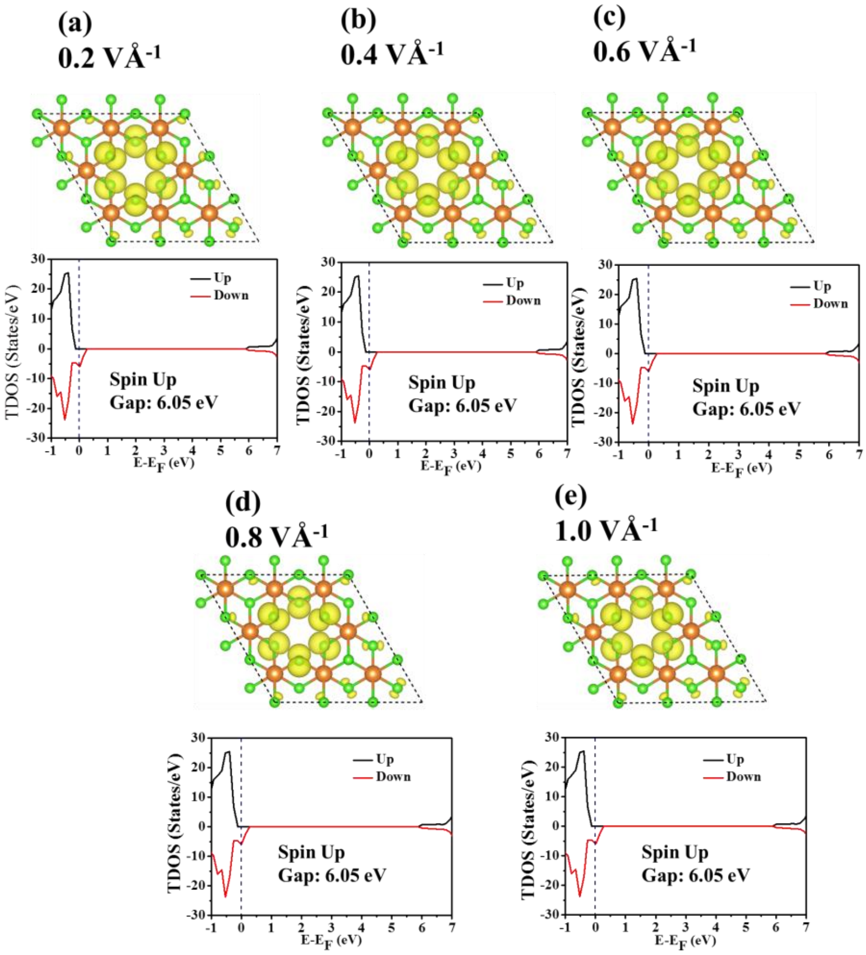

Figure 2.15: (a)-(e) Spin density distribution and TDOS plot of $Mg_{0.89}\delta_{0.11}Cl_2$ under the application of transverse electric field ranging from 0.0 to 1.0 $VÅ^{-1}$.

We have found that the spin-up gap decreases very slightly from 6.135 eV to 6.05 eV (Fig. 2.16) after the application of an external electric field and this value is constant with an increasing value of electric field from 0.1 to 0.3 V $Å^{-1}$. To further comprehend the phenomenon, we have analyzed the spin density distribution (Fig. 2.16) and Bader charge of $Mg_{0.89}\delta_{0.11}Cl_2$ under the application of an electric field from 0.1 to 0.3 V $Å^{-1}$. We have not found any significant change in the spin density distribution. Moreover, the Bader charge analysis also concurs with this phenomenon. Therefore, the net effective charge on Mg and Cl atoms surrounding to the vacancy does not changes, which is also consistent with our spin density distribution results (Table 2.7).

Table 2.7: Bader charge analysis of $Mg_{0.89}\delta_{0.11}Cl_2$ system with and without application of electric field

$Mg_{0.89}\delta_{0.11}Cl_2$	Electric Field 0.0 V/Å	Electric Field 0.1 V/Å	Electric Field 0.2 V/Å	Electric Field 0.3 V/Å
Net effective charge 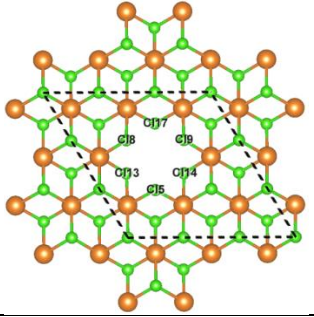	Mg ~ +1.66 Cl ~ -0.58 (Cl_5, Cl_8, Cl_9, Cl_{13}, Cl_{14}, Cl_{17})	Mg ~ +1.66 Cl ~ -0.58 (Cl_5, Cl_8, Cl_9, Cl_{13}, Cl_{14}, Cl_{17})	Mg ~ +1.66 Cl ~ -0.58 (Cl_5, Cl_8, Cl_9, Cl_{13}, Cl_{14}, Cl_{17})	Mg ~ +1.66 Cl ~ -0.58 (Cl_5, Cl_8, Cl_9, Cl_{13}, Cl_{14}, Cl_{17})

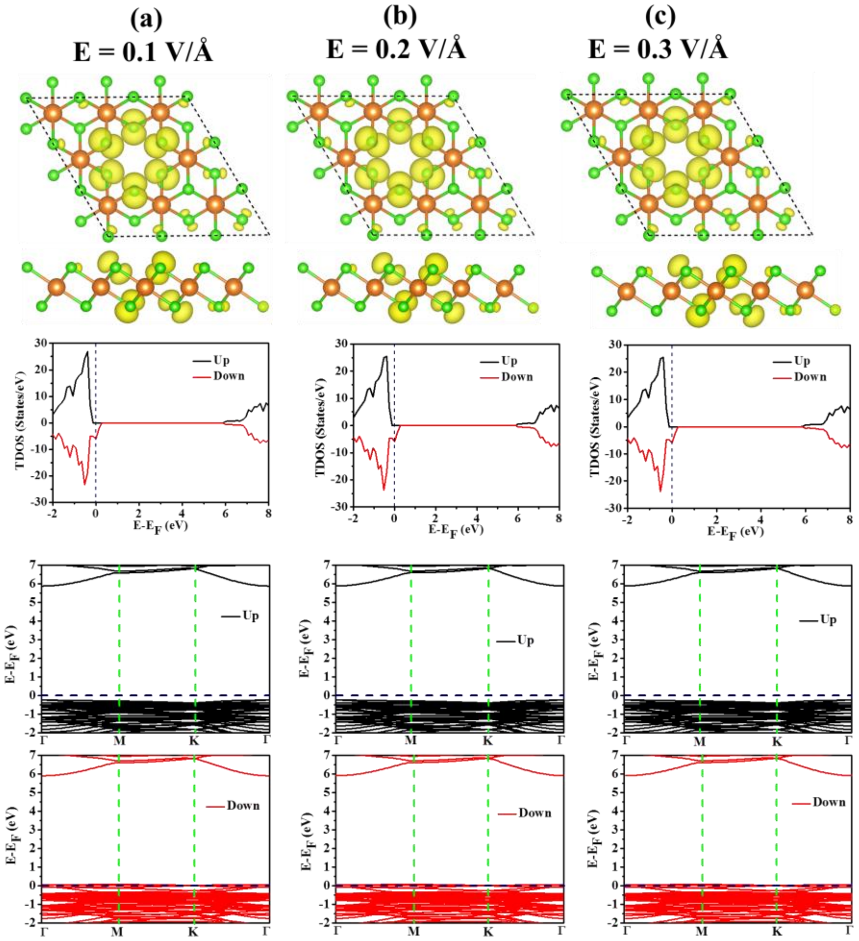

Figure 2.16: (Spin density distribution, spin-polarized density of states and bandstructure with the application of (a) 0.1 VÅ^{-1} (b) 0.2 VÅ^{-1} and (c) 0.3 VÅ^{-1} transverse electric field.

Since our $Mg_{0.89}\delta_{0.11}Cl_2$ monolayer system has a large spin-up gap, the bottom of the conduction band minima will not be considerably affected by the applied electric field (0.1–0.3 V $Å^{-1}$) because they are high energy. The possibility of electronic transition from the lower energy level to the higher band is very less, as there are no states up to 6 eV. They may require very high energy to cross the barrier. However, the spin-down band at the Fermi energy can be stabilized in the presence of electric field. Consequently, the Dirac cone shifts further down as soon as we apply an electric field of 0.1 V $Å^{-1}$. Therefore, we believe that 0.1 V $Å^{-1}$ is the threshold electric field for our system, beyond which the spin-up gap values became constant.

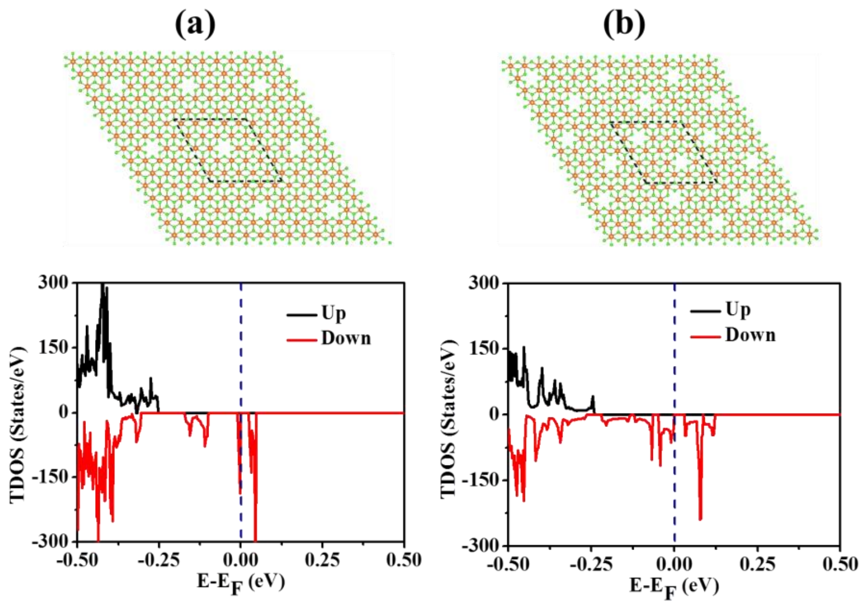

Figure 2.17: Optimized structure and spin-polarized density of states of $Mg_{0.96}\delta_{0.04}Cl_2$ and $Mg_{0.92}\delta_{0.08}Cl_2$ systems.

Further investigations revealed that the $MgCl_2$ based systems with lower defect concentrations ($Mg_{0.96}\delta_{0.04}Cl_2$ and $Mg_{0.92}\delta_{0.08}Cl_2$) exhibit weak half-metallic nature due to the presence of very small gap in the spin-down channel (Figure 2.17).

2.4. Conclusion

In conclusion, using first-principles DFT calculations, we propose a series of robust half-metallic magnesium chloride monolayer based systems with high spin-up gap. Due to the strong spin density overlap between p orbitals, spin-down electronic hopping in our system can be faster, which may be promising for faster spin-transport based devices. Our exploration reveals that the magnesium chloride based magnetic monolayers (including $Mg_{0.89}\delta_{0.11}Cl_2$) are a mixture of $MgCl_2$ and $MgCl_3$ ($Mg_{0.67}\delta_{0.33}Cl_2$) phases. Interestingly, this half-metallic character originates from the $MgCl_3$ phase. The $MgCl_3$ phase has a similar pattern as CrI_3, which has drawn remarkable attention worldwide as a first intrinsic 2D magnet. Amongst the remaining phases, $Mg_{0.89}\delta_{0.11}Cl_2$ shows ferromagnetic ground state with a Curie temperature of 250 K, which is crucial for its application in spintronic device. We find that the total magnetism (2.00μB per vacancy) in $Mg_{0.89}\delta_{0.11}Cl_2$ comes from six Cl atoms rather than a single Cl atom. Interestingly, $Mg_{0.89}\delta_{0.11}Cl_2$ possesses a half-metallic Dirac cone with linear energy dispersion and massless electrons, which is highly desirable and fascinating for its potential application in ultrafast spintronic device. Our calculated formation energy indicates the experimental synthesis possibility of $MgCl_2$ based magnetic monolayer $Mg_{0.89}\delta_{0.11}Cl_2$ under a Cl-rich environment. Lastly, the high magnetic anisotropy energy (MAE) in $Mg_{0.89}\delta_{0.11}Cl_2$ (452.84 μeV) encourages the implementation of $MgCl_2$ in main group based spintronic devices.

Note: This is copyrighted material from Royal Society of Chemistry, Nanoscale, 2018, 10, 22280–22292 (DOI: 10.1039/c8nr07429a).

2.5. References

[1] İmamoğlu A., Awschalom D. D., Burkard G., DiVincenzo D. P., Loss D., Sherwin M., Small A. (1999), Quantum Information Processing Using Quantum Dot Spins and Cavity QED, Phys. Rev. Lett., 83, 4204-4207 (DOI: 10.1103/PhysRevLett.83.4204)

[2] Hanson R., Awschalom D. D. (2008), Coherent manipulation of single spins in semiconductors, Nature, 453, 1043-1049 (DOI: 10.1038/nature07129)

[3] Li X., Wu X., Yang J. (2014), Half-Metallicity in $MnPSe_3$ Exfoliated Nanosheet with Carrier Doping, J. Am. Chem. Soc., 136, 11065-11069 (DOI: 10.1021/ja505097m)

[4] McGuire M. A., Dixit H., Cooper V. R., Sales B. C. (2015), Coupling of Crystal Structure and Magnetism in the Layered, Ferromagnetic Insulator CrI_3, Chem. Mater., 27, 612-620 (DOI: 10.1021/cm504242t)

[5] Gong C., Li L., Li Z., Ji H., Stern A., Xia Y., Cao T., Bao W., Wang C., Wang Y., Qiu Z. Q., Cava R. J., Louie S. G., Xia J., Zhang X., (2017), Discovery of intrinsic ferromagnetism in two-dimensional van der Waals crystals, Nature, 546, 265-269 (DOI: 10.1038/nature22060)

[6] Huang B., Clark G., Navarro-Moratalla E., Klein D. R., Cheng R., Seyler K. L., Zhong D., Schmidgall E., McGuire M. A., Cobden D. H., Yao W., Xiao D., Jarillo-Herrero P., Xu X. (2017), Layer-dependent ferromagnetism in a van der Waals crystal down to the monolayer limit, Nature, 546, 270-273 (DOI: 10.1038/nature22391)

[7] Wang H., Eyert V., Schwingenschl¨ogl U. (2011), Electronic structure and magnetic ordering of the semiconducting chromium trihalides $CrCl_3$, $CrBr_3$, and CrI_3, J. Phys.: Condens. Matter., 23, 116003 (8pp) (DOI: 10.1088/0953-8984/23/11/116003)

[8] Zhang W. B., Qu Q., Zhua P., Lam C. H. (2015), Robust intrinsic ferromagnetism and half semiconductivity in stable two-dimensional single-layer chromium trihalides, J. Mater. Chem. C, 3, 12457-12468. (DOI: 10.1039/c5tc02840j)

[9] Lado J. L., Fernández-Rossier J. (2017), On the origin of magnetic anisotropy in two dimensional CrI_3, 2D Mater., 4 , 035002 (DOI: 10.1088/2053-1583/aa75ed)

[10] Seyler K. L., Zhong D., Klein D. R., Gao S., Zhang X., Huang B., Navarro-Moratalla E., Yang L., Cobden D. H., McGuire M. A., Yao W., Xiao D., Jarillo-Herrero P., Xu X. (2018), Ligand-field helical luminescence in a 2D ferromagnetic insulator, Nat. Phys., 14, 277-281 (DOI: 10.1038/s41567-017-0006-7)

[11] Jiang S., Shan J., Mak K. F. (2018), Electric-field switching of two-dimensional van der Waals magnets, Nat. Mater., 17, 406-410 (DOI: 10.1038/s41563-018-0040-6)

[12] Chabungbam S., Sen P. (2017), Computational design of a robust two-dimensional antiferromagnetic semiconductor, Phy. Rev. B, 96, 045404 (1-10) (DOI: 10.1103/PhysRevB.96.045404)

[13] Besrest P. F., Jaulmes S. (1973), Structure Cristalline de l'Iodure de Chrome: CrI_2, Acta Cryst., B29, 1560 (DOI: 10.1107/S0567740873005030)

[14] Li X., Yang J. (2014), $CrXTe_3$ (X = Si, Ge) nanosheets: two dimensional intrinsic ferromagnetic semiconductors, J. Mater. Chem. C, 2, 7071-7076 (DOI: 10.1039/c4tc01193g)

[15] Lin M. W., Zhuang H. L., Yan J., Ward T. Z., Puretzky A. A., Rouleau C. M., Gai Z., Liang L., Meunier V., Sumpter B. G., Ganesh P., Kent P. R. C., Geohegan D. B., Mandrus D. G., Xiao K. (2016), Ultrathin nanosheets of $CrSiTe_3$: a semiconducting two-dimensional ferromagnetic material, J. Mater. Chem. C, 4, 315-322 (DOI: 10.1039/c5tc03463a)

[16] Sivadas N., Daniels M. W., Swendsen R. H., Okamoto S., Xiao D. (2015), Magnetic ground state of semiconducting transition-metal trichalcogenide monolayers, Phys. Rev. B, 91, 235425 (1-6) (DOI: 10.1103/PhysRevB.91.235425)

[17] Li H., Hu H., Bao C., Hua J., Zhou H., Liu X., Liu X., Zhao M. (2015), Tensile strain induced half-metallicity in graphene-like carbon nitride, Phys. Chem. Chem. Phys., 17, 6028-6035 (DOI: 10.1039/c4cp05560h)

[18] Chintalapati S., Yang M., Lau S. P., Feng Y. P. (2014), Surface magnetism of Mg doped AlN: a first principle study, J. Phys.: Condens. Matter., 26, 435801 (6pp) (DOI: 10.1088/0953-8984/26/43/435801)

[19] Lin S. H., Kuo J. L. (2014), Towards the ionic limit of two-dimensional materials: monolayer alkaline earth and transition metal halides, Phys. Chem. Chem. Phys., 16, 20763-20771 (DOI: 10.1039/c4cp02048k)

[20] Pauling L. (1929), ON THE CRYSTAL STRUCTURE OF THE CHLORIDES OF CERTAIN BIVALENT ELEMENTS, Proc. Natl. Acad. Sci., 15, 709–712 (DOI: 10.1073/pnas.15.9.709)

[21] Fairbrother D. H., Roberts J. G., Rizzi S., Somorjai G. A. (1997), Structure of Monolayer and Multilayer Magnesium Chloride Films Grown on Pd(111), Langmuir, 13, 2090-2096 (DOI: 10.1021/la960680c)

[22] Fairbrother D. H., Roberts J. G., Rizzi S., Somorjai G. A. (1998), The growth of magnesium chloride monolayer and multilayer structures on different transition metal (Pt, Pd, Rh) single crystals with varied orientations, Surf. Sci., 399,109-122 (DOI: 10.1016/S0039-6028(97)00816-9)

[23] Cai L., He J., Liu Q., Yao T., Chen L., Yan W., Hu F., Jiang Y., Zhao Y., Hu T., Sun Z., Wei S. (2015), Vacancy-Induced Ferromagnetism of MoS_2 Nanosheets, J. Am. Chem. Soc., 137, 2622–2627 (DOI: 10.1021/ja5120908)

[24] Kulish V. V., Malyi O. I., Persson C., Wu P. (2015), Adsorption of metal adatoms on single-layer phosphorene, Phys. Chem. Chem. Phys., 17, 992−1000 (DOI: 10.1039/c4cp03890h)

[25] Hu T., Hong J. (2015), First-Principles Study of Metal Adatom Adsorption on Black Phosphorene, J. Phys. Chem. C, 119, 8199−8207 (DOI: 10.1021/acs.jpcc.5b01300)

[26] Cai Y., Ke Q., Zhang G., Zhang Y.-W. (2015), Energetics, Charge Transfer, and Magnetism of Small Molecules Physisorbed on Phosphorene, J. Phys. Chem. C, 119, 3102−3110 (DOI: 10.1021/jp510863p)

[27] Khan I., Hong J. (2015), Manipulation of magnetic state in phosphorene layer by nonmagnetic impurity doping, New J. Phys., 17, 023056 (DOI: 10.1088/1367-2630/17/2/023056)

[28] Fischbein M. D., Drndić M. (2008), Electron beam nanosculpting of suspended graphene sheets, Appl. Phys. Lett., 93, 113107 (1-3) (DOI: 10.1063/1.2980518)

[29] Lehtinen O., Kotakoski J., Krasheninnikov A. V., Tolvanen A., Nordlund K., Keinonen J. (2010), Effects of ion bombardment on a

two-dimensional target: Atomistic simulations of graphene Irradiation, Phys. Rev. B, 81, 153401 (DOI: 10.1103/PhysRevB.81.153401)

[30] Kresse G., Joubert D. (1999), From ultrasoft pseudopotentials to the projector augmented-wave method, Phys. Rev. B, 59, 1758–1775 (DOI: 10.1103/PhysRevB.59.1758)

[31] Perdew J. P., Burke K., Ernzerhof M. (1996), Generalized Gradient Approximation Made Simple, Phys. Rev. Lett., 77, 3865-3868 (DOI: 10.1103/PhysRevLett.77.3865)

[32] Perdew J. P., Chevary J. A., Vosko S. H., Jackson K. A., Pederson M. R., Singh D. J., Fiolhais C. (1992), Atoms, molecules, solids, and surfaces: Applications of the generalized gradient approximation for exchange and correlation, Phys. Rev. B, 46, 6671–6687 (DOI: 10.1103/PhysRevB.46.6671)

[33] Blöchl P. E. (1994), Projector augmented-wave method, Phys. Rev. B, 50, 17953−17979 (DOI: 10.1103/PhysRevB.50.17953)

[34] Grimme S., Antony J., Ehrlich S., Krieg H. (2010), A consistent and accurate ab initio parametrization of density functional dispersion correction (DFT-D) for the 94 elements H-Pu, J. Chem. Phys., 132, 154104 (1-19) (DOI: 10.1063/1.3382344)

[35] Bader R. F. W. (1991), A Quantum Theory of Molecular Structure and Its Applications, Chem. Rev., 91, 893-928 (DOI: 10.1021/cr00005a013)

[36] Henkelman G., Arnaldsson A., Jo´nsson H. (2006), A fast and robust algorithm for Bader decomposition of charge density, Comput. Mater. Sci., 36, 354-360 (DOI: 10.1016/j.commatsci.2005.04.010)

[37] Sanville E., Kenny S. D., Smith R., Henkelman G. J. (2007), Improved Grid-Based Algorithm for Bader Charge Allocation, J. Comput. Chem., 28, 899-908 (DOI: 10.1002/jcc.20575)

[38] Tang W., Sanville E., Henkelman G. (2009), A grid-based Bader analysis algorithm without lattice bias, J. Phys.: Condens. Matter., 21, 084204 (7pp) (DOI: 10.1088/0953-8984/21/8/084204)

[39] Choudhuri I., Bhattacharyya G., Kumar S., Pathak B. (2016), Metal-free half-metallicity in a high energy phase C-doped gh-C_3N_4

system: a high Curie temperature planar system, J. Mater. Chem. C, 4, 11530-11539 (DOI: 10.1039/c6tc04163a)

[40] Jund P., Viennois R., Colinet C., Hug G., F`evre M. T´edenac J. C. (2013), Lattice stability and formation energies of intrinsic defects in Mg_2Si and Mg_2Ge via first principles simulations, J. Phys.: Condens. Matter, 25, 035403 (10pp) (DOI: 10.1088/0953-8984/25/3/035403)

[41] Walker G. B., Marezio M. (1959), Lattice parameters and zone overlap in solid solutions of lead in magnesium, Acta Metall., 7, 769-773 (DOI: 10.1016/0001-6160(59)90090-2)

[42] Sun Y., Zhuo Z., Wu X., Yang J. (2017), Room-Temperature Ferromagnetism in Two-Dimensional Fe_2Si Nanosheet with Enhanced Spin-Polarization Ratio, Nano Lett., 17, 2771−2777 (DOI: 10.1021/acs.nanolett.6b04884)

[43] Stavrou E., Yao Y., Zaug J. M., Bastea S., Kalkan B., Konôpková Z., Kunz M. (2016), High-pressure X-ray diffraction, Raman, and computational studies of $MgCl_2$ up to 1 Mbar: Extensive pressure stability of the β-$MgCl_2$ layered structure, Sci. Rep., 6, 30631 (DOI: 10.1038/srep30631)

[44] Liu J., Sun Q., Kawazoe Y., Jena P. (2016), Exfoliating biocompatible ferromagnetic Cr-trihalide monolayers, Phys. Chem. Chem. Phys., 18, 8777-8784 (DOI: 10.1039/c5cp04835d)

[45] Sarikurt S., Kadioglu Y., Ersan F., Vatansever E., U¨zengi Aktu¨rk O., Yu¨ksel Y., Akıncı U¨., Aktu¨rk E. (2018), Electronic and magnetic properties of monolayer a-$RuCl_3$: a first-principles and Monte Carlo study, Phys. Chem. Chem. Phys., 20, 997-1004 (DOI: 10.1039/c7cp07953b)

[46] Zhu J., Schwingenschlögl U. (2014), Structural and Electronic Properties of Silicene on MgX_2 (X = Cl, Br, and I), ACS Appl. Mater. Interfaces, 6, 11675-11681 (DOI: 10.1021/am502469m)

[47] Zhou Y., Lu H., Zu X., Gao F. (2016), Evidencing the existence of exciting half-metallicity in two-dimensional $TiCl_3$ and VCl_3 sheets, Sci. Rep., 6, 19407 (1-9) (DOI: 10.1038/srep19407)

[48] Kulish V. V., Huang W. (2017), Single-layer metal halides MX_2 (X = Cl, Br, I): stability and tunable magnetism from first principles and Monte Carlo simulations, J. Mater. Chem. C, 5, 8734-8741 (DOI: 10.1039/c7tc02664a)

[49] Feng Y., Wu X., Han J., Gao G. (2018), Robust half-metallicities and perfect spin transport properties in 2D transition metal dichlorides, J. Mater. Chem. C, 6, 4087-4094 (DOI: 10.1039/c8tc00443a)

[50] He J., Ma S., Lyu P., Nachtigall P. (2016), Unusual Dirac half-metallicity with intrinsic ferromagnetism in vanadium trihalide monolayers, J. Mater. Chem. C, 4, 2518-2526 (DOI: 10.1039/c6tc00409a)

[51] Chen M. X., Weinert M. (2016), Half-metallic Dirac cone in zigzag graphene nanoribbons on graphene, Phys. Rev. B, 94, 035433 (1-6) (DOI: 10.1103/PhysRevB.94.035433)

[52] Ma Y., Dai Y., Li X., Sun Q., Huang B. (2014), Prediction of two-dimensional materials with half-metallic Dirac cones: $Ni_2C_{18}H_{12}$ and $Co_2C_{18}H_{12}$, Carbon, 73, 382-388 (DOI: 10.1016/j.carbon.2014.02.080)

[53] Wang B., Yuan S., Li Y., Shi L., Wang J. (2017), A new Dirac cone material: a graphene-like Be_3C_2 Monolayer, Nanoscale, 9, 5577-5582 (DOI: 10.1039/c7nr00455a)

[54] Skelton J. M., Tiana D., Parker S. C., Togo A., Tanaka I., Walsh A. (2015), Influence of the exchange-correlation functional on the quasi-harmonic lattice dynamics of II-VI semiconductors, J. Chem. Phys., 143, 064710 (1-14) (DOI: 10.1063/1.4928058)

[55] Mather P. G., Read J. C., Buhrman R. A. (2006), Disorder, defects, and band gaps in ultrathin (001) MgO tunnel barrier layers, Phys. Rev. B, 73, 205412 (1-5) (DOI: 10.1103/PhysRevB.73.205412)

[56] Shayeganfar F., Vasu K. S., Nair R. R., Peeters F. M., Neek-Amal M. (2017), Monolayer alkali and transition-metal monoxides: MgO, CaO, MnO, and NiO, Phys. Rev. B, 95, 144109 (1-10) (DOI: 10.1103/PhysRevB.95.144109)

[57] Zhou W., Zou X., Najmaei S., Liu Z., Shi Y., Kong J., Lou J., Ajayan P. M., Yakobson B. I., Idrobo J.-C. (2013), Intrinsic Structural

Defects in Monolayer Molybdenum Disulfide, Nano Lett.,13, 2615−2622 (DOI: 10.1021/nl4007479)

[58] Liu D., Guo Y., Fang L., Robertson J. (2013), Sulfur vacancies in monolayer MoS_2 and its electrical contacts, Appl. Phys. Lett., 103, 183113 (1-4) (DOI: 10.1063/1.4824893)

[59] Lin Z., Carvalho B. R., Kahn E., Lv R., Rao R., Terrones H., Pimenta M. A., Terrones M. (2016), Defect engineering of two-dimensional transition metal Dichalcogenides, 2D Mater., 3, 022002 (DOI: 10.1088/2053-1583/3/2/022002)

[60] Baroni S., Giannozzi P., Testa A. (1987), Green's-Function Approach to Linear Response in Solids, Phys. Rev. Lett., 58, 1861 (DOI: 10.1103/PhysRevLett.58.1861)

[61] Togo A., Oba F., Tanaka I. (2008), First-principles calculations of the ferroelastic transition between rutile-type and $CaCl_2$-type SiO_2 at high pressures, Phys. Rev. B, 78, 134106 (1-9) (DOI: 10.1103/PhysRevB.78.134106)

[62] Allard A., Wirtz L. (2010), Graphene on Metallic Substrates: Suppression of the Kohn Anomalies in the Phonon Dispersion, Nano Lett., 10, 4335–4340 (DOI: 10.1021/nl101657v)

[63] Karmodak N., Jemmis E. D. (2017), The Role of Holes in Borophenes: An Ab Initio Study of Their Structure and Stability with and without Metal Templates, Angew. Chem. Int. Ed., 56, 10093 – 10097 (DOI: 10.1002/anie.201610584)

[64] Liu H., Gao J., Zhao J. (2013), From Boron Cluster to Two-Dimensional Boron Sheet on Cu (111) Surface: Growth Mechanism and Hole Formation, Sci. Rep., 3, 3238 (DOI: 10.1038/srep03238)

[65] Souvatzis P., Rudin S. P. (2008), Dynamical stabilization of cubic ZrO_2 by phonon-phonon interactions: Ab initio calculations, Phys. Rev. B, 78, 184304 (1-6) (DOI: 10.1103/PhysRevB.78.184304)

[66] Souvatzis P., Legut D., Eriksson O., Katsnelson M. I. (2010), Ab *initio* study of interacting lattice vibrations and stabilization of the β phase in Ni-Ti shape-memory alloy, Phys. Rev. B, 81, 092201 (1-4) (DOI: 10.1103/PhysRevB.81.092201)

[67] Souvatzis P., Eriksson O., Katsnelson M. I., Rudin S. P. (2008), Entropy Driven Stabilization of Energetically Unstable Crystal Structures Explained from First Principles Theory, Phys. Rev. Lett., 100, 095901 (1-4) (DOI: 10.1103/PhysRevLett.100.095901)

[68] Beecher A. N., Semonin O. E., Skelton J. M., Frost J. M., Terban M. W., Zhai H., Alatas A., Owen J. S., Walsh A., Billinge S. J. L. (2016), Direct Observation of Dynamic Symmetry Breaking above Room Temperature in Methylammonium Lead Iodide Perovskite, ACS Energy Lett., 1, 880−887 (DOI: 10.1021/acsenergylett.6b00381)

[69] Yang J., Wen X., Xia H., Sheng R., Ma Q., Kim J., Tapping P., Harada T., Kee T. W., Huang F., Cheng Y.-B., Green M., Ho-Baillie A., Huang S., Shrestha S., Patterson R., Conibeer G. (2017), Acoustic-optical phonon up-conversion and hot-phonon bottleneck in lead-halide perovskites, Nat. Comm., 8, 14120 (DOI: 10.1038/ncomms14120)

[70] Li B., Zhang Y., Fu L., Yu T., Zhou S., Zhang L., Yin L. (2018), Surface passivation engineering strategy to fully-inorganic cubic $CsPbI_3$ perovskites for high-performance solar cells, Nat. Comm., 9, 1076 (DOI: 10.1038/s41467-018-03169-0)

[71] Marronnier A., Lee H., Geffroy B., Even J., Bonnassieux Y., Roma G. (2017), Structural Instabilities Related to Highly Anharmonic Phonons in Halide Perovskites, J. Phys. Chem. Lett., 8, 2659−2665 (DOI: 10.1021/acs.jpclett.7b00807)

[72] Nose S. (1984), A unified formulation of the constant temperature molecular dynamics Methods, J. Chem. Phys., 81, 511-519 (DOI: 10.1063/1.447334)

[73] Belhadji B., Bergqvist L., Zeller R., Dederichs P. H., Sato K., Katayama-Yoshida H. (2007), Trends of exchange interactions in dilute magnetic Semiconductors, J. Phys.: Condens. Matter, 19, 436227 (12pp) (DOI: 10.1088/0953-8984/19/43/436227)

[74] Wasilewski B., Marciniak W., Werwiński M. (2018), Curie temperature study of $Y(Fe_{1-x}Co_x)_2$ and $Zr(Fe_{1-x}Co_x)_2$ systems using mean field theory and Monte Carlo method, J. Phys. D: Appl. Phys., 51, 175001 (6pp) (DOI: 10.1088/1361-6463/aab75b)

[75] Kan M., Adhikari S., Sun Q. (2014), Ferromagnetism in MnX_2 (X = S, Se) monolayers, Phys. Chem. Chem. Phys., 16, 4990-4994 (DOI: 10.1039/c3cp55146f)

[76] Hu L., Wu X., Yang J. (2016), Mn_2C monolayer: a 2D antiferromagnetic metal with high Néel temperature and large spin–orbit coupling, Nanoscale, 8, 12939-12945 (DOI: 10.1039/c6nr02417c)

[77] Asselin P., Evans R. F. L., Barker J., Chantrell R. W., Yanes R., Chubykalo-Fesenko O., Hinzke D., Nowak U. (2010), Constrained Monte Carlo method and calculation of the temperature dependence of magnetic anisotropy, Phys. Rev. B., 2010, 82, 054415 (DOI: 10.1103/PhysRevB.82.054415)

[78] Sun Y., Zhuo Z., Wu X., Yang J. (2017), Room-Temperature Ferromagnetism in Two-Dimensional Fe_2Si Nanosheet with Enhanced Spin-Polarization Ratio, Nano Lett., 17, 2771−2777 (DOI: 10.1021/acs.nanolett.6b04884)

[79] Feng L., Liu E. K., Zhang W. X., Wang W. H., Wu G. H. (2014), First-principles investigation of half-metallic ferromagnetism of half-Heusler compounds XYZ, J. Magn. Magn. Mater., 351, 92–97 (DOI: 10.1016/j.jmmm.2013.09.054)

[80] Liu B.-G. (2003), Robust half-metallic ferromagnetism in zinc-blende CrSb, Phys. Rev. B, 67, 172411 (1-4) (DOI: 10.1103/PhysRevB.67.172411)

[81] Ashton M., Gluhovic D., Sinnott S. B., Guo J., Stewart D. A., Hennig R. G. (2017), Two-Dimensional Intrinsic Half-Metals With Large Spin Gaps, Nano Lett., 17, 5251−5257 (DOI: 10.1021/acs.nanolett.7b01367)

[82] Kumar A., He H., Pandey R., Ahluwaliad P. K., Tankeshwar K. (2015), Pressure and electric field-induced metallization in the phase-engineered ZrX_2 (X = S, Se, Te) bilayers, Phys. Chem. Chem. Phys., 17, 19215-19221 (DOI: 10.1039/c5cp01445j)

[83] Lu N., Guo H., Li L., Dai J., Wang L., Mei W.-N., Wu X., Zeng X. C. (2014), MoS_2/MX_2 heterobilayers: bandgap engineering via tensile strain or external electrical field, Nanoscale, 6, 2879-2886 (DOI: 10.1039/c3nr06072a)

[84] Nigam S., Gupta S. K., Majumder C., Pandey R. (2015), Modulation of band gap by an applied electric field in silicene-based hetero-bilayers, Phys. Chem. Chem. Phys., 17, 11324-11328 (DOI: 10.1039/c4cp05462h)

[85] Shang J., Zhang S., Cheng X., Wei Z., Li J. (2017), Electric field induced electronic properties modification of ZrS_2/HfS_2 van der Waals heterostructure, RSC Adv., 7, 14625–14630 (DOI: 10.1039/c6ra28383g)

[86] Yang M., Zhang C., Wang S., Feng Y., Ariando (2011), Graphene on β-Si_3N_4: An ideal system for graphene-based Electronics, AIP Advances, 1, 032111 (1-6) (DOI: 10.1063/1.3623567)

[87] Ni Z., Liu Q., Tang K., Zheng J., Zhou J., Qin R., Gao Z., Yu D., Lu J. (2012), Tunable Bandgap in Silicene and Germanene, Nano Lett., 12, 113–118 (DOI: 10.1021/nl203065e)

[88] Mardanya S., Thakur V. K., Bhowmick S., Agarwal A. (2016), Four allotropes of semiconducting layered arsenic that switch into a topological insulator via an electric field: Computational study, Phys. Rev. B, 94, 035423 (1-8) (DOI: 10.1103/PhysRevB.94.035423)

Chapter 3

Defect Induced Ferromagnetism and Half-Metallicity in CaI_2 Based Monolayer for Spintronics Applications

3.1. Introduction

Ever since the successful isolation of graphene *[1]* and the discovery of its outstanding electronic properties *[2]*, tremendous research efforts have been initiated for exploration of new two dimensional (2D) materials with novel electronic and magnetic properties. In this regard, transition metal di-chalcogenides (TMDs) have attracted significant attention due to their interesting properties such as nonzero band gap, superconductivity, and robust ferromagnetism *[3-8]*. Similar to TMD monolayers, another class of monolayer, transition metal di-halide (MX_2, M = transition metal, X = Cl, Br, I) based systems, have also attracted much attention from researchers due to their layered structures and interesting magnetic properties *[9]*. Similar to metal di-halides, layered transition metal tri-halides (MX_3) have also drawn significant attention for showing ferromagnetism and half-metallic characteristics *[10-12]*. Recently, a single crystal of CrI_3 has drawn tremendous attention worldwide after successful experimental demonstration of intrinsic magnetic order down to its monolayer limit *[13]*. Layered chromium triiodide *[13-15]* is considered as a potential candidate for 2D magnets and was established as the thinnest intrinsic ferromagnet with a Curie temperature (T_C) of 45 K. These findings open up high potential for 2D halides from fundamental as well as applied perspectives.

Inspired by the recent reports on the 2D layered thin magnet CrI_3 *[13]* and other transition metal halide based systems *[9-12]*, we have found that alkaline earth based halides have not been much explored. Moreover, most of these magnetic transition metal (TM) halide materials possess very low Curie temperature, which limits their application at room temperature. Therefore, we focused on alkaline earth based halides for exploring magnetism. In addition to that, exploring magnetism in these main group based materials would be very interesting as such main group based materials do not show any intrinsic magnetism. Furthermore, due to strong d−d interactions, metal dopants in main group based materials tend to form clusters resulting in nonhomogeneous magnetization *[9]*. Consequently, researchers have favoured main group based systems *[16-19]* over TM based systems due to their longer spin relaxation time, which is an important criterion for spintronics application *[20-22]*.

Inspired by this, we have found that the alkaline earth based material calcium iodide (CaI_2) possesses a layered structure with (AA) stacking pattern similar to that in CdI_2 *[23-24]*. Since experimental realization of monolayers via exfoliation is a very common technique for layered materials, we are more interested in alkaline earth halides having stable layered structures in their bulk. It has been reported that layered calcium iodide (CaI_2) crystals have a hexagonal layered structure with pronounced cleavage, which indicates that monolayer CaI_2 can be cleaved easily *[25]*. The plasticity and the low hardness of CaI_2 indicate the possibility of fabrication of very thin wafers (up to 0.05 mm) by splitting off and cutting into desired shape from a crystal *[25]*. Thin film of CaI_2 (with thickness >1 nm) has been fabricated and widely used as a long-wavelength X-ray scintillation detector *[25]*. Recently, CaI_2 has been established as an effective passivator of perovskite films for high efficiency and long-term stability of perovskite solar cells *[26]*. Inspired by these previous studies, we have investigated whether CaI_3 monolayer (ML) can be realized (similar to CrI_3) for possible spintronics application.

Inducing magnetism in a nonmagnetic material via low concentration specific point defects is an interesting path to realize new magnetic materials. To the best of our knowledge, magnetism in a Ca-based monolayer system has not been reported to date. Although Ca vacancy induced magnetism has been reported (theoretically as well as experimentally) in bulk CaO *[27, 28]* and CaB_6 (theoretically) *[29]*, none of these previously reported studies (CaO or CaB_6) investigates magnetic anisotropy energy (MAE), strain sustainability of the magnetic ground state, and Curie temperature, which are essential for evaluating the robustness of half-metallic character and implementation of any magnetic material in spintronic devices and its practical application. Therefore, we are interested to know whether creating a single defect or patterned Ca defects in a CaI_2 monolayer can create new transition metal free half-metallic magnetic monolayers, which can be useful for spintronics application. Furthermore, patterned Ca vacancies in a CaI_2 monolayer can form a CaI_3 based magnetic monolayer system as reported for CrI_3 *[13]*. Hence, motivated by defect induced magnetism and half-metallicity, we have presented a methodical study of acquiring magnetism and half-metallicity in CaI_2 monolayers by creating Ca vacancies. Furthermore, the energetic, thermal, and dynamic stabilities are confirmed from total energy, ab initio molecular dynamics simulation, and phonon dispersion calculations, respectively. Electronic properties of the Ca vacancy induced systems have been analyzed from spin-polarized density of states and band structure calculations. Magnetic coupling (ferromagnetism or antiferromagnetism) is calculated from exchange energy. Most of the materials have undergone stress while growing on substrates during device fabrication. Hence, we have inspected the effect of strain on their magnetic properties. Additionally, we have calculated magnetic anisotropy energy and Curie temperature for them, which are very important parameters for their practical use in spintronics devices at room temperature.

3.2. Computational Methods

Spin-polarized density functional theory (DFT) calculations have been carried out for all the structures using the Vienna Ab initio Simulation Package (VASP) *[30]*. Generalized gradient approximation (GGA) with Perdew−Burke−Ernzerhof (PBE) functional was adopted for all our calculations *[31, 32]* for describing correctly the electron−electron exchange and correlation energies of delocalized s and p electrons. Projected augmented wave (PAW) pseudopotential *[33]* was employed for treating core electrons. A plane wave energy cut-off of 320 eV was used to treat interactions between ion cores and valence electrons. We have used a 3 × 3 × 1 hexagonal supercell containing 27 atoms for modelling pure and defect induced CaI_2 monolayers. The first Brillouin zone of pure and vacancy induced CaI_2 monolayers was sampled using a 7 × 7 × 1 and 15 × 15 × 1 k-point grid centered at the gamma (Γ) point for geometry optimization and spin-polarized density of states calculations, respectively. We have also implemented van der Waals corrected density functional theory (DFT-D3) proposed by Grimme to overcome the deficiencies of DFT in treating dispersion interactions and correcting potential energy and interatomic forces *[34]* since van der Waals interactions play a very crucial role for the layered systems. A large vacuum spacing of 20 Å is employed along the z-direction to avoid interactions between the periodic images. The convergence tolerance for energy was set as 10^{-6} eV between two consecutive electronics cycles in a self-consistent run, and the atomic positions are relaxed until Hellmann−Feynman forces acting on each atom were smaller than 0.005 eV·Å^{-1} upon ionic relaxation. Bader charge analysis *[35-37]* was done using the Henkelman program *[38]* with a near-grid algorithm refine-edge method to comprehend the charge transfer process.

Defects formation energies (E_D) under two different environmental conditions (Ca-rich environment and I-rich environment) are calculated to evaluate the stability of various phases of CaI_2 systems. Defect formation energy under Ca-rich environment can be calculated from the following equation *[39, 40]*

$$E_{D@Ca-rich} = E_{def-phase} - (E_{CaI2} - N \times \mu_{Ca-max}) \qquad (3.1)$$

The total energy of the Ca vacancy induced phases of CaI_2 monolayer is denoted by $E_{def-phase}$, and total energy of pure CaI_2 is denoted by E_{CaI2}. The chemical potential of Ca under Ca-rich environment is μ_{Ca-max} and N is the number vacancy created in the CaI_2 supercell. Under Ca-rich environment, $\mu_{Ca-max} = E_{Ca(Bulk)}$, where $E_{Ca(Bulk)}$ is the single atom energy of Ca atom from its respective bulk structure *[41]*. Defect formation energy under I-rich environment can be calculated from the following equation *[39, 40]*

$$E_{D@I-rich} = E_{def-phase} - (E_{CaI2} - N \times \mu_{Ca-min}) \qquad (3.2)$$

Where μ_{Ca-min} (chemical potential of Ca under I-rich environment) can be calculated as

$$\mu_{Ca-min} = (E_{CaI2-unit} - 2 \times \mu_{I-max}) \qquad (3.3)$$

Here, $E_{CaI2-unit}$ is the total energy of the CaI_2 unit cell containing one Ca and two I atoms and μ_{I-max} is the chemical potential of I, which is energy of single I atom from gaseous phase. Furthermore, we have calculated the exchange energy *[18]* (E_{ex}) per unit cell and magnetic anisotropic energy *[18]* for predicting magnetic ground state of defect induced CaI_2 monolayer. The exchange energy per supercell (E_{ex}) is calculated using the following equation where E_{FM} and E_{AFM} denotes the energies of ferromagnetic and antiferromagnetic states.

$$E_{ex} = E_{AFM} - E_{FM} \tag{3.4}$$

Likewise, magnetic anisotropic energy *[42]* (MAE) per unit cell is calculated including spin-orbit coupling (SOC) effect using the equation described below where E_{EA} is the energy of the system along easy axis when an external magnetic field is applied and E_{HA} is the energy of the system along hard axis under application of magnetic field. We have considered our calculation along magnetizing direction (100), (010), (110), (111) and (001).

$$MAE = E_{HA} - E_{EA} \tag{3.5}$$

Additionally, to comprehend the nature of electron spin density on the unpaired electron after creation of Ca vacancy in CaI_2 monolayer, the spin density distribution (SDD) is plotted. The SDD is calculated using the following equation

$$\rho_{SD} = \rho_{up} - \rho_{down} \tag{3.6}$$

Here, the up and down electron spin density are denoted as ρ_{up} and ρ_{down}, respectively. In the SDD, the up spin density of wave functions for different lobes are indicated by yellow colours and the down spin density of wave functions for different lobes are indicated by blue colours. The direct mapping of the electron spin density is measured by the neutron diffraction in electron spin resonance (ESR) spectroscopy *[18]*.

3.3. Results and Discussion:

3.3.1 Cleavage Energy of Monolayer CaI_2 from Bulk

Owing to the existence of large van der Waals gap in bulk CaI_2 (Fig. 3.1), the interlayer interaction is weak, which provides a possibility to obtain CaI_2 monolayers by the exfoliation method. Therefore, to scrutinize the feasibility of exfoliation of 2D CaI_2, cleavage energy or exfoliation energy is calculated. Bulk calcium iodide (CaI_2) has a CdI_2-type layered structure with space group *P*3m1 *[23, 24]*. Our calculated optimized lattice parameters of bulk CaI_2 are a = b = 4.49 Å and c = 7.00 Å (Fig. 3.1), and these values match earlier experimental reports (a = b = 4.49 Å and c = 6.975 Å) *[43, 44]*. Surprisingly, we have not found any experimental papers where they have reported the band gap of CaI_2.

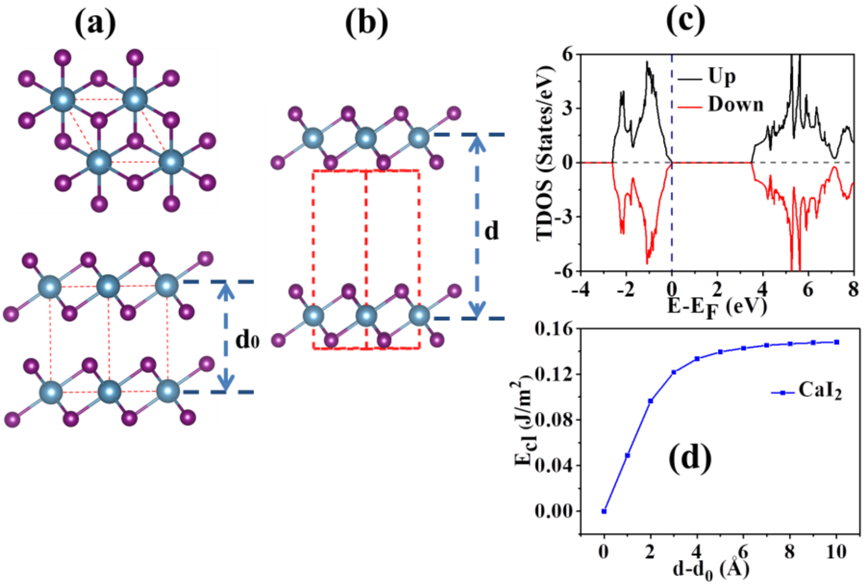

Figure 3.1: (a) Crystal structure of bulk CaI_2 (top and side views; d_0 denotes the interlayer spacing), (b) unit cell geometry of bulk CaI_2 with induced fracture (d is the distance between two fractured parts) to simulate the exfoliation procedure, (c) spin-polarized density of states of bulk CaI_2, where the Fermi level is set to zero and indicated by the blue dashed line, and (d) cleavage energy, E_{cl} (J/m^2), as a function of the separation between two fractured parts.

Our calculated band gap (3.496 eV) of bulk CaI_2 (Fig. 3.1) also matches the previously calculated values (3.46 eV, 3.53 eV) *[45, 46]*. We have also used HSE06 and PBE+U (with U = 1, 2, 3, 4, 5 and J = 0) for the bulk CaI_2 system, and we have found that the calculated band gap values (Table 3.1, Fig. 3.2) are higher than the previously reported theoretical values. Therefore, we believe that the PBE functional is good enough for calculating the properties of CaI_2 based systems.

Table 3.1: Variation of band gap calculated using HSE06 and PBE+U (U=0, 1, 2, 3, 4, 5) calculations

System CaI_2	HSE 06	PBE+ U (U=0)	PBE+ U (U=1)	PBE+ U (U=2)	PBE+ U (U=3)	PBE+ U (U=4)	PBE+ U (U=5)
Band Gap	4.5 eV	3.50 eV	3.86 eV	3.84 eV	3.82 eV	3.82 eV	3.83 eV

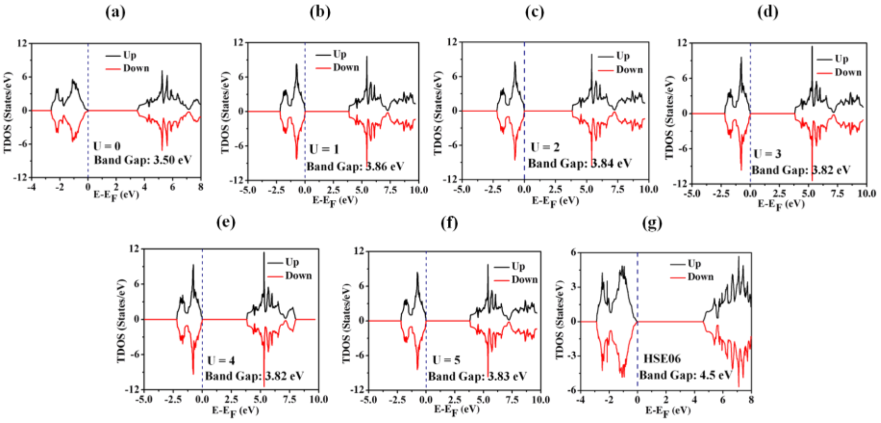

Figure 3.2: Total density of states (TDOS) plot of CaI_2 system using (a)-(f) PBE+U (U=0, 1, 2, 3, 4, 5) and (g) HSE06 calculations.

In order to simulate the exfoliation process, a fracture has been implemented in the bulk CaI_2 structure, and the distance between the two fractured parts has been increased gradually. The variation of total energy was measured thoroughly for all the possible structures with increased distance between the two fractured parts. The parameters d_0 and d (Fig. 3.1a-b) denote the interlayer spacing between the two consecutive layers in CaI_2 bulk structure and distance between the two fractured parts. This method is a very well-known and effective way to calculate exfoliation or cleavage energy *[46-48]*. We have also included van der Waals (vdW) correction terms in our calculations *[34]*. The calculated cleavage energy (Fig. 3.1) for calcium iodide (CaI_2) monolayer is 0.15 J/m^2, which falls in a similar range to those of the previously reported halide materials $CrCl_3$ (0.10 J/m^2), $CrBr_3$ (0.14 J/m^2), and CrI^3 (0.16 J/m^2) *[48]*. The calculated cleavage energy of CaI_2 is even smaller than that of graphite (0.36 J/m^2) *[48]*, which indicate that the CaI_2 monolayer can be cleaved from the layered bulk phases.

3.3.2 Introduction of Magnetism in CaI_2 Monolayer

Our spin-polarized density of states calculations show that bulk CaI_2 is nonmagnetic. Magnetism in CaI_2 based systems has never been reported earlier. Thus, we are interested in exploring magnetism in CaI_2 based systems. In this work, we have focused on defect induced magnetism in a CaI_2 monolayer. Therefore, we have systematically studied the Ca defects in a CaI_2 monolayer. Interestingly, we have found that creating a particular type of defect pattern in metal di-halides creates a metal tri-halide like structure. Therefore, this would be interesting if such alkali metal based tri-halide shows interesting magnetic properties as found in the case of transition metal based tri-halide (CrI_3). For this, a three atom hexagonal unit cell (Fig. 3.3) of CaI_2 monolayer (ML) has been considered for our study.

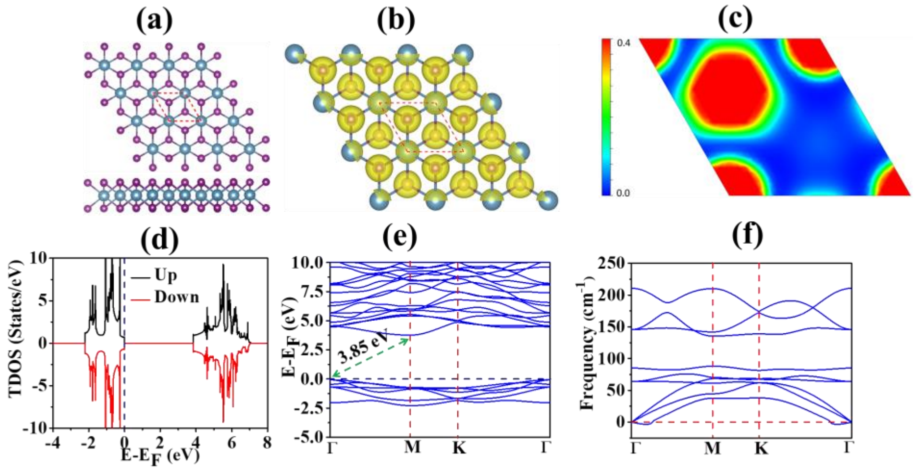

Figure 3.3: (a) Optimized structure (top and side views; the red dashed box indicates the unit cell of the CaI_2 system), (b) total electron density (isosurface value, 0.07 e Å^{-3}), (c) electron localization function (maximum saturation level 0.4 e Å^{-3}; minimum saturation level 0.0 Å^{-3}), (d) spin polarized total density of states (TDOS), (e) band structure, and (f) phonon dispersion plot of the CaI_2 monolayer. The Fermi level is shifted to zero and indicated by a navy blue dashed line.

Optimized lattice parameters of CaI_2 monolayer are calculated as a = b = 4.484 Å. The calculated Ca−I bond distance is found as 3.14 Å. We have observed that the lattice parameters of monolayer are slightly lower than the bulk one. The total electron density distribution of the CaI_2 monolayer shows (Fig. 3.3b) that the electrons are mainly localized around I atoms, while partial localization of electron density has been observed around Ca atoms too. Further, it can be visualized from the electron localization function (ELF plot, Fig. 3.3c) of the CaI_2 monolayer that the electron cloud is not completely centered on I atoms; rather it has some contribution on the Ca atoms also. The Bader charge analysis shows that there is a significant amount of charge transfer from Ca to I (Ca $\approx +1.47|e|$ and I $\approx -0.74|e|$). All these data indicate a strong ionic character between Ca and I atoms in CaI_2. We have found from our spin-polarized density of states (Fig. 3.3d) and band structure (Fig. 3.3e) that CaI_2 ML has an indirect band gap of 3.85 eV, which matches the previous theoretical reports of 3.91 eV *[49]*. The phonon dispersion plot of the CaI_2 monolayer (Fig. 3.3f) shows very few imaginary frequencies ($0.16i$ cm^{-1}, $0.36i$ cm^{-1}, and $0.51i$ cm^{-1}), which is due to pure translational motion of the ML; thus, it can be said that CaI_2 is dynamically stable.

We have considered a 3 × 3 × 1 supercell of the CaI_2 monolayer (9 Ca and 18 I atoms) to model Ca-defect structures $Ca_{0.89}\delta_{0.11}I_2$, $Ca_{0.78}\delta_{0.22}I_2$, and $Ca_{0.67}\delta_{0.33}I_2$ (CaI_3) structures by removing one, two, and three Ca atoms, respectively (Fig. 3.4). Here "δ" refers to the Ca vacancy in the CaI_2 monolayer. Optimized lattice parameters of the pure (CaI_2) and Ca-defect structures $Ca_{0.89}\delta_{0.11}I_2$, $Ca_{0.78}\delta_{0.22}I_2$, and $Ca_{0.67}\delta_{0.33}I_2$ structures are a = b = 13.46, 13.30, 12.94, and 12.41 Å, respectively. Our calculations show that $Ca_{0.89}\delta_{0.11}I_2$ is magnetic with a total magnetic moment of 2.00μB per Ca vacancy. The distribution of magnetic moment can be explained from partial magnetic moments and the charge distributions (from Bader charge analysis). We have found that iodine atoms (I) surrounding the vacancy (in the $Ca_{0.89}\delta_{0.11}I_2$ system) hold an average magnetic moment of 0.193μB per I atom, and the main contribution of magnetic moments comes from the six I atoms as shown in Fig. 3.4a (indicated by pink atoms). Since Ca is bonded with I with their two outermost 4s electrons, removal of a single Ca atom creates two holes in the system, which in turn induces a total magnetic moment of 2.00μB in the $Ca_{0.89}\delta_{0.11}I_2$ system.

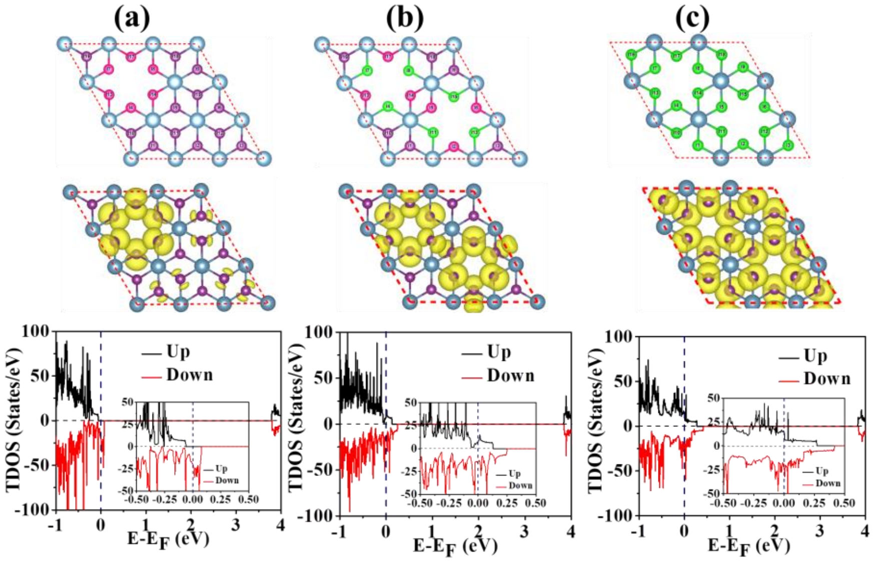

Figure 3.4: Optimized structures, spin density distribution, and spin polarized density of states (inset, magnified spin-polarized TDOS around the Fermi level) of (a) $Ca_{0.89}\delta_{0.11}I_2$, (b) $Ca_{0.78}\delta_{0.22}I_2$, (c) $Ca_{0.67}\delta_{0.33}I_2$ (CaI_3) systems. The Fermi level is set to zero and indicated by the blue dashed line.

Bader charge analysis of the CaI_2 system reveals that the Ca atoms hold an amount of +1.5|e| charges, which implies that Ca gives its two outermost 4s electrons to the iodine atoms in the CaI_2 system. Therefore, the removal of a Ca atom induces a total magnetic moment of 2.00μB, which in turn creates a p doped system. Interestingly, an asymmetric spin density along with half-metallicity has been perceived from the spin polarized density of states in $Ca_{0.89}\delta_{0.11}I_2$ system. However, the other two systems do not show half-metallic character as observed (Fig. 3.4) from their electronic structures. This half-metallic system $Ca_{0.89}\delta_{0.11}I_2$ exhibits an insulating spin-up gap of 3.84 eV and a metallic spin-down channel. Our detailed band structure, TDOS plot, and PDOS plot (Fig. 3.5) further confirm the robust half-metallic character of the $Ca_{0.89}\delta_{0.11}I_2$ system. Orbital resolved band structure has been plotted in Figure 3.5c, where red circle, green square, and blue triangle symbols are proportional to the I p_x, I p_y and I p_z spin-down orbital contribution. To investigate the origin of magnetism and half-metallicity in the $Ca_{0.89}\delta_{0.11}I_2$ system, we have observed the partial density of states (Fig. 3.5d, e) of the CaI_2 and $Ca_{0.89}\delta_{0.11}I_2$ systems. Creation of a single Ca vacancy in the CaI_2 monolayer leads to destabilization of spin-down orbitals of I atoms, and therefore, spin-down orbitals of I in the $Ca_{0.89}\delta_{0.11}I_2$ system have crossed the Fermi level, thus introducing half-metallicity in this system (Fig. 3.5e). Specially, from the orbital resolved band structure, we can say that the I p_x and I p_y spin-down orbitals are the main contributors toward half-metallicity.

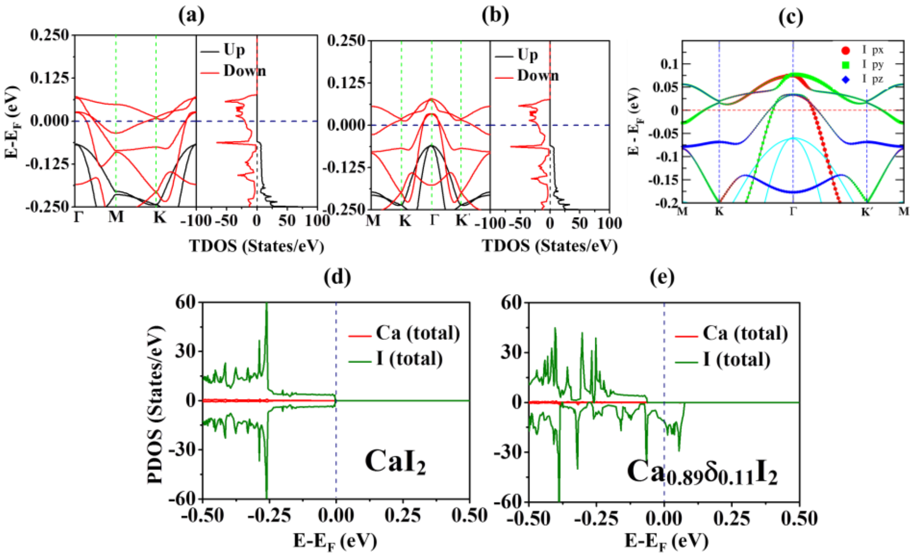

Figure 3.5: (a) Spin polarized band structure and density of states of $Ca_{0.89}\delta_{0.11}I_2$ system, (b) spin polarized band structure covering all the equivalent high symmetry points of the Brillouin zone and density of states of $Ca_{0.89}\delta_{0.11}I_2$ system. (c) Orbital resolved band structure of $Ca_{0.89}\delta_{0.11}I_2$ system, where size of the red, green, and blue dots in the lines are proportional to the I p_x, I p_y and I p_z orbital contribution (spin-down), respectively. The cyan line indicates the spin-up character. Partial density of states (PDOS) of (d) CaI_2 and (e) $Ca_{0.89}\delta_{0.11}I_2$ systems. The Fermi level is set to zero and indicated by the blue dashed line.

To further check the Ca-defect concentration dependence of half-metallicity, we have lowered the defect concentrations to 6.25% ($Ca_{0.94}\delta_{0.06}I_2$) and 4% ($Ca_{0.96}\delta_{0.04}I_2$) by creating a single Ca vacancy in 4 × 4 × 1 and 5 × 5 × 1 supercell structures, respectively. We have found that both $Ca_{0.94}\delta_{0.06}I_2$ and $Ca_{0.96}\delta_{0.04}I_2$ systems are magnetic with a total magnetic moment of 2.00μB. It is also observed from the spin density distribution (Fig. 3.6) that the magnetic moment comes from the iodine atoms surrounding the Ca vacancy similar to that in $Ca_{0.89}\delta_{0.11}I_2$. Spin polarized density of states reveals (Fig. 3.6) that $Ca_{0.94}\delta_{0.06}I_2$ is half-metallic (with an insulating spin-up channel and a metallic spin-down channel), while $Ca_{0.96}\delta_{0.04}I_2$ is semiconducting (Fig. 3.6).

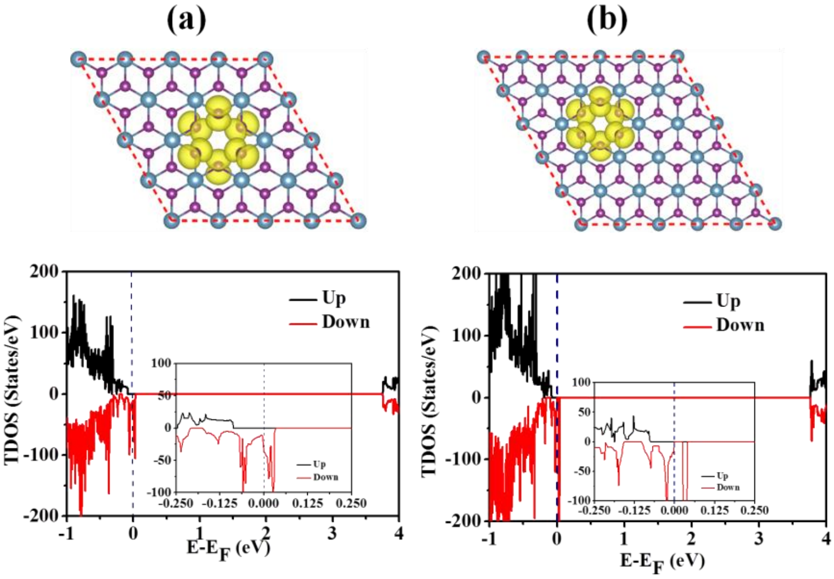

Figure 3.6: Spin density distribution and spin polarized density of states of (a) $Ca_{0.94}\delta_{0.06}I_2$, and (b) $Ca_{0.96}\delta_{0.04}I_2$ systems. The Fermi level is set to zero and indicated by the blue dashed line.

The calculated spin-up gap for $Ca_{0.94}\delta_{0.06}I_2$ is found to be 3.83 eV. So, among the five different Ca-defect-based systems (4.00%, 6.25%, 11.11%, 22.22%, 33.33%), it has been found that only 6.25% and 11.11% defect induced structures exhibit half-metallicity. The systems ($Ca_{0.78}\delta_{0.22}I_2$, $Ca_{0.67}\delta_{0.33}I_2$) with greater than 11.11% vacancies are found to be metallic, and the system with less than 6.25% vacancies is found to be semiconducting in nature. Further analysis of the two metallic systems ($Ca_{0.78}\delta_{0.22}I_2$ and $Ca_{0.67}\delta_{0.33}I_2$) reveals that these two systems have total magnetic moments of 2.19μB (per two Ca vacancies) and 2.64μB (per three Ca vacancies), respectively.

As the numbers of vacancies are increased, the interaction between the two or three magnetic centers is increased resulting in a reduction of total magnetic moment in these $Ca_{0.78}\delta_{0.22}I_2$ and $Ca_{0.67}\delta_{0.33}I_2$ systems.

We have also investigated the underlying reason for disappearance of half-metallic character in $Ca_{0.96}\delta_{0.04}I_2$, $Ca_{0.78}\delta_{0.22}I_2$, and $Ca_{0.67}\delta_{0.33}I_2$ monolayers. As the vacancy density is increased (22.22% and 33.33% corresponding to $Ca_{0.78}\delta_{0.22}I_2$ and $Ca_{0.67}\delta_{0.33}I_2$), the destabilization of I orbitals increases; thus both the spin-up and spin-down orbitals of I are destabilized crossing the Fermi level (Fig. 3.7), which results in the introduction of metallicity in those systems. In contrast to that, when the vacancy density is very small (4.00% corresponding to $Ca_{0.96}\delta_{0.04}I_2$), the destabilization of I orbitals are minimal, and it retains the semiconducting nature (Fig. 3.7) of the CaI_2 system. Finally, among the two half-metallic systems (6.25% and 11.11%), we have mainly focused on the $Ca_{0.89}\delta_{0.11}I_2$ (11.11%) system due to its smaller size and computational cost as well as maximum spin-up gap.

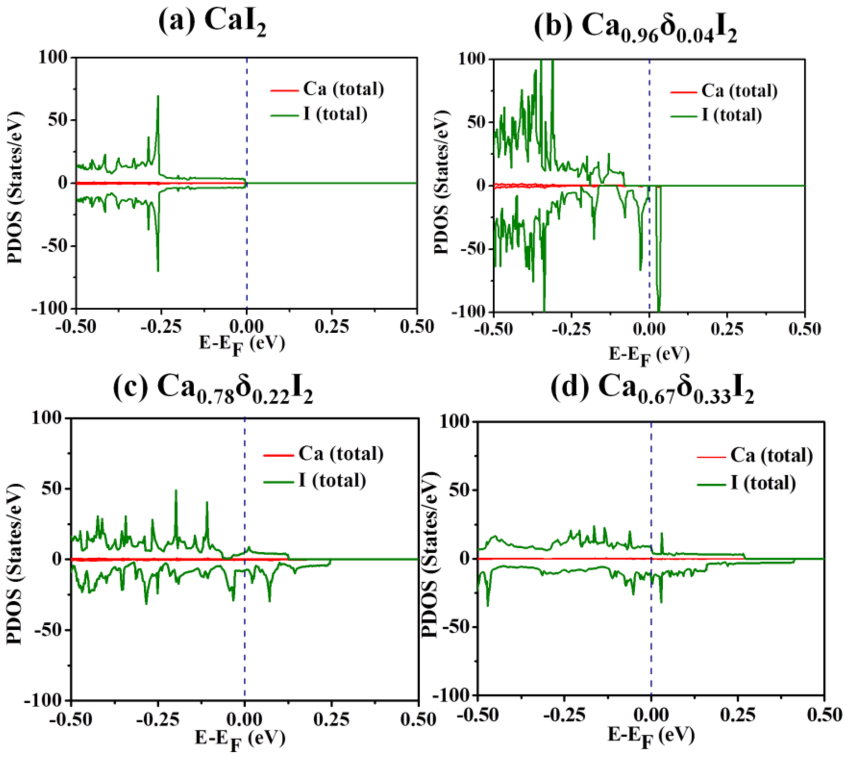

Figure 3.7: Partial density of states (PDOS) plot of Ca and I atoms of (a) CaI_2, (b) semiconducting $Ca_{0.96}\delta_{0.04}I_2$, (c) metallic $Ca_{0.78}\delta_{0.22}I_2$ and

(d) metallic $Ca_{0.67}\delta_{0.33}I_2$ systems. The Fermi level is set to zero and indicated by the blue dashed line.

3.3.3 Analysis of Oxidation State of Ca in CaI_3

To comprehend the oxidation state of Ca in a magnetic monolayer with Ca defects, we have performed Bader charge analysis.

Table 3.2: Bader charge analysis and bond distance of pure CaI_2, $Ca_{0.89}\delta_{0.11}I_2$, $Ca_{0.78}\delta_{0.22}I_2$ and $Ca_{0.67}\delta_{0.33}I_2$.

System		**Bond-distance (Å)**	**Net effective charge**
CaI_2	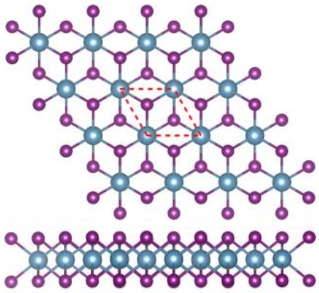	Ca-I ~ 3.14 Å	Ca ~ +1.47|e|, I ~ -0.74|e|
$Ca_{0.89}\delta_{0.11}I_2$	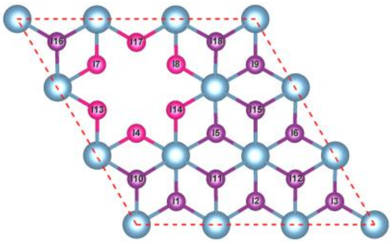 I16 I17 I18 I7 I8 I9 I13 I14 I15 I4 I5 I6 I10 I11 I12 I1 I2 I3	Ca-I ~ 3.10 Å (pink iodines) Ca-I ~ 3.14 Å (violet iodines)	Ca ~ +1.47|e| , I ~ -0.53|e| (pink iodines) I ~ -0.71|e| (violet iodines)
$Ca_{0.78}\delta_{0.22}I_2$	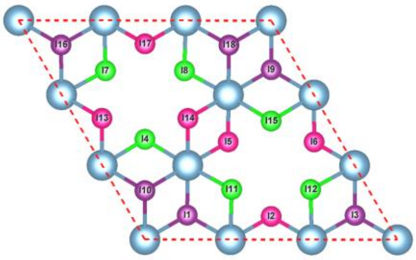 I16 I17 I18 I7 I8 I9 I13 I14 I15 I4 I5 I6 I10 I11 I12 I1 I2 I3	Ca-I ~ 3.09 Å (pink iodines) Ca-I ~ 3.14 Å (green iodines) Ca-I ~ 3.11 Å (violet iodines)	Ca ~ +1.46|e| , I ~ -0.53|e| (pink iodines) I ~ -0.48|e| (green iodines) I ~ -0.69|e| (violet iodines)

$Ca_{0.67}\delta_{0.33}I_2$	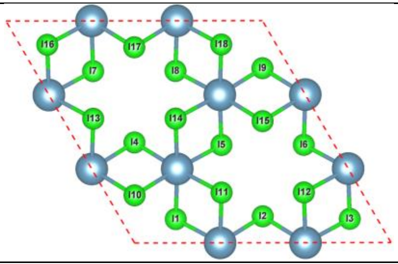 I16 I17 I18 I7 I8 I9 I13 I14 I15 I4 I5 I6 I10 I11 I12 I1 I2 I3	Ca-I ~ 3.11 Å (green iodines)	Ca ~ +1.45|e| , I ~ -0.48|e| (green iodines)

It has been found from the Bader charge distribution (Table 3.2) that for all the three systems ($Ca_{0.89}\delta_{0.11}I_2$, $Ca_{0.78}\delta_{0.22}I_2$, $Ca_{0.67}\delta_{0.33}I_2$ (CaI_3)) Ca has +1.47|e|, +1.46|e|, and +1.45|e|, respectively. These values are almost same for all the cases and also match the net effective charge (+1.47|e|) of Ca atoms in the CaI_2 monolayer. This implies that a Ca vacancy does not alter the oxidation state of Ca in CaI_2 based vacancy induced system including CaI_3 monolayer.

3.3.4 Magnetic Properties of $Ca_{0.89}\delta_{0.11}I_2$ Monolayer

We have considered different competing magnetic ordering in $Ca_{0.89}\delta_{0.11}I_2$ since determination of magnetic ground state plays a very decisive role in the application of any magnetic material in the spintronics domain. We have already found that the magnetic moments in $Ca_{0.89}\delta_{0.11}I_2$ are coming from the iodine atoms. Similar to $Ca_{0.89}\delta_{0.11}I_2$, the magnetic moment in $Ca_{0.67}\delta_{0.33}I_2$ (CaI_3) is also coming from the iodine atoms, and this particular phase has a similar pattern to that observed in CrI_3 *[13]*. However, we have found earlier that $Ca_{0.67}\delta_{0.33}I_2$ (CaI_3) does not hold half-metallic character, which is the main concern in our work. Similar to $Ca_{0.67}\delta_{0.33}I_2$ (CaI_3), $Ca_{0.78}\delta_{0.22}I_2$ also holds metallic character. Hence, we have mainly considered $Ca_{0.89}\delta_{0.11}I_2$ for its magnetic ground states.

To explore the magnetic ground state of $Ca_{0.89}\delta_{0.11}I_2$, first we have considered each iodine atom (I) as a magnetic center and checked whether the six iodine atoms can be treated as a magnetic center. The spin density distribution (Fig. 3.8a,b) shows two magnetic configurations ferromagnetic (FM) and antiferromagnetic (AFM) respectively. It has been found that FM configuration (Fig. 3.8a) is energetically more stable than the AFM one (Fig. 3.8b) by 30.34 meV. Furthermore, we have created a 2 × 2 × 1 supercell of our half-metallic system $Ca_{0.89}\delta_{0.11}I_2$ to investigate three different other possibilities of magnetic configurations (Fig. 3.8c-e). Since, it has been already established that the FM configuration (Fig. 3.8a) is more stable, we can consider the six iodine atoms (I) as a single magnetic center and while considering different magnetic configurations in a bigger supercell. Hence, we have considered two magnetic configurations, FM and AFM-I (Fig. 3.8c,d) where six iodine atoms are considered as single magnetic center. Finally, we have found that the FM configuration (Fig. 3.8c) is energetically more stable by 52.77 and 122.26 meV than AFM-I (Fig. 3.8d) and AFM-II (Fig. 3.8e) configurations respectively. We have also observed that among the two AFM configurations, AFM-I is more stable than AFM-II by 69.49 meV, which again confirms that the six iodine atoms are acting as a single magnetic center giving magnetic moment of 2.00μB. We have also plotted the spin polarized total density of states of all these three configurations. The total density of states (TDOS) plot exhibits that the two AFM configurations are metallic.

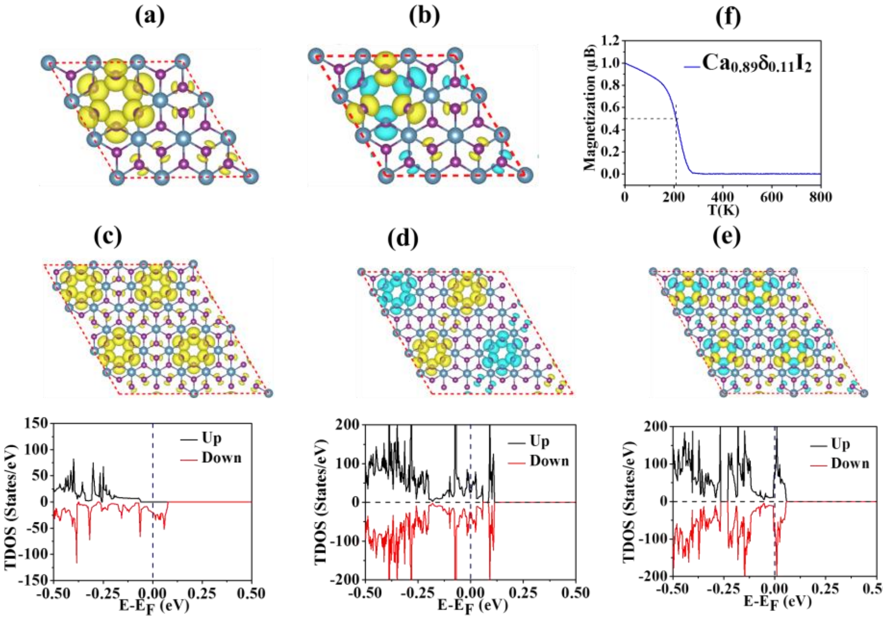

Figure 3.8: (a, b) Optimized structures of $Ca_{0.89}\delta_{0.11}I_2$ in FM and AFM configurations considering a single iodine (I) as the magnetic center, (c-e) optimized structures of $Ca_{0.89}\delta_{0.11}I_2$ in FM, AFM-I, and AFM-II configurations in 2 × 2 × 1 supercell and their corresponding TDOS

plot. The Fermi level is set to zero and indicated by the blue dashed line. (f) Variation of magnetic moment as a function of temperature.

Magnetic anisotropic energy (MAE) *[50]* is an important parameter for magnetic materials in determining the magnetic orientation at low-temperature with respect to the lattice structure. Thus, this parameter is connected to the thermal stability of magnetic data storage *[51]*. It describes the energy required to flip the spin between the two spin states and thus it relates to the blocking temperature below which the magnetic anisotropy can prevent spin fluctuation. Therefore, we have calculated magnetic anisotropy energy (MAE) using noncollinear magnetic calculation with spin−orbit coupling (SOC) for $Ca_{0.89}\delta_{0.11}I_2$ monolayer. The magnetic easy axis (EA) of $Ca_{0.89}\delta_{0.11}I_2$ is found along the (010) direction. Interestingly, we have found that our system, $Ca_{0.89}\delta_{0.11}I_2$, has a large magnetic anisotropy energy (MAE) of 14.11 meV per Ca vacancy in the (010) direction. These data are collected in Table 3.3.

Table 3.3: Summary of magnetic anisotropy energies in meV/vacancy and the easy axis for $Ca_{0.89}\delta_{0.11}I_2$

$Ca_{0.89}\delta_{0.11}I_2$	**Easy Axis (010)**	**(001)-(010)**	**(100)-(010)**	**(110)-(010)**	**(111)-(010)**
	0	14.11 meV	0.35 meV	0.13 meV	3.24 meV

This MAE value (14.11 meV) is comparatively larger than the earlier reported halide based system CrF_3 (119.0 μeV per Cr atom), $CrCl_3$ (31.5 μeV per Cr atom), $CrBr_3$ (185.0 μeV per Cr atom), and CrI_3 (685.5 μeV per Cr atom) *[15]*. Very recently, high magnetic anisotropy energy (1.1 and 1.5 meV) was also observed in one stannene based half-metallic system *[52]*. It is known that elements with 4d or 5d electrons possess strong spin−orbit coupling (SOC) interaction. Such strong SOC could be the reason for high magnetic anisotropic energy (MAE). For example, Ru and Os adatoms on MgO (001) produce giant magnetic anisotropy energy (MAE) of 110 meV per Ru atom and 208 meV per Os atom, respectively *[53]*.

However, in our case, high MAE is observed due to the strong SOC contribution of 5p orbitals of iodine atoms. To analyse the underlying reason for strong SOC, we have checked the partial contribution of SOC for our system. We have found that the main contribution to SOC is coming from the iodine atoms, among which the six iodine atoms surrounding the Ca vacancy contribute the most toward the total SOC for the system. Moreover, for all the iodine atoms, the contribution of SOC is coming from azimuthal quantum number l = 1. For all the other cases (l = 2 and l = 3), we have found much less or no contribution. This establishes the iodine 5p orbitals as the main contributor toward SOC for our system. Moreover, we have reported MAE per Ca vacancy ($Ca_{0.89}\delta_{0.11}I_2$) with 18 I atoms. Thus, the reported high MAE value 14.11 meV is coming from 18 I atoms, which is quite reasonable. Higher magnetic anisotropic energy indicates the required energy to deflect the spin is high; therefore, this material is good for spintronics and magnetoelectronics applications.

Curie temperature (T_C) of a material is one of the significant parameters that determine the prospect of application of that material in spintronics devices. The Curie temperature of the material should be comparable to or higher than room temperature to use it in a spintronics device. Therefore, we have calculated Curie temperature for our system $Ca_{0.89}\delta_{0.11}I_2$. We have employed the mean field theory (MFT) to estimate the Curie temperature of $Ca_{0.89}\delta_{0.11}I_2$ and further confirmed the value with Monte Carlo (MC) simulation. We have found that the Curie temperature of our system $Ca_{0.89}\delta_{0.11}I_2$ is 353.12 K as calculated from MFT theory with $K_B T_{C-MFT} = \frac{2}{3}\Delta E$ where K_B, $T_{C\text{-}MFT}$ and ΔE are Boltzmann's constant, Curie temperature, and exchange energy *[19]*. We have further checked the value of Curie temperature using Monte Carlo (MC) simulation *[54]* based on the Heisenberg Model of $H = -\sum_{i,j} J_{i,j} S_i S_j$ where $J_{i,j}$ is the nearest-neighbour exchange parameter and S_i and S_j represents the spin operators of magnetic moments at neighbour site *i* and *j*, since it is reported that mean field theory (MFT) generally overestimates the Curie temperature while the Monte Carlo (MC) simulation gives more reliable results *[19, 22, 55-57]*. A supercell of 40 × 40 × 1 with periodic boundary conditions was created for the MC simulation of $Ca_{0.89}\delta_{0.11}I_2$. Magnetic moment versus temperature (K) of the $Ca_{0.89}\delta_{0.11}I_2$ system is plotted in Fig. 3.8f. We have observed from the plot that there is a transition from ferromagnetic phase to paramagnetic phase at 208.13 K, which indicates that the Curie temperature for our $Ca_{0.89}\delta_{0.11}I_2$ system is 208.13 K, which is slightly lower than room temperature. However, the calculated value of Curie temperature for $Ca_{0.89}\delta_{0.11}I_2$ system is found to be higher than previously established halide based $CrBr_3$ (theoretical value 32.5 K) and CrI_3 (experimental value 45 K) systems *[13, 14]*. Curie temperature for CrI_3 was calculated as ∼50 K by Monte Carlo simulation, which is very close to the experimental reported value proving the rationality of this Monte Carlo simulation *[58]*. Since our system has a very high MAE value, higher Tc may be obtained if we include the spin-orbital coupling term into the Hamiltonian in the Heisenberg model *[59]*. The simplest model that describes the isotropic interactions between local magnetic moments is the Heisenberg model, $H = -\sum_{i,j} J_{i,j} S_i S_j$ where $J_{i,j}$ is the nearest-neighbour exchange parameter and S_i and S_j represents the spin operator of magnetic moments at neighbour site i and j. It is widely known that at nonzero temperature the isotropic Heisenberg model does not have spontaneous symmetry breaking in two dimensions, due to the divergent contributions of gapless spin-waves *[59]*. In reality, due to spin-orbit coupling, magnetic anisotropy almost always exists, such that long-range magnetic order is generally observed with the addition of even a small amount of anisotropy. The extreme case is the Ising model, which corresponds to infinitely large magnetic anisotropy; hence the spin vectors can only point toward the z-direction. We have found two realistic models (model 1 and model 2) that can predict more realistic Tc values for 2D FM systems considering finite magnetic anisotropy. Model 1, that is, the anisotropic Heisenberg model, incorporates the magnetic anisotropy by exchange anisotropy *[59, 60]*:

$$\mathrm{H} = -\mathrm{J}\sum_{<i,j>}\left[(1-\gamma)\left(\mathrm{S}_\mathrm{i}^\mathrm{x}\mathrm{S}_\mathrm{j}^\mathrm{x} + \mathrm{S}_\mathrm{i}^\mathrm{y}\mathrm{S}_\mathrm{j}^\mathrm{y}\right) + \mathrm{S}_\mathrm{i}^\mathrm{z}\mathrm{S}_\mathrm{j}^\mathrm{z}\right] \quad (3.7)$$

where $\mathrm{S}_\mathrm{i} = \left(\mathrm{S}_\mathrm{i}^\mathrm{x} + \mathrm{S}_\mathrm{i}^\mathrm{y} + \mathrm{S}_\mathrm{i}^\mathrm{z}\right)$ denotes unit vector of a classical magnetic moments at site i, J is magnetic exchange constant and γ is dimensionless constant which indicates the strength of exchange anisotropy *[59, 60]*. The exchange anisotropy parameter γ can take the any values between 0 and 1. Classical Ising model and Heisenberg model can be obtained for the extreme case with $\gamma = 1$, and limit $\gamma = 0$ respectively.

Model 2 assumes isotropic exchange interactions *[58, 59]*, taking into consideration the presence of uniaxial single-ion anisotropy. This model imposes an energy penalty on magnetic moments pointing toward directions other than the magnetic easy axis (chosen to be the z axis), irrespective of the spins at neighbouring sites:

$$\mathrm{H} = -\mathrm{J}\left[\sum_{<i,j>}\mathrm{S}_\mathrm{i}\mathrm{S}_\mathrm{j} + 2\gamma\sum_\mathrm{i}(S_\mathrm{i}^\mathrm{z})^2\right] \quad (3.8)$$

In this model the strength of magnetic anisotropy (γ) can take any positive value.

From the Monte Carlo simulations using the model 1 and model 2, Curie temperature (T_C) can be expressed as a function of strength of magnetic anisotropy (γ) *[59]*. Strength of magnetic anisotropy (γ) can be calculated from the equation $\mathrm{MAE} = 2\gamma\mathrm{J}$ *[59]*. The calculated magnetic exchange J and magnetic anisotropy parameter (γ) for our system $Ca_{0.89}\delta_{0.11}I_2$ is 3.66×10^{-21} Joule and 0.309, respectively. So, our system follows XY model of magnetism, rather than simple Heisenberg model. In a previous report *[59]*, it has been observed and reported that when the magnetic anisotropy parameter (γ) reaches 1, the model 1 predicts $\mathrm{Tc} \approx {}^{0.9\mathrm{J}}/_{\mathrm{K_B}}$ and model 2 predicts $\mathrm{Tc} \approx {}^{1.2\mathrm{J}}/_{\mathrm{K_B}}$. In our case magnetic anisotropy parameter (γ) reaches ~ 0.3.

Hence, in our case, according to model 1, the equation will be $\mathrm{Tc} \approx$

$^{0.85J}/_{K_B}$, and for model 2 the equation becomes Tc ≈ $^{0.9J}/_{K_B}$, where K_B is Boltzmann's constant and J is the exchange constant *[59]*. From model 1 and model 2, the calculated T_C values are 225.11 K and 238.36 K respectively which is considerable higher than previously reported iodide based systems such as CrI_3 *[13]*. Hence, $Ca_{0.89}\delta_{0.11}I_2$ system can be considered to be suitable for spintronic device based applications.

3.3.5. Effect of Strain on Magnetism and Half-Metallicity in $Ca_{0.89}\delta_{0.11}I_2$

Tuning the magnetic properties with the application of external strain is very significant for any 2D materials because during synthesis it undergoes structural modification (change in the lattice parameters) while growing on a substrate. Lattice parameters play a crucial role in defining the fundamental gap in a material. Thus, structural parameters are also directly related to magnetic properties of any materials. Moreover, it is also mandatory to consider the effect of strain on the half-metallicity in any magnetic materials for their practical application. Therefore, we have investigated the effect of strain on magnetism and half-metallicity in the $Ca_{0.89}\delta_{0.11}I_2$ system, applying both uniaxial and biaxial tensile and compressive strain ranging from 1% to 5% to examine the nature of the system and the modulation of spin-up gap in the $Ca_{0.89}\delta_{0.11}I_2$ system.

Table 3.4: Modulation of spin-up gap (eV) in $Ca_{0.89}\delta_{0.11}I_2$ system and nature of the system with % of applied strain along biaxial-tensile and biaxial-compressive direction

% of applied Strain	**Biaxial-compressive**		**Biaxial-tensile**	
	Spin-Up Gap (eV)	**Nature of the system**	**Spin-Up Gap (eV)**	**Nature of the system**
1%	3.763	Half-metallic	3.925	Half-metallic
2%	3.680	Half-metallic	3.711	Half-metallic
3%	3.583	Half-metallic	3.743	Half-metallic
4%	-	Metallic	3.771	Half-metallic
5%	-	Metallic	-	Metallic

Table 3.5: Modulation of spin-up gap (eV) in $Ca_{0.89}\delta_{0.11}I_2$ system and nature of the system with % of applied Strain along uniaxial-tensile and uniaxial-compressive direction

% of applied Strain	**Uniaxial-compressive**		**Uniaxial-tensile**	
	Spin-Up Gap (eV)	**Nature of the system**	**Spin-Up Gap (eV)**	**Nature of the system**
1%	3.822	Half-metallic	3.871	Half-metallic
2%	3.728	Half-metallic	3.88	Half-metallic
3%	-	Metallic	-	Semiconducting
4%	-	Metallic	-	Semiconducting
5%	-	Metallic	-	Semiconducting

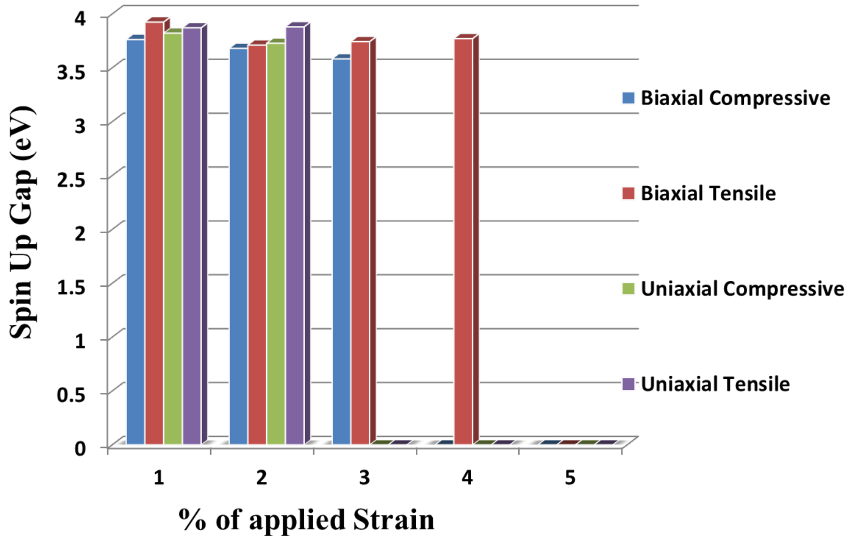

Figure 3.9: Graphical representation of spin-up gap of the half-metallic system $Ca_{0.89}\delta_{0.11}I_2$ under the application of 1% to 5% biaxial compressive, biaxial tensile, uniaxial compressive, and uniaxial tensile strain.

It has been observed that $Ca_{0.89}\delta_{0.11}I_2$ displays various interesting properties under the application of strain. Our system $Ca_{0.89}\delta_{0.11}I_2$ sustains its half-metallic properties (Fig. 3.9) upon application of biaxial compressive strain (up to 3%), biaxial tensile strain (up to 4%), uniaxial compressive strain (up to 2%), and uniaxial tensile strain (up to 2%). The details of the nature of the system upon application of strain and the spin-up gap value are tabulated in Table 3.4-3.5. The spin density distribution and details of TDOS plot under all types of strain from 1% to 5% are included in Fig. 3.10−3.13. It has been observed from the TDOS plot (Fig. 3.13) that under the application of uniaxial tensile strain, our system, $Ca_{0.89}\delta_{0.11}I_2$, holds its half-metallic character up to a critical strain, and beyond that critical strain the structure gets distorted thus introducing a semiconducting state in this system. These results indicate that our system sustains its interesting half-metallic properties under external strain.

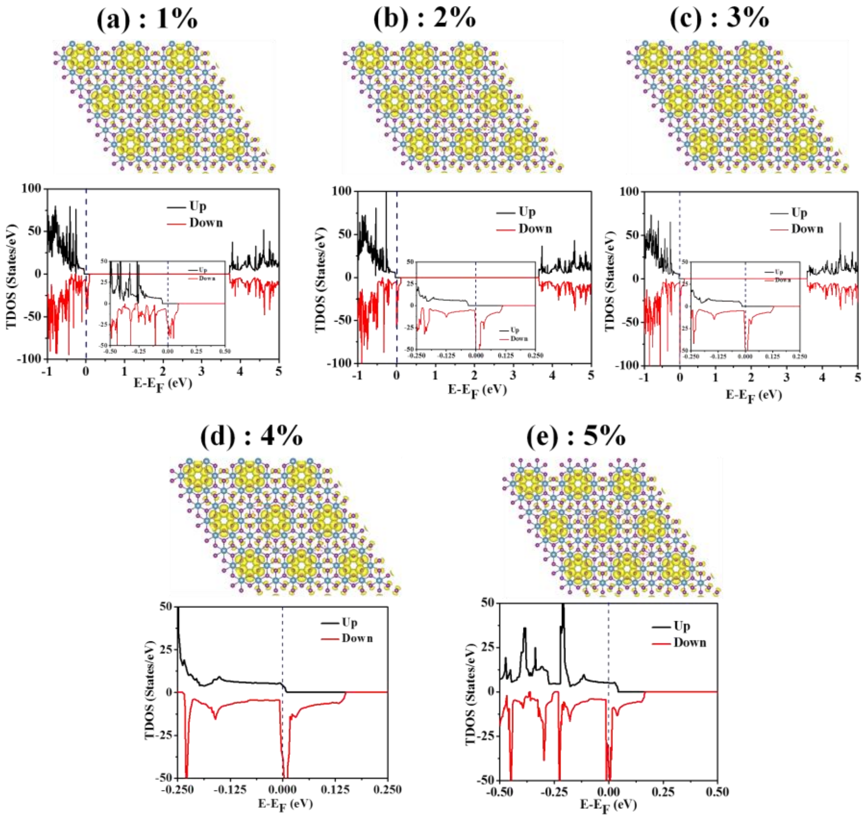

Figure 3.10: (a)-(e) Spin density distribution and TDOS plot of $Ca_{0.89}\delta_{0.11}I_2$ under the application of biaxial compressive strain from 1% to 5% along with magnified spin-polarized TDOS around the Fermi for the three half-metallic systems.

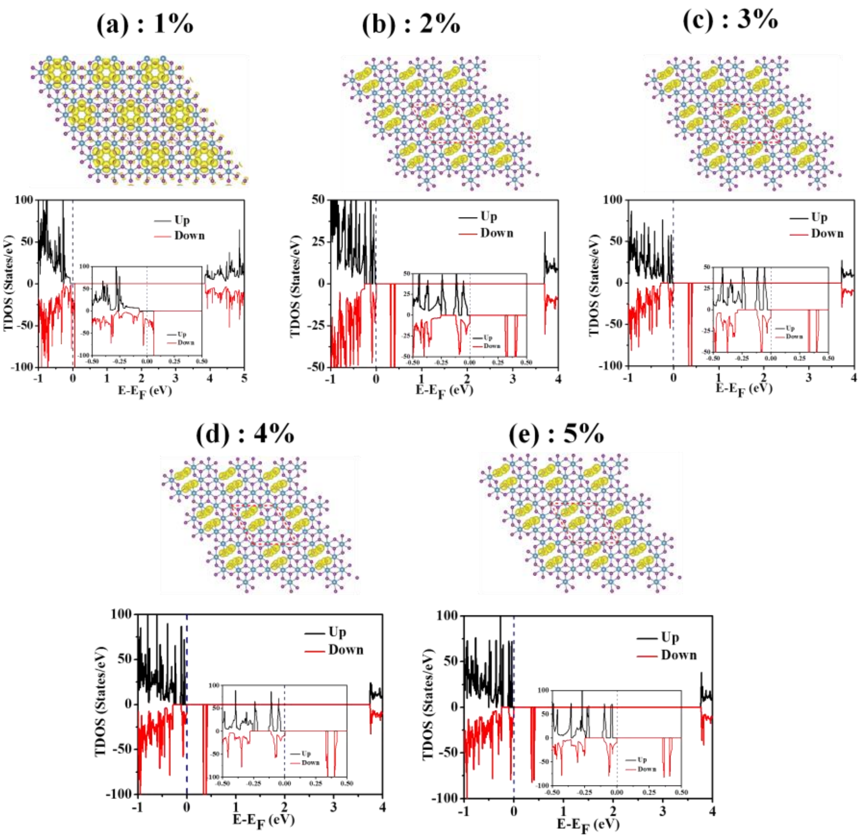

Figure 3.11: (a)-(e) Spin density distribution and TDOS plot of $Ca_{0.89}\delta_{0.11}I_2$ under the application of biaxial tensile strain from 1% to 5% along with magnified spin-polarized TDOS around the Fermi for the systems.

Furthermore, to analyze the magnetic ground state of the strained systems, we have taken a 2 × 2 × 1 supercell of four types of 2% strained systems as up to 2% the system sustains half-metallicity for all types of strain. We have observed that under the application of 2% compressive strain (both biaxial and uniaxial), $Ca_{0.89}\delta_{0.11}I_2$ has a ferromagnetic ground state, whereas, under the application of 2% tensile strain, our system shows an anitiferromagnetic ground state (Fig. 3.14-3.17). The relative energy difference has been tabulated in Table 3.6.

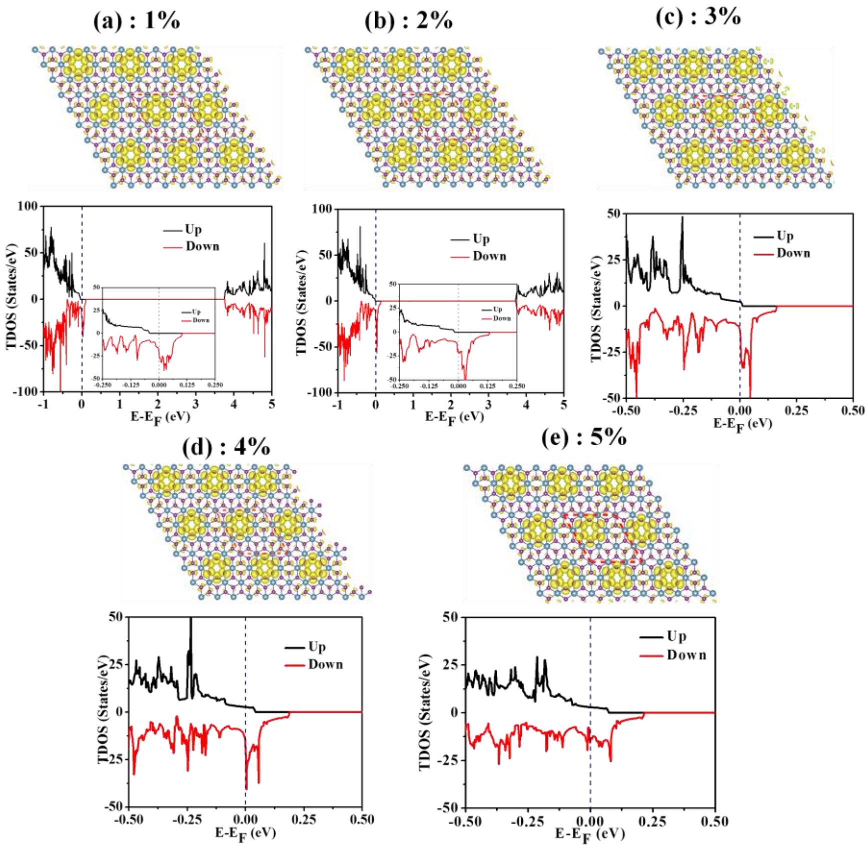

Figure 3.12: (a)-(e) Spin density distribution and TDOS plot of $Ca_{0.89}\delta_{0.11}I_2$ under the application of uniaxial compressive strain from 1% to 5% along with magnified spin-polarized TDOS around the Fermi for the two half-metallic systems.

Table 3.6: Relative energy difference of magnetic ground states (FM, AFM-I and AFM-II) under 2% biaxial and uniaxial strain

System $Ca_{0.89}\delta_{0.11}I_2$	**FM (meV)**	**AFM-I (meV)**	**AFM-II (meV)**
Biaxial-compressive Strain (2%)	0	87.55	38.92
Biaxial-tensile Strain (2%)	643.66	0	10.78
Uniaxial-compressive Strain (2%)	0	92.93	75.18
Uniaxial-tensile Strain (2%)	0.05	0	941.07

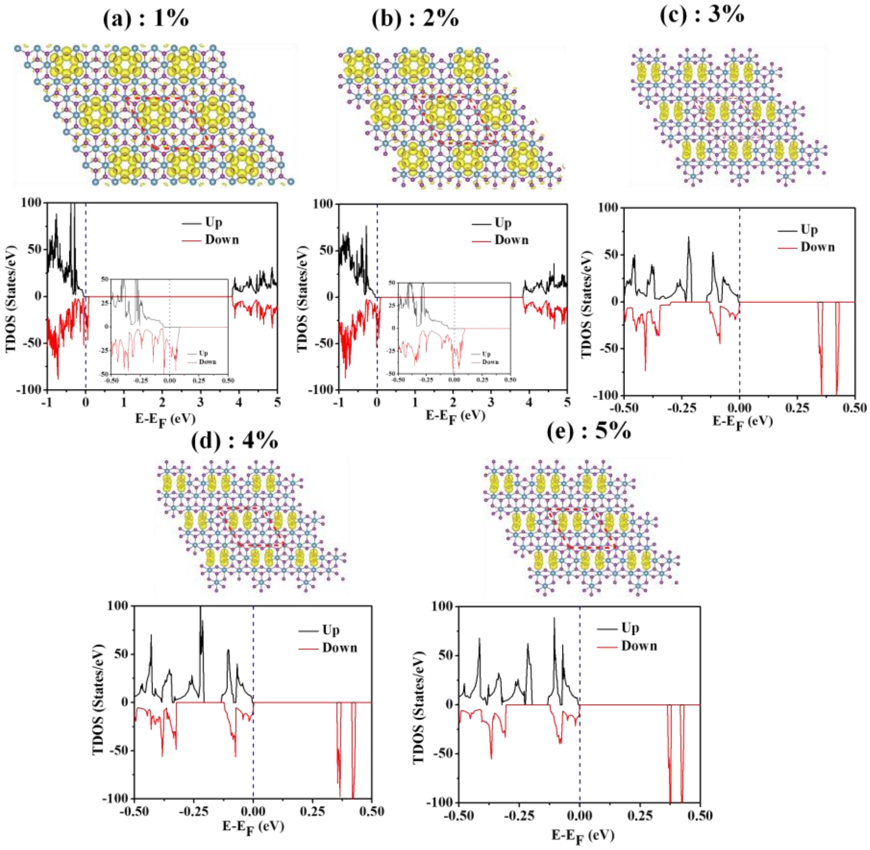

Figure 3.13: (a)-(e) Spin density distribution and TDOS plot of $Ca_{0.89}\delta_{0.11}I_2$ under the application of uniaxial tensile strain from 1% to 5% along with magnified spin-polarized TDOS around the Fermi for the two half-metallic systems.

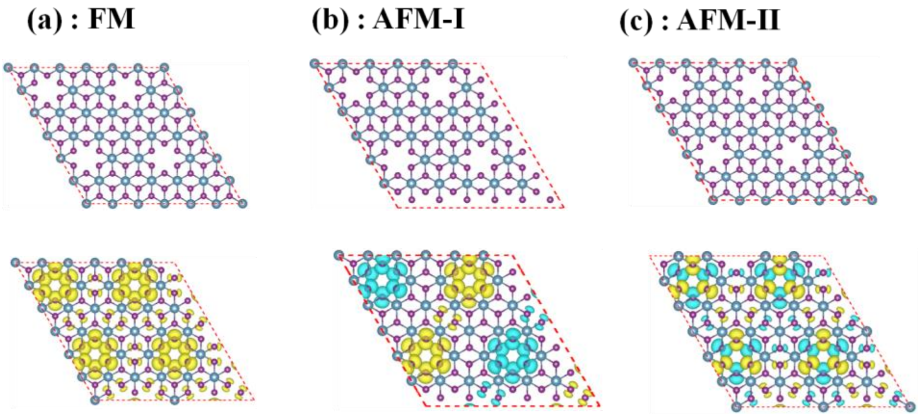

Figure 3.14: Optimized structure and spin density distribution (SDD) of $Ca_{0.89}\delta_{0.11}I_2$ system under 2% biaxial compressive strain with (a) FM, (b) AFM-I and (c) AFM-II configurations in 2 × 2 × 1 supercell.

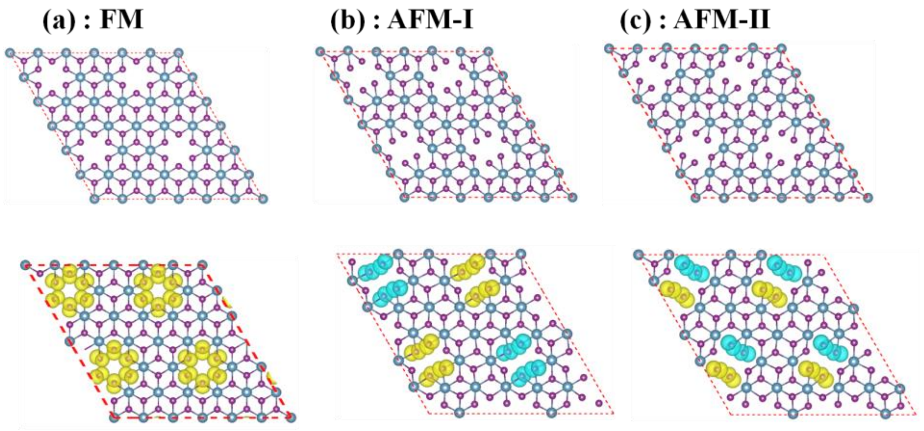

Figure 3.15: Optimized structure and spin density distribution (SDD) of $Ca_{0.89}\delta_{0.11}I_2$ system under 2% biaxial tensile strain with (a) FM, (b) AFM-I and (c) AFM-II configurations in 2 × 2 × 1 supercell.

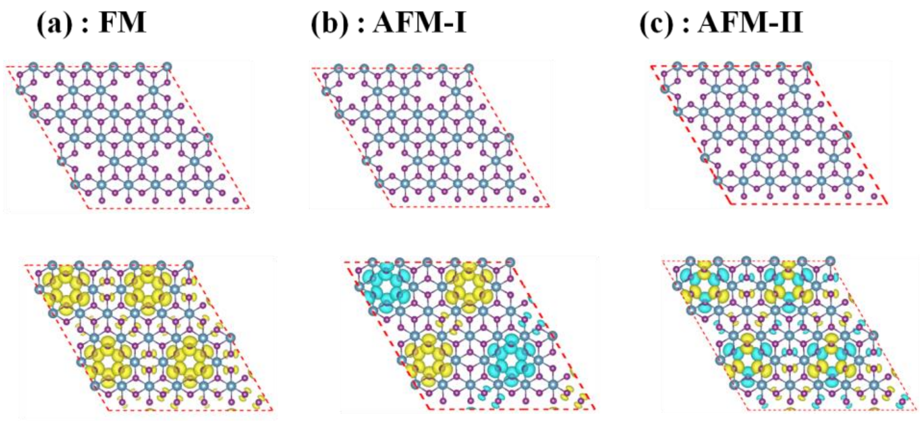

Figure 3.16: Optimized structure and spin density distribution (SDD) of $Ca_{0.89}\delta_{0.11}I_2$ system under 2% uniaxial compressive strain with (a) FM, (b) AFM-I and (c) AFM-II configurations in 2 × 2 × 1 supercell.

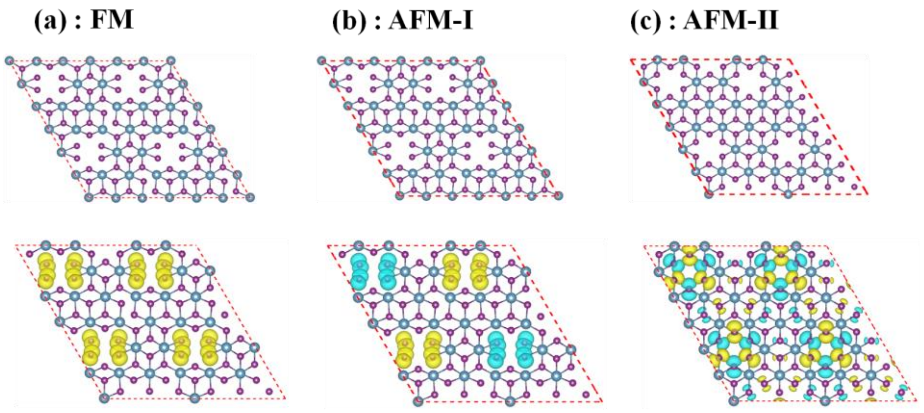

Figure 3.17: Optimized structure and spin density distribution (SDD) of $Ca_{0.89}\delta_{0.11}I_2$ system under 2% uniaxial tensile strain with (a) FM, (b) AFM-I and (c) AFM-II configurations in 2 × 2 × 1 supercell.

3.3.6. Energetic stability and experimental realization of $Ca_{0.89}\delta_{0.11}I_2$

We have calculated the vacancy formation energy (Table 3.7) of Ca defected phases to evaluate the energetic stabilities of these systems under different experimental growth conditions as explained in section 3.2. It has been found that the formation energy of all these Ca vacancy induced phases $Ca_{0.89}\delta_{0.11}I_2$, $Ca_{0.78}\delta_{0.22}I_2$ and $Ca_{0.67}\delta_{0.33}I_2$ (CaI_3) under Ca-rich environment are 6.94, 6.85 and 6.71 eV/ vacancy respectively, while the formation energy of all these Ca vacancy induced phases under I-rich environment are 1.39, 1.30 and 1.16 eV/vacancy respectively (Table 3.7). Hence, the creation of Ca vacancy is favorable under I-rich environment.

Table 3.7: Summary of formation energy/vacancy (E_F) under Ca-rich and I-rich environments and nature of the material for with different Ca-vacancy concentrations

Ca Vacancy in CaI_2	**Formation energy (eV/vacancy)**		**Nature**
	Under Ca-rich environment	**Under I-rich environment**	
$Ca_{0.67}\delta_{0.33}I_2$	6.71	1.16	Metallic
$Ca_{0.78}\delta_{0.22}I_2$	6.85	1.30	Metallic
$Ca_{0.89}\delta_{0.11}I_2$	6.94	1.39	Half-Metallic

We have primarily focused Ca vacancy induced CaI_2 monolayer ($Ca_{0.89}\delta_{0.11}I_2$) since this is half-metallic and thus central concern in our study. While analyzing the possibility of synthesizing of $Ca_{0.89}\delta_{0.11}I_2$, we have found that incorporation of Ca vacancy in CaO nanopowder (experimentally grown by sol-gel method) has already been experimentally evidenced *[61]*. Point defect can be achieved deliberately by irradiation by high energy particles, including electron beam, ion beam, high energy laser, or by chemical etching *[62]*. For the generation of a point defect via electron beam irradiation, the electron beam energy should be higher than the knock-on damage threshold *[62]* for the system. However, it has been also found in literature that various defects concentration can be controlled by regulating the synthesis process *[62]*. Therefore, single Ca vacancy in CaI_2 monolayer ($Ca_{0.89}\delta_{0.11}I_2$) may also be achieved experimentally.

3.3.7. Dynamic, and Thermal Stability of $Ca_{0.89}\delta_{0.11}I_2$

To analyze the dynamic stability of $Ca_{0.89}\delta_{0.11}I_2$ system, phonon frequency has been calculated using density functional perturbation theory (DFPT) *[63]* as implemented in VASP and phonon dispersion calculations has been carried out using the Phonopy code *[64]*. Phonon dispersion plot of $Ca_{0.89}\delta_{0.11}I_2$ system (Fig. 3.18a) reveals that it has five imaginary frequencies (0.98*i*, 2.15*i*, 16.80*i*, 21.74*i* and 25.40*i* cm^{-1} respectively). Precisely, there are two acoustic modes where no non-trivial motion of atoms has been observed (0.98*i*, 2.15*i* cm^{-1}); rather it exhibits only translation motion of the whole system together (Fig. 3.19d-e). These values are also very small and thus can be considered as numerical noise *[65]*. The other three imaginary frequencies (16.80*i*, 21.74*i* and 25.40*i* cm^{-1}) corresponds to mainly slight vibration motions of six I atoms (marked within the red circle; Fig. 3.19a-c) in which every two I are oppositely displaced.

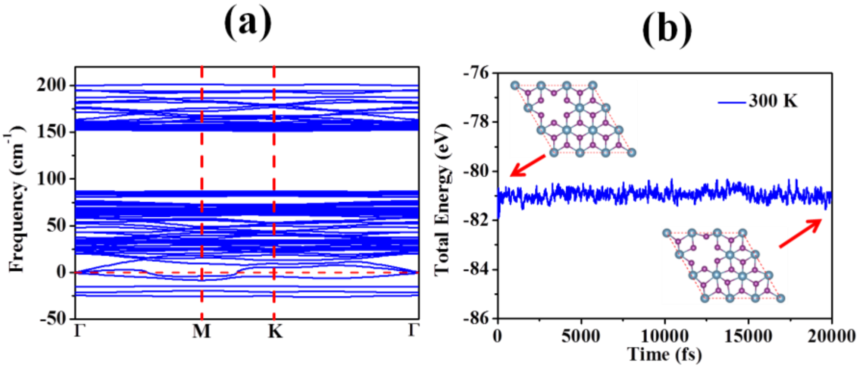

Figure 3.18: (a) Phonon dispersion plot of $Ca_{0.89}\delta_{0.11}I_2$ system, and (b) total energy fluctuation of AIMD simulation of $Ca_{0.89}\delta_{0.11}I_2$ system.

Therefore, we have relaxed the soft modes of our $Ca_{0.89}\delta_{0.11}I_2$ system by moving these I atoms along the displacement vectors. We have taken two displaced structures and optimized the two structures (named as structure-1 and structure-2). Further, we have calculated the phonon dispersion for these two structures. Although, these two new structures also hold imaginary frequencies, the values of these imaginary frequencies are much lower than our earlier imaginary frequencies.

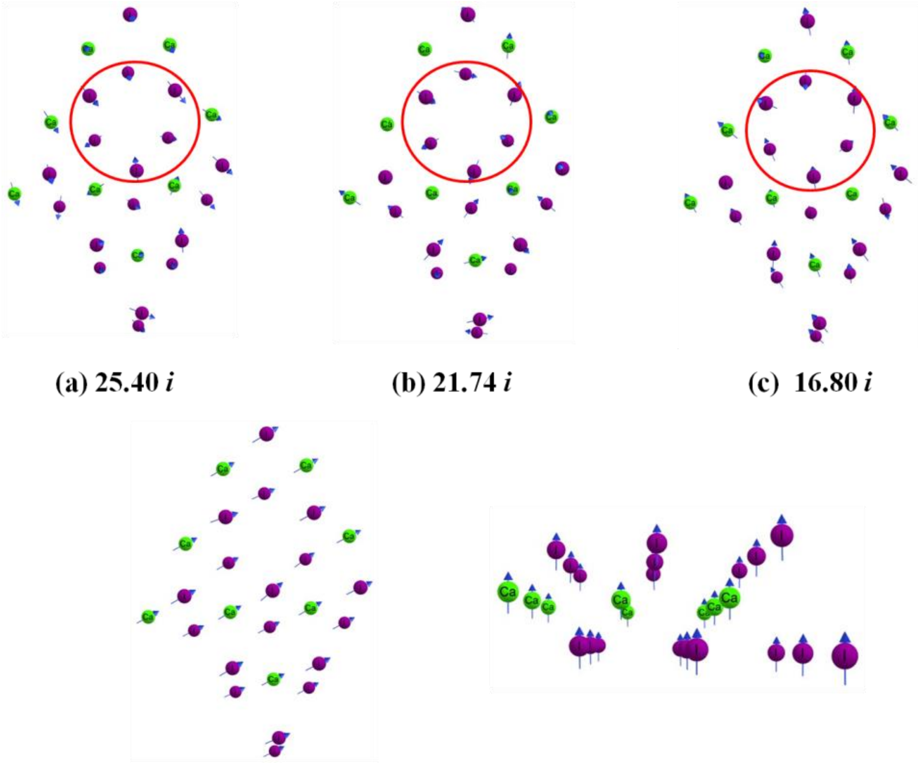

(a) 25.40 *i* (b) 21.74 *i* (c) 16.80 *i*

(d) 2.15 *i* (e) 0.98 *i*

Figure 3.19: Displacement eigenvectors (indicated by blue arrows) corresponding to the soft phonon mode with imaginary frequencies of (a) 25.40*i* cm^{-1}, (b) 21.74*i* cm^{-1} (c) 16.80*i* cm^{-1} (d) 2.15*i* cm^{-1} and (e) 0.98*i* cm^{-1} of $Ca_{0.89}\delta_{0.11}I_2$ system. The violet and green atoms respectively denote I and Ca.

We have chosen $Ca_{0.89}\delta_{0.11}I_2$ (structure-2) for our main system since it has lower imaginary frequency. Phonon dispersion plot for $Ca_{0.89}\delta_{0.11}I_2$ (structure-2) is shown in Fig. 3.20. Precisely, structure-2 has four imaginary frequencies out of which three imaginary frequencies (0.29*i*, 0.37*i*, and 0.45*i* cm^{-1}) are coming from purely translational motion, thus cannot be considered as actual unstable mode. Only one imaginary frequency (20.13*i* cm^{-1}) is coming from the vibration of iodine atoms (Fig. 3.21). Therefore, we believe that our structure may be stable on proper substrate.

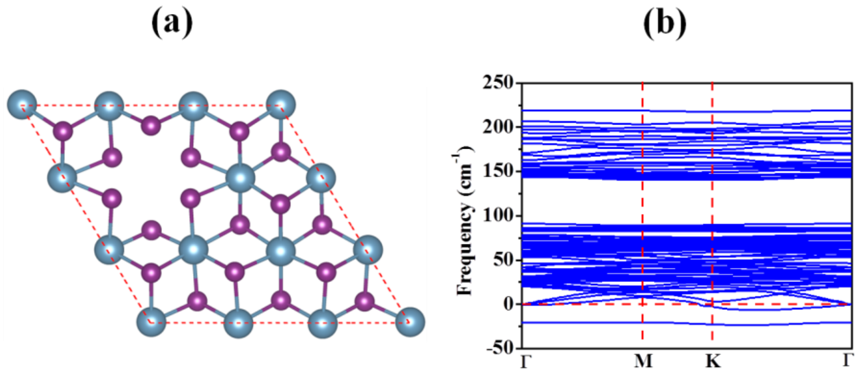

Figure 3.20: (a) Soft mode relaxed optimized structure and (b) phonon dispersion plot of soft mode relaxed $Ca_{0.89}\delta_{0.11}I_2$ (structure-2) system.

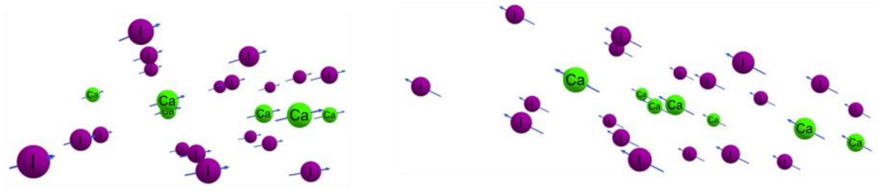

(a) 0.29 *i*　**(b) 0.37 *i***

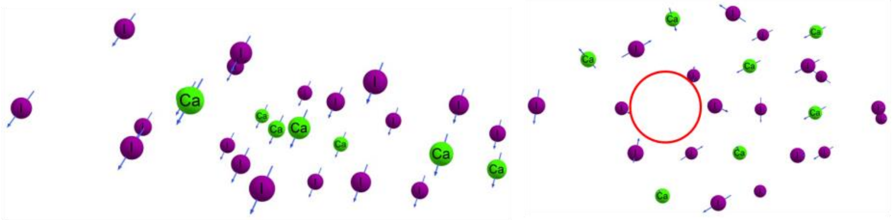

(c) 0.45 *i*　**(d) 20.13 *i***

Figure 3.21: Displacement eigenvectors (indicated by blue arrows) corresponding to the soft phonon mode with imaginary frequencies of (a) 0.29*i* cm^{-1}, (b) 0.37*i* cm^{-1} (c) 0.45*i* cm^{-1} and (d) 20.13*i* cm^{-1} of $Ca_{0.89}\delta_{0.11}I_2$ (structure-2) system. The violet and green atoms respectively denote I and Ca.

Thermal stability of $Ca_{0.89}\delta_{0.11}I_2$ system (Fig. 3.18b) is analyzed from AIMD simulations *[66]* using an NVT ensemble at 300 K with a time step of 1 fs (femto second) for 20 ps (pico second). Room temperature AIMD simulation shows no possibility of inter-conversion or structural distortion from the optimized $Ca_{0.89}\delta_{0.11}I_2$ system. Thus, it can be concluded that the $Ca_{0.89}\delta_{0.11}I_2$ system is thermally stable in room temperature.

Since, free standing monolayer ($Ca_{0.89}\delta_{0.11}I_2$) shows stability, we believe substrate can provide more stability to our monolayer system. On the other hand, we have found that monolayer and multilayer of another alkaline earth based halide system ($MgCl_2$) was synthesized on various transition metal single crystal surfaces, such as Pd (111) and (100), Pt (111) and (100)-hex and Rh (1l1), by H. Fairbrother and co-workers using molecular beam epitaxy (MBE) and low energy electron diffraction (LEED) method [*67-68]*. Moreover, another Ca based halide system, CaF_2 thin film, was grown by molecular beam epitaxy (MBE) method on Si (111) substrate *[69]*. So, we believe that CaI_2 ML based systems can also be synthesized on transition metal single crystal surfaces.

3.4. Conclusion

In conclusion, using first-principles DFT calculations, we report a series of calcium iodide based magnetic monolayers. Our report reveals that a certain pattern defect can produce a magnetic monolayer, $Ca_{0.67}\delta_{0.33}I_2$ (CaI_3) that has a similar pattern to that in CrI_3. We find that a CaI_2 monolayer with a single vacancy ($Ca_{0.89}\delta_{0.11}I_2$) exhibits ferromagnetic half-metallicity (high spin-up gap of 3.84 eV) with Curie temperature as high as 238 K (XY model), which is considerably higher than the reported first intrinsic 2D magnet CrI_3 (45 K) monolayer. Furthermore, we have observed considerably higher magnetic anisotropy energy of 14.11 meV for the $Ca_{0.89}\delta_{0.11}I_2$ system than the earlier reported halide based systems, CrF_3 (119.0 μeV), $CrCl_3$ (31.5 μeV), $CrBr_3$ (185.0 μeV), and CrI_3 (685.5 μeV), which indicates that the alkali halide based material can be resistive to spin fluctuation. Our calculated formation energy values indicate the possibility of experimental synthesis of the CaI_2 based magnetic monolayer under an I-rich environment. Thus, such alkali halide based materials can be promising for applications in spintronic devices.

Note: This is copyrighted material from American Chemical Society, ACS Appl. Nano Mater, 2019, 2, 6152−6161 (DOI: 10.1021/acsanm.9b00967).

3.5. References

[1] Novoselov K. S., Geim A. K., Morozov S. V., Jiang D., Zhang Y., Dubonos S. V., Grigorieva I. V., Firsov A. A. (2004), Electric Field Effect in Atomically Thin Carbon Films, Science, 306, 666−669 (DOI: 10.1126/science.1102896)

[2] Castro Neto A. H., Guinea F., Peres N. M. R., Novoselov K. S., Geim A. K. (2009), The Electronic Properties of Graphene, Rev. Mod. Phys., 81, 109–162 (DOI: 10.1103/RevModPhys.81.109)

[3] Radisavljevic B., Whitwick M. B., Kis A. (2012), Small-Signal Amplifier Based on Single-Layer MoS_2, Appl. Phys. Lett., 101, 043103 (1-4) (DOI: 10.1063/1.4738986)

[4] Chhowalla M., Shin H. S., Eda G., Li L. J., Loh K. P., Zhang, H. (2013), The Chemistry of Two-Dimensional Layered Transition Metal Dichalcogenide Nanosheets, Nat. Chem., 5, 263-275 (DOI: 10.1038/NCHEM.1589)

[5] Wang Q. H., Zadeh K. K., Kis A., Coleman J. N., Strano M. S. (2012), Electronics and Optoelectronics of Two-Dimensional Transition Metal Dichalcogenides, Nat. Nanotechnol, 7, 699-712 (DOI: 10.1038/NNANO.2012.193)

[6] Kuc A., Zibouche N., Heine T. (2011), Influence of Quantum Confinement on the Electronic Structure of the Transition Metal Sulfide TS_2, Phys. Rev. B, 83, 245213 (1-4) (DOI: 10.1103/PhysRevB.83.245213)

[7] Hsu Y. T., Vaezi A., Fischer M. H., Kim E. A. (2017), Topological Superconductivity in Monolayer Transition Metal Dichalcogenides, Nat. Comm., 8, 14985 (1-6) (DOI: 10.1038/ncomms14985)

[8] Zhang Y., Pang J., Zhang M., Gu X., Huang L. (2017), Two-Dimensional Co_2S_2 Monolayer with Robust Ferromagnetism, Sci. Rep., 7, 15993 (1-8) (DOI: 10.1038/s41598-017-16032-x)

[9] Kulish V. V., Huang W. (2017), Single-Layer Metal Halides MX_2 (X = Cl, Br, I): Stability and Tunable Magnetism from First Principles and Monte Carlo Simulations, J. Mater. Chem. C, 5, 8734-8741 (DOI: 10.1039/c7tc02664a)

[10] Zhou Y., Lu H., Zu X., Gao F. (2016), Evidencing the Existence of Exciting Half-Metallicity in Two-Dimensional $TiCl_3$ and VCl_3 Sheets, Sci. Rep., 6, 19407 (1-9) (DOI: 10.1038/srep19407)

[11] He J., Ma S., Lyu P., Nachtigall P. (2016), Unusual Dirac Half-Metallicity with Intrinsic Ferromagnetism in Vanadium Trihalide Monolayers, J. Mater. Chem. C, 4, 2518-2526 (DOI: 10.1039/c6tc00409a)

[12] McGuire M. A. (2017), Crystal and Magnetic Structures in Layered, Transition Metal Dihalides and Trihalides, Crystals, 7, 121 (1-25) (DOI: 10.3390/cryst7050121)

[13] Huang B., Clark G., Navarro-Moratalla E., Klein D. R., Cheng R., Seyler K. L., Zhong D., Schmidgall E., McGuire M. A., Cobden D. H., Yao W., Xiao D., Jarillo-Herrero P., Xu X. (2017), Layer-Dependent Ferromagnetism in a van der Waals Crystal Down to the Monolayer Limit, Nature, 546, 270-273 (DOI: 10.1038/nature22391)

[14] Wang H., Eyert V., Schwingenschl¨ogl U. (2011), Electronic Structure and Magnetic Ordering of the Semiconducting Chromium Trihalides $CrCl_3$, $CrBr_3$, and CrI_3, J. Phys.: Condens. Matter, 23, 116003 (8pp) (DOI: 10.1088/0953-8984/23/11/116003)

[15] Zhang W. B., Qu Q., Zhu P., Lam C. H. (2015), Robust Intrinsic Ferromagnetism and Half Semiconductivity in Stable Two-Dimensional Single-Layer Chromium Trihalides, J. Mater. Chem. C, 3, 12457-12468 (DOI: 10.1039/c5tc02840j)

[16] Hashmi A., Hong J. (2014), Metal Free Half Metallicity in 2D System: Structural and Magnetic Properties of g-C_4N_3 on BN, Sci. Rep., 4, 4374 (1-6) (DOI: 10.1038/srep04374)

[17] Li H., Hu H., Bao C., Hua J., Zhou H., Liu X., Liu X., Zhao M. (2015), Tensile Strain Induced Half-Metallicity in Graphene-like Carbon Nitride, Phys. Chem. Chem. Phys., 17, 6028–6035 (DOI: 10.1039/c4cp05560h)

[18] Choudhuri I., Bhattacharyya G.; Kumar S.; Pathak B. (2016), Metal-Free Half-Metallicity in a High Energy Phase C-doped gh-C_3N_4

System: A High Curie Temperature Planar System, J. Mater. Chem. C, 4, 11530-11539 (DOI: 10.1039/c6tc04163a)

[19] Bhattacharyya G., Choudhuri I., Pathak B. (2018), High Curie Temperature and Half-Metallicity in an Atomically Thin Main Group-Based Boron Phosphide System: Long Range Ferromagnetism, Phys. Chem. Chem. Phys., 20, 22877-22889 (DOI: 10.1039/c8cp03440k)

[20] Li H., Hu H., Bao C., Hua J., Zhou H., Liu X., Liu X., Zhao M. (2015), Tensile Strain Induced Half-Metallicity in Graphene-like Carbon Nitride, Phys. Chem. Chem. Phys., 17, 6028-6035 (DOI: 10.1039/c4cp05560h)

[21] Chintalapati S., Yang M., Lau S. P., Feng Y. P. (2014), Surface Magnetism of Mg Doped AlN: A First Principle Study, J. Phys.: Condens. Matter, 26, 435801 (6pp) (DOI: 10.1088/0953-8984/26/43/435801)

[22] Bhattacharyya G., Choudhuri I., Bhauriyal P., Garg P., Pathak B. (2018), Ferromagnetism in Magnesium Chloride Monolayer with an Unusually Large Spin-up Gap, Nanoscale, 10, 22280-22292 (DOI: 10.1039/c8nr07429a)

[23] Blum H. (1933), The Crystal Structure of the Anhydrous Magnesium Iodide and Calcium Iodide. Journal of Physical Chemistry, Department B: Chemistry of Elementary Processes, Structure of Matter, 22, 298-304

[24] Wyckoff R. W. G. (1963), Cadmium Iodide Structure Crystal Structures, 2nd ed; Interscience Publishers, NY, 1, 239-444

[25] Novosad S. S. (1998), Scintillation Characteristics of Thin-Film Calcium Iodide Crystal X-Ray Detectors, Tech. Phys., 43, 956-958 (DOI: 10.1134/1.1259107)

[26] Chen C., Xu Y., Wu S., Zhang S., Yang Z., Zhang W., Zhu H., Xiong Z., Chen W., Chen W. (2018), CaI_2: A More Effective Passivator of Perovskite Films than PbI_2 for High Efficiency and Long-Term Stability of Perovskite Solar Cells, J. Mater. Chem. A, 6, 7903-7912 (DOI: 10.1039/c7ta11280g)

[27] Elfimov I. S., Yunoki S., Sawatzky G. A. (2002), Possible Path to a New Class of Ferromagnetic and Half-Metallic Ferromagnetic

Materials, Phys. Rev. Lett., 89, 216403 (1-4) (DOI: 10.1103/PhysRevLett.89.216403)

[28] Gao D., Li J., Li Z., Zhang Z., Zhang J., Shi H., Xue D. (2010), Defect-Mediated Magnetism in Pure CaO Nanopowders, J. Phys. Chem. C, 114, 11703-11707 (DOI: 10.1021/jp911957j)

[29] Monnier R., Delley B. (2001), Point Defects, Ferromagnetism, and Transport in Calcium Hexaboride, Phys. Rev. Lett., 87, 157204 (1-4) (DOI: 10.1103/PhysRevLett.87.157204)

[30] Kresse G., Joubert D. (1999), From Ultrasoft Pseudopotentials to the Projector Augmented-Wave Method, Phys. Rev. B., 59, 1758–1775 (DOI: 10.1103/PhysRevB.59.1758)

[31] Perdew J. P., Burke K., Ernzerhof M. (1996), Generalized Gradient Approximation Made Simple, Phys. Rev. Lett., 77, 3865-3868 (DOI: 10.1103/PhysRevLett.77.3865)

[32] Perdew J. P., Chevary J. A., Vosko S. H., Jackson K. A., Pederson M. R., Singh D. J., Fiolhais C. (1992), Atoms, Molecules, Solids, and Surfaces: Applications of the Generalized Gradient Approximation for Exchange and Correlation, Phys. Rev. B, 46, 6671–6687 (DOI: 10.1103/PhysRevB.46.6671)

[33] Blöchl P. E. (1994), Projector Augmented-Wave Method, Phys. Rev. B, 50, 17953−17979 (DOI: 10.1103/PhysRevB.50.17953)

[34] Grimme S., Antony J., Ehrlich S., Krieg H. (2010), A Consistent and Accurate ab initio Parametrization of Density Functional Dispersion Correction (DFT-D) for the 94 elements H-Pu, J. Chem. Phys., 132, 154104 (1-19) (DOI: 10.1063/1.3382344)

[35] Bader R. F. W. (1991), A Quantum Theory of Molecular Structure and its Application, Chem. Rev., 91, 893-928 (DOI: 10.1021/cr00005a013)

[36] Henkelman G., Arnaldsson A., Jo´nsson H. (2006), A Fast and Robust Algorithm for Bader Decomposition of Charge Density, Comput. Mater. Sci., 36, 354-360 (DOI: 10.1016/j.commatsci.2005.04.010)

[37] Sanville E., Kenny S. D., Smith R., Henkelman G. J. (2007), Improved Grid-Based Algorithm for Bader Charge Allocation, Comput. Chem., 28, 899-908 (DOI: 10.1002/jcc.20575)

[38] Tang W., Sanville E., Henkelman G. J. (2009), A Grid-Based Bader Analysis Algorithm without Lattice Bias, J. Phys.: Condens. Matter, 21, 084204 (7pp) (DOI: 10.1088/0953-8984/21/8/084204)

[39] Jund P., Viennois R., Colinet C., Hug G., F`evre M., T´edenac J. C. (2013), Lattice Stability and Formation Energies of Intrinsic Defects in Mg_2Si and Mg_2Ge via First Principles Simulations, J. Phys.: Condens. Matter, 25, 035403 (10pp) (DOI: 10.1088/0953-8984/25/3/035403)

[40] Lin Z., Carvalho B. R., Kahn E, Lv R., Rao R., Terrones H., Pimenta M. A., Terrones M. (2016), Defect Engineering of Two-Dimensional Transition Metal Dichalcogenides, 2D Mater., 3, 022002 (1-21) (DOI: 10.1088/2053-1583/3/2/022002)

[41] Bernstein B. T., Smith J. F. (1959), Coefficients of Thermal Expansion for Face-Centered Cubic and Body-Centered Cubic Calcium, Acta Crystallogr., 12, 419-420 (DOI: 10.1107/S0365110X59001268)

[42] Sun Y., Zhuo Z., Wu X., Yang J. (2017), Room-Temperature Ferromagnetism in Two-Dimensional Fe_2Si Nanosheet with Enhanced Spin-Polarization Ratio, Nano Lett., 17, 2771−2777 (DOI: 10.1021/acs.nanolett.6b04884)

[43] Boatner L. A., Ramey J. O., Kolopus J. A., Neal J. S. (2015), Divalent Europium Doped and Undoped Calcium Iodide Scintillators: Scintillator Characterization and Single Crystal Growth, Nucl. Instrum. Methods Phys. Res. A, 786, 23-31 (DOI: 10.1016/j.nima.2015.02.031)

[44] Rude L. H., Filinchuk Y., Sørby M. H., Hauback B. C., Besenbacher F., Jensen T. R. (2011), Anion Substitution in $Ca(BH4)_2$−CaI_2: Synthesis, Structure and Stability of Three New Compounds, J. Phys. Chem. C, 115, 7768–7777 (DOI: 10.1021/jp111473d)

[45] Chaudhry A., Boutchko R., Chourou S., Zhang G., Grønbech-Jensen N., Canning A. (2014), First-Principles Study of

Luminescence in Eu^{2+}-Doped Inorganic Scintillators, Phys. Rev. B, 89, 155105 (1-9) (DOI: 10.1103/PhysRevB.89.155105)

[46] Li X., Wu X., Yang J. (2014), Half-Metallicity in $MnPSe_3$ Exfoliated Nanosheet with Carrier Doping, J. Am. Chem. Soc., 136, 11065−11069 (DOI: 10.1021/ja505097m)

[47] Li X., Yang J. (2014), $CrXTe_3$ (X = Si, Ge) Nanosheets: Two Dimensional Intrinsic Ferromagnetic Semiconductors, J. Mater. Chem. C, 2, 7071-7076 (DOI: 10.1039/c4tc01193g)

[48] Liu J., Sun Q., Kawazoe Y., Jena P. (2016), Exfoliating Biocompatible Ferromagnetic Cr-Trihalide Monolayers, Phys. Chem. Chem. Phys., 18, 8777-8784 (DOI: 10.1039/c5cp04835d)

[49] Lin S-H., Kuo J.-L. (2014), Towards the Ionic Limit of Two-Dimensional Materials: Monolayer Alkaline Earth and Transition Metal Halides, Phys. Chem. Chem. Phys., 16, 20763-20771 (DOI: 10.1039/c4cp02048k)

[50] Lado J. L., Rossier J. F. (2017), On the Origin of Magnetic Anisotropy in Two Dimensional CrI_3, 2D Mater., 4, 035002 (1-9) (DOI: 10.1088/2053-1583/aa75ed)

[51] Sun Y., Zhuo Z., Wu X., Yang J. (2017), Room-Temperature Ferromagnetism in Two-Dimensional Fe_2Si Nanosheet with Enhanced Spin-Polarization Ratio, Nano Lett., 17, 2771−2777 (DOI: 10.1021/acs.nanolett.6b04884)

[52] Zhang M. H., Zhang C. W., Wang P. J., Li S. S. (2018), Prediction of High-Temperature Chern Insulator with Half-Metallic Edge States in Asymmetry Functionalized Stanene, Nanoscale, 10, 20226–20233 (DOI: 10.1039/c8nr07503d)

[53] Wang Y., Li F., Zheng H., Han X., Yan Y. (2018), Large Magnetic Anisotropy and its Strain Modulation in Two-Dimensional Intrinsic Ferromagnetic Monolayer RuO_2 and OsO_2 Phys. Chem. Chem. Phys., 20, 28162-28168 (DOI: 10.1039/c8cp05467c)

[54] Asselin P., Evans R. F. L., Barker J., Chantrell R. W., Yanes R., Chubykalo-Fesenko O., Hinzke D., Nowak U. (2010), Constrained Monte Carlo Method and Calculation of the Temperature Dependence

of Magnetic Anisotropy, Phys. Rev. B, 82, 054415 (1-12) (DOI: 10.1103/PhysRevB.82.054415)

[55] Hu L., Wu X., Yang J. (2016), Mn_2C Monolayer: A 2D Antiferromagnetic Metal with High Néel Temperature and Large Spin–Orbit Coupling, Nanoscale, 8, 12939-12945 (DOI: 10.1039/c6nr02417c)

[56] Kan M., Adhikari S., Sun Q. (2014), Ferromagnetism in MnX_2 (X = S, Se) Monolayers, Phys. Chem. Chem. Phys., 16, 4990-4994 (DOI: 10.1039/c3cp55146f)

[57] Zhang L., Zhang S. F, Ji W. X., Zhang C. W., Li P., Wang P. J., Li S. S., Yan S. S. (2018), Discovery of a Novel Spin-Polarized Nodal Ring in a Two-Dimensional HK Lattice, Nanoscale, 10, 20748-20753 (DOI: 10.1039/c8nr05383a)

[58] Huang C., Feng J., Wu F., Ahmed D., Huang B., Xiang H., Deng K., Kan E. (2018), Toward Intrinsic Room-Temperature Ferromagnetism in Two-Dimensional Semiconductors, J. Am. Chem. Soc., 140, 11519−11525 (DOI: 10.1021/jacs.8b07879)

[59] Li W., Sun L., Qi J., Jarillo-Herrero P., Dinca M., Li Ju. (2017), High Temperature Ferromagnetism in p-Conjugated Two-Dimensional Metal–Organic Frameworks, Chem. Sci., 8, 2859–2867 (DOI: 10.1039/c6sc05080h)

[60] Frey N. C., Kumar H., Anasori B., Gogotsi Y., Shenoy V. B. (2018), Tuning Noncollinear Spin Structure and Anisotropy in Ferromagnetic Nitride MXenes, ACS Nano, 12, 6319−6325 (DOI: 10.1021/acsnano.8b03472)

[61] Gao D., Li J., Li Z., Zhang Z., Zhang J., Shi H., Xue D. (2010), Defect-Mediated Magnetism in Pure CaO Nanopowders, J. Phys. Chem. C, 114, 11703-11707 (DOI: 10.1021/jp911957j)

[62] Zhou W., Zou X., Najmaei S., Liu Z., Shi Y., Kong J., Lou J., Ajayan P. M., Yakobson B. I., Idrobo J. C. (2013), Intrinsic Structural Defects in Monolayer Molybdenum Disulfide, Nano Lett., 13, 2615-2622 (DOI: 10.1021/nl4007479)

[63] Baroni S., Giannozzi P., Testa A. (1987), Green's-Function Approach to Linear Response in Solids, Phys. Rev. Lett., 58, 1861-1864 (DOI: 10.1103/PhysRevLett.58.1861)

[64] Togo A., Oba F., Tanaka I. (2008), First-Principles Calculations of the Ferroelastic Transition Between Rutile-Type and $CaCl_2$-Type SiO_2 at High Pressures, Phys. Rev. B, 78, 134106 (1-9) (DOI: 10.1103/PhysRevB.78.134106)

[65] Nose S. (1984), A Unified Formulation of the Constant Temperature Molecular Dynamics Methods, J. Chem. Phys., 81, 511-519 (DOI: 10.1063/1.447334)

[66] Fairbrother D. H.., Roberts J. G., Rizzi S., Somorjai G. A. (1997), Structure of Monolayer and Multilayer Magnesium Chloride Films Grown on Pd (111), Langmuir, 13, 2090–2096 (DOI: 10.1021/la960680c)

[67] Fairbrother D. H., Roberts J. G., Rizzi S., Somorjai G. A. (1998), The Growth of Magnesium Chloride Monolayer and Multilayer Structures on Different Transition Metal (Pt, Pd, Rh) Single Crystals with Varied Orientations, Surf. Sci., 399, 109–122 (DOI: 10.1016/S0039-6028(97)00816-9)

[68] Monner A., Schneper M., Jaaniso R., Bill H. (1995), Samarium Doped Alkaline Earth Halide Thin Halide Thin Films as Spectrally Selective Materials for Hole Burning, Radit. Eff. Def. S., 135, 253-256 (DOI: 10.1080/10420159508229846)

Chapter 4

High Curie temperature and Half-Metallicity in an Atomically Thin Main Group-Based Boron Phosphide System: Long Range Ferromagnetism

4.1. Introduction

Continuous miniaturization of electronic devices has reached a limit due to the limitation of Moore’s law *[1]*. Spintronics offers an alternative path to next generation electronic devices by exploiting the spin degrees of freedom of electrons rather than their charges. To accomplish this in solid-state devices, injecting spin into the electronic materials is essential; thus, searching for materials which can generate 100% spin-polarization at the Fermi level has become a fundamental concern. Half-metals *[2]*, in which one spin channel is metallic while the other is semiconducting or insulating, can filter the current into a single spin channel without any external operation; thus, half-metals can provide completely spin-polarized currents and play a vital role in the study of spintronics *[3]*. Hence, this type of material, having theoretically infinite magnetoresistance *[4]*, shows potential for use in spin filters, detectors, and sensors in the spintronics domain. On the other hand, research on antiferromagnetic (AFM) materials has received increasing interest because they have several advantages over ferromagnetic (FM) materials *[5]*. Unlike FM spintronics, AFM spintronics is based on the effect of tunnel anisotropy magnetoresistance (TAMR), which is unaffected by parasitic external magnetic fields and preserves the signal of magnetoresistance with increasing device miniaturization *[5-7]*. AFM materials also have the advantage of not forming magnetic domains and stray fields (demagnetizing fields); hence, they do not restrict the spin-polarized current *[4]*. These AFM materials have potential applications in novel spin-polarized STM tips, spin injection devices, etc. *[4]*. Moreover, the characteristic frequencies of switching between different AFM states are higher than those of traditional FM materials, which enables the fabrication of high-speed spintronic devices *[5, 8]*.

Although profound repercussions in the electronic and magnetic properties have been observed in transition metal (TM)-doped or adsorbed graphene-based 2D systems and nanoribbons *[9-12]* as well as in numerous other TM-embedded materials *[13-16]*, researchers have recently started to show more interest in main group-based systems due to their longer spin relaxation times compared to TM-based systems *[17]*. Moreover, it has been found that the magnetism in TM-doped systems arises from cluster/secondary phase formation from the doped TM atoms *[18]*. However, in most metal-free materials, intrinsic spin ordering is absent, which greatly hampers their scope in spintronics *[19]*. Hence, to overcome all these issues with TM embedded materials, several researchers have made considerable efforts towards the realization of ferromagnetic materials at room temperature by doping non-magnetic elements *[18, 20-23]*.

Because the spin relaxation time is inversely proportional to the strength of spin–orbit coupling, the magnetism arising from pure p electrons offers long spin relaxation times because it has weak spin–orbit coupling *[24]*. Therefore, several attempts to introduce magnetism in p electron-based systems in graphene, hexagonal boron nitride (h-BN) sheets, g-C_3N_4 nanosheets and graphyne monolayers have been initiated; some of these contemporary studies have been successfully implemented *[25-30]*. Recently, Du and co-workers showed intrinsic ferromagnetism in experimentally realized graphitic carbon nitride by replacing an N atom of gt-C_3N_4 with a C atom; the resulting doped system (gt-C_4N_3) becomes magnetic because C has one less valence electron than N *[31]*. A hole-doping approach was also implemented with the help of DFT studies by replacing two N atoms with two C atoms in an AlN monolayer to achieve antiferromagnetism *[32]*. However, none of these previous literature reports have thrown light on the detailed mechanism and origin of FM/AFM magnetic coupling in p electron-based magnetism and variation of exchange energy with the spatial separation of doped atoms. Previously, long range FM coupling with high exchange energy was explored in several materials; this can be useful for spintronics because the magnetism does not arise from clustering *[20, 33, 34]*. These previous literature reports provoked us to introduce magnetism in main group-based materials via a hole doping strategy and to explore the origin of FM/AFM coupling and long range interactions between magnetic domains for the progression of future-generation metal free spintronics.

In recent times, one 2D class of group-III/V elements, graphene-like hexagonal boron phosphide (h-BP), has attracted considerable attention *[35-39]*. Because monolayer (ML) h-BP exhibits a moderate direct band gap (0.81 to 1.81 eV) *[35, 40]*, high carrier mobility (10^4 $cm^2V^{-1}s^{-1}$ for electrons and 5×10^3 cm^2 $V^{-1}s^{-1}$ for holes) *[41]*, and high mechanical strength *[42]*, it is considered to be a good candidate for metal-free spintronics. Recently, Yu *et al.* and Onat *et al.* reported strain-induced magnetism in pristine and semihydrogenated h-BP and magnetism in h-BP with group III, IV and V atom adsorption and substitution using density functional theory *[42, 43]*. Recently, boron phosphide (BP) films were synthesized experimentally on an aluminum nitride(0001)/sapphire substrate by chemical vapor deposition *[35, 44]*. Motivated by these previous findings, we systematically investigated the BP ML system for possible application in spintronic devices via hole doping. Be and Mg doping at the B-sites and P-sites introduces holes in the BP ML system, which may induce magnetism. Actually, this doping may have a pronounced effect on the hybridization of h-BP ML. Thereafter, spin-polarized DFT calculations were performed to predict the magnetism of the doped BP systems. We have investigated in detail the origin of the magnetism and half metallicity from the projected densities of states. Furthermore, we have analyzed the origin of AFM/FM coupling in the BP ML system and the coupling strengths with variable distances between the two doped atoms (Be and Mg). One of the key difficulties in ferromagnetic systems is the fast degeneration of the exchange coupling strength with increasing spatial separation between the magnetic centers *[45]*. In the present work, we have presented a methodical study of securing magnetism in BP ML via a hole-doping mechanism and proposed a mechanism of long range ferromagnetic coupling between two identical non-magnetic impurities (Mg) substituted in BP ML. The stability of the h-BP ML system is also discussed for their future synthesis and practical use. We have calculated formation and binding energies to confirm the energetic stabilities of Be and Mg-doped BP ML. Further, we have confirmed the dynamical, thermal and mechanical stabilities of the systems by phonon dispersion calculations, molecular dynamics simulations and stress vs. strain calculations, respectively. To assess the importance of these systems in spintronics devices, the electronic properties (spin-polarized density of states and band structure) and magnetic properties (magnetic anisotropic energy, exchange energy, Curie temperature) are calculated and investigated. During device fabrication, these systems are generally grown on a substrate, which generates strain; thus, it is very necessary to inspect the strain sustainability and strain effects on the magnetic properties of these systems for their practical use in high performance spintronic devices.

4.2. Computational Methods

We carried out spin-polarized calculations for all the structures using the projector augmented wave (PAW) pseudopotential method as implemented in the Vienna ab initio Simulation Package (VASP) *[46]*. The generalized gradient approximation (GGA) was used to accurately describe the electron–electron exchange and correlation energies of delocalized s and p electrons using the Perdew–Burke–Ernzerhof (PBE) functional *[47, 48]*. The projected augmented wave (PAW) method *[49, 50]* was employed using a 470 eV energy cutoff to describe the electronic wave function. The Be and Mg-doped structures were modeled using a (4 × 4 × 1) hexagonal supercell containing 32 atoms. A gamma-centered k-point grid of 9 × 9 × 1 was used to sample the first Brillouin zone of the Be and Mg-doped BP supercells for geometry optimization, and 15 × 15 × 1 was used to calculate the spin-polarized electronic properties (density of states). A 20 Å vacuum was employed along the z-direction to avoid any interactions between periodic images. We achieved self-consistency by setting the convergence tolerance to 10^{-6} eV and 10^{-3} eV Å^{-1} for the total energy and force calculations, respectively. Bader charge analysis was performed *[51-53]* using the Henkelman programme *[54]* with a near-grid algorithm edge-refinement method to understand the charge transfer process The thermal stability of the Mg-doped BP (6.25%) system was verified by carrying out ab initio molecular dynamics simulations (AIMD) using a canonical ensemble at 300 and 500 K with a time step of 1 fs for 30 ps. The Nose´ thermostat model was used to control the temperature throughout the MD simulations *[55]*. The phonon frequency calculations were performed using the density functional perturbation theory (DFPT) *[56]* as implemented in VASP, and phonon dispersion calculations were carried out using Phonopy code *[57]*. Furthermore, energetic stability *[24]* of the Be and Mg doped boron phosphide monolayer are investigated from the formation energy (E_F) and binding energy (E_B) calculations. The formation energy are calculated using the following equations *[24]*

$$E_{F(P-site)} = \left(E_{Be/Mg@BP} - E_{BP}\right) - \left(\mu_{Be/Mg(Bulk)} - \mu_{P(Bulk)}\right) \quad (4.1)$$

$$E_{F(B-site)} = \left(E_{Be/Mg@BP} - E_{BP}\right) - \left(\mu_{Be/Mg(Bulk)} - \mu_{B(Bulk)}\right) \quad (4.2)$$

Here $E_{Be/Mg@BP}$ is total energy of the Be/Mg doped BP monolayer system, E_{BP} is the total energy of undoped BP monolayer, $\mu_{Be/Mg(Bulk)}$, $\mu_{P(Bulk)}$ and $\mu_{B(Bulk)}$ are the chemical potential of Be/Mg atom , P atom and B atom from their respective bulk structures *[58-61]*. Binding energy refers to the energy required to isolate single Be or Mg atom from Be^P@BP and Mg^P@BP systems. Therefore, we have considered the energy of single isolated Be and Mg atom while calculating the binding energy. Binding energy is calculated by the following equation *[24]*

$$E_B = E_{Be/Mg@BP} - \left(E_{BP} + E_{Be/Mg(single\ atom)}\right) \quad (4.3)$$

Here $E_{Be/Mg@BP}$ is total energy of the Be/Mg doped BP monolayer system, E_{BP} is the total energy of undoped BP monolayer, $E_{Be/Mg(single\ atom)}$ is the total energy of isolated Be/Mg atom.

Cohesive energy of Be and Mg bulk systems are calculated from the following equation

$$E_{Coh} = \frac{E_{Be/Mg(Bulk)} - N \times E_{Be/Mg(single\ atom)}}{N} \quad (4.4)$$

Furthermore, to predict the magnetic ground state of Be^P@BP and Mg^P@BP ML system, we have calculated the exchange energy *[1, 6-*

8] (E_{ex}) per unit cell and magnetic anisotropic energy *[1, 6-8]* of Be and Mg doped BP monolayer. The exchange energy per supercell (E_{ex}) is calculated using the following equation where E_{FM} and E_{AFM} denotes the energies of ferromagnetic and antiferromagnetic states.

$$E_{ex} = E_{AFM} - E_{FM} \tag{4.5}$$

Similarly, magnetic anisotropic energy (MAE) *[65]* per unitcell is calculated incorporating spin-orbit coupling (SOC) effect using the following equation where E_{HA} is the energy of the system (along hard axis) with application of magnetic field along magnetizing direction (100), (010), (110), (111) and (001). E_{EA} is the energy of the system in present of a magnetic easy axis, which is an energetically favourable direction for spontaneous magnetization. We have also tried two out of plane direction (001) and (111) magnetizing direction.

$$MAE = E_{HA} - E_{EA} \tag{4.6}$$

The spin density distribution (SDD) is plotted to understand the nature of electron spin density on the unpaired electron in the Be^P@BP and Mg^P@BP ML system. The SDD is calculated using the following equation

$$\rho_{SD} = \rho_{up} - \rho_{down} \tag{4.7}$$

Here, ρ_{up} and ρ_{down} are the up and down electron spin density, respectively. In the SDD, the wave functions for spin up and spin down electrons are indicated by yellow and blue colors respectively. The direct mapping of the electron spin density is measured by the neutron diffraction in electron spin resonance (ESR) spectroscopy.

4.3. Results and Discussion:

4.3.1. BP ML and Be- and Mg@BP

In this work, we considered a two atom hexagonal unit cell (Fig. 4.1) of BP monolayer (ML) for our study. Our optimized lattice parameters (a = b = 3.21 Å) and band gap (~0.91 eV) match previous reports (0.90 eV) on BP ML *[35, 40, 66-67]*. The calculated B–P bond length is 1.85 Å, which is consistent (1.85 Å) with a previous theoretical report *[66]*. Fig. 4.1 shows the total electron density distribution in BP ML; it can be seen that the electrons are highly delocalized. The contour electron localization function (ELF) plot shows that there is a strong covalent overlap between B–P, which agrees with a previously reported result *[68]*. Furthermore, our calculated Bader charge values (Table 4.1) are also consistent with these findings.

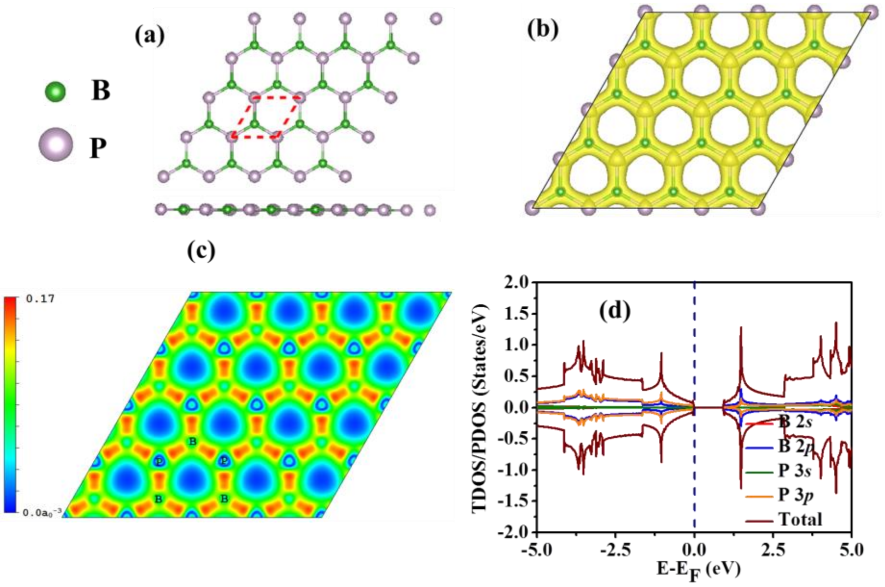

Figure 4.1: (a) Optimized structure (top/side view), (b) total electron density (isosurface value: 0.08 e Å^{-3}), (c) electron localization function (ELF; maximum saturation level 0.17 e Å^{-3}, minimum saturation level 0.0 Å^{-3}), (d) spin polarized total/partial density of states (TDOS/PDOS) of the BP monolayer. Here, the red dashed box indicates the unit cell of the system. The Fermi level is shifted to zero and is indicated by a navy blue dashed line.

Table 4.1: Bader charge analysis of pure BP and Mg^{P}@BP

System: Pure BP	**Net Effective Charge (Average)**		
	B		**P**
	B = +0.79		P = -0.79
System: Mg^{P}@BP			
	Mg	**B**	**P**
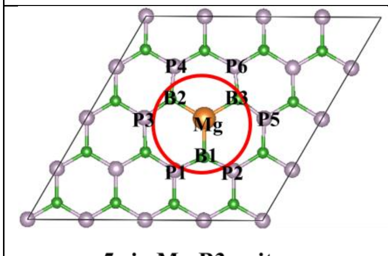 **5e in Mg-B3 unit**	+1.43	B1=+0.38, B2=+0.38 and B3=+0.39	P1=-0.78, P2=-0.81, P3=-0.78, P4=-0.81, P5=-0.79 and P6=-0.79

Inspired by many previous reports *[24, 31, 32]*, we considered hole doping in h-BP ML to induce magnetism. For this, we considered Be and Mg doping in a (4 × 4 × 1) supercell of BP ML because they have one fewer electron than B and P, respectively, in their outermost shells. To investigate the effects of doping concentration on BP ML, we considered doping concentrations of 6.25%, 4.00%, 2.78% and 2.04%. Hereafter, Be-doped BP ML at the B- and P-sites will be referred to as Be^B@BP and Be^P@BP. Similarly, Mg-doped BP ML at the B- and P-sites will be referred to as Mg^B@BP and Mg^P@BP. We have systematically studied the electronic and magnetic properties of these doped systems. It has been found that the Be^B@BP and Mg^B@BP systems are non-magnetic, while both the Be^P@BP and Mg^P@BP systems are magnetic, with total magnetic moments of 1.00 μB per dopant (Fig. 4.2). We found from the spin density distribution (Fig. 4.2) that a single B vacancy in BP monolayer induces a magnetic moment (2.60 μB). However, incorporation of Be and Mg atoms in the B-vacancy position cancels the total magnetic moment in the system, which can be observed from the spin density distribution (Fig. 4.2b-c).

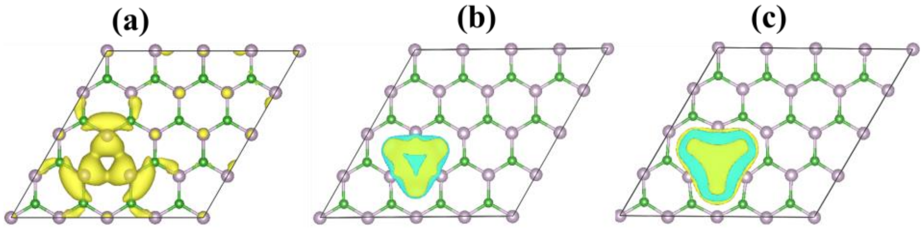

Figure 4.2: Spin Density Distribution of (a) BP monolayer with single B-vacancy, (isosurface value: 0.002337 e $Å^{-3}$) (b) Be^B@BP system (isosurface value: 5.0 e-8 $Å^{-3}$) and (c) Mg^B@BP (isosurface value: 1.0 e-8 $Å^{-3}$).

The Be/Mg doping at the P-site introduces holes in the BP system, which leads to magnetism. Therefore, asymmetric spin density and spin-splitting was found from the spin-polarized density of states (Fig. 4.3) of the Be^P@BP and Mg^P@BP systems. The effects of doping concentration on the magnetism/electronic properties of the Be^P@BP and Mg^P@BP systems was thoroughly investigated by considering a series of concentrations, including 2.04%, 2.78%, 4.00% and 6.25%

(Fig. 4.3 and 4.4). Interestingly, the calculated electronic properties (TDOS/PDOS) of Be^P@BP show half-metallicity at particular concentrations (4.00% and 6.25%). However, Mg^P@BP exhibits half-metallic character for all the doping concentrations (2.04%, 2.78%, 4.00% and 6.25%). For both Be^P@BP and Mg^P@BP, the half-metallic systems, the spin up channel (majority) is semiconducting and the spin-down (minority) channel is metallic.

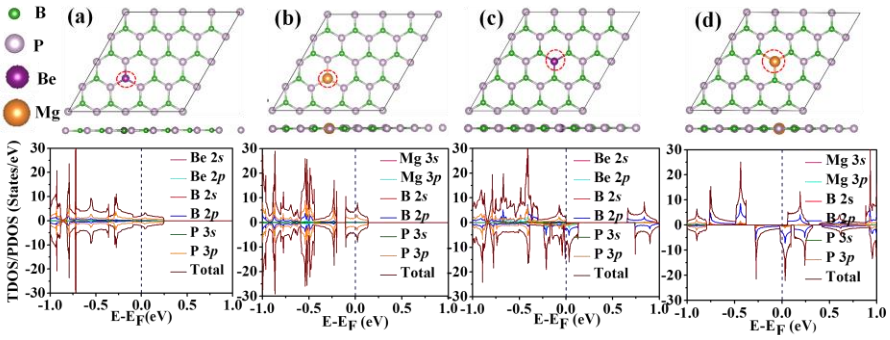

Figure 4.3: Optimized structures (top/side view) and spin polarized density of states of 6.25% doped (a) Be^B@BP, (b) Mg^B@BP, (c) Be^P@BP and (d) Mg^P@BP systems. The Fermi level is set to zero and is indicated by a blue dashed line. The doped Be and Mg atoms are denoted by violet and orange colors. Red dotted circles show the doped Be/Mg atoms in the systems.

The spin majority state gaps of both half-metallic systems, Be^P@BP and Mg^P@BP, increases with the doping concentration (Table 4.2).

Table 4.2: Magnetic moments per dopant (μB), nature of the system and spin gaps (eV) for the Be^P@BP and Mg^P@BP systems with different doping concentrations

Be^P@BP Doping concentration (%)	**Magnetic moment /dopant(μB)**	**Nature**	**Spin-Up Band Gap (eV)**
6.25	0.99	Half-metallic	0.65
4.00	1.00	Half-metallic	0.79
2.78	0.69	Metallic	0
2.04	0.74	Metallic	0
Mg^P@BP Doping concentration (%)			
6.25	1.00	Half-metallic	0.44
4.00	1.00	Half-metallic	0.61
2.78	1.00	Half-metallic	0.67
2.04	1.00	Half-metallic	0.68

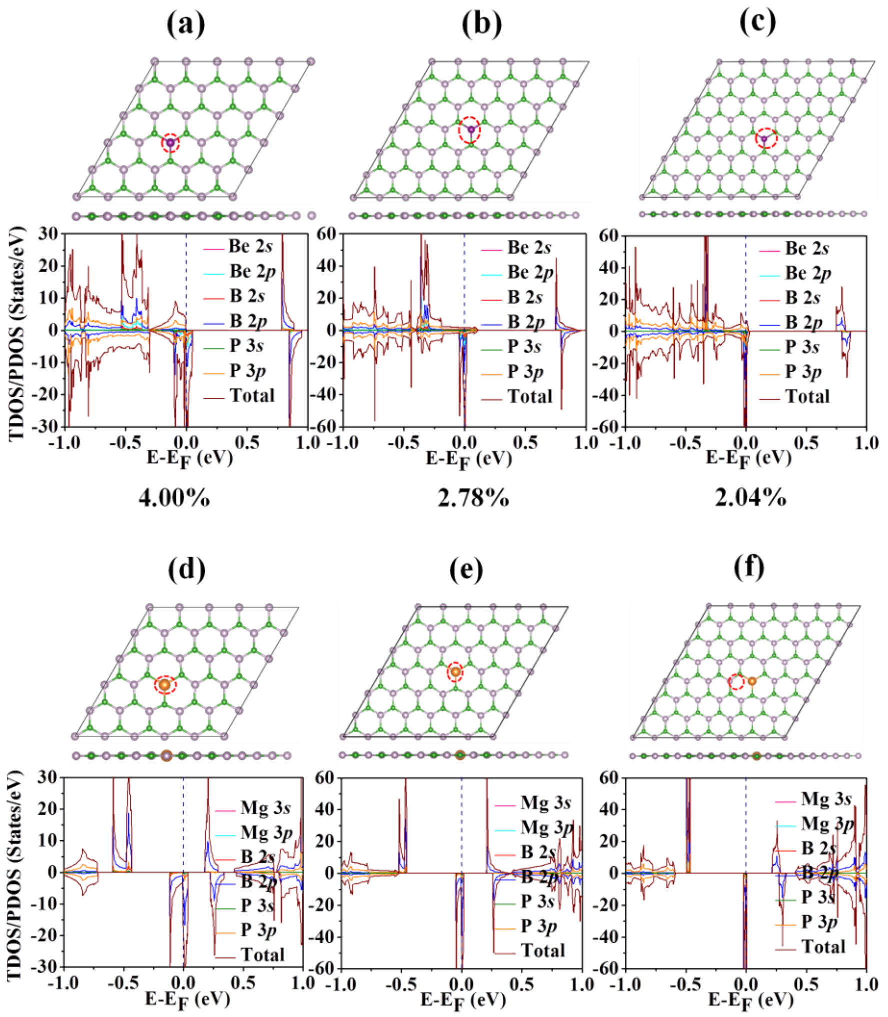

4.00% 2.78% 2.04%

Figure 4.4: Optimized structures (top/side view) and spin polarized density of states of (a) 4.00%, (b) 2.78%, (c) 2.04% Be^P@BP and (d) 4.00%, (e) 2.78%, (f) 2.04% Mg^P@BP systems. The Fermi level is set to zero and indicated by a blue dashed line. Red dotted circles show the doped Be/Mg atoms of the system.

In recent times, various research groups reported *[62-63, 69-70]* magnetism and half metallicity by incorporating different transitional metals in carbon nitride-based systems. Previous reports also suggested metal-free half-metallicity in carbon/boron nitride-based 2D systems by self-doping of C atom with a particular doping concentration *[24, 28, 71]*. Hence, the exhibition of half-metallic character in the electronic properties of the Mg^P@BP system influenced us to carry out further investigations with this system and determine the origin of the half-metallic character. The detailed analysis of the density of states (Fig. 4.3c and d) shows that the 2p orbitals of the B atoms give rise to half-metallicity in both the Be^{P}@BP and Mg^{P}@BP systems. The valence band (spin up) is more stabilized in the case of Mg^{P}@BP (0.30 eV to 0.48 eV) compared to Be^{P}@BP (0.01 eV to 0.20 eV). This is because the van der Waals radius of Mg (173 pm) *[72]* is much closer to that of P (180 pm) *[72]* than of Be (153 pm) *[72]*. This leads to better hybridization between Mg and B and, hence, to stability in the overall system *[24]*. The higher abundance of Mg over Be *[73]* and the half-metallic character of Mg^{P}@BP influenced us to perform a systematic study of the magnetic properties of this system.

Subsequently, it is quite interesting to determine whether excess holes or excess electrons can induce magnetism in BP by doping different main group elements. Hence, we doped BP with various other main group elements X (X = Li, Na, C, N, Al, Si, S) both at the B-sites and P-sites. We found that only the Li^{P}@BP, Na^{B}@BP and Na^{P}@BP systems exhibited magnetism, with magnetic moments of 2.00 μB per dopant. However, Li^{B}@BP and the other doped systems did not induce magnetism (Fig. 4.5-4.10).

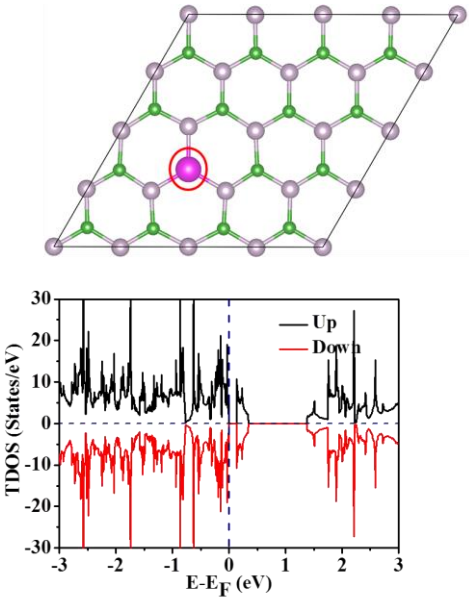

Figure 4.5: Optimized structure and TDOS of (a) Li^{B}@BP with 6.25% doping concentration. The Fermi level is shifted to zero and indicated by a blue dashed line. B, P and Li atoms are indicated by green, gray and pink color respectively. Doped Li atom is indicated by red circle.

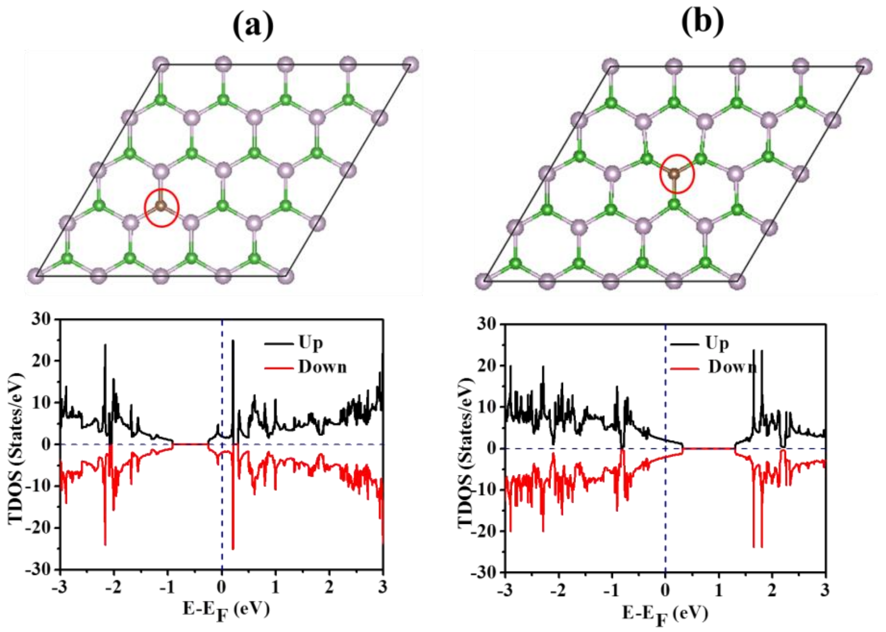

Figure 4.6: Optimized structure and TDOS of (a) C^B@BP (b) C^P@BP with 6.25% doping concentration. The Fermi level is shifted to zero and indicated by a blue dashed line. B, P and C atoms are indicated by green, gray and brown color respectively. Doped C atom is indicated by red circle.

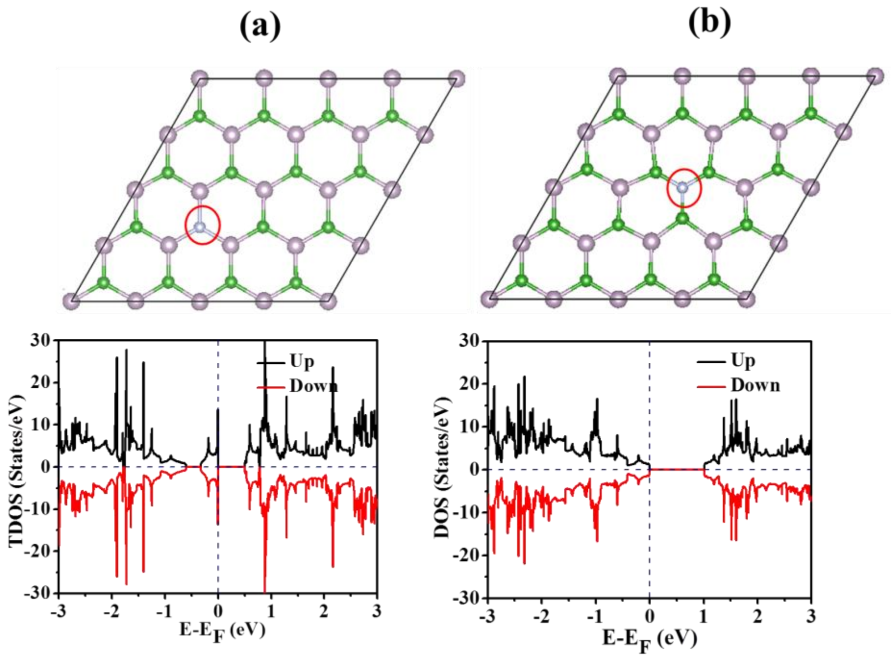

Figure 4.7: Optimized structure and TDOS of (a) N^B@BP (b) N^P@BP with 6.25% doping concentration. The Fermi level is shifted to zero and indicated by a blue dashed line. B, P and N atoms are indicated by

green, gray and bluish silver color respectively. Doped N atom is indicated by red circle.

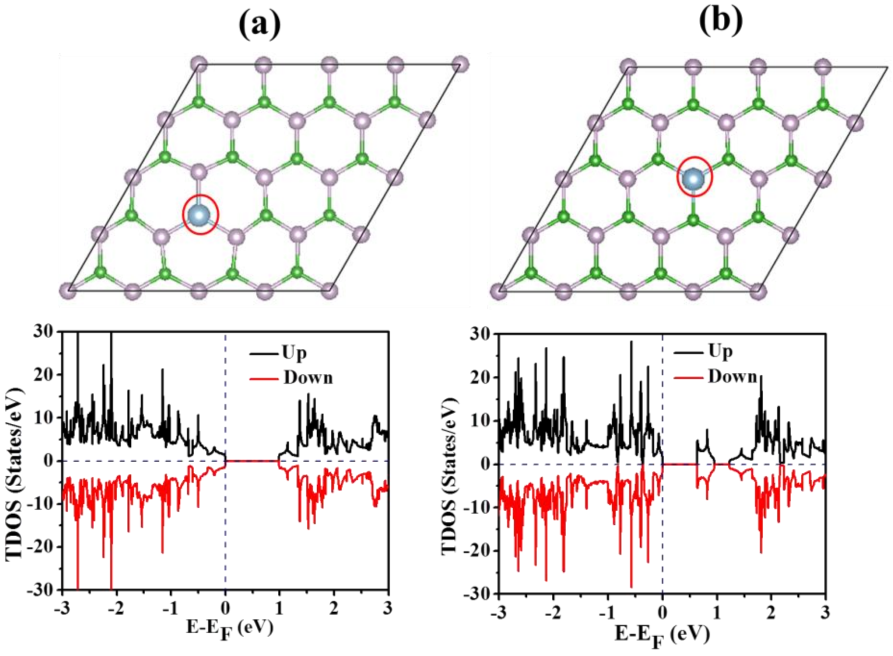

Figure 4.8: Optimized structure and TDOS of (a) Al^B@BP (b) Al^P@BP with 6.25% doping concentration. The Fermi level is shifted to zero and indicated by a blue dashed line. B, P and Al atoms are indicated by green, gray and light blue color respectively. Doped Al atom is indicated by red circle.

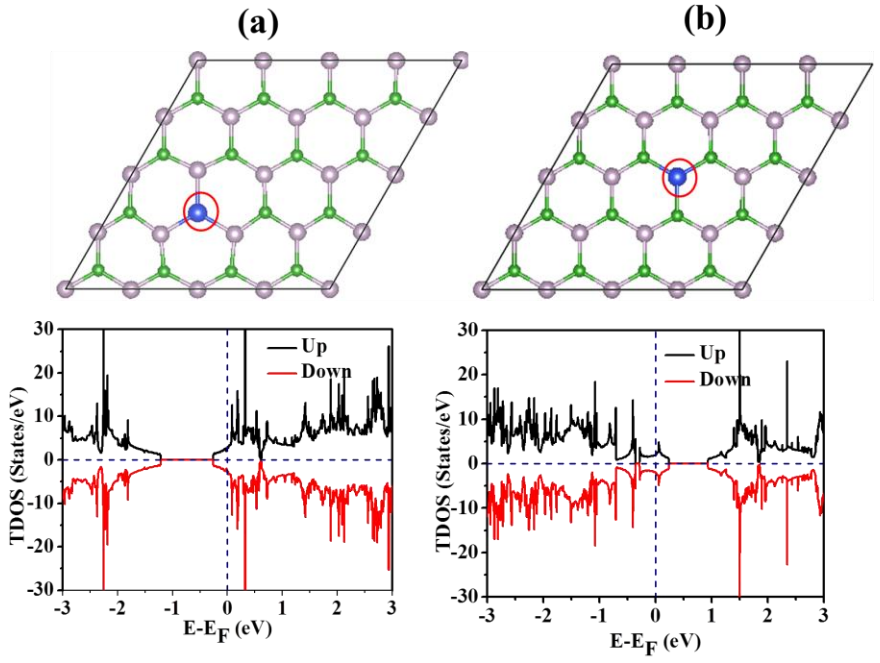

Figure 4.9: Optimized structure and TDOS of (a) Si^B@BP (b) Si^P@BP with 6.25% doping concentration. The Fermi level is shifted to zero and indicated by a blue dashed line. B, P and Si atoms are indicated by green, gray and dark blue color respectively. Doped Si atom is indicated by red circle.

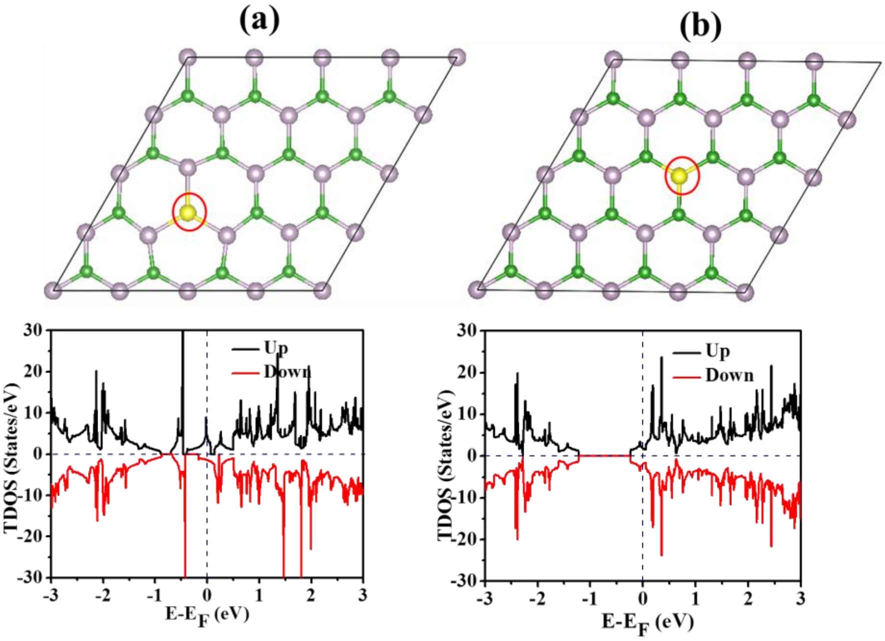

Figure 4.10: Optimized structure and TDOS of (a) S^B@BP (b) S^P@BP with 6.25% doping concentration. The Fermi level is shifted to zero and indicated by a blue dashed line. B, P and S atoms are indicated by green, gray and yellow color respectively. Doped S atom is indicated by red circle.

Asymmetric spin density and spin-splitting was observed for the Li^P@BP, Na^B@BP and Na^P@BP systems (Fig. 4.11) from their corresponding spin-polarized densities of states. It was observed that Li^P@BP is weakly half-metallic and Na^P@BP is semiconducting in nature. However, Na^B@BP is half-metallic, with a spin-up gap of 1.02 eV. Because the formation energy is higher for the Na^B@BP system (6.00 eV) than the Mg^P@BP system (5.46 eV), we focused on the Mg^P@BP system in this work for further study.

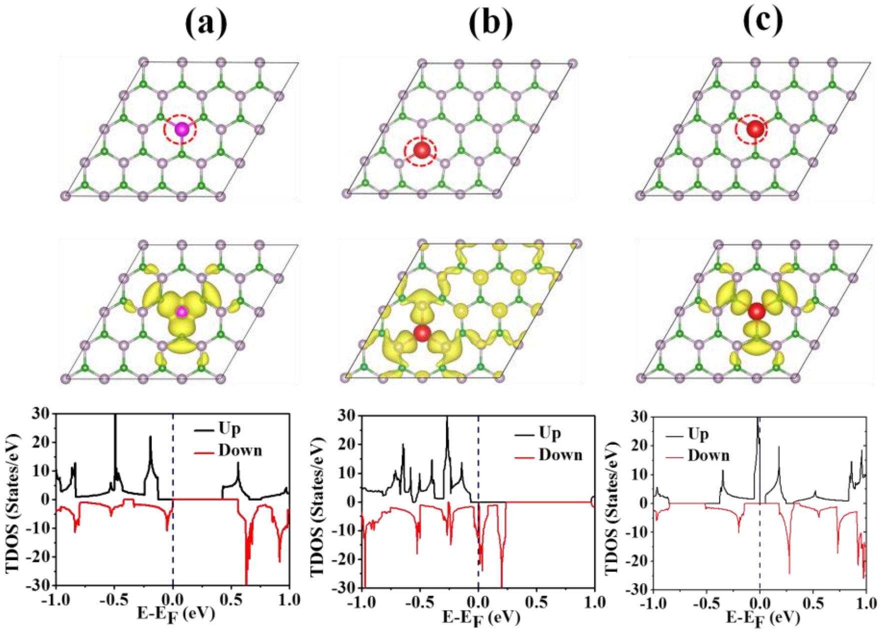

Figure 4.11: Optimized structures (top view), spin density distributions (isosurface value: 0.00244284 e Å^{-3}) and spin polarized densities of states of the (a) Li^P@BP (6.25%) (b) Na^B@BP (6.25%) (c) Na^P@BP (6.25%) systems. The doped Li and Na atoms are denoted by dark pink and red colors. Red dotted circles show the doped Li/Na atoms in the systems.

4.3.2. Magnetic properties of Be^P@BP and Mg^P@BP

The source of the magnetism and half-metallicity in the Mg^P@BP (6.25% doped) system was investigated by analysing its partial residual spin, spin density distribution (SDD) and partial density of states (Fig. 4.12 and 4.13). The 3s orbital of doped Mg hybridizes (sp^2) with the in plane 2p (2p$_x$ and 2p$_y$) orbitals of the surrounding B atoms, which carry a residual spin (Fig. 4.12) due to the hole doping. Hence, the maximum contributions of the total magnetic moment (1.00 μB) arise mainly from the residual spin Mg–B3 unit, which is also evident from the spin density distribution (SDD) (Fig. 4.13a).

Moreover, the partial density of states of Mg^P@BP (6.25%) (Fig. 4.13c–e and Fig. 4.14) shows that the half-metallicity primarily originates from the Mg–B3 unit of the Mg^P@BP (6.25%) system. A detailed study of the partial density of states (Fig. 4.13c–e) evidenced that the in plane 2p orbitals (2p$_x$ and 2p$_y$) of B provide the maximum

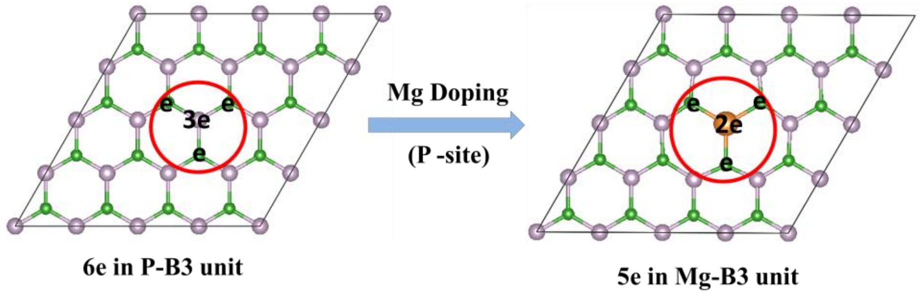

Figure 4.12: Schematic of the presence of residual spin in the Mg^P@BP (6.25%) system due to Mg doping in the BP monolayer.

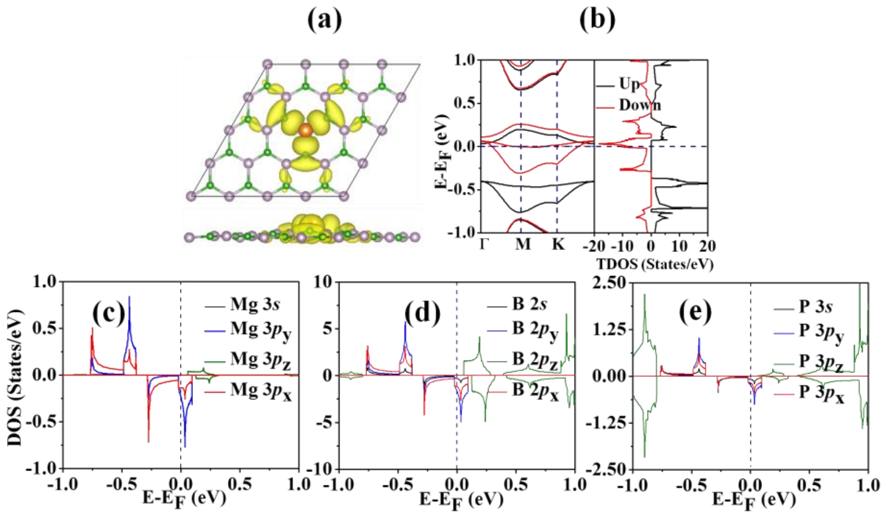

Figure 4.13: (a) Spin density distribution (isosurface value: 0.001191 e Å^{-3}), (b) electronic structure (band structure, DOS), (c)–(e) PDOS plots of the Mg, B and P atoms of Mg^P@BP (6.25%).

contribution towards the half metallicity of the system. The strong p–p overlap around the Fermi region (energy range -0.5 to 0.5 eV) results in a strong interaction between Mg and B atoms, which is clearly shown in the partial density plot (Fig. 4.13c–e). Recently, Chintalapati *et al.* showed ferromagnetic coupling due to the strong sp–p interaction between Mg and N atoms in an Mg-doped AlN surface *[18]*. Hence, in this case, the half-metallicity in Mg^P@BP (6.25%) arises due to splitting of the spin-up and spin-down states of the p orbitals near the Fermi level.

This result is also supported by the Bader charge analysis (Table 4.1) which shows that the valence electrons transfer from Mg to the surrounding B atoms. In the pure BP monolayer, the average net effective charge of the B atoms is +0.79 |e| and the average net effective charge of the P atoms is 0.79 |e|. However, in Mg^P@BP (6.25%), the net effective charges of the three B atoms surrounding Mg become +0.38, +0.38 and +0.39 |e|, respectively, which indicates that 0.4 e is transferred to each B atom on average. Mg atom loses +1.43 |e|, which supports that Mg is transferring electrons to the three B atoms.

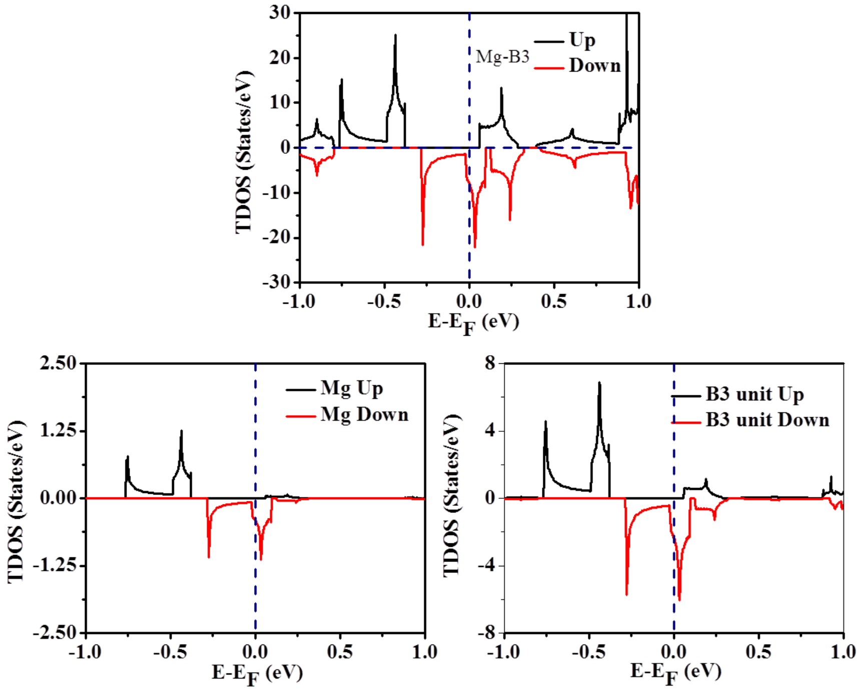

Figure 4.14: TDOS plot of (Mg-B3) unit in Mg^P@BP system. The Fermi level is shifted to zero and indicated by a blue dashed line.

The band-structure plot (Fig. 4.13b) shows that only two down spin bands are crossing the Fermi level due to the half-metallic character, similar to the density of states plot. Similarly, as in Mg^P@BP (6.25%), the main contribution of the total magnetic moment (1.00 μB) in Be^P@BP (6.25%) arises from the Be atom and the three B atoms around it. The total and partial density of states of semiconducting Be^P@BP (6.25%) also shows p–p coupling between the Be and B atoms (Fig. 4.15).

The effects of magnetic coupling between the two neighboring dopants are highly crucial to their overall effects on the magnetic properties of the system. Hence, we studied the relationship between the magnetic couplings and the distance of the two dopant atoms. We considered

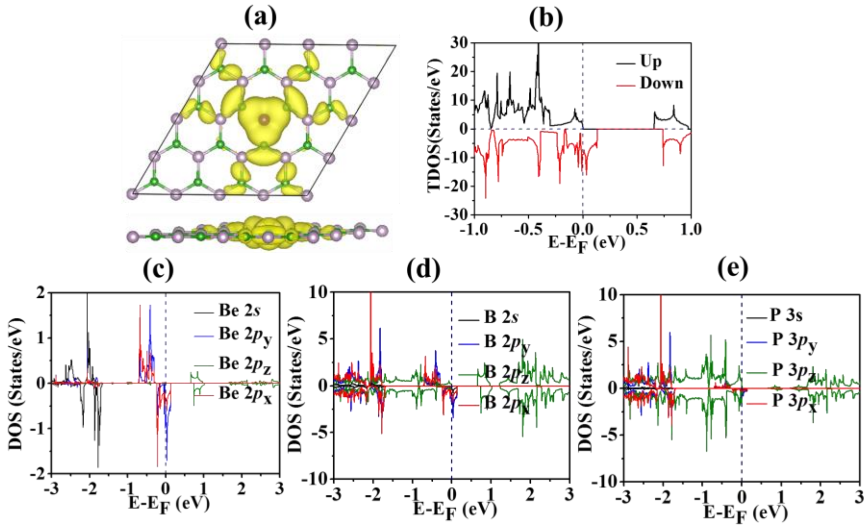

Figure 4.15: (a) Spin density distribution (SDD) (isosurface value: 0.0005 e Å^{-3}), (b) TDOS plot, (c)-(e) PDOS plots of Be, B and P atoms of Be^P@BP (6.25%). The Fermi level is shifted to zero and indicated by a blue dashed line.

two Be and Mg atoms in an 8 × 4 × 1 BP supercell because of the computational limit. To observe the magnetic coupling between two dopant atoms, we substituted two Be and Mg atoms in P sites with different spatial separations (2.59 Å to 12.94 Å) to study the magnetic coupling. The optimized structures of Mg^P@BP with different distances of dopant atoms are tabulated in Table 4.3. Similarly, the optimized structures of Be^P@BP with different distances of dopant atoms are tabulated in Table 4.4.

We then compared the energy differences (Table 4.3) of the Mg-doped systems and found that the system with Mg–Mg distance of 5.83 Å is the most stable. This may be due to structural distortion, where B–B bond formation takes place. Similarly, the other nonmagnetic structure with Mg–Mg distance of 2.99 Å is energetically more stable than the other two magnetic structures. The magnetic systems with Mg–Mg distances of 9.74 Å and 12.94 Å have energies relatively 1.89 eV and 2.00 eV higher than that of the most stable structure, respectively. Therefore, these are high energy phase structures. However, these doped Mg atoms are well (and equally) separated, and they may not aggregate, as may occur for the other two configurations. When we have increased the distance to 9.74 Å and 12.94 Å, the Mg^{P}@BP structure was found to be antiferromagnetic, with a very low value (1.00 meV) of exchange energy, and ferromagnetic, with a high exchange energy (67.80 meV), respectively.

Table 4.3: Optimized spatial separations between two dopants (Å), optimized structures, relative energies (eV), exchange energies (meV) and magnetic ground states of the Mg^{P}@BP systems

Spatial Separation between dopants (Å)	**Optimized Structure of Mg^{P}@BP**	**Relative Energy (eV)**	**Magnetic Ground State**	
2.99 Å	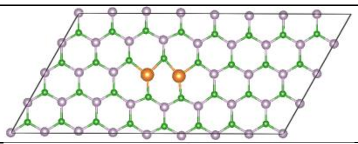	0.63	Non-magnetic (0.00 µB)	
5.83 Å	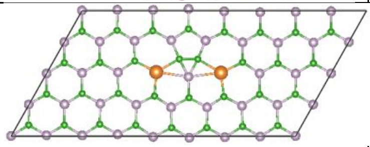	0.00	Non-magnetic (0.00 µB)	
			Exchange Energy (meV)	**Magnetic Ground State**
9.74 Å	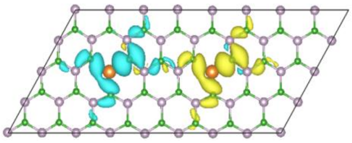	1.89	1.00	Antiferromagnetic
12.94 Å	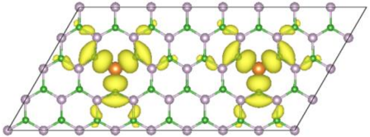	2.00	67.80	Ferromagnetic

Hence, this particular configuration, with 9.74 Å distance between the (Mg–B3) units, has a metastable antiferromagnetic ground state; thus, under certain experimental conditions, it may show a ferromagnetic half-metallic ground state *[74]*. Similar studies show that Be doping with spatial separation results in different magnetic ground states in the Be^{P}@BP system (Table 4.4). Previously, some theoretical studies have reported long distance antiferromagnetic coupling due to charge transfer from the metal to the ligand in a family of dinuclear transition metal complexes with derivatives of 1–3 or 1,4-dicyanamidobenzene as bridging ligands *[45]*. We believe that this long distance FM and AFM coupling arises from charge transfer from the alkaline earth metal (Be, Mg) to the B site and delocalized extended boron p orbital coupling in the BP systems.

Table 4.4: Optimized spatial separation between two dopants (Å), Optimized structure, Exchange energy (meV) and Magnetic ground state of Be^P@BP systems

Spatial Separation between dopants (Å)	**Optimized Structure of Be^P@BP**	**Magnetic Ground State**	
2.59 Å	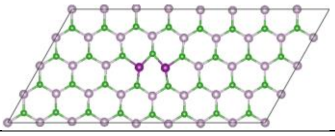	Non-magnetic (0.00 µB)	
6.19 Å	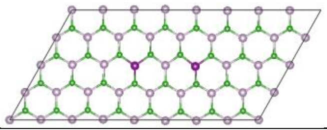	Non-magnetic (0.00 µB)	
		Exchange Energy (meV)	**Magnetic Ground State**
9.62 Å	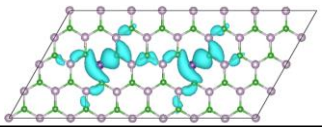	3.29	Ferromagnetic
12.84 Å	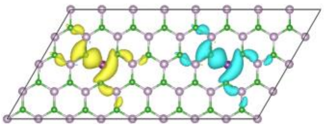	18.95	Antiferromagnetic

The spin density distributions (SDD) (Fig. 4.16a and b) show that p electron coupling exists between the two magnetic domains (Mg–B3) in the Mg^P@BP (6.25%) system through the B p orbitals. Similar long distance antiferromagnetic coupling up to 33 Å in dinuclear transition metal complexes was previously reported by Nunzi *et al.* and was thoroughly explained by extended p electron coupling theory. Further, we found that the structure with 12.94 Å distance between two (Mg–B3) units is ferromagnetic, with a large value (67.80 meV) of exchange energy; this indicates that the system will have a high Curie temperature, which is suitable for room temperature spintronics.

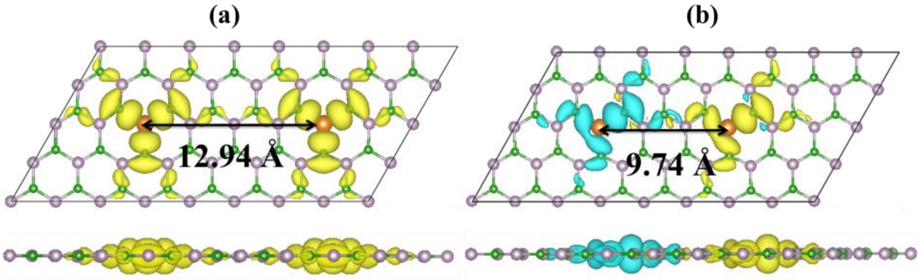

Figure 4.16: Spin density distributions of the Mg^P@BP ground states at distances of (a) 12.94 Å between two Mg–B3 magnetic units [FM coupling, (isosurface value: 0.0010 e Å^{-3})] and (b) 9.74 Å between two Mg–B3 magnetic units [AFM coupling, (isosurface value: 0.0011 e Å^{-3})].

Therefore, at a distance of <12 Å, the two magnetic domains (Mg–B3) can influence each other, giving rise to AFM coupling. However, with increasing distance (>12 Å), the AFM coupling becomes weak; hence, the two magnetic domains act as separate single spins, giving rise to FM ordering with a magnetic moment of 2.00 μB. Recently, long range FM ordering was demonstrated in Mn-doped two dimensional di-chalcogenides, where the long-range ferromagnetism of Mn spins is mediated by an antiferromagnetic (AFM) exchange between the localized Mn d states and the delocalized p states of the S, Se, and Te atoms *[75]*. Here, the long range FM coupling (>12 Å) between the two magnetic units (Mg–B3) is protected by AFM coupling at close proximity (<12 Å). Hence, we can conclude that the p electron coupling causes the long distance FM and AFM coupling in Mg^P@BP and the long range ferromagnetism does not arise from clustering effects, as observed in TM-doped systems *[18, 33]*. To investigate the magnetic coupling between two Mg–B3 units at a distance greater than 12.94 Å, we considered a larger supercell (10 × 5 × 1) with two Mg atoms at a distance of 16.16 Å. After considering the two configurations (FM and AFM), it was found that the AFM configuration is the most stable (Fig. 4.17), with an exchange energy of 6.08 eV. Hence, this FM coupling at 12.94 Å is a special case. We also considered a larger BP supercell (8 × 8 × 1) with 6.25% doping concentration (Fig. 4.18) to understand whether the magnetic ground state is affected by the periodic boundary conditions.

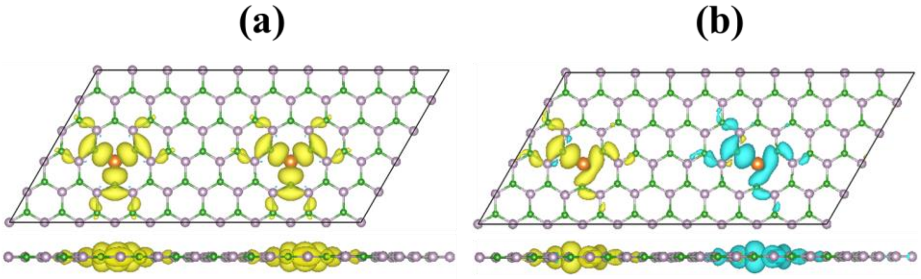

Figure 4.17: Spin density distribution (SDD) (isosurface value: 0.0012 e Å^{-3}) of (a) FM and (b) AFM configuration of Mg^P@BP system in a larger (10 × 5 × 1) BP supercell.

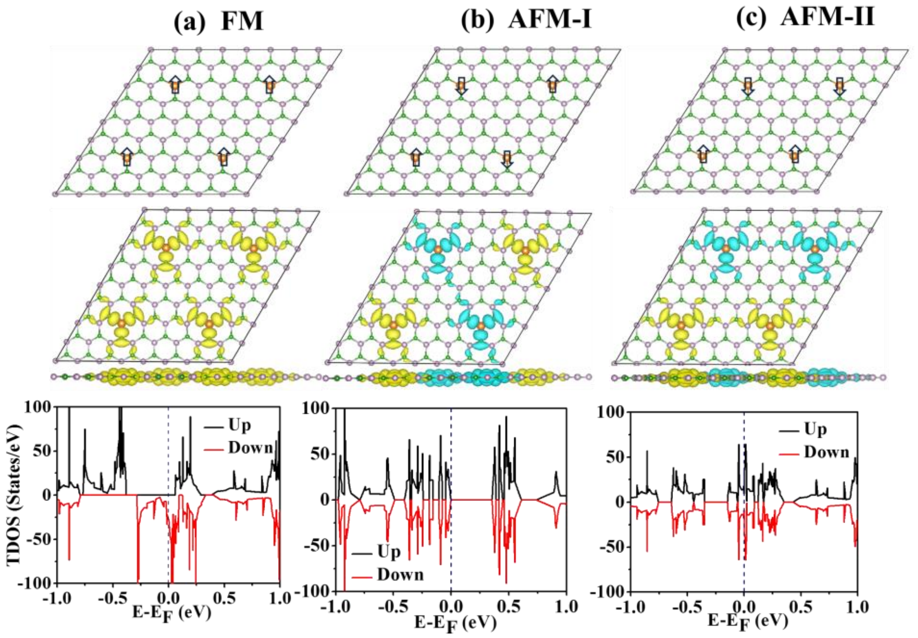

Figure 4.18: Optimized structures, Spin Density Distribution (isosurface value: 0.0012 e Å^{-3}), and TDOS of (a) FM, (b) AFM-I and (c) AFM-II configuration of Mg^P@BP (6.25%) in 8 × 8 × 1 BP supercell. The Fermi level is indicated by the blue dashed line.

It was found that the FM state is more stable than the two different AFM states (AFM-I and AFM-II) by 129.48 meV and 129.47 meV per supercell, respectively. Therefore, the magnetic ground state is not affected by the periodic boundary conditions. Hence, the Mg^P@BP (6.25%) system has a stable FM ground state; this type of long range FM ordering, which does not arise from clustering, is very promising for spintronics applications. Furthermore, we calculated the magnetic anisotropy energy (MAE) using non-collinear magnetic calculations with spin–orbit coupling (SOC) for the half-metallic Mg^P@BP (6.25%) system. The magnetic anisotropic energy (MAE) is an important parameter of magnetic materials to determine the low-temperature magnetic orientation with respect to the lattice structure, which is directly related to the thermal stability of magnetic data storage *[76]*. The magnetic easy axis (EA) of Mg^P@BP (6.25%) was found to lie in the (001) direction. The calculated MAEs for Mg^P@BP (6.25%) are 21.6 meV per Mg based on the PBE calculation level. These data are tabulated in Table 4.5. Mg^P@BP (6.25%) possesses comparatively larger MAE values than those of bulk Fe (1.4 meV per Fe atom) and Ni (2.7 meV per Ni atom) and similar to those of Mn (69 and 20 meV per Mn atom for the (100), (010) directions in the ab-plane and 47 and 25 meV per Mn atom for the (001), (111) directions out of the ab-plane, respectively) in 2D Mn_2C sheets *[5]*. Due to these large MAEs, Mg^P@BP (6.25%) is interesting for magnetoelectronics and spintronics applications.

Table 4.5: Summary of Magnetic Anisotropy Energies in μeV/dopant and the EA for Mg^P@BP (6.25%)

Mg^P@BP (6.25%)	**Easy Axis (001)**	**(100)-(001)**	**(010)-(001)**	**(110)-(001)**	**(111)-(001)**
	0 meV	21.6 meV	21.6 meV	21.6 meV	14.2 meV

Moreover, the effects of strain on the magnetic properties were verified due to their importance in practical applications. We studied the half-metallicity of the Mg^P@BP system by TDOS analysis under applications of biaxial tensile strain (1% to 3%). We found that the Mg^P@BP system sustains its half-metallic character upon application of 2% biaxial tensile strain (Fig. 4.19a). To develop a spintronics material, the Curie temperature (T_C) of that material should be compatible with or higher than the room temperature. Here, mean field theory (MFT) *[63]* was adopted to estimate the Curie temperatures

(T_C) of the Mg^P@BP system. The Curie temperature can be estimated by MFT with $K_BT_{C-MFT} = \frac{2}{3}\Delta E$; where K_B is Boltzmann's constant and ΔE is the exchange energy per spin coupling interaction *[77]*. The Curie temperature of the Mg^P@BP system was found to be 524.52 K from our MFT calculations. It is well known that the Curie temperature predicted by MFT is overestimated and that Monte Carlo (MC) simulations give reliable results *[5, 77]*. Therefore, we calculated the Curie temperature (T_C) of Mg^P@BP (6.25%) sheets using Monte Carlo (MC) simulations *[78]* based on the Heisenberg model of $H = -\sum_{i,j} J_{i,j} S_i S_j$, where $J_{i,j}$ is the nearest-neighbor exchange parameter and S_i and S_j represents the total magnetic moments per unit formula. A 40 × 40 × 1 supercell was constructed for the MC simulation of Mg^P@BP (6.25%) system, and the average magnetic moment per formula unit was taken after the system reached equilibrium at a given temperature.

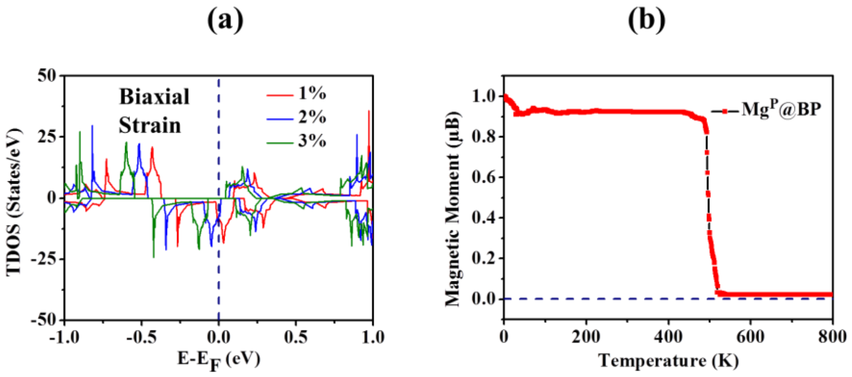

Figure 4.19: (a) Sustainability of the half-metallicity of Mg^P@BP under application of biaxial strain (1% to 3%). The Fermi level is indicated by a blue dashed line. (b) Variation of the total magnetic moment (μB) per formula unit of Mg^P@BP (6.25% doping) as a function of temperature.

We have plotted the magnetic moment (μB) vs. temperature (K) for the Mg^P@BP (6.25%) system (Fig. 4.19b) and found that the magnetic moment of the system gradually decreases at ~494 K. Therefore, the Curie temperature of the Mg^P@BP (6.25%) system is much higher than those of many previously studied systems, such as carbon-nitride-based *[24]*, MnX_2 (X = S, Se) *[77]*, and $FeCl_2$ *[79]* systems. Hence, due to its high Curie temperature, Mg^P@BP (6.25%) is suitable for spintronics functions at room temperature.

Stability of Mg^P@BP (6.25%) is very necessary for experimental realization of this type of system. Hence, we thoroughly studied its energetic, dynamic, thermal and mechanical stabilities to confirm its potential for practical applications in spintronic devices.

4.3.3. Energetic stability

We have calculated the formation energies and binding energies of the Be^P@BP and Mg^P@BP systems to evaluate the energetic stabilities of these systems (Table 4.6).

Table 4.6: Formation energies per dopant (E_F) and binding energies per dopant (E_B) for the Be^P@BP and Mg^P@BP systems with different doping concentrations

Be^P@BP Doping concentration (%)	**Formation energy (eV/atom)**	**Binding Energy (eV/atom)**
6.25	4.62	6.25
4.00	4.65	6.28
2.78	4.65	6.28
2.04	4.65	6.29
Mg^P@BP Doping concentration (%)		
6.25	5.46	9.35
4.00	5.49	9.38
2.78	5.51	9.39
2.04	5.51	9.40

We found that the formation energy of the Be^P@BP system remains almost unchanged (4.62 to 4.65 eV per dopant) with changes in the doping concentration (6.25% to 2.04%). Although the Mg^P@BP systems have higher formation energies (5.46 to 5.51 eV per dopant) compared to Be^P@BP, these values were also almost unchanged with variation of the doping concentration. The slightly higher formation energy values for Mg can be justified by the greater size mismatch between P (0.98 Å) and Mg (1.45 Å) compared to P and Be (1.12 Å). It was found from the formation energy values (Table 4.7) of Be^B@BP and Mg^B@BP are energetically more favorable by 3.55 eV and 2.19 eV than the Be^P@BP and Mg^P@BP systems. This can be explained by the closer atomic radii of Be and B compared to Be and P. However, the main concern of this work is to introduce half-metallicity in BP monolayer which can only be found at Be^P@BP and Mg^P@BP systems.

Table 4.7: Formation energy/dopant (E_F), binding energy/dopant (E_B), magnetic moments/dopant (μB) and band gap (eV) for Be^B@BP and Mg^B@BP systems

Be^B@BP (%)	**Formation energy (eV/atom)**	**Binding Energy (eV/atom)**	**Magnetic moment /dopant(μB)**	**Band Gap (eV)**
6.25	1.06	4.03	0.00 (Metallic)	0
Mg^B@BP (%)				
6.25	3.26	7.99	0.00 (Metallic)	0

Although the formation energies of Be^P@BP and Mg^P@BP systems (4.62 eV and 5.46 eV) are high, such high formation energy-based systems have been realized experimentally. For example, a C-doped BN system (C doping at both B- and N-sites) has been synthesized experimentally via in situ electron beam irradiation by Wei and co-workers *[80]*, although the reported value of formation energy for C_B (C doping at the B-sites) in a B-rich environment is 4.07 eV and that for C_N (C doping at the N-sites) in a N-rich environment is 4.27 eV *[81]*. Later, C-doped BN sheets were synthesized, also via pyrolysis, by Huang and co-workers *[82]*. We also found that the formation energy of 15.60% B doping in graphene (7.56 eV) is higher than that of N doping in graphene (2.68 eV) *[24, 83]*. However, B-doped graphene has been synthesized up to a dopant concentration of 13% *[24, 84, 85]*. Furthermore, we note that 27% B–N co-doped graphene has been synthesized experimentally *[86]*, although 31% B–N co doped graphene has a formation energy of 4.08 eV *[83]*. Therefore, based on the above theoretical predictions and experimental synthesis, we can predict the possibility of experimental realization of our systems (Be^P@BP and Mg^P@BP). We also checked the solubility and the possibilities of ionization of the dopants (Be and Mg) whether or not Be^{P}@BP and Mg^{P}@BP are dispersed in polar solvent based on electron localization function (ELF) calculations. The ELF calculations of the Be^{P}@BP and Mg^{P}@BP systems (Fig. 4.20) indicated that both these systems have strong covalent bonds between Mg/Be–B, which suggests that the dopant atoms will not be ionized in polar solvents.

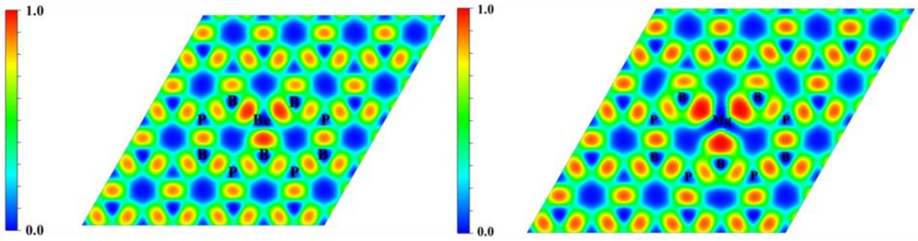

(a) Be^{P}@BP

(b) Mg^{P}@BP

Figure 4.20: Electron localization function (ELF; maximum saturation level 1.0 e Å^{-3}, minimum saturation level 0.0 Å^{-3}) of (a) Be^{P}@BP (6.25%) and (b) Mg^{P}@BP (6.25%)

The binding energy values (Table 4.6 and Table 4.7) show that the doped Be and Mg atoms bind more strongly at the P-site (6.25 and 9.35 eV) compared with the B-site (4.03 and 7.99 eV). It was observed that the binding energy values of Be^{P}@BP and Mg^{P}@BP are quite comparable for different doping concentrations (Table 4.6). We also compared our binding energy results with a previous reported study of a transitional metal doped BN monolayer (5.99 to 8.82 eV) *[87]* and found that the binding energy values of Be^{P}@BP (6.25 to 6.29 eV) are in a similar range, while the values are quite high (9.35 to 9.40 eV) for Mg^{P}@BP. This indicates that Mg binds more strongly than Be with the BP monolayer. The binding energy values of 6.25% Be^{P}@BP and Mg^{P}@BP (6.35 eV and 9.35 eV) are higher than the cohesive energies (3.73 eV and 1.47 eV) of bulk Be and Mg, which minimizes the possibility of cluster formation within the system. Hence, we can conclude that Be^{P}@BP and Mg^{P}@BP are thermodynamically stable. Furthermore, we have predicted a possible method for the experimental synthesis of Mg^{P}@BP. It was reported earlier that an Mg-incorporated GaN epilayer was grown by metal organic chemical vapor deposition (MOCVD) using bis(cyclopentadienyl)magnesium (Cp_2Mg) as the Mg precursor *[88-91]*. Thus, we assume that Mg^P@BP can also be synthesized via an MOCVD process.

4.3.4. Dynamic stability

The dynamic stability of the Mg^P@BP sheets was confirmed from phonon frequency calculations. We calculated the phonon frequency of Mg^P@BP for a doping concentration of 6.25%. The lattice dynamics of the Mg^P@BP sheets were examined from their respective phonon dispersion plots (Fig. 4.21).

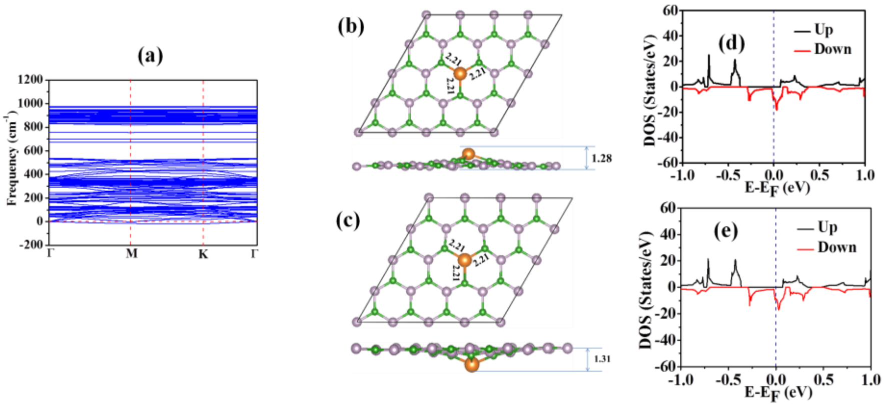

Figure 4.21: (a) Phonon dispersion plot of Mg^P@BP (6.25%) after 2nd soft mode relaxation, (b) - (c) optimized structures (Mg^P@BP (6.25%)) corresponding to the maximum Mg vibration due to lattice dynamical instability and (d) – (e) TDOS plots of the two structures. The Fermi level is shifted to zero and is indicated by a blue dashed line.

We have found that Mg^P@BP has an imaginary frequency (69.22 cm^{-1}) for 6.25% doping concentration (Fig. 4.22a); thus, we further investigated Mg^P@BP (6.25%) by relaxing the phonon soft mode and calculating the phonon frequency. Interestingly, Mg^P@BP (6.25%) shows small imaginary frequencies (37.97 cm^{-1}) after relaxing the phonon soft mode (Fig. 4.22b). To analyze whether this instability of the structure can affect the magnetic properties, we took two unstable structures (4.21b-c) where the maximum vibration of Mg atom occurs (corresponding to the maximum imaginary frequency) and investigated their corresponding magnetic properties. We found that both of these systems are magnetic, with total magnetic moments of 1.00 µB. Further, we found from spin-polarized density of states calculations that the systems also retain their half-metallic properties with a spin-up band gap of 0.43 eV (Fig. 4.21d–e). Therefore, due to lattice instability, the spin-up band gap slightly changes from 0.44 eV to 0.43 eV.

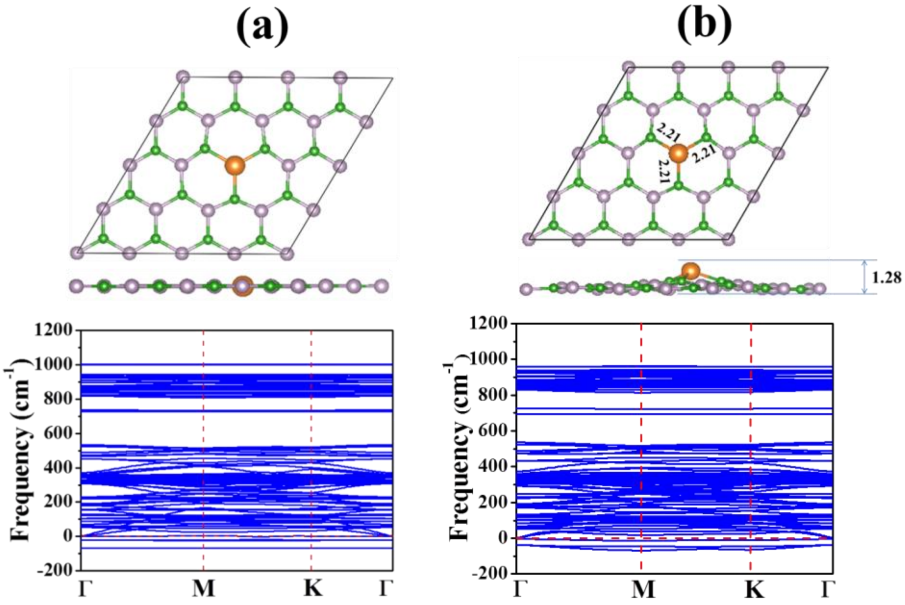

Figure 4.22: (a) Optimized structure and phonon dispersion plot of Mg^P@BP (6.25%), (b) Optimized structure and phonon dispersion plot of Mg^P@BP (6.25%) after 1st soft mode relaxation.

Since dynamic stability is highly crucial for experimental realization, we have further relaxed the unstable modes in Mg^P@BP. Further relaxation of the soft mode indicates that Mg^P@BP has a very small imaginary frequency (maximum 0.11 cm^{-1}) (Fig. 4.21a). To be very specific, there are three acoustic modes which have imaginary frequencies of 0.038*i*, 0.052*i* and 0.11*i* cm^{-1}, respectively. The modes corresponding to the imaginary frequencies are very small; they can be attributed to numerical noise of structural minimization, which is inevitable when the minimization method DFPT is used to compute phonons.

Apart from this, all three modes correspond to lattice translation degrees of freedom without any abnormal starching or breaking of bonds between atoms. Any non-trivial motion of atoms against each other is an actual indication of an unstable mode *[92]*. However, the two acoustic modes corresponding to the frequencies 0.038*i* and 0.052*i* cm^{-1} arise due to in-plane (in x–y plane) lattice translations (Fig. 4.23a and b), whereas the other acoustic mode corresponding to the frequency 0.11*i* cm^{-1} arises due to out-of-plane translation (Fig. 4.23c).

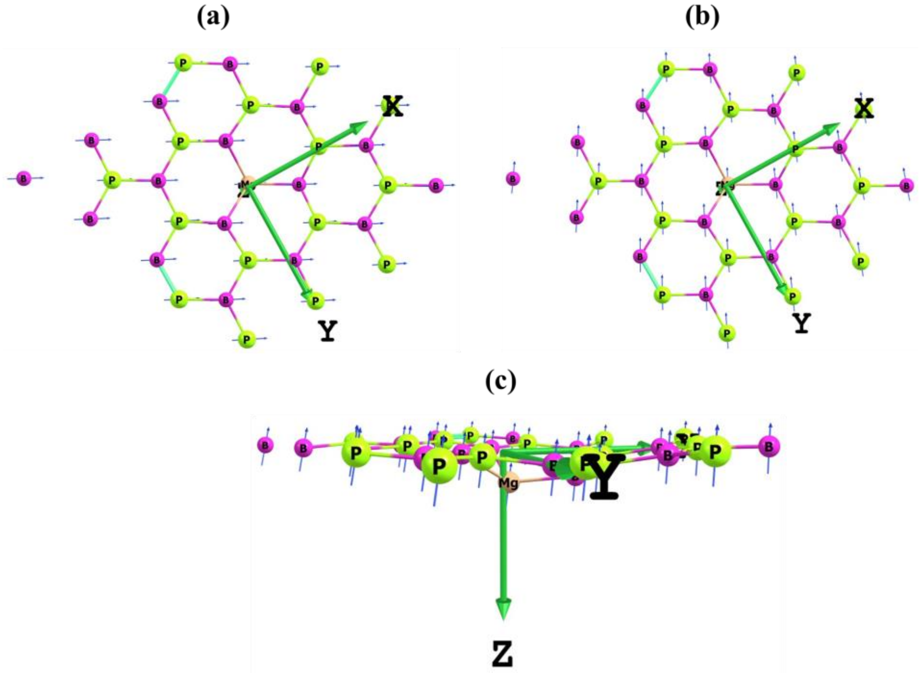

Figure 4.23: Displacement eigenvectors (indicated by blue arrows) corresponding to the soft phonon mode with imaginary frequencies of (a) 0.038*i* cm^{-1}, (b) 0.052*i* cm^{-1} and (c) 0.11*i* cm^{-1} of Mg^P@BP (6.25%). The light orange, pink and green atoms respectively denote Mg, B and P.

These small translation modes are not sufficient for the lattice to undergo structural phase transitions. These small imaginary modes due to translation degrees of freedom can be stabilized using a proper substrate. We believe that a substrate which interacts with Mg^P@BP through van der Waals interactions may stabilize these imaginary modes without affecting the desired properties.

4.3.5. Thermal stability

The thermal stability of Mg^P@BP (6.25%) was studied to determine the possibility of inter-conversion of Mg^P@BP (6.25%) sheets to other conformers. To check this for Mg^P@BP (6.25%), AIMD simulations were carried out on a 4 × 4 × 1 supercell (32 atoms) using an NVT ensemble at 300 K and 500 K with a time step of 1 fs (femtosecond) for 30 ps (picoseconds). We also found several earlier reports that considered 32 atoms *[93]*, 34 atoms *[94]* and 24 atoms *[63]* for AIMD simulations. Hence, we assumed that a 32-atom system would be sufficient for AIMD simulations. Room temperature AIMD simulations showed no possibility of inter-conversion of the optimized structure. No structural deformation was observed for the 300 K and 500 K simulations (Fig. 4.24). Thus, it can be concluded that Mg^P@BP (6.25%) is thermally stable up to 500 K temperature with a very low energy fluctuation.

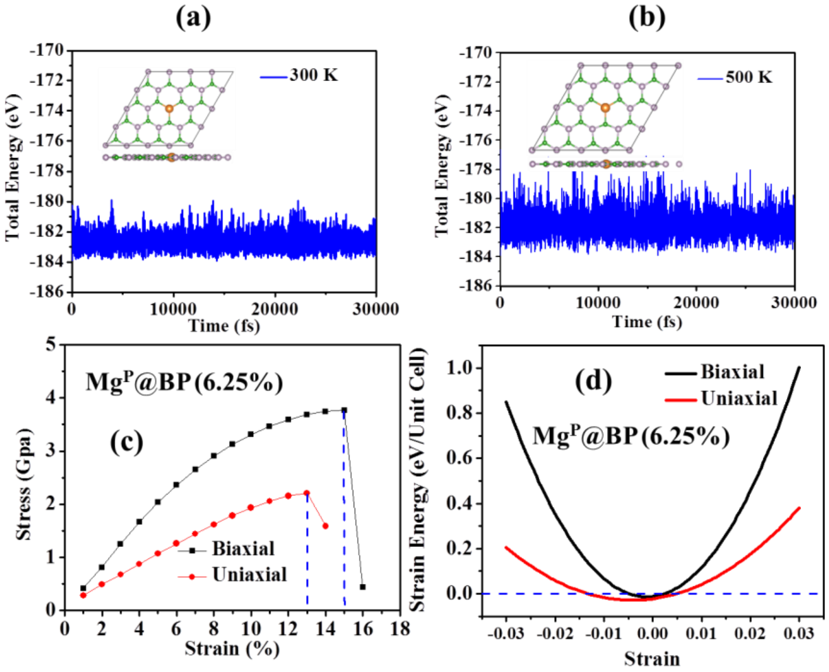

Figure 4.24: Total energy fluctuations of the AIMD simulation of Mg^P@BP (6.25%) at (a) 300 K, (b) 500 K. (c) Tensile strain vs. stress plot for Mg^P@BP (6.25%). (d) Strain energy vs. applied strain plot for MgP@BP (6.25%).

4.3.6. Mechanical stability and mechanical properties of Mg^P@BP (6.25%)

Strain technology is essential to estimate and understand the fundamental nature of the chemical bonding, the effects of lattice distortion on the structural stability and the elastic limit of a single-layered system because a material must sustain strain during synthesis and any practical applications. Application of strain can also alter the electronic and magnetic properties of a material. Hence, we performed a systematic analysis of the mechanical stability of Mg^P@BP (6.25%)

by applying ideal equi-biaxial tensile strain or equi-biaxial compressive strain and uniaxial tensile or compressive strain to understand the strain sustainability and the electronic and magnetic properties of Mg^P@BP (6.25%). Tensile strain was applied by gradually increasing the lattice parameters and compressive strain was applied by gradually reducing the lattice parameters. The percentage (%) of applied strain can be calculated as follows *[95]*

$$\%\, of\ strain = \frac{a-a_1}{a} \times 100 \tag{4.8}$$

Here 'a' and 'a_1' are the lattice constants of Mg^P@BP (6.25%) sheet before and after the strain.

The effects of uniaxial and biaxial strains for Mg^P@BP (6.25%) are examined on a supercell (4×4×1) of 32 atoms. Atomic positions are relaxed until the forces on each atom are less than 10^{-2} eV $Å^{-1}$. Elastic limit is calculated from the stress-strain curve under the tensile stretch (Fig. 4.24c) *[96]*.

Further, the mechanical properties of the Mg^P@BP (6.25%) sheet can be calculated from the strain vs. strain energy plot (Fig. 4.24d). The elastic energy (U/per unit cell) near the equilibrium position can be calculated using the following formula:

$$U = \frac{1}{2} C_{11}\varepsilon_{xx}^2 + \frac{1}{2} C_{22}\varepsilon_{yy}^2 + C_{12}\varepsilon_{xx}\varepsilon_{yy} + 2C_{44}\varepsilon_{xy}^2 \tag{4.9}$$

Here C_{11} , C_{22} , C_{22} and C_{22} are the linear elastic constants, whereas the ε_{xx} , ε_{yy} and ε_{xy} are the in plane stress along x , y and xy directions (according to vigot notation) *[97]* respectively. The value of elastic constants can be calculated from the polynomial fitting of strain vs energy plot *[97-99]*. The main criteria for mechanical stability are are $C_{11} > C_{12}$ and $C_{44} > 0$. Young's modulus (Y) is calculated using the following formula *[93, 100]*.

$$Y = \frac{(C_{11}^2 - C_{22}^2)}{C_{11}} \tag{4.10}$$

Our calculation shows that an Mg^P@BP (6.25%) sheet can sustain a maximum equi-biaxial strain of 15% with a maximum stress of 3.77 GPa as well as a maximum uniaxial strain of 13% with a maximum stress of 2.21 GPa (Fig. 4.24). Hence, the elastic limit of Mg^P@BP

(6.25%) is similar to those of previously reported TM free magnetic systems, such as C_{N2}@gh-C_3N_4 (maximum uniaxial strain 15%, biaxial strain 14%) *[24]*, and slightly lower than those of the C_B@h-BN (maximum uniaxial strain 13%, biaxial strain 14%) *[28]* systems. We calculated the mechanical properties of Mg^P@BP (6.25%) by calculating Young's modulus. From our calculations, we found that the elastic constants of Mg^P@BP (6.25%) are C_{11} = 66.81 N m^{-1}, C_{12} = 17.01 N m^{-1} and C_{44} = 41.88 N m^{-1}. Thus, Mg^P@BP (6.25%) satisfies all stability criteria (such as $C_{11} > |C_{12}|$ and $C_{44} = 41.88 > 0$) to be mechanically stable. Although our calculated Young's modulus value (62.48 N m^{-1}) for Mg^P@BP (6.25%) is much lower than that of the pure BP system (135.6 N m^{-1}) *[66]*, it is very comparable with that of silicene (62 N m^{-1}) *[93]*.

4.4. Conclusion

A thorough investigation has been conducted based on second and third row main group element-doped BP ML systems using density functional theory (DFT) for possible spintronics applications. We have found that only Li, Na, Mg and Be substitution at the P-site and Na substitution at the B-site show magnetism in the BP systems. Amongst these, only Na^B@BP, Be^P@BP and Mg^P@BP were found to be strongly half-metallic in nature. Due to the high formation energy of the Na^B@BP system, our study mainly focused on Be^P@BP and Mg^P@BP; we found that single Be and Mg-doped BP monolayers induce local spin states, leading to a magnetic moment of 1.00 μB, which is distributed in the Mg–B3 and Be–B3 units. We have also reported long range ferromagnetic (FM) coupling (> 12 Å) between the two magnetic units (Mg–B3) protected by AFM coupling at close proximity (<12 Å). Hence, this long range ferromagnetism coupling is indisputably not arising from clustering, which is very promising for next generation spintronics. Stability analysis shows that Mg-doped BP systems show excellent dynamical, thermal and mechanical properties. The Mg^P@BP system exhibits a strikingly high Curie temperature (T_C = ~ 494 K) amongst the contemporary main group-based 2D materials studied to date. Therefore, this material with long range FM coupling and a high Curie temperature is very promising for spintronics devices.

Note: This is copyrighted material from Royal Society of Chemistry, Phys. Chem. Chem. Phys., 2018, 20, 22877-22889 (DOI: 10.1039/c8cp03440k).

4.5. References

[1] Gao D., Liu Y., Song M., Shi S., Si M., Xue D. (2015), Manifestation of high-temperature ferromagnetism in fluorinated graphitic carbon nitride nanosheets, J. Mater. Chem. C, 3, 12230-12235 (DOI: 10.1039/c5tc02911b)

[2] Pan H., Sun Y., Zheng Y., Tang N., Du Y. (2016), B_4CN_3 and B_3CN_4 monolayers as the promising candidates for metal-free spintronic materials, New J. Phys., 18 , 093021 (DOI: 10.1088/1367-2630/18/9/093021)

[3] Gao D., Liu Y., Liu P., Si M., Xue D. (2016), Atomically Thin B doped g-C_3N_4 Nanosheets: High-Temperature Ferromagnetism and calculated Half-Metallicity, Sci. Rep., 6, 35768 (DOI: 10.1038/srep35768)

[4] He J., Zhou P., Jiao N., Chen X., Luc W., Sun L. Z. (2015), Prediction of half-semiconductor antiferromagnets with vanishing net magnetization, RSC Adv., 5, 46640-46647 (DOI: 10.1039/c5ra05257b)

[5] Hu L., Wu X., Yang J. (2016), Mn_2C monolayer: a 2D antiferromagnetic metal with high Néel temperature and large spin–orbit coupling, Nanoscale, 8, 12939-12945 (DOI: 10.1039/c6nr02417c)

[6] Barthem V. M., Colin C. V., Mayaffre H., Julien M. H., Givord D. (2013), Revealing the properties of Mn_2Au for antiferromagnetic spintronics, Nat. Commun., 4, 2892 (DOI: 10.1038/ncomms3892)

[7] Shick A. B., Khmelevskyi S., Mryasov O. N., Wunderlich J., Jungwirth T. (2010), Spin-orbit coupling induced anisotropy effects in bimetallic antiferromagnets: A route towards antiferromagnetic spintronics, Phys. Rev. B, 81, 212409 (DOI: 10.1103/PhysRevB.81.212409)

[8] Fiebig M., Duong N. P., Satoh T., Van Aken B. B., Miyano K., Tomioka Y., Tokura Y. (2008), Ultrafast magnetization dynamics of antiferromagnetic compounds, J. Phys. D: Appl. Phys., 41, 164005 (11pp) (DOI: 10.1088/0022-3727/41/16/164005)

[9] Krasheninnikov A. V., Lehtinen P. O., Foster A. S., Pyykk¨o P., Nieminen R. M. (2009), Embedding Transition-Metal Atoms in Graphene: Structure, Bonding, and Magnetism, Phys. Rev. Lett., 102, 126807 (DOI: 10.1103/PhysRevLett.102.126807)

[10] Sevinçli H., Topsakal M., Durgun E., Ciraci S. (2008), Electronic and magnetic properties of 3d transition-metal atom adsorbed graphene and graphene nanoribbons, Phys. Rev. B, 77, 195434 (DOI: 10.1103/PhysRevB.77.195434)

[11] Cao C., Wu M., Jiang J., Cheng H.-P. (2010), Transition metal adatom and dimer adsorbed on graphene: Induced magnetization and electronic structures, Phys. Rev. B, 81, 205424 (DOI: 10.1103/PhysRevB.81.205424)

[12] Wehling T. O., Lichtenstein A. I., Katsnelson M. I. (2011), Transition-metal adatoms on graphene: Influence of local Coulomb interactions on chemical bonding and magnetic moments, Phys. Rev. B, 84, 235110 (DOI: 10.1103/PhysRevB.84.235110)

[13] Shishidou T., Freeman A. J., Asahi R. (2001), Effect of GGA on the half-metallicity of the itinerant ferromagnet CoS_2, Phys. Rev. B., 64, 180401 (1-4) (DOI: 10.1103/PhysRevB.64.180401)

[14] Wu F., Huang C., Wu H., Lee C., Deng K., Kan E., Jena P. (2015), Atomically Thin Transition-Metal Dinitrides: High-Temperature Ferromagnetism and Half-Metallicity, Nano. Lett., 15, 8277-8281 (DOI: 10.1021/acs.nanolett.5b03835)

[15] Ye L. H., Freeman A. J., Delley B. (2006), Half-metallic ferromagnetism in Cu-doped ZnO: Density functional calculations, Phys. Rev. B., 73, 033203 (1-4) (DOI: 10.1103/PhysRevB.73.033203)

[16] Saini H. S., Singh M., Reshak A. H., Kashyap M. K. (2013), Variation of half metallicity and magnetism of $Cd_{1-x}Cr_xZ$ (Z = S, Se and Te) DMS compounds on reducing dilute limit, J. Mag. Mag. Mater., 331, 1-6 (DOI: 10.1016/j.jmmm.2012.10.044)

[17] Li H., Hu H., Bao C., Hua J., Zhou H., Liu X., Liu X., Zhao M. (2015), Tensile strain induced half-metallicity in graphene-like carbon nitride, Phys. Chem. Chem. Phys., 17, 6028-6035 (DOI: 10.1039/c4cp05560h)

[18] Chintalapati S., Yang M., Lau S. P., Feng Y. P. (2014), Surface magnetism of Mg doped AlN: a first principle study, J. Phys.: Condens. Matter, 26, 435801 (6pp) (DOI: 10.1088/0953-8984/26/43/435801)

[19] Xu K., Li X., Chen P., Zhou D., Wu C., Guo Y., Zhang L., Zhao J., Wu X., Xie Y. (2015), Hydrogen dangling bonds induce ferromagnetism in two-dimensional metal-free graphitic-C_3N_4 nanosheets, Chem. Sci., 6, 283-287 (DOI: 10.1039/c4sc02576h)

[20] Luo M., Yin H. H., Shen Y. H. (2018), Magnetic and Electronic Properties of BN Nanosheets with Different Nonmagnetic Metal Dopants: a First-Principles Study, J Supercond Nov Magn., 31, 2211-2216 (DOI: 10.1007/s10948-017-4474-x)

[21] Maassen J., Ji W., Guo H. (2011), Graphene Spintronics: The Role of Ferromagnetic Electrodes, Nano Lett., 11, 151-155 (DOI: 10.1021/nl1031919)

[22] Hashmi A., Hong J. (2014), Metal free half metallicity in 2D system: structural and magnetic properties of g-C_4N_3 on BN, Sci. Rep., 4, 4374 (DOI: 10.1038/srep04374)

[23] Gao D., Xu Q., Zhang J., Yang Z., Si M., Yan Z., Xue D. (2014), Defect-related ferromagnetism in ultrathin metal free g-C_3N_4 nanosheets, Nanoscale, 6, 2577-2581 (DOI: 10.1039/c3nr04743a)

[24] Choudhuri I., Bhattacharyya G., Kumar S., Pathak B. (2016), Metal-free half-metallicity in a high energy phase C-doped gh-C_3N_4 system: a high Curie temperature planar system, J. Mater. Chem. C, 4, 11530-11539 (DOI: 10.1039/c6tc04163a)

[25] Błoński P., Tuček J., Sofer Z., Mazánek V., Petr M., Pumera M., Otyepka M., Zbořil R. (2017), Doping with Graphitic Nitrogen Triggers Ferromagnetism in Graphene, J. Am. Chem. Soc., 139, 3171−3180 (DOI: 10.1021/jacs.6b12934)

[26] Miao Q., Wang L., Liu Z., Wei B., Xu F., Fei W. (2016), Magnetic properties of N-doped graphene with high Curie temperature, Sci. Rep., 6, 21832 (DOI: 10.1038/srep21832)

[27] Liu Y.-J., Gao B., Xu D., Wang H.- M., Zhao J.-X. (2014), Theoretical study on Si-doped hexagonal boron nitride (h-BN) sheet: Electronic, magnetic properties, and reactivity, Phys. Lett. A, 378, 2989–2994 (DOI: 10.1016/j.physleta.2014.07.053)

[28] Choudhuri I., Pathak B. (2018), Ferromagnetism and Half-Metallicity in a High-Band-Gap Hexagonal Boron Nitride System, ChemPhysChem, 19, 153–161 (DOI: 10.1002/cphc.201700759)

[29] Liu Y., Liu P., Sun C., Wang T., Tao K., Gao D. (2017), P dopants induced ferromagnetism in g-C_3N_4 nanosheets: Experiments and Calculations, Appl. Phys. Lett., 110, 222403 (1-5) (DOI: 10.1063/1.4984584)

[30] Bhattacharya B., Sarkar U. (2016), The Effect of Boron and Nitrogen Doping in Electronic, Magnetic, and Optical Properties of Graphyne, J. Phys. Chem. C, 120, 26793−26806 (DOI: 10.1021/acs.jpcc.6b07478)

[31] Du A., Sanvito S., Smith S. C. (2012), First-Principles Prediction of Metal-Free Magnetism and Intrinsic Half-Metallicity in Graphitic Carbon Nitride, Phys. Rev. Lett., 108, 197207 (1-5) (DOI: 10.1103/PhysRevLett.108.197207)

[32] Bai Y., Deng K., Kan E. (2015), Electronic and magnetic properties of an AlN monolayer doped with first-row elements: a first principles study, RSC Adv., 5, 18352-18358 (DOI: 10.1039/c4ra13522a)

[33] Ao L., Pham A., Xiao H. Y., Zu X. T., Li S. (2016), Theoretical prediction of long-range ferromagnetism in transition-metal atom-doped d^0 dichalcogenide single layers SnS_2 and ZrS_2, Phys. Chem. Chem. Phys., 18, 25151-25160 (DOI: 10.1039/c6cp02206e)

[34] Hashmi A., Farooq M. U., Hong J. (2016), Long-Range Magnetic Ordering and Switching of Magnetic State by Electric Field in Porous Phosphorene, J. Phys. Chem. Lett., 7, 647-652 (DOI: 10.1021/acs.jpclett.5b02600)

[35] Zeng B., Li M., Zhang X., Yi Y., Fu L., Long M. (2016), First-Principles Prediction of the Electronic Structure and Carrier Mobility in Hexagonal Boron Phosphide Sheet and Nanoribbons, J. Phys. Chem. C, 120, 25037-25042 (DOI: 10.1021/acs.jpcc.6b07048)

[36] López-Castillo A. (2012), Prediction of Boron–Phosphorous nanographene-like material, Int. J. Quantum Chem., 112, 3152-3157 (DOI: 10.1002/qua.24096)

[37] Wang S. F., Wu X. J. (2015), First-Principles Study on Electronic and Optical Properties of Graphene-Like Boron Phosphide Sheets, Chin. J. Chem. Phys., 28, 588-594 (DOI: 10.1063/1674-0068/28/cjcp1505100)

[38] Wu M., Zhang Z., Zeng X. C. (2010), Charge-injection induced magnetism and half metallicity in single-layer hexagonal group III/V (BN, BP, AlN, AlP) systems, Appl. Phys. Lett., 97, 093109 (1-3) (DOI: 10.1063/1.3484957)

[39] Sohbatzadeh Z., Roknabadi M. R., Shahtahmasebi N., Behdani M. (2015), Spin-dependent transport properties of an armchair boron-phosphide nanoribbon embedded between two graphene nanoribbon electrodes, Phys. E, 65, 61-67 (DOI: 10.1016/j.physe.2014.08.003)

[40] Zhuang H. L., Hennig R. G. (2012), Electronic structures of single-layer boron pnictides, Appl. Phys. Lett., 101, 153109 (1-4) (DOI: 10.1063/1.4758465)

[41] Du L., Zheng K., Cui H., Wang Y., Tao L., Chen X. (2018), Novel electronic structures and enhanced optical properties of boron phosphide/blue phosphorene and F4TCNQ/blue phosphorene heterostructures: a DFT + NEGF study, Phys. Chem. Chem. Phys., 20, 28777-28785 (DOI: 10.1039/c8cp05119d)

[42] Yu J., Guo W. (2015), Strain tunable electronic and magnetic properties of pristine and semi hydrogenated hexagonal boron phosphide, Appl. Phys. Lett., 106, 043107 (1-5) (DOI: 10.1063/1.4906998)

[43] Onat B., Hallioglu L., İpek S., Durgun E. (2017), Tuning Electronic Properties of Monolayer Hexagonal Boron Phosphide with

Group III−IV−V Dopants, J. Phys. Chem. C, 121, 4583-4592 (DOI: 10.1021/acs.jpcc.6b10334)

[44] Padavala B., Frye C. D., Wang X., Ding Z., Chen R., Dudley M., Raghothamachar B., Lu P., Flanders B. N., Edgar J. H. (2016), Epitaxy of Boron Phosphide on Aluminum Nitride(0001)/Sapphire Substrate, Cryst. Growth Des., 16, 981-987 (DOI: 10.1021/acs.cgd.5b01525)

[45] Nunzi F., Ruiz E., Cano J., Alvarez S. (2007), Strong Antiferromagnetic Coupling at Long Distance through a Ligand to Metal Charge Transfer Mechanism, J. Phys. Chem. C, 111, 618-621 (DOI: 10.1021/jp0668753)

[46] Kresse G., Joubert D. (1999), From ultrasoft pseudopotentials to the projector augmented-wave method, Phys. Rev. B, 59, 1758-1775 (DOI: 10.1103/PhysRevB.59.1758)

[47] Perdew J. P., Burke K., Ernzerhof M. (1996), Generalized Gradient Approximation Made Simple, Phys. Rev. Lett., 77, 3865-3868 (DOI: 10.1103/PhysRevLett.77.3865)

[48] Perdew J. P., Chevary J. A., Vosko S. H., Jackson K. A., Pederson M. R., Singh D. J., Fiolhais C. (1992), Atoms, molecules, solids, and surfaces: Applications of the generalized gradient approximation for exchange and correlation, Phys. Rev. B, 46, 6671–6687 (DOI: 10.1103/PhysRevB.46.6671)

[49] Anisimov V. I., Aryasetiawan F., Lichtenstein A. I. (1997), First-principles calculations of the electronic structure and spectra of strongly correlated systems: the LDA + U method, J. Phys. Condens. Matter, 9, 767-808 (DOI: 10.1088/0953-8984/9/4/002)

[50] Blochl P. E. (1994), Projector augmented-wave method, Phys. Rev. B, 50, 17953-17977 (DOI: 10.1103/PhysRevB.50.17953)

[51] Bader R. F. W. (1991), A quantum theory of molecular structure and its applications, Chem. Rev., 91, 893-928 (DOI: 10.1021/cr00005a013)

[52] Henkelman G., Arnaldsson A., Jo´nsson H. (2006), A fast and robust algorithm for Bader decomposition of charge density, Comput. Mater. Sci., 36, 354-360 (DOI: 10.1016/j.commatsci.2005.04.010)

[53] Sanville E., Kenny S. D., Smith R., Henkelman G. J. (2007), Improved Grid-Based Algorithm for Bader Charge Allocation, Comput. Chem., 28, 899-908 (DOI: 10.1002/jcc.20575)

[54] Tang W., Sanville E., Henkelman G. J. (2009), A grid-based Bader analysis algorithm without lattice bias, J. Phys.: Condens. Matter, 21, 084204 (7pp) (DOI: 10.1088/0953-8984/21/8/084204)

[55] Nose´ S. (1984), A unified formulation of the constant temperature molecular dynamics methods, J. Chem. Phys., 81, 511-519 (DOI: 10.1063/1.447334)

[56] Baroni S., Giannozzi P., Testa A. (1987), Green's-function approach to linear response in solids, Phys. Rev. Lett., 58, 1861-1864 (DOI: 10.1103/PhysRevLett.58.1861)

[57] Togo A., Oba F., Tanaka I. (2008), First-principles calculations of the ferroelastic transition between rutile-type and $CaCl_2$-type SiO_2 at high pressures, Phys. Rev. B, 78, 134106 (1-9) (DOI: 10.1103/PhysRevB.78.134106)

[58] Yang Y.W., Coppens P. (1978), The Electron Density and Bonding in Beryllium Metal as Studied by Fourier Methods, Acta Crystallogr., A 34, 61-65 (DOI: 10.1107/S0567739478000121)

[59] Walker C. B., Marezio M. (1959), Lattice parameters and zone overlap in solid solutions of lead in magnesium, Acta Met., 7, 769-773 (DOI: 10.1016/0001-6160(59)90090-2)

[60] McCarty L., Kasper J. S., Horn F. H., Decker B. F., Newkirk A. E. (1958), A NEW CRYSTALLINE MODIFICATION OF BORON, J. Am. Chem. Soc., 80, 2592-2592 (DOI: 10.1021/ja01543a066)

[61] Simon A., Borrmann H., Craubner H. (1987), Crystal Structure of Ordered White Phosphorus (β-P), Phosphorus and Sulfur and the Related Elements, 30, 507-510 (DOI: 10.1080/03086648708080631)

[62] Choudhuri I., Kumar S., Mahata A., Rawat K. S., Pathak B. (2016), Transition-metal embedded carbon nitride monolayers: high-temperature ferromagnetism and half-metallicity, Nanoscale, 8, 14117-14126 (DOI: 10.1039/C6NR03282F)

[63] Choudhuri I., Garg P., Pathak B. (2016), TM@gt-C_3N_3 monolayers: high-temperature ferromagnetism and high anisotropy, J. Mater. Chem. C, 4, 8253-8262 (DOI: 10.1039/c6tc03030k)

[64] Kumar S., Choudhuri I., Pathak B. (2016), An atomically thin ferromagnetic half-metallic pyrazine-fused Mn-porphyrin sheet: a slow spin relaxation system, J. Mater. Chem. C, 4, 9069-9077 (DOI: 10.1039/c6tc03438a)

[65] Sun Y., Zhuo Z., Wu X., Yang J. (2017), Room-Temperature Ferromagnetism in Two-Dimensional Fe_2Si Nanosheet with Enhanced Spin-Polarization Ratio, Nano Lett., 17, 2771−2777 (DOI: 10.1021/acs.nanolett.6b04884)

[66] Çakır D., Kecik D., Sahin H., Durgun E., Peeters F. M. (2015), Realization of a p–n junction in a single layer boron-phosphide, Phys. Chem. Chem. Phys., 17, 13013-13020 (DOI: 10.1039/c5cp00414d)

[67] Onat B., Hallioglu L., İpek S., Durgun E. (2017), Tuning Electronic Properties of Monolayer Hexagonal Boron Phosphide with Group III−IV−V Dopants, J. Phys. Chem. C, 121, 4583−4592 (DOI: 10.1021/acs.jpcc.6b10334)

[68] Zhang X., Qin J., Liu H., Zhang S., Ma M., Luo W., Liu R., Ahuja R. (2015), Pressure-induced zigzag phosphorus chain and superconductivity in boron monophosphide, Sci. Rep., 5, 8761 (DOI: 10.1038/srep08761)

[69] Ghosh D., Periyasamy G., Pati S. K. (2014), Transition Metal Embedded Two-Dimensional C_3N_4−Graphene Nanocomposite: A Multifunctional Material, J. Phys. Chem. C, 118, 15487-15494 (DOI: 10.1021/jp503367v)

[70] Ghosh D., Periyasamy G., Pandey B., Pati S. K. (2014), Computational studies on magnetism and the optical properties of transition metal embedded graphitic carbon nitride sheets, J. Mater. Chem. C, 2, 7943-7951 (DOI: 10.1039/c4tc01385a)

[71] Park H., Wadehra A., Wilkins J. W., Castro Neto A. H. (2012), Magnetic states and optical properties of single-layer carbon-doped hexagonal boron nitride, Appl. Phys. Lett., 100, 253115 (1-4) (DOI: 10.1063/1.4730392)

[72] Mann J. ., Atomic Structure Calculations II. Hartree-Fock wave functions and radial expectation values: hydrogen to lawrencium, Technical Report. LA-3691, Los Alamos Scientific Lab., USA, 1968 (DOI: 10.2172/4553157)

[73] Barbalace K., "Periodic Table of Elements".Environmental Chemistry.com. http://environmentalchemistry.com/yogi/periodic/. Retrieved 2007-04-14

[74] Wu X., Han J., Feng Y., Li G., Wang C., Ding G., Gao G. (2017), Half-metals and half-semiconductors in a transition metal doped $SnSe_2$ monolayer: a first-principles study, RSC Adv., 7, 44499-44504 (DOI: 10.1039/c7ra07648g)

[75] Mishra R., Zhou W., Pennycook S. J., Pantelides S. T., Idrobo J.-C. (2013), Long-range ferromagnetic ordering in manganese-doped two-dimensional dichalcogenides, Phys. Rev. B, 88, 144409 (1-5) (DOI: 10.1103/PhysRevB.88.144409)

[76] Sun Y., Zhuo Z., Wu X., Yang J. (2017), Room-Temperature Ferromagnetism in Two-Dimensional Fe_2Si Nanosheet with Enhanced Spin-Polarization Ratio, Nano Lett., 17, 2771−2777 (DOI: 10.1021/acs.nanolett.6b04884)

[77] Kan M., Adhikari S., Sun Q. (2014), Ferromagnetism in MnX_2 (X = S, Se) monolayers, Phys. Chem. Chem. Phys., 16, 4990-4994 (DOI: 10.1039/c3cp55146f)

[78] Asselin P., Evans R. F. L., Barker J., Chantrell R. W., Yanes R., Chubykalo-Fesenko O., Hinzke D., Nowak U. (2010), Constrained Monte Carlo method and calculation of the temperature dependence of magnetic anisotropy, Phys. Rev. B, 82, 054415 (1-12) (DOI: 10.1103/PhysRevB.82.054415)

[79] Torun E., Sahin H., Singh S. K., Peeters F. M. (2015), Stable half-metallic monolayers of $FeCl_2$, Appl. Phys. Lett., 106, 192404 (1-4) (DOI: 10.1063/1.4921096)

[80] Wei X., Wang M. -S., Bando Y., Golberg D. (2011), Electron-Beam-Induced Substitutional Carbon Doping of Boron Nitride Nanosheets, Nanoribbons, and Nanotubes, ACS Nano, 5, 2916−2922 (DOI: 10.1021/nn103548r)

[81] Zhao J., Chen Z. (2015), Carbon-Doped Boron Nitride Nanosheet: An Efficient Metal-Free Electrocatalyst for the Oxygen Reduction Reaction, J. Phys. Chem. C, 119, 26348−26354 (DOI: 10.1021/acs.jpcc.5b09037)

[82] Huang C., Chen C., Zhang M., Lin L., Ye X., Lin S., Antonietti M., Wang X. (2015), Carbon-doped BN nanosheets for metal-free photoredox catalysis, Nat. Commun., 6, 7698 (DOI: 10.1038/ncomms8698)

[83] Choudhuri I., Patra N., Mahata A., Ahuja R., Pathak B. (2015), B−N@Graphene: Highly Sensitive and Selective Gas Sensor, J. Phys. Chem. C, 119, 24827−24836 (DOI: 10.1021/acs.jpcc.5b07359)

[84] Rao C. N. R., Gopalakrishnan K., Govindaraj A. (2014), Synthesis, properties and applications of graphene doped with boron, nitrogen and other elements, Nano Today, 9, 324-343 (DOI: 10.1016/j.nantod.2014.04.010)

[85] Tang Y.-B., Yin L.-C., Yang Y., Bo X.-H., Cao Y.-L., Wang H.-E., Zhang W.-J., Bello I., Lee S.-T., Cheng H.-M., Lee C.-S. (2012), ACS Nano, 6, 1970-1978 (DOI: 10.1021/nn3005262)

[86] Chang C.-K., Kataria S., Kuo C.-C., Ganguly A., Wang B.-Y., Hwang J.-Y., Huang K.-J., Yang W.-H., Wang S.-B., Chuang C.-H., Chen M., Huang C.-I, Pong W.-F., Song K.-J., Chang S.-J., Guo J.-H., Tai Y., Tsujimoto M., Isoda S., Chen C.-W., Chen L.-C., Chen K.-H. (2013), Band Gap Engineering of Chemical Vapor Deposited Graphene by in Situ BN Doping, ACS Nano, 7, 1333−1341 (DOI: 10.1021/nn3049158)

[87] He J., Jiao N., Zhang C., Xiao H., Chen X., Sun L. (2014), Spin Switch of the Transition-Metal-Doped Boron Nitride Sheet through H/F Chemical Decoration, J. Phys. Chem. C, 118, 8899−8906 (DOI: 10.1021/jp410716q)

[88] Hatano A., ltumiya T. , Ohba Y. (1991), New magnesium doping source for metalorganic chemical vapor deposition: Octamethyldialuminummonomagnesium, Appl. Phys. Lett., 58, 1488-1490 (DOI: 10.1063/1.105179)

[89] Mazalov A. V., Sabitov D. R., Kureshov V. A., Padalitsa A. A., Marmalyuk A. A., Akchurin R. K. (2016), Modern Electronic Materials, 2 , 45–47 (DOI: 10.1016/j.moem.2016.09.003)

[90] Chung S. J., Kumar M. S, Lee Y. S., Suh E-K., An M. H. (2010), J. Phys. D: Appl. Phys., 43, 185101 (4pp) (DOI: 10.1088/0022-3727/43/18/185101)

[91] Kang D. S., Cheong M. G., Lee S.-K., Suh E.-K., Hong C.-H., Lee H. J. (2004), Phys. Stat. Sol. (b), 241, 2759–2762 (DOI: 10.1002/pssb.200405115)

[92] Bhattacharyya G., Mahata A., Choudhuri I., Pathak B. (2017), Semiconducting phase in borophene: role of defect and strain, J. Phys. D: Appl. Phys., 50 405103 (13pp) (DOI: 10.1088/1361-6463/aa81b8)

[93] Ding Y., Wang Y. (2013), Density Functional Theory Study of the Silicene-like SiX and XSi_3 (X = B, C, N, Al, P) Honeycomb Lattices: The Various Buckled Structures and Versatile Electronic Properties, J. Phys. Chem. C, 117, 18266–18278 (DOI: 10.1021/jp407666m)

[94] Yun W. S., Lee J. D. (2017), Two-dimensional semiconductors ZrNCl and HfNCl: Stability, electric transport, and thermoelectric properties, Sci. Rep., 7, 17330 (DOI: 10.1038/s41598-017-17590-w)

[95] Topsakal M., Ciraci S. (2010), Elastic and plastic deformation of graphene, silicene, and boron nitride honeycomb nanoribbons under uniaxial tension: A first-principles density-functional theory study, Phys. Rev. B, 81, 024107 (DOI: 10.1103/PhysRevB.81.024107)

[96] Zhang S., Zhou J., Wang Q., Chen X., Yoshiyuki K., Jena P. (2015), Penta-graphene: A new carbon allotrope, Proc. Natl. Acad. Sci., 112, 2372-2377 (DOI: 10.1073/pnas.1416591112)

[97] Andrew R. C., Mapasha R. E., Ukpong A. M., Chetty N. (2012), Mechanical properties of graphene and boronitrene, Phys. Rev. B, 85, 125428 (1-9) (DOI: 10.1103/PhysRevB.85.125428)

[98] Wright K., Gale J. D. (2004), Interatomic potentials for the simulation of the zinc-blende and wurtzite forms of ZnS and CdS: Bulk structure, properties, and phase stability, Phys. Rev B, 70, 035211 (1-8) (DOI: 10.1103/PhysRevB.70.035211)

[99] Ding Y., Wang Y. (2013), Density Functional Theory Study of the Silicene-like SiX and XSi_3 (X = B, C, N, Al, P) Honeycomb Lattices: The Various Buckled Structures and Versatile Electronic Properties, J. Phys. Chem. C, 117, 18266–18278 (DOI: 10.1021/jp407666m)

[100] de Sousa J. M., Botari T., Perim E., Bizao R. A., Galvao D. S. (2016), Mechanical and Structural Properties of Graphene-like Carbon Nitride Sheets, RSC Adv., 6, 76915-76921 (DOI: 10.1039/C6RA14273G)

Chapter 5

Porphyrin Nanoribbon Based Spin Filtering Device

5.1. Introduction

In recent times, spintronics has gained enormous interests due to its advantage in transport properties, power consumption, and high dense memory circuits *[1]*. More specifically, developing materials with well-arranged spin structure and 100% spin polarization has become a fundamental concern in spintronics industry. Such 100% spin-polarization can occur in a special type of material named as half-metal due to the coexistence of the metallic nature for one spin orientation and semiconducting/insulating nature for the other spin orientation. Therefore, the importance of half-metals *[2]* for their potential use in spintronics device has been enlarged significantly and considerable effort has been made to search and develop for new half-metallic materials. Researchers have recently started to focus on main group-based systems because of their weak spin-orbit coupling which results in longer spin relaxation time and spin scattering length compared to metal-based systems *[2-3]*.

On the other side, one-dimensional nanostructure based materials, such as nanowires, nanotubes, and nanoribbons have drawn substantial attention lately due to their interesting electronic, physical and chemical properties *[4]*. Besides, their properties are extremely sensitive to their compositions *[4]*, and geometrical structures which results in a wide range of applicability in the domain of sensors, transistors and optoelectronics *[5]*. Therefore, it will be thought-provoking to explore the domain of spintronics with 1-D system such as nanoribbon based materials.

Magnetism, half-metallicity, and spin transport are most important properties for spintronics which have already been evidenced in graphene nanoribbon (GNR) by various contemporary theoretical researches *[6-8]*. Although GNR can be synthesized both by top-down (via lithography) and bottom-up (via epitaxial growth) approach *[9]*, several problems may arise during fabrication as reported by Xu and co-workers *[10]*. It has been reported that compared to conventional E-beam lithography (EBL), inorganic nanowire (INW) lithography can produce GNRs with smoother edges and INWs are perfect etch masks for the production of narrow GNRs with smooth edges *[10]*. However, precise alignment of INWs on a large area remains a problem *[10]*. On the other hand, with the recent advancement of technologies, 1D based nanostructures can be experimentally realizable by assembling simple molecular segments *[11]*.

Porphyrin molecules and its derivatives have been considered as a potential candidate for molecular devices due to their unique electronic structures and interesting properties such as long-range electron tunnelling *[12]*. Interestingly, charge transport properties of many porphyrin-based prototype devices have been studied theoretically and some fascinating properties, such as field effect characteristics, current switching, and current rectification have also been reported *[12]*.

Moreover, Cho and co-workers reported that porphyrin based one dimensional array can be fabricated by simple synthetic method *[13]*. For example, Zn based porphyrin array has already been experimentally synthesized and characterized by Osuka and co-workers *[14-15]*. Therefore, these previous reports open up a new possibility to realize a 1-D nanostructure assembling C=C embedded porphyrin unit via bottom-up approach since C=C embedded porphyrin unit has already been experimentally synthesized *[16]*. Here in this context, we would like to mention that, recently in 2015, a new C=C embedded porphyrin monolayer has been proposed theoretically and reported to be thermodynamically stable *[17]*. Hence, C=C embedded porphyrin 1-D nanodevice may be realized experimentally in near future. In addition to that, this C=C embedded porphyrin nanoribbon could be the first metal free spintronic device because all the other porphyrin-based spintronic devices reported till date *[12-13]*, are based on metal (Mn, Cr) embedded porphyrin units.

This idea motivated us whether magnetism and half-metallicity can be evidenced in metal-free C=C embedded porphyrin nanoribbon/array structures and can be utilized in molecular spintronics device. Fascinatingly, we have found some previous reports where the researchers have investigated the possibility of synthesis of porphyrin complexes with smaller atoms particularly boron and carbon *[16]*.

Specifically experimental investigation of some boron porphyrin complex containing B-B unit have been carried out such as unexpected formation of diborane from diborylporphyrin, synthesis of diboryl and diboranyl porphyrin complexes and synthesis of porphyrin complexes containing coordinated B-O-B groups *[18-21]*. Hence, it will be very motivating to investigate porphyrin nanostructure containing two centrally coordinated hetero atoms (carbon-boron) due to the novelty of such porphyrin unit. Moreover, replacing single carbon with boron among the two centrally coordinated carbons (-C=C-) may induce magnetism due to hole doping *[2]*. Here, in this work, we have investigated C=C embedded porphyrin nanoribbon/array for possible spintronics application via hole doping. Such hole doping can be achieved by substituting B and Al with one C atom in the C=C bond which can introduce magnetism in porphyrin-based nanoribbon/array. Thereafter, we have performed spin-polarized DFT calculations to predict the magnetism and half-metallicity in B and Al-doped porphyrin nanoribbon systems. Hereafter, porphyrin nanoribbon will be refereed as porphyrin array (PA). The detailed analysis of the origin of the magnetism and half-metallicity has been analyzed from the spin-polarized projected densities of states. Furthermore, the type of magnetism/magnetic exchange is also investigated for porphyrin array based systems. Additionally, our best system has been implemented in a molecular spintronic device where porphyrin molecular unit is placed between two Au (111) electrodes and spin-resolved electron transport properties and current-voltage (I-V) characteristics has been analyzed from the transmission function and non-equilibrium Green's function (NEGF) within DFT approach *[22-27]*.

5.2. Computational Methods

Spin-polarized density functional theory (DFT) calculations have been carried out for all the structures using projected augmented wave (PAW) pseudopotential method *[28-29]* as implemented in the Vienna ab initio Simulation Package (VASP) code *[29]*. We have used generalized gradient approximation (GGA) for describing accurately the electron-electron exchange and correlation energies of delocalized s and p electrons using the Perdew–Burke–Ernzerhof (PBE) functional *[30-31]*. The plane wave basis set with cut-off energy of 480 eV is used for describing the electron wave function. We have achieved self-consistency in all our calculations by setting the convergence tolerance to 10^{-6} eV/ Å for the total energy calculations. We have also relaxed both the lattice parameters and atomic positions until the Hellman−Feynman forces per atom are less than 0.005 eV/Å. The models of porphyrin arrays are constructed by cutting the C=C embedded porphyrin monolayer along *a* and *b* directions. The one-dimensional periodic boundary condition is applied along the nanoribbon axis and 15 Å vacuum spaces have been used along the two non-periodic directions to circumvent any interactions between periodic images.

Basically nanoribbons have dangling bonds at their edges which provide active sites for chemical bonding. Therefore, the nanoribbons are suitable for chemical modification *[32]*. Besides, the unique electronic properties (metallic/semiconducting/insulating) and magnetic properties (ferromagnetic/antiferromagnetic/half-metallic) of the nanoribbons are associated with their edge states, thus edge modification can drastically control electronic and magnetic properties of the nanoribbons *[32]*. In recent times, hydrogen and halogens were considered for edge functionalization of graphene and other nanoribbons to improve the stability of nanoribbon structure and to alter their electronic and magnetic properties *[33-34]*. Therefore, based on the earlier reports, we have considered hydrogen (H) and fluorine (F) for functionalization of our porphyrin array structures. The optimized lattice parameters of hydrogen (H) and fluorine (F) terminated arrays along *a* are (a = 8.41 Å) and (a = 8.43 Å) respectively. Similarly, we have observed lattice parameters of (b = 8.07 Å) and (b = 8.12 Å) for hydrogen (H) and fluorine (F) terminated arrays along b respectively. For geometry optimization, the first Brillouin zone of the unit cells of arrays periodic along '*a*' and '*b*' directions are sampled by Γ centred 13 × 1 × 1 and 1 × 13 × 1 K-point grids respectively. Further to this, for calculating their electronics properties, the Brillouin zones were sampled by 27 × 1 × 1 and 1 × 27 × 1 Γ centred K-point grids for the systems periodic along ‘a’ and ‘b’ direction respectively. We have doped single boron/aluminium atom (B/Al) at C-site of the C=C unit in the porphyrin array. The Bader charge analysis was performed using the Henkelman program *[35-38]* with a near-grid algorithm edge-refinement method to analyze the charge transfer process.

Energetic stability of B/Al doped H-terminated and F-terminated C=C embedded porphyrin nanoribbon are investigated from formation energy (E_F) calculation. The formation energy is calculated using the following equation *[2]*

$$E_F = \left(E_{B/Al@Porphyrin-NR} - E_{Porphyrin-NR}\right) - \left(\mu_{B/Al(Bulk)} - \mu_{C(Bulk)}\right) \quad (5.1)$$

Where $E_{B/Al@Porphyrin-NR}$ is the total energy of B/Al doped C=C embedded porphyrin nanoribbon, $E_{Porphyrin-NR}$ is the total energy of pure C=C embedded porphyrin nanoribbon, $\mu_{B/Al(Bulk)}$ is the chemical potential of B/Al atom from its bulk from α-rhombohedral boron/aluminium bulk BCC structure *[39, 40]* and $\mu_{C(Bulk)}$ is the chemical potential of C atom from graphene structure *[41]*.

Magnetic anisotropic energy (MAE) *[1]* is also calculated for our best system B doped C=C embedded porphyrin nanoribbon unit, i.e. $B@(C = C)_a^F - PA$ system to investigate the thermal stability of spin fluctuation upon external thermal energy. MAE *[42]* per unitcell is calculated including spin-orbit coupling (SOC) effect using the equation described below where E_{EA} is the energy of the system along easy axis when an external magnetic field is applied and E_{HA} is the energy of the system along hard axis under application of magnetic field. We have considered our calculation along magnetizing direction (100), (010), (110), (111) and (001).

$$MAE = E_{HA} - E_{EA} \quad (5.2)$$

Additionally, to comprehend the nature of electron spin density in B doped C=C embedded porphyrin monolayer; the spin density distribution (SDD) *[43]* is plotted. The SDD is calculated using the following equation

$$\rho_{SD} = \rho_{up} - \rho_{down} \tag{5.3}$$

Here, the up and down electron spin density are denoted as ρ_{up} and ρ_{down}, respectively. In the SDD, the up spin density of wave functions for different lobes are indicated by yellow colours and the down spin density of wave functions for different lobes are indicated by blue colours. The direct mapping of the electron spin density is measured experimentally by the neutron diffraction in electron spin resonance (ESR) spectroscopy.

Dynamic stability of our proposed system $B@(C=C)_a^F - PA$ is investigated from phonon frequency and phonon dispersion calculations. The phonon frequency calculations were performed using the density functional perturbation theory (DFPT) *[44]* as implemented in VASP, and phonon dispersion calculations were carried out using Phonopy code *[45]*. Furthermore, thermal stability of $B@(C=C)_a^F - PA$ system was verified by carrying out ab initio molecular dynamics simulations (AIMD) using a canonical ensemble at 300 K with a time step of 1 fs for 20 ps. The Nose´ thermostat model was used to control the temperature throughout the MD simulations *[46]*.

Moreover, we have modelled porphyrin-based nano-device for spin-filtering application where porphyrin array based unit was used as scattering region. We have used gold (Au (111)) nanowires as electrodes and central scattering region. After relaxation, thiol (-SH) groups are deprotonated and covalently connected to gold (Au) contact in the “atop” position. The Au-S bond distances are fixed at ~2.32 Å, and the Au contacts are modelled according to the Au nano-contact geometry *[22]*. We have used here the optimized structures of pure $[(C=C)_a^F - PA_n\ (n=1)]$ and B doped C=C embedded porphyrin

$[B@(C=C)_a^F - PA_n\ (n=1,2)]$ with edges terminated with fluorine (F) as our scattering region. Each Au unit cell has two sublayers of either three or seven Au atoms with periodic boundary conditions along the z-direction (transport direction). An extra seven-atom layer is inserted between the right electrode and the molecule to ensure the same attachment of the molecule to the left and right electrodes. We have used here the optimized structures of pure $[(C=C)_a^F - PA_n\ (n=1)]$ and B doped C=C embedded porphyrin $[B@(C=C)_a^F - PA_n\ (n=1,\ 2)]$ with edges terminated with fluorine (F) to model the metal-molecule-metal nanoscale devices. The proposed system is divided into three parts: left (L), right (R), and a central scattering region as shown in Fig. 5.1. Transport properties are computed by using the extended three-system model (Fig. 5.1). First principles DFT calculations are performed employing the SIESTA (Spanish Initiative for Electronic Simulations with Thousands of Atoms) code *[23]* within the generalized gradient approbation (GGA) with the Perdew, Burke, and Ernzerhof (PBE) functional for geometrical relaxation *[30]*. Norm-conserved Troullier-Martins pseudopotentials *[47]* are employed to describe the interaction between the core and valence electrons. The energy cut off for the real space grid is 150 Ry. To sample the Brillouin zone integration, we employed the gamma point sampling for the extended molecular region and a 1 × 1 × 50 within the Monkhorst-Pack scheme for electrodes with a double-ζ polarized basis set. The systems are fully relaxed by employing the conjugate gradient (CG) algorithm. The tolerance in density matrix difference is 0.0001 and the residual forces on the atoms are less than 0.01 eV/Å. The transmission function and I-V characteristics curves are computed within the framework of the Landauer-Buttiker methodology *[48-50]* by using the NEGF+DFT approach as implemented in TranSIESTA module of SIESTA code *[23]*.

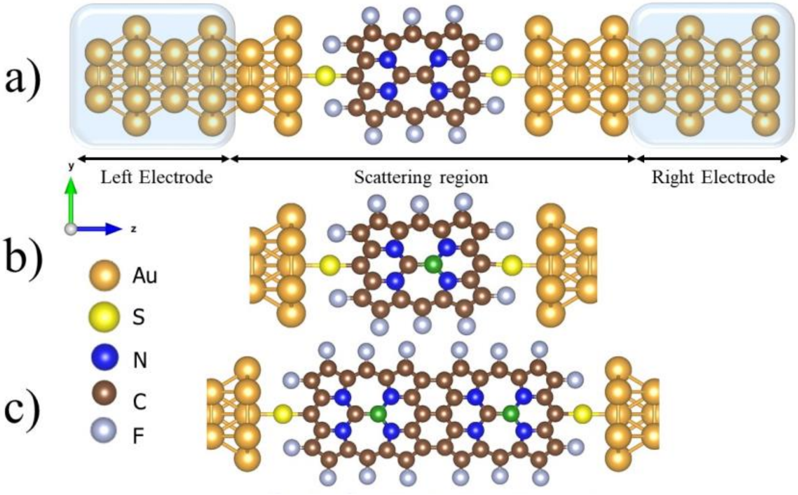

Figure 5.1: Schematic illustration of the proposed molecular nanoscale devices containing: (a) $[(C=C)_a^F - PA_n\ (n=1)]$, (b) $[B@(C=C)_a^F - PA_n\ (n=1)]$, and (c) $[B@(C=C)_a^F - PA_n\ (n=2)]$ units.

The transmission function, which defines the possibility of an electron to be transmitted from left electrode to right electrode through the central scattering region with specific energy (E), has been calculated form the given equation: *[23, 51]*

$$T(E,V) = tr[\mathit{\Gamma}_R(E,V)\mathcal{G}_C(E,V)\mathit{\Gamma}_L(E,V)\mathcal{G}_c{}^{\dagger}(E,V)] \tag{5.1}$$

Where $\mathcal{G}_C$ is the Green's function of the central scattering region and is the coupling matrix of L/R electrodes. Further, the integration of transmission function provides the electric current as by given equation: *[23, 51]*

$$I(V_b) = \frac{2e}{h}\int_{\mu_R}^{\mu_L} T(E,V_b)\,[f(E-\mu_L) - f(E-\mu_R)]dE \tag{5.2}$$

Where $T(E,V_b)$ is to represent the transmission spectrum of the electrons entering at energy (E) from L to R electrode in presence of an applied finite bias voltage V_b, $f\left(E - \mu_{\mathrm{L,R}}\right)$ is showing the Fermi-Dirac distribution of electrons in the L and R electrodes and $\mu_{\mathrm{L,R}}$ the chemical potential where $\mu_{\mathrm{L/R}} = E_F \pm V_b/2$ are moved correspondingly up and down according to the Fermi energy E_F *[23, 51]*.

5.3. Results and Discussion:

5.3.1. C=C embedded porphyrin MLs/PAs:

Our methodical study begins with the C=C embedded porphyrin monolayer and its geometric optimization. The C=C embedded porphyrin monolayer consists of 22 C atoms and 4 N atoms in its unit cell. This unit cell contains two covalently bonded (π-overlapping) C=C unit, which covalently bonded with four N atoms surrounding to it. The optimized lattice parameters of the rectangular unit cell are found as 8.52 Å and 8.11 Å which match with an earlier theoretical report (8.53 Å and 8.11 Å) *[17]*. The of C-C bond length of the C=C unit in the monolayer is computed as 1.39 Å which is slightly higher than the previously reported theoretical value of 1.38 Å in (C=C)tetra-*p*-tolylporphyrin system (calculated by B3LYP/6-31G(d)) and experimental value of 1.35 Å *[16]* and this could be due to the enlargement of C=C bond because of the periodic arrangement in the monolayer *[17]*.

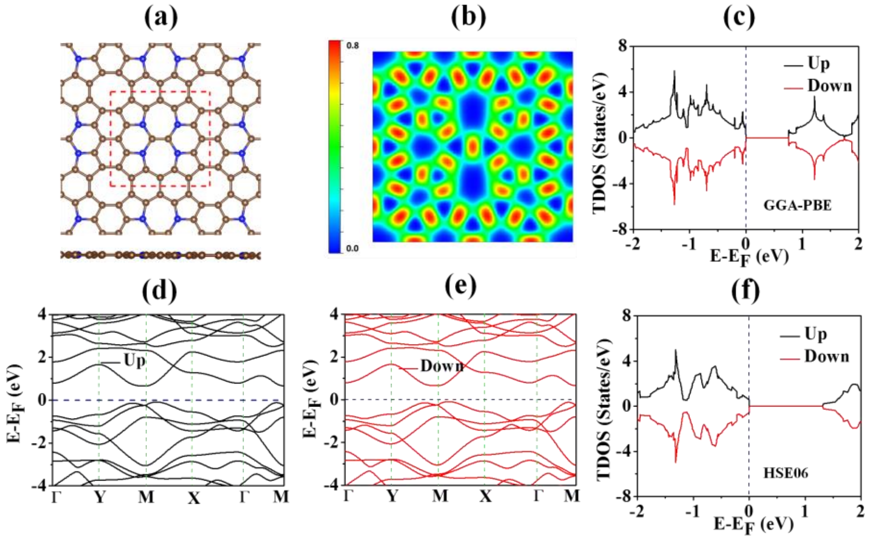

Figure 5.2: (a) Top view of C=C embedded porphyrin monolayer with unit cell showing in the red dotted line, (b) Electron localization function (ELF; maximum saturation level 0.8 e Å^{-3}, minimum saturation level 0.0 Å^{-3}), (c)-(e) Spin-polarized density of states and bandstructure of C=C embedded porphyrin monolayer calculated by GGA-PBE, (f) Spin-polarized density of states of C=C embedded porphyrin monolayer calculated by HSE06.

The spin-polarized density of states and band structure (GGA-PBE) of this monolayer exhibits a band gap of 0.76 eV (Fig. 5.2). The pattern of spin-polarized bandstructure (GGA-PBE) also matches with the previously reported bandstructure (HSE06). Further to this, we have also calculated the electronic properties such as density of states (DOS) using HSE06 functional *[52]*. The calculated value of band gap using HSE06 (1.27 eV) also matches with earlier theoretical reports (1.14 eV). The contour electron localization function (ELF) plot (Fig. 5.2) shows a strong covalent character of C-N and C-C bond. Furthermore, H- and F-functionalized porphyrin arrays are investigated for their possible magnetic properties. It has been observed that none of the functionalized arrays exhibits magnetic properties due to their symmetric spin-polarized density of states (Fig. 5.3).

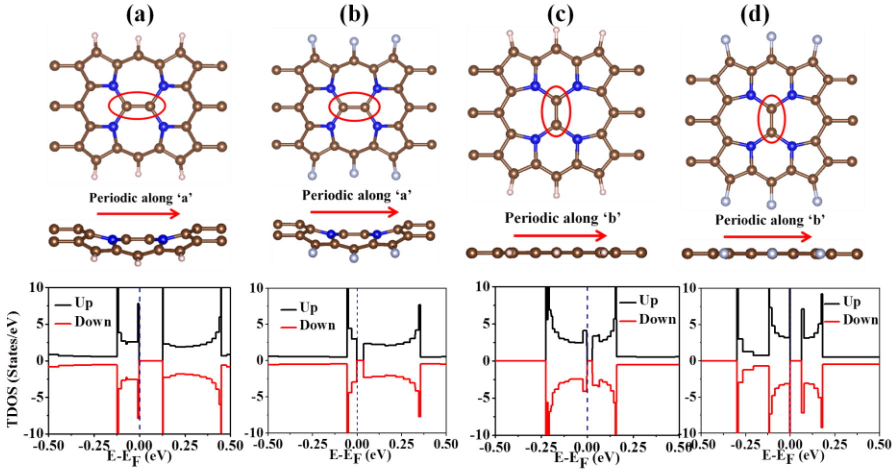

Figure 5.3: Optimized structures and spin-polarized density of states of (a) $(C=C)_a^H - PA$, (b) $(C=C)_a^F - PA$, (c) $(C=C)_b^H - PA$ and (d) $(C=C)_b^F - PA$ systems. The Fermi level is set to zero and is indicated by a blue dashed line. The C, N, H and F atoms are denoted by brown, blue, white and light gray colours.

Hereafter, H-terminated and F-terminated array along *a* will be referred to as $(C=C)_a^H - PA$ and $(C=C)_a^F - PA$ respectively. Similarly, H-terminated and F-terminated array along *b* will be referred as $(C=C)_b^H - PA$ and $(C=C)_b^F - PA$ respectively. Here, 'PA' represents porphyrin array. The best system among these four systems is considered for spin-filtering device which is analyzed further in section 5.3.8 and 5.39.

5.3.2. Introduction of magnetism and half-metallicity in C=C embedded PA:

Our spin-polarized calculations reveal that undoped C=C embedded PAs are non-magnetic. Thus, we attempt to design a novel metal free porphyrin array with two hetero atoms (C and B) embedded porphyrin array rather than one single atom embedded system. For this, we have substituted one carbon atom with boron among the two carbon in C=C unit and further investigated the possibility of magnetism and half-metallicity. Although the porphyrin unit containing C-B unit in its centre has not been synthesized yet, porphyrin unit with C=C in its centre has been synthesized *[16]*, and it is also reported that boron is one of the atoms that can replace carbon from its lattice very efficiently *[53]*. Therefore, it will be very fascinating to investigate the electronic and magnetic properties of C-B contained porphyrin nanostructures. The possible method regarding synthesization of B doped C=C embedded porphyrin array has been discussed in section 5.3.5.

First, we have performed B doping in C=C embedded porphyrin unit for all the arrays as we believe the doping of B at C-site may introduce magnetism in the nanostructure. Hereafter, B doped various PAs will be referred as $@(C=C)_a^H-PA$, $B@(C=C)_a^F-PA$, $B@(C=C)_b^H-PA$ and $B@(C=C)_b^F-PA$ and these B-doped nanostructures exhibit magnetism with magnetic moments of 0.4126 μB, 1.00 μB, 1.00 μB and 1.00 μB respectively. The spin polarized density of states (Fig. 5.4 & 5.5) show that only $B@(C=C)_a^F-PA$, $B@(C=C)_b^H-PA$ hold half-metallicity. The respective spin densities are shown in Fig. 5.6. Spin-polarized density of states and magnified density of states of $B@(C=C)_b^H-PA$ and $B@(C=C)_b^F-PA$ indicates (Fig. 5.5) that only $B@(C=C)_b^H-PA$ is half-metallic in nature. However, $B@(C=C)_a^F-PA$ has more robust half-metallicity (spin-down gap 0.37 eV; Fig. 5.4) than that of $B@(C=C)_b^H-PA$ (spin-up gap 0.21

eV).Therefore, we have mainly concentrated on $B@(C=C)_a^F-PA$ system for our detailed study among all the B doped arrays.

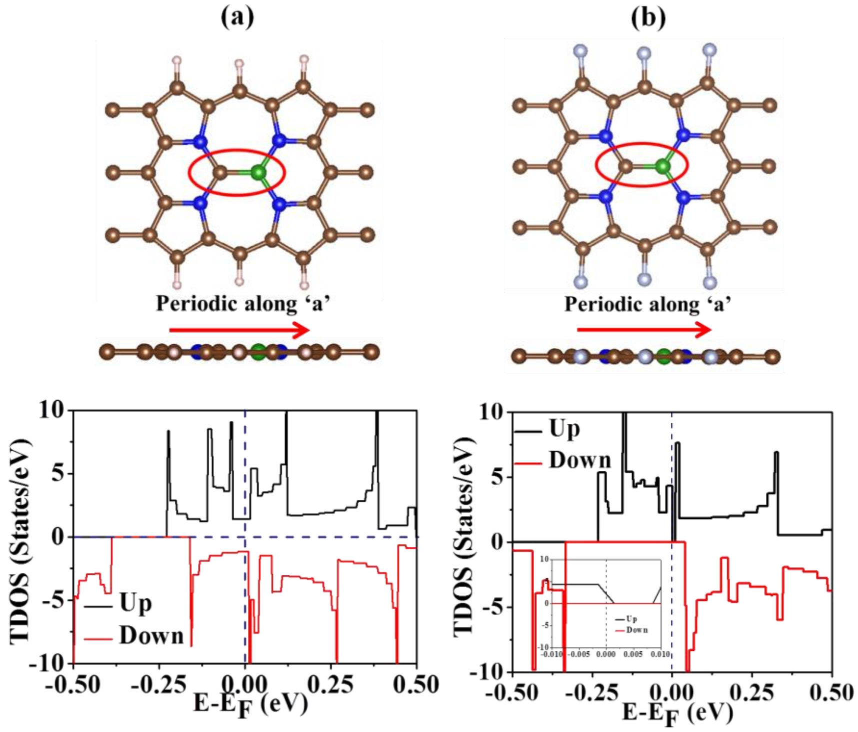

Figure 5.4: Optimized structures and spin-polarized density of states of (a) $B@(C=C)_a^H-PA$ and (b) $B@(C=C)_a^F-PA$ systems along with the magnified spin-polarized density of states (in the inset) around the Fermi level. The Fermi level is set to zero and is indicated by a blue dashed line. The B, C, N, H and F atoms are denoted by green, brown, blue, white and light gray colours.

Now, further we have analysed the probable reason of observing half-metallicity only in fluorinated nanoribbon rather than hydrogenated one. Although both of the undoped porphyrin array $(C=C)_a^H-PA$ and $(C=C)_a^F-PA$ systems are semiconducting with a similar density of states (DOS) pattern (Fig. 5.3a-b), doping B atom replacing C atom results introduction of half-metallicity only in $B@(C=C)_a^F-PA$ system. To analyze the origin of half-metallicity in $B@(C=C)_a^F-PA$ system, we have plotted the partial density of states for both the two systems $B@(C=C)_a^H-PA$ and $B@(C=C)_a^F-PA$ (Fig. 5.7).

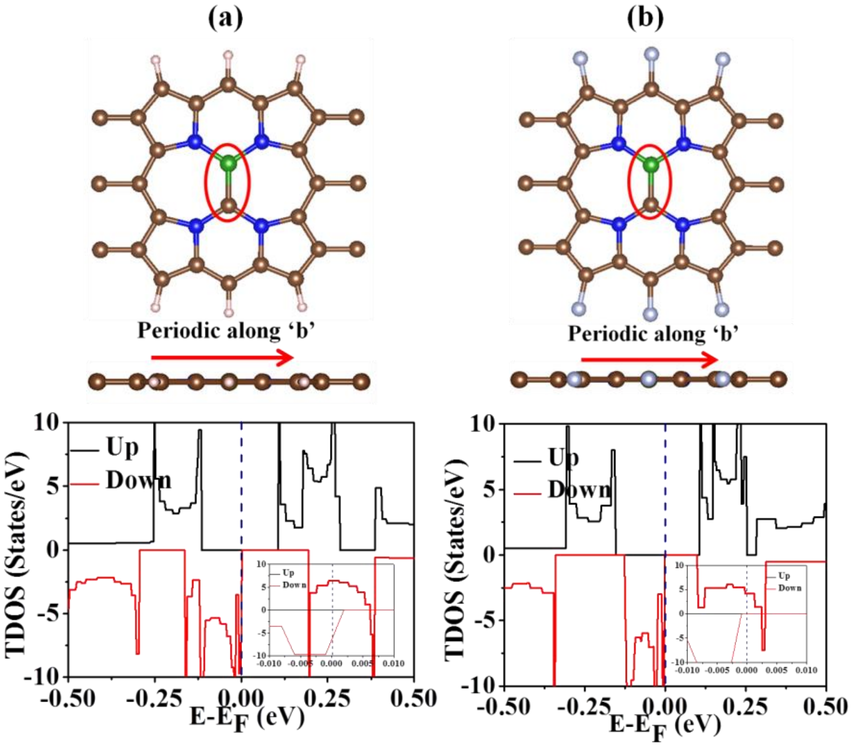

Figure 5.5: Optimized structures and spin-polarized density of states along with the magnified spin-polarized density of states (in the inset) around the Fermi level of (a) $B@(C=C)_b^H-PA$ and (b) $B@(C=C)_b^F-PA$ systems. The Fermi level is set to zero and is indicated by a blue dashed line. The B, C, N, H and F atoms are denoted by green, brown, blue, white and light gray colours.

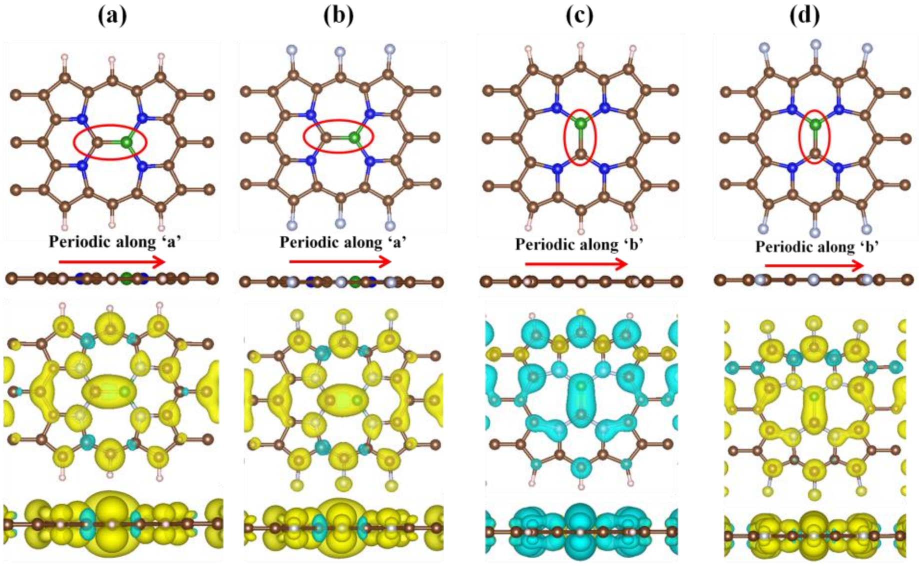
(a)
(b)
(c)
(d)
Periodic along 'a'
Periodic along 'a'
Periodic along 'b'
Periodic along 'b'

Figure 5.6: Spin density distribution of (a) $B@(C=C)_a^H-PA$, (b) $B@(C=C)_a^F-PA$, (c) $B@(C=C)_b^H-PA$ and (d) $B@(C=C)_b^F-PA$ systems.

B doping in $(C=C)_a^H-PA$ destabilizes both the spin-up and spin-down states near the Fermi level, thus introduces metallic nature in the system. However, B doping in $(C=C)_a^F-PA$ system only destabilizes only the spin-up states, while stabilizes the spin-down states leading to half-metallicity in $B@(C=C)_a^F-PA$ system.

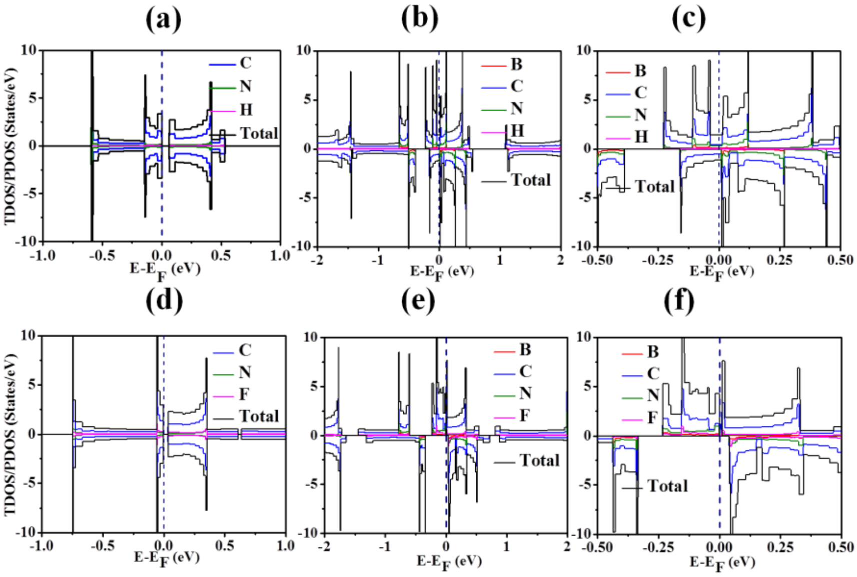

Figure 5.7: Total and partial density of states of (a) $(C=C)_a^H-PA$, (b) $B@(C=C)_a^H-PA$ and (c) magnified partial density of states of $B@(C=C)_a^H-PA$ system. Total and partial density of states of (d) $(C=C)_a^F-PA$, (e) $B@(C=C)_a^F-PA$ and (f) magnified partial density of states of $B@(C=C)_a^F-PA$ system. The Fermi level is set to zero and is indicated by a blue dashed line.

Similar to single B-doped nanoribbons, we have also investigated single Al-doped nanoribbons as well as porphyrin nanoribbons containing B-B unit in its centre. We have found that single Al-doped nanoribbon systems [$Al@(C=C)_a^H-PA$, $Al@(C=C)_a^F-PA$, $Al@(C=C)_b^H-PA$ and (b) $Al@(C=C)_b^F-PA$] also exhibits magnetism with magnetic moments of 0.0085 μB, 1.00 μB, 1.00 μB and 0.2077 μB respectively. Spin polarized density of states and spin density distribution of Al-doped systems are shown in Fig. 5.8 and Fig. 5.9 which indicates that, none of the Al-doped nanoribbons holds half-metallic characteristics except $Al@(C=C)_b^H-PA$ (Fig. 5.8).

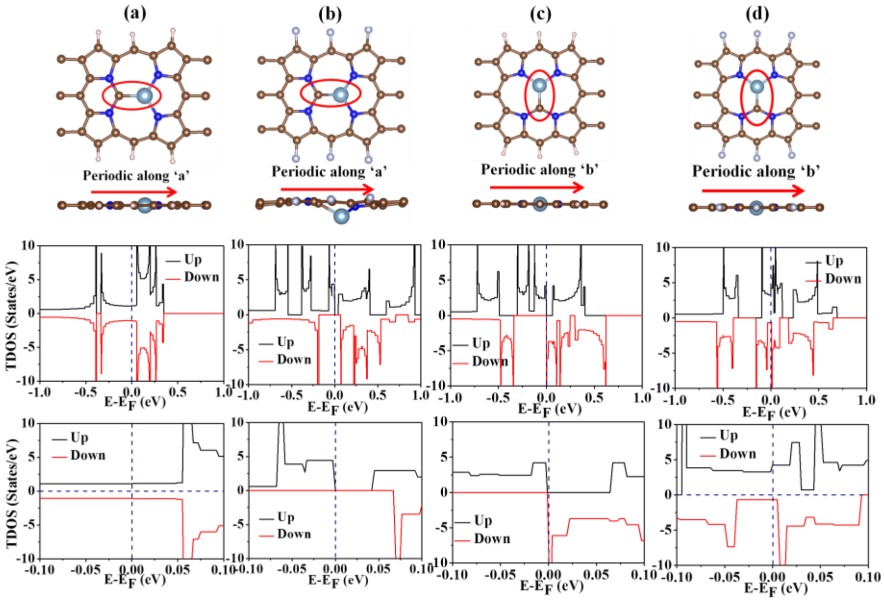

Figure 5.8: Optimized structures, spin polarized density of states and magnified spin polarized density of states (third panel) of (a) $Al@(C=C)_a^H-PA$, (b) $Al@(C=C)_a^F-PA$, (c) $Al@(C=C)_b^H-PA$ and (d) $Al@(C=C)_b^F-PA$ systems. The Fermi level is set to zero and is indicated by a blue dashed line. The Al, C, N, H and F atoms are denoted by sky blue, brown, blue, white and light gray colors.

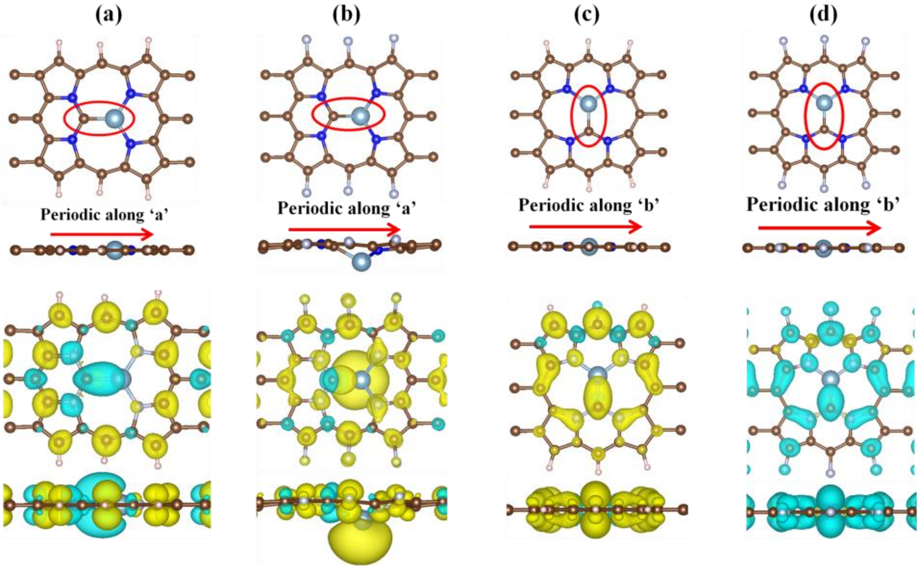
(a)
(b)
(c)
(d)
Periodic along 'a'
Periodic along 'a'
Periodic along 'b'
Periodic along 'b'

Figure 5.9: Spin density distribution of (a) $Al@(C=C)_a^H - PA$, (b) $Al@(C=C)_a^F - PA$, (c) $Al@(C=C)_b^H - PA$ and (d) $Al@(C=C)_b^F - PA$ systems.

However, $Al@(C=C)_b^H - PA$ shows very weak half-metallicity (spin-up gap: 0.064 eV) compared to $B@(C=C)_a^F - PA$ system (spin down gap 0.37 eV).

Furthermore, our spin-polarized calculation reveals that porphyrin nanoribbon with B-B unit in its centre does not exhibit half-metallicity (Fig. 5.10). However, only $(B-B)_a^F - PA$ and $(B-B)_b^F - PA$ systems exhibits magnetism with total magnetic moment of 0.307 and 1.0769 μB. Spin density distributions of porphyrin nanoribbon containing B-B unit have been incorporated in the Fig. 5.11.

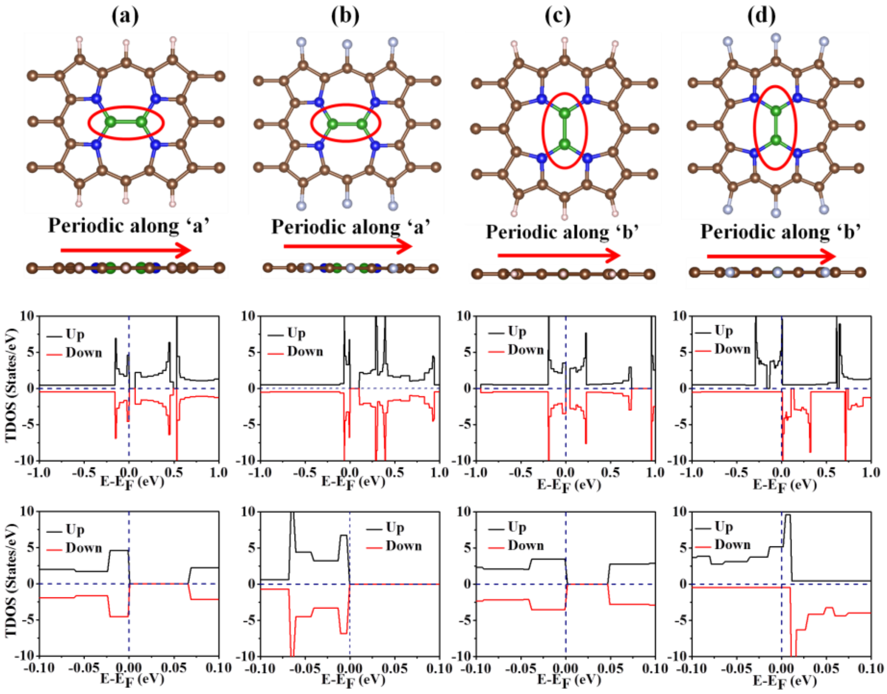

Figure 5.10: Optimized structures, spin polarized density of states and magnified spin polarized density of states (third panel) of (a) $(B-B)_a^H - PA$, (b) $(B-B)_a^F - PA$, (c) $(B-B)_b^H - PA$ and (d) $(B-B)_b^F - PA$ systems. The Fermi level is set to zero and is indicated by a blue dashed line. The B, C, N, H and F atoms are denoted by green, brown, blue, white and light gray colours.

Moreover, we have also tried to achieve magnetism and half-metallicity in C=C embedded porphyrin unit based monolayer system with elemental doping (B, Al, B-B). However, all these systems are found to be non-magnetic (Fig. 5.12) and thus we have not discussed much detail about these systems.

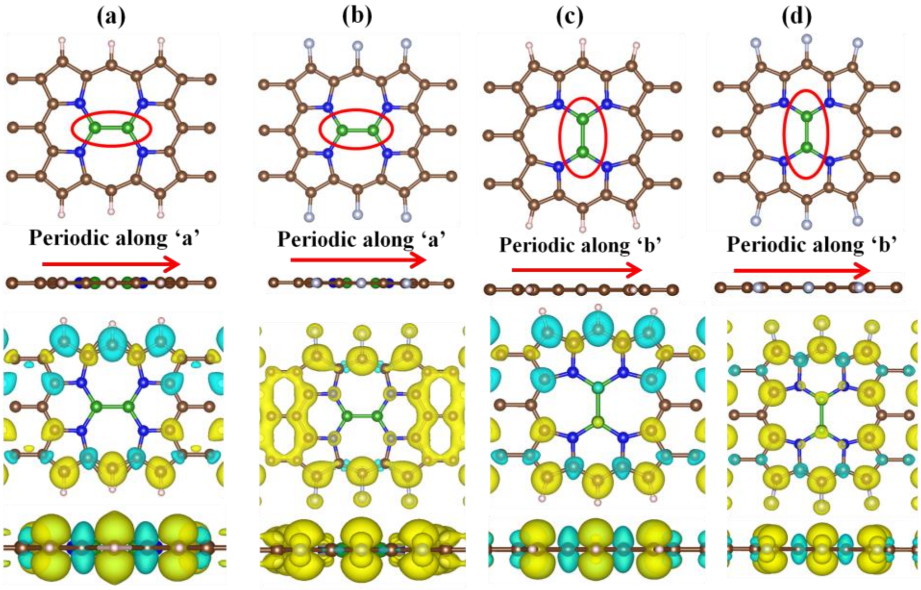

Figure 5.11: Spin density distribution of (a) $(B-B)_a^H - PA$, (b) $(B-B)_a^F - PA$, (c) $(B-B)_b^H - PA$ and (d) $(B-B)_b^F - PA$ systems.

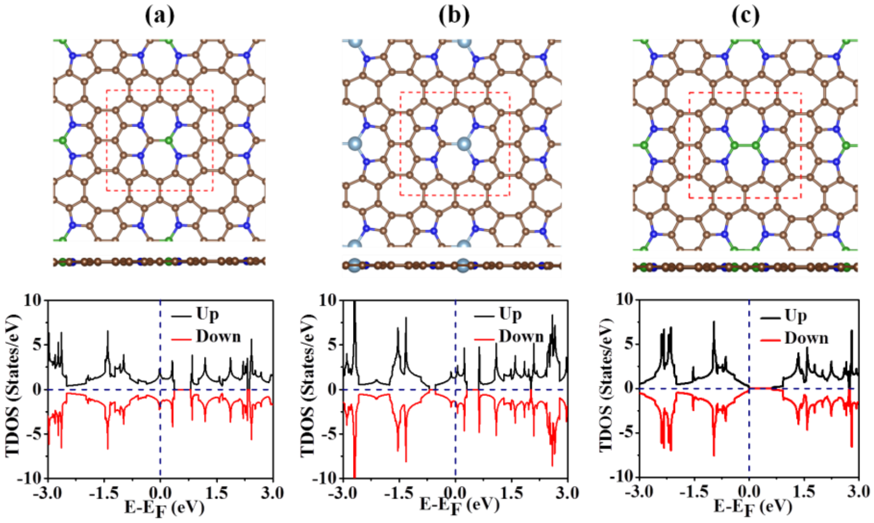

Figure 5.12: Optimized structures and spin polarized density of states of (a) B doped, (b) Al doped, and (c) two B doped C=C embedded porphyrin monolayer systems (unit cell is shown in the red dotted line).

5.3.3. Energetic stability of B and Al-doped C=C embedded PA:

Our stability analysis of the nanostructures begins with energetic stability analysis. To evaluate the stability of these systems we have calculated formation energy values of these doped systems. The formation energy values of B and Al-doped systems are given in Table 5.1 where nature of the systems are indicated as M (Metallic), SHM (Strong Half-metallic), WHF (Weak Half-metallic) and S (Semiconducting). It has been found that the formation energies of the B-doped nanoribbon systems are lower than the Al-doped nanoribbons. A negative value of formation energies indicates that formations of B-doped nanoribbons are thermodynamically favourable. Interestingly, it has been also found that B-doped C_3N monolayer has negative formation energy (-1.54 eV/atom) where C has been replaced by B atoms similar to our case *[54]*. Moreover; the possibility of B-doping in C-matrix has also been discussed in earlier experimental reports *[54-55]*. Among all the B doped arrays, $B@(C=C)_a^F - PA$ has half-metallic character and formation energy of -2.59 eV/atom. Therefore we can also conclude the possibility of realization of our proposed $B@(C=C)_a^F - PA$ structure.

Table 5.1: Formation energies per dopant (E_F), magnetic moments per dopant (μB), nature of the system and spin gap (eV) for the B and Al doped C=C embedded PA

System	E_F (eV/atom)	Magnetic moment (μB)	Nature	Spin Gap (eV)
$B@(C=C)_a^H - PA$	-2.50	0.4126	M	0
$B@(C=C)_a^F - PA$	-2.59	1.0000	SHM	0.37
$B@(C=C)_b^H - PA$	-2.84	1.0000	WHM	0.21
$B@(C=C)_b^F - PA$	-2.97	1.0000	S	-
$Al@(C=C)_a^H - PA$	3.11	0.0085	M	0
$Al@(C=C)_a^F - PA$	2.82	1.0000	S	-
$Al@(C=C)_b^H - PA$	3.05	1.0000	WHM	0.06
$Al@(C=C)_b^F - PA$	2.92	0.2077	S	-

5.3.4. Dynamic and thermal stability of B doped C=C embedded PA:

Further to this, we have analyzed dynamic and thermal stability (Fig. 5.13) through phonon dispersion calculations and ab initio molecular dynamics (AIMD) simulation, respectively. Phonon dispersion calculation of $B@(C=C)_a^F - PA$ reveals that our system has small imaginary frequencies. To be precise, there are three imaginary frequencies with the values of 0.15, 1.29 and 30.72 cm^{-1} respectively. Analysis of phonon frequency discloses that these imaginary modes do not originate from any non-trivial motion of atoms against each other rather the first two modes (0.15, 1.29 cm^{-1}) originate from pure translational motion and the third mode (30.72 cm^{-1}) originates from bending motions of a group of atoms (Fig. 5.13d-f). Moreover, we have found that undoped fluorinated array also exhibits slight imaginary frequencies (4.00 cm^{-1}) in its phonon dispersion plot (Fig. 5.14). Any non-trivial motion of atoms against each other is an actual sign of unstable mode *[56]*, thus it can be stated that our system $B@(C=C)_a^F-PA$ is not dynamically unstable and it may be stabilized after connecting to electrodes while making spin-filtering device.

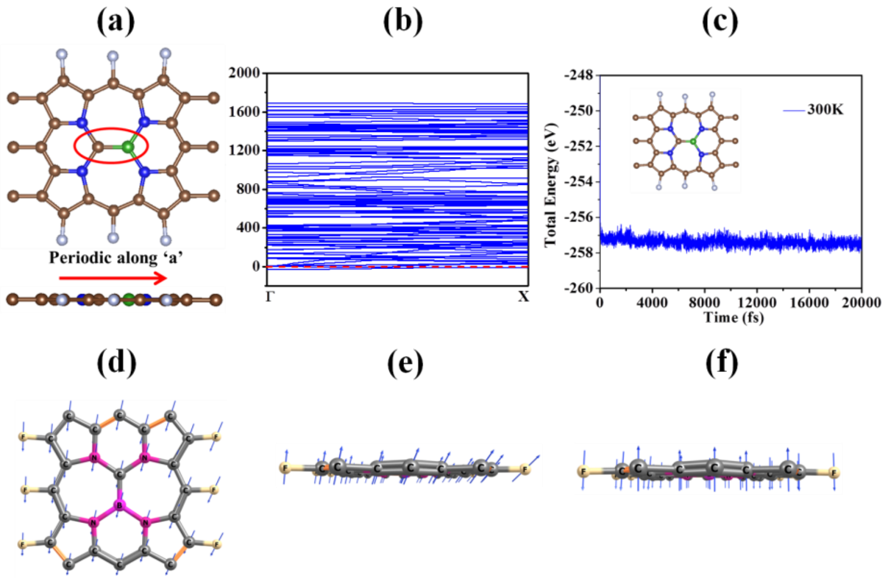

Figure 5.13: (a) Optimized structures, (b) phonon dispersion plot and (c) total energy fluctuation of AIMD simulations of $B@(C=C)_a^F-PA$ system. Displacement eigenvectors (indicated by blue arrows) corresponding to the soft phonon mode with imaginary frequencies of (d) 0.15 cm^{-1}, (e) 1.29 cm^{-1} and (f) 30.72 cm^{-1} of $B@(C=C)_a^F-PA$ system.

Thermal stability of $B@(C=C)_a^F-PA$ is analyzed by ab initio molecular dynamics (AIMD) simulation using an NVT ensemble at 300 K with a time step of 1 fs (femtosecond) for 20 ps (picoseconds).

Room temperature AIMD simulation does not show any possibility of inter-conversion of the optimized structure (Fig. 5.13c). Thus, it can be stated that our system $B@(C = C)_a^F - PA$ is thermally stable.

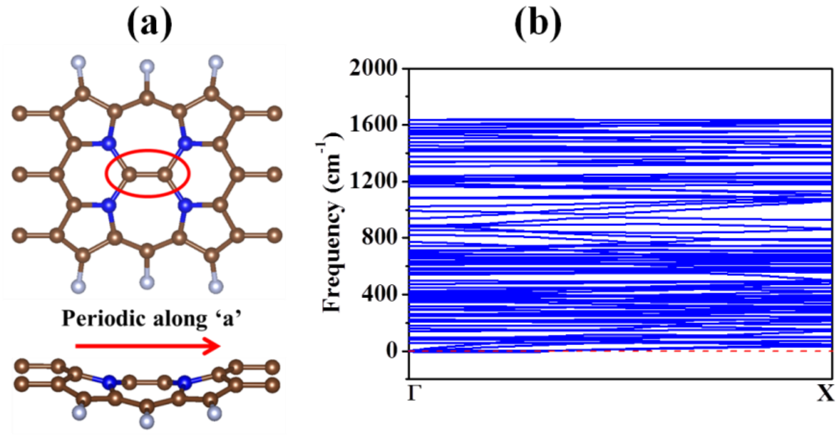

Figure 5.14: Optimized structure and phonon dispersion plot of $(C = C)_a^F - PA$ system.

5.3.5. Possibility of an experiential realization of B doped C=C embedded PA:

Elemental boron (B) and nitrogen (N) have already been attracted researcher's attention as dopant for graphene due to their similar atomic radii like carbon (C) *[54]*. Boron doped graphene has been also synthesized by several research groups using different approaches *[54]*. Most widely used method for the synthesis of B doped graphene is solid state reaction between graphite powder or GO and a boron precursor mainly H_3BO_3, B_2O_3 or B_4C and subsequently exfoliation of single B-G sheets *[57-58]*. B doped graphene nanoribbons have also been synthesized experimentally by Kawai *et al.* *[59]* and Xing *et al.* *[60]* using a separate method. Moreover, it is also mentioned that porphyrin complexes with smaller atoms (like boron (B) and carbon-carbon (C=C)) bonded to nitrogen (N) have been synthesized *[16]*.

In recent past, Brothers *et al.* also explored experimental synthesization of boron porphyrin complexes *[61]*. Therefore, we believe that B doped C=C embedded porphyrin nanoribbon may be synthesized in the near future.

5.3.6. Introduction of magnetism in B doped C=C embedded PA:

To analyze the origin of magnetism, we have investigated spin density distribution (Fig. 5.15a-c) as well as the density of states (Fig. 5.15d-f) of $B@(C=C)_a^F - PA_n$ system, where ‘n’ is length of nanoribbon. We have also increased the length of the nanoribbon with n = 1, 2, and 3. It has been observed that magnetic moments are distributed over all the atoms in the nanoribbon/array (Fig. 5.15). Although local moment magnetism has been studied and understood well, area of itinerant moment magnetism along with half-metallic property has not been gained progress so far compared to the earlier one *[62]*.

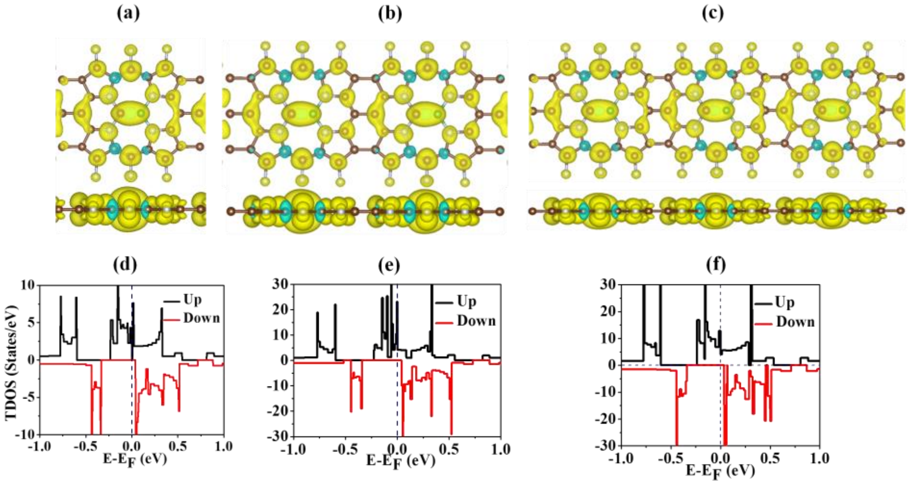

Figure 5.15: (a)-(c) Spin density distribution (SDD) of $B@(C=C)_a^F - PA_n$ system (where n=1, 2, 3 respectively) and (d)-(f) total density of states of $B@(C=C)_a^F - PA_n$ system (where n=1, 2, 3 respectively).

Most of the practical system generally exhibits a behaviour which is intermediate between local-itinerant moment extremes. In the local moment magnetism, the magnetism is arising from partially-filled electrons shells of ions, which can be understood by real-space localized magnetic moments and fluctuations *[62]*. These collective behaviours of local moments were accurately predicted by intra-atomic exchange interaction I along with a mean molecular field (introduced by Weiss within the framework of Heisenberg model) which is proportional to average magnetization M. Most of the magnetic system fit well into this mean-field scenario; however, the remarkable deviation has been observed in itinerant magnetism (e.g. intermetallic materials) due to the enhancement of interaction between conduction electrons *[62]*. We have also observed a strong interaction between conduction electrons in our system which drove the system into itinerant magnetism. In this case of itinerant magnetism, I is regarded as inter-atomic coupling constant and spontaneous splitting of energy bands gives rise to the itinerant magnetic moment where moments and fluctuation are localized in reciprocal space *[62]*.

Itinerant magnetism was modelled by Stoner criterion *[63]*, in which a large density of states $\rho(E_F)$ arise at Fermi level (E_F) and large coupling constant I is observed, which can predict the long-range magnetic order below the ordering temperature. Our spin-density and density of states suggest (Fig. 5.15) that our system also follows the Stoner criterion of magnetism since it has a large density in the spin-up channel at the Fermi level.

The strength of magnetism (i.e how “strong” or “weak” the magnetism is) is determined by the magnitude of the $n_{\uparrow} - n_{\downarrow}$ difference. In our system, we have already observed a large spin density difference from the spin density distribution which is also supported by the total density of states. In fact, all the conduction electrons in our systems are coming from the spin-up states, thus introducing half-metallicity. Hence, our system is a perfect example of strong itinerant ferromagnetism (IFM). Even though the magnetic moment is distributed in our system, partial magnetic moment and Bader charge analysis reveals (Table 5.2) that the main contribution of magnetism is coming from the carbon (C) and the two nitrogen atoms (N) bonded to the boron atom (B). While TM metal based strong IFM system has been reported earlier literature *[64]*, very few metal free itinerant ferromagnetic system has been reported so far *[65]*. Thus, half-metallic B doped C=C embedded nanoribbon will be exciting for spintronics application. Throughout our calculation, we have considered a simple collinear model of magnetism in which the spin-component is decomposed into two components such as spin-up and spin-down.

However, in the presence of spin-orbit coupling (SOC), orientation spin components cannot be simply treated as spin-up and spin-down. Therefore, to further check the effect of spin-orbit coupling (SOC) for our system, we have considered the SOC effect and calculated magnetic anaisotropic energy (MAE) for our system. The small value of magnetic anisotropy energy (0.05 μeV) indicates (Table 5.3) very weak spin-orbit coupling in our system which also confirms the long spin-relaxation time for our system. Thus, it can be concluded that collinear model of magnetism is sufficient to predict our system correctly.

Table 5.2: Bader charge analysis of pure $(C=C)_a^F-PA$ and B doped $B@(C=C)_a^F-PA$

Net Effective Charge in System $(C=C)_a^F-PA$	**Net Effective Charge in System** $B@(C=C)_a^F-PA$
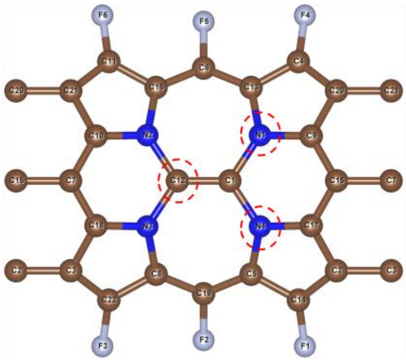	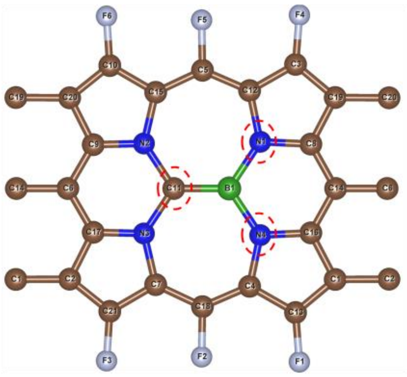
C_{12}=+0.6888|e|, N_1=-1.1692|e|, N_4=-1.1836|e|	C_{11}=-0.1022|e|, N_1=-1.4814|e|, N_4=-1.4729|e|

Table 5.3: Summary of magnetic anisotropy energies in μeV/vacancy and the easy axis for $B@(C=C)_a^F-PA$ system

$B@(C=C)_a^F-PA$	**Easy Axis (100)**	**(001)-(100)**	**(010)-(100)**	**(110)-(100)**	**(111)-(100)**
	0	0.04 μeV	0.03 μeV	**0.05 μeV**	0.02 μeV

Curie temperature of any magnetic material is very important parameter for its practical application. Thus, we have also calculated

Curie temperature for our $B@(C=C)_a^F - PA$ system. However, Monte Carlo simulation based on local magnetiam model is not appropriate for itinerant magnetic system *[66]*. Therefore we have gradually increased the Gauss smearing factor to investigate the effect of temperature (K_BT) on magnetic moment of our system. Gauss smearing factor is related to the temperature by the equation $\sigma = K_BT$. As the smearing factor increases, the temperature also increases, which enhances the thermal excitation and thus eventually weaken the magnetic moments. Therefore, at a certain temperature magnetic moment becomes zero, results in the Curie transition. We have also plotted (Fig. 5.16) the variation of magnetic moments with increasing smearing factor (σ). It has been observed from this plot that the magnetic moment decreases from 0.6340 μB to 0.00 μB when the smearing factor (σ) increases from 0.05 to 0.06 respectively. Therefore, the Curie temperature for our system $B@(C=C)_a^F - PA$ may lie in between 580.23 K to 696.27 K. Therefore, our system can be very useful for high temperature spintronics application.

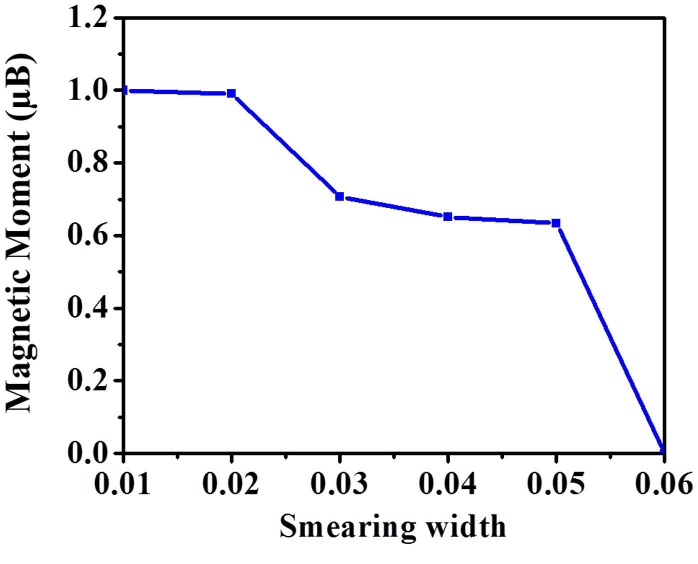

Figure 5.16: Variation of magnetic moments in $B@(C=C)_a^F - PA$ with increasing smearing factor (σ).

5.3.7. Effect of strain on magnetism and half-metallicity in B doped C=C embedded PA:

Strain technology is very crucial to understand the fundamental nature of the chemical bonding and the effects of lattice distortion on the structural, electronics and magnetic properties since electronic and magnetic properties can be altered with the application of strain. Moreover, it is also important for any material to sustain strain because synthesization of material for practical application generally introduces stress in that material due to structural modification. It is also very vital to analyze the effect of strain on magnetism and half-metallic properties on $B@(C=C)_a^F-PA$ for its practical application. Therefore, we have applied both uniaxial tensile and compressive strain ranging from 1% to 5% to scrutinize the nature of the system and the modulation of the spin-up gap in $B@(C=C)_a^F-PA$ system.

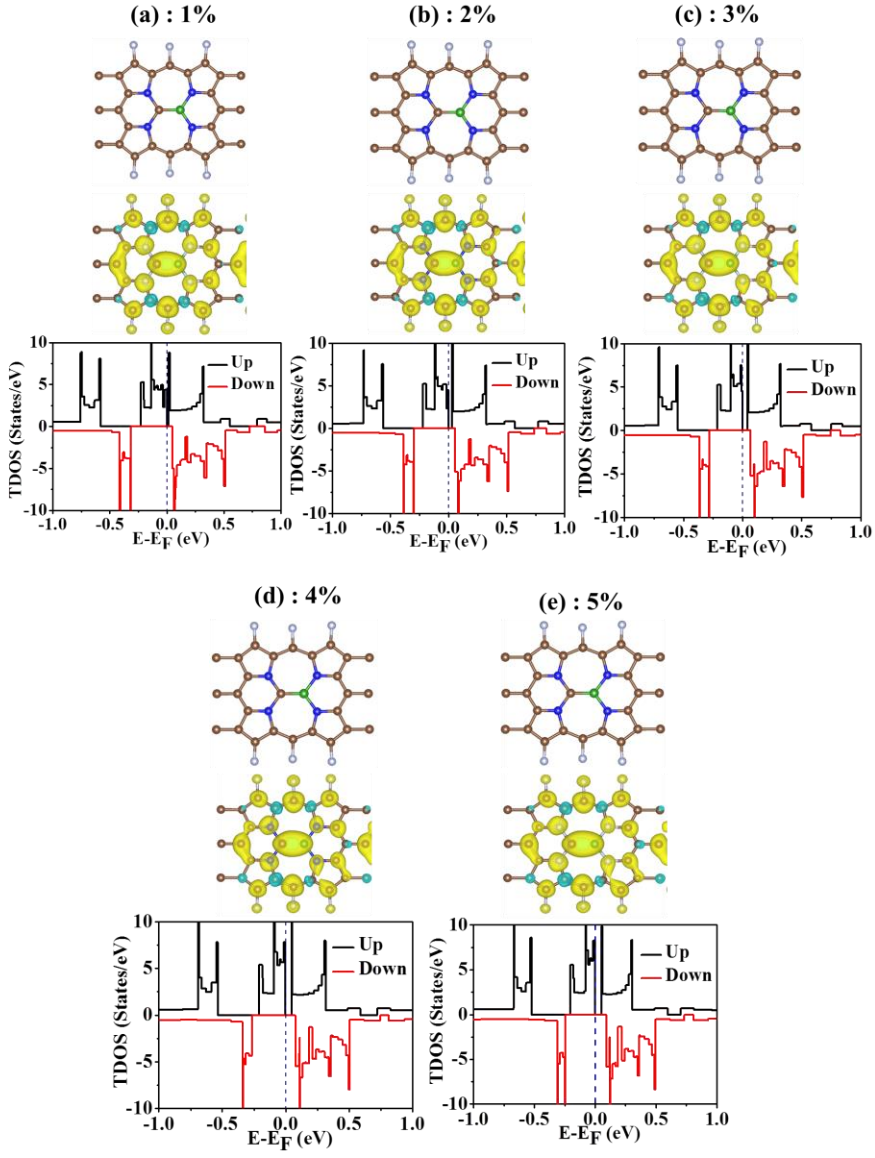

Figure 5.17: (a)-(e) Optimized structure, spin density distribution and TDOS plot of $B@(C=C)_a^F - PA$ under the application of uniaxial tensile strain from 1% to 5%.

It has been observed that our system only holds its half-metallic characteristics under 2% and 3% uniaxial tensile strain. Under uniaxial compressive strain, our system became semiconducting at lower % of strain (1% - 2%), and then we observe a semiconducting to metallic phase transition which continues up to 5% applied strain.

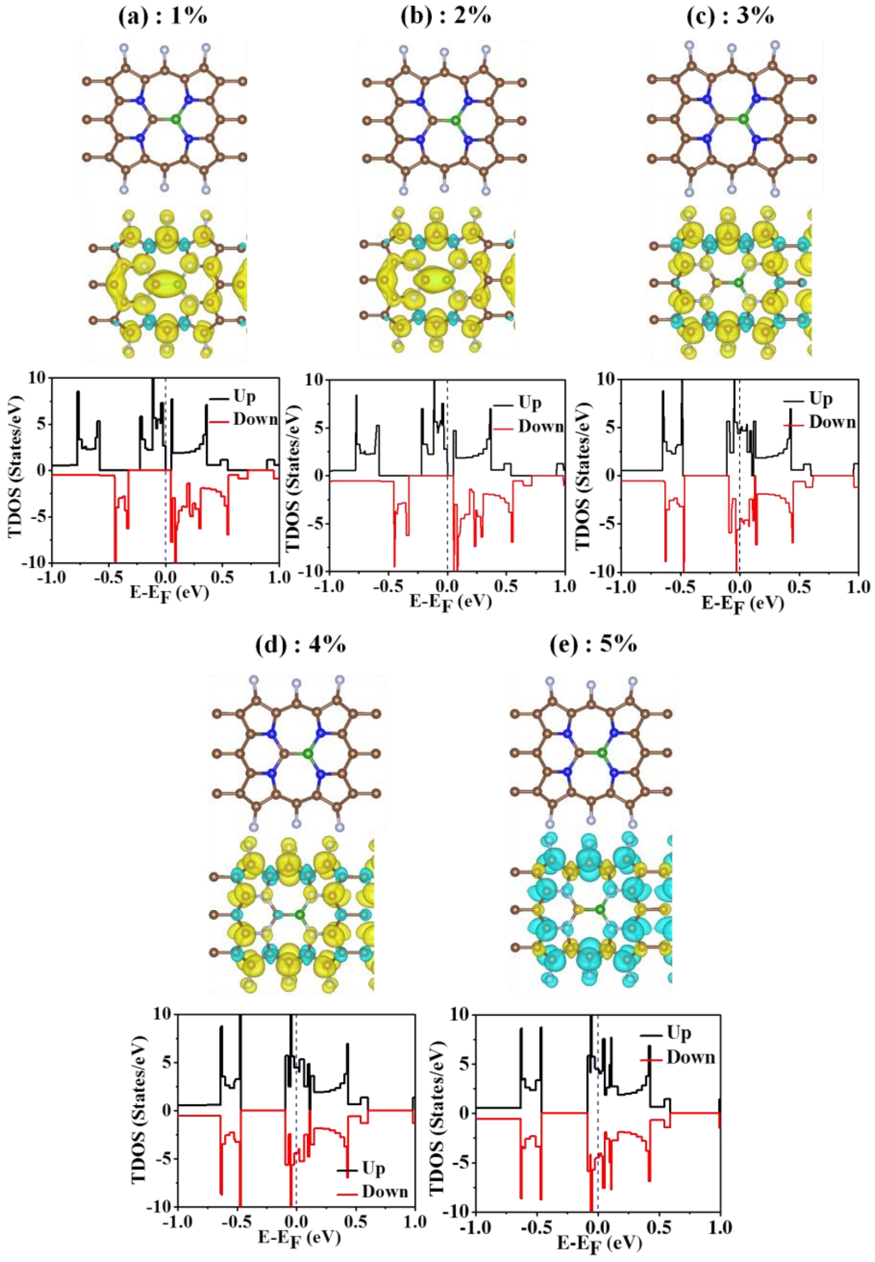

Figure 5.18: (a)-(e) Optimized structure, spin density distribution and TDOS plot of $B@(C=C)_a^F - PA$ under the application of uniaxial compressive strain from 1% to 5%.

Spin gap of half-metallic systems has been tabulated in Table 5.4 where natures of the systems are indicated as M (Metallic), HM (Half-metallic) and S (Semiconducting). We have also included the optimized structure, spin density distribution and TDOS plot under the application of strain from 1% to 5% in Fig. 5.17-5.18.

Table 5.4: Modulation of spin-up gap (eV) in and nature of the $B@(C=C)_a^F - PA$ system with % of applied strain along uniaxial-tensile and uniaxial-compressive direction

% of applied Strain	**Uniaxial-tensile**		**Uniaxial-compressive**	
	Spin-Up Gap (eV)	**Nature of the system**	**Spin-Up Gap (eV)**	**Nature of the system**
1%	-	S	-	S
2%	0.355	HM	-	S
3%	0.347	HM	-	M
4%	-	S	-	M
5%	-	S	-	M

5.3.8. Spin transport in B doped C=C embedded PA:

Observing spin-polarized current in a metal-molecule-metal nanodevice has always been an interesting topic in spintronics domain. Therefore, we have modelled $Au\,(111) - B@(C=C)_a^F - PA_n - Au(111)$ device using B doped C=C embedded porphyrin nanoribbon $[B@(C=C)_a^F - PA_n]$ and studied the spin-polarized transport properties of our proposed nanoscale device. Primary modelling of our nanodevice begins with pure C=C embedded porphyrin nanoribbon as already shown in the section 5.2 (Fig. 5.1).

Spin polarized current of the device is analysed from $(I-V)$ characteristics using NEGF+DFT approach (Fig. 5.19) *[67]*. We have gradually increased the length of the scattering region with n = 1 and 2 and calculated current-voltage $(I-V)$ characteristics for all the devices considered here. Here, at each applied bias voltage, the spin-polarized current is determined self-consistently under the non-equilibrium conditions. Spin-polarized current has been calculated for all the devices up to 0.5 V. It can be seen (Fig. 5.19) that the $I-V$ curve for spin-up and spin-down channels shows the distinctive properties. Form the Fig. 5.19a ($I-V$ curve), we have not observed much difference in magnitude of spin-up and spin-down current for pure $(C=C)_a^F-PA$ system. Surprisingly, the current magnitude decreases for increasing bias voltage in the range of 0.3 to 0.5 V, which implies that the NDR phenomenon appears. The NDR effect has also been observed in several molecule systems *[68-69]*. This could be because of the misalignment of electronic states between molecules and electrodes. We find that for device the current values increases as the voltage increase up to 0.3 V.

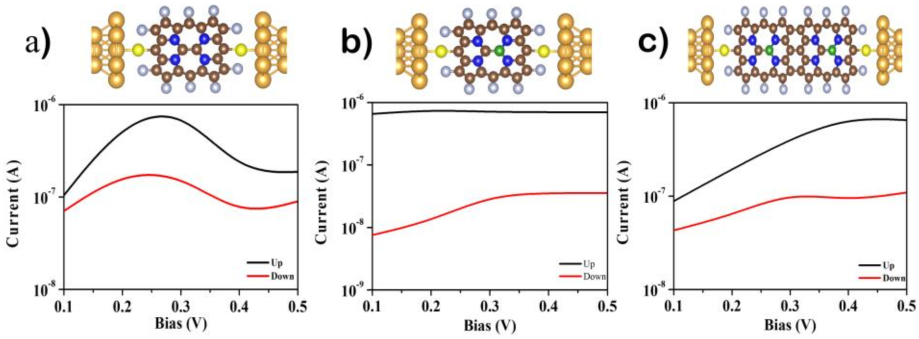

Figure 5.19: (a) The metal-molecule-metal nanodevice consisting C=C embedded porphyrin and its spin-polarized current-voltage pattern with applied bias voltages up to 0.5 V, (b)-(c) The metal-molecule-metal nanodevices consisting B doped C=C embedded porphyrin $B@(C=C)_a^F-PA_n$ with increasing length (n=1, and 2) and their spin-polarized $I-V$ curves for the corresponding device.

After that, there is a rapid drop in the magnitude of the current (Fig. 5.19a) is observed. To understand this, we have plotted the transmission spectra (Fig. 5.20) at different bias voltages. We have found that, at 0.3 V bias, there is a rise in the spin-up and spin-down transmission peaks, whereas, at 0.4 V bias, there is a drop in the transmission spectra for both the spins. This is very much consistent with our NDR effect from the I-V curve. This could be due to the discreteness in the molecule energy level close to Fermi-energy. When the bias voltage changes, a mismatch in the molecular state alignment occur, this corresponds to the drop in the current magnitude.

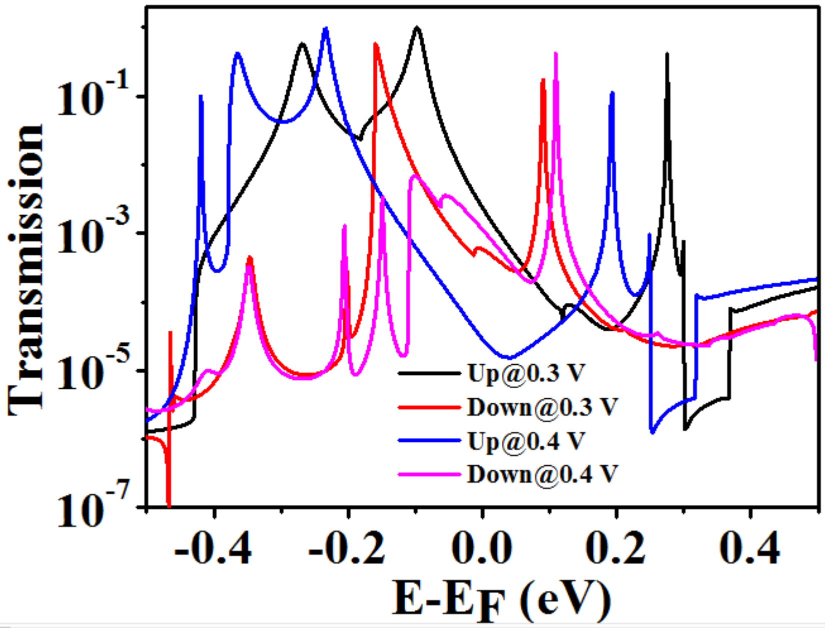

Figure 5.20: A comparison of the transmission spectra for the system $(C=C)_a^F - PA$ computed at different bias voltages ranging from 0.3 to 0.4 V.

We have observed a large difference in magnitude of current (around 2 order of magnitude) between spin-up and spin-down has been observed for the device $B@(C=C)_a^F - PA_n$ (n=1) (Fig. 5.19b) due to its half-metallic nature. Likewise, in the case of $B@(C=C)_a^F - PA_n$ (n=2), we see that the $I-V$ curves for the spin-up and spin-down display the dramatically distinct properties (Fig. 5.19c). The current magnitude through spin-up is significantly larger than that of the spin-down. Thus, this nanodevice with interesting properties has ample applications in future molecular spintronic nanodevices.

5.3.9. Spin filtering efficiency (SFE):

We have calculated the Spin Filtering Efficiency (SFE) at different biases as shown in Fig. 5.21. The SFE is calculated by employing the following equation $SFE = |I_{up} - I_{down}|/|I_{up} + I_{down}|$, where I_{up} and I_{down} are current in spin-up and spin-down channels, respectively. It is presented as a percentage in Fig. 5.21. We have observed that the

$B@(C=C)_a^F - PA_n$ system shows higher spin filtering efficiency compared to the pure $(C=C)_a^F - PA_n$ (n=1) device. The B doped C=C embedded porphyrin nanoribbon has an effect on the states close to Fermi-energy and hence enhances the spin filtering property. The effect of spin filtering reaches about 69% for $(C=C)_a^F - PA_n$ (n=1), even reaches 98% for $B@(C=C)_a^F - PA_n$ (n=1) and 78% for $B@(C=C)_a^F - PA_n$ (n=2). Our result demonstrates a perfect spin filtering effect for $B@(C=C)_a^F - PA_n$ (n=1), for example, only one spin state allows electron flowing through the device, whereas another spin state electron is forbidden. Therefore, our device can be very useful for molecular spintronics application.

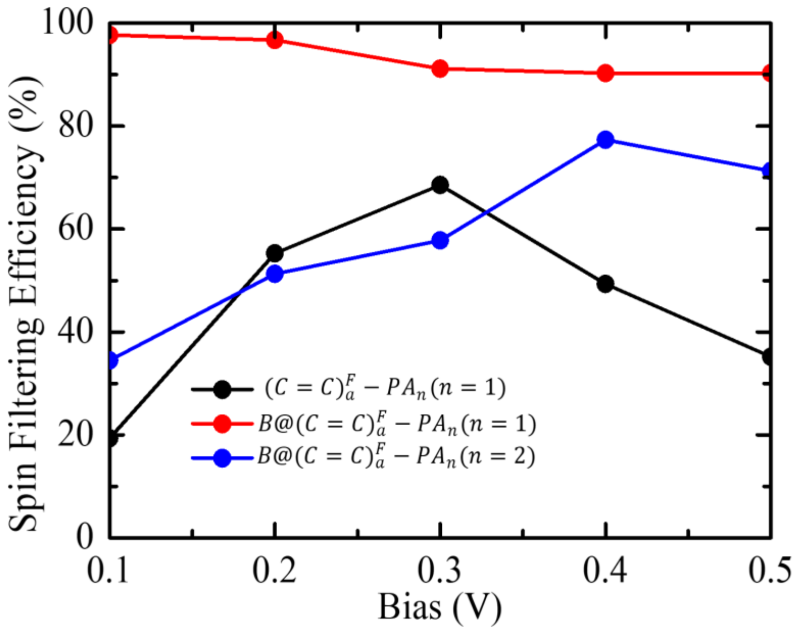

Figure 5.21: Spin filtering efficiency as function of the bias voltage for all the nanoscale devices.

5.4. Conclusion

In conclusion, we propose a novel molecular spintronics device for spin-filtering application based on metal free C=C embedded porphyrin unit using first-principles DFT + NEGF calculations. Single B doping in C=C embedded porphyrin array based system ($B@(C=C)_a^F - PA_n$) exhibits half-metallic property which is very important for such device. Magnetism and half-metallicity originates due to hole doping approach. Interestingly our system shows itinerant magnetism with strong coupling between conducting electrons. Moreover, the Curie temperature for our system is found to be very high (580.23 K to 696.27 K) which indicates that this device could perform above room temperature. Further to this, the calculated negative formation energy (-2.59 eV) also indicates the possibility of experimental realization of such system. In addition to that, our system is also found to be dynamically and thermally stable. The high spin-filtering efficiency (98%) indicates that our proposed device can be very useful for high temperature molecular spintronics application.

5.5. References

[1] Bhattacharyya G., Choudhuri I., Bhauriyal P., Garg P., Pathak B. (2018), Ferromagnetism in magnesium chloride monolayer with an unusually large spin-up gap, Nanoscale, 10, 22280-22292 (DOI: 10.1039/C8NR07429A)

[2] Bhattacharyya G., Choudhuri I., Pathak B. (2018), High Curie temperature and half-metallicity in an atomically thin main group-based boron phosphide system: long range ferromagnetism, Phys. Chem. Chem. Phys., 20, 22877-22889 (DOI: 10.1039/C8CP03440K)

[3] Bhattacharyya G., Garg P., Bhauriyal P., Pathak B. (2019), Density Functional Theory Study of Defect Induced Ferromagnetism and Half-Metallicity in CaI_2 Based Monolayer for Spintronics Applications, ACS Appl. Nano Mater., 2, 6152-6161 (DOI: 10.1021/acsanm.9b00967)

[4] Zhang J., Gong X., Xu B., Xia Y., Yin J., Liu Z. (2014), Half-metallicity in graphitic C_3N_4 nanoribbons: An ab initio study, Phys. Status Solidi B, 251, 1386-1392 (DOI: 10.1002/pssb.201451110)

[5] Li X., Lv H., Dai J., Ma L., Cheng Zeng X., Wu X., Yang J. (2017), Half-Metallicity in One-Dimensional Metal Trihydride Molecular Nanowires, J. Am. Chem. Soc., 139, 6290-6293 (DOI: 10.1021/jacs.7b01369)

[6] Liu H., Kondo H., Ohno T. (2016), Spintronic Transport in Armchair Graphene Nanoribbon with Ferromagnetic Electrodes: Half-

Metallic Properties, Nanoscale Res. Lett., 11, 456 (1-8) (DOI: 10.1186/s11671-016-1673-5)

[7] Pan L., An J., Jun Liu Y. (2013), Noncollinear magnetism and half-metallicity in biased bilayer zigzag graphene nanoribbons, New J. Phys., 15, 043016 (13pp) (DOI: 10.1088/1367-2630/15/4/043016)

[8] Houchins G., Crook C. B., Xin Zhu J., Balatsky A. V., Haraldsen J. T. (2017), Voltage-dependent spin flip in magnetically substituted graphene nanoribbons: Towards the realization of graphene-based spintronic devices, Phys. Rev. B, 95, 155450 (1-6) (DOI: 10.1103/PhysRevB.95.155450)

[9] Celis A., Nair M. N., Taleb-Ibrahimi A., Conrad E. H., Berger C., Heer W A de., Tejeda A. (2016), Graphene nanoribbons: fabrication, properties and devices, J. Phys. D: Appl. Phys., 49, 143001 (17pp) (DOI: 10.1088/0022-3727/49/14/143001)

[10] Xu W., Woo Lee Tae. (2016), Recent progress in fabrication techniques of graphene nanoribbons, Mater. Horiz., 3, 186-207 (DOI: 10.1039/c5mh00288e)

[11] Kumar S., Kumawat R. L., Pathak B. (2019), Spin-Polarized Current in Ferromagnetic Half-Metallic Transition-Metal Iodide Nanowires, J. Phys. Chem. C, 123, 15717-15723 (DOI: 10.1021/acs.jpcc.9b02464)

[12] Zeng J., Qiu Chen K. (2013), Spin filtering, magnetic and electronic switching behaviors in manganese porphyrin-based spintronic devices, J. Mater. Chem. C, 1, 4014–4019 (DOI: 10.1039/c3tc30431k)

[13] Cho W. J., Cho Y., Min S. K., Kim W. Y., Kim K. S. (2011), Chromium Porphyrin Arrays As Spintronic Devices, J. Am. Chem. Soc., 133, 9364-9369 (DOI: 10.1021/ja111565w)

[14] Tsuda A., Osuka A. (2001), Fully Conjugated Porphyrin Tapes with Electronic Absorption Bands That Reach into Infrared, Science, 293, 79-82 (DOI: 10.1126/science.1059552)

[15] Aratani N., Osuka A., Kim Y. H., Jeong D. H., Kim D. (2000), Extremely Long, Discrete meso-meso-Coupled Porphyrin Arrays,

Angew. Chem., Int. Ed., 39, 1458-1462 (DOI: 10.1002/(SICI)1521-3773(20000417)39:8<1458::AID-ANIE1458>3.0.CO;2-E)

[16] Vaid Thomas P. (2011), A Porphyrin with a C=C Unit at Its Center, J. Am. Chem. Soc., 133, 15838-15841 (DOI: 10.1021/ja205738z)

[17] Li Y., Zhang S., Yu J., Wang Q., Sun Q., Jena P. (2015), A new C=C embedded porphyrin sheet with superior oxygen reduction performance, Nano Res., 8(9), 2901–2912 (DOI: 10.1007/s12274-015-0795-x)

[18] Weiss A., Pritzkow H., Brothers P. J., Siebert W. (2001), Coordinated B_2 Bridges in Porphyrins-Unexpected Formation of a Diborane(4)- from a Diborylporphyrin, Angew. Chem., Int. Ed., 40, 4182-4184 (DOI: 10.1002/1521-3773(20011119)40:22<4182::AID-ANIE4182>3.0.CO;2-F)

[19] Weiss A., Hodgson M. C., Boyd P. D. W., Siebert W., Brothers P. J. (2007), Diboryl and Diboranyl Porphyrin Complexes: Synthesis, Structural Motifs, and Redox Chemistry: Diborenyl Porphyrin or Diboranyl Isophlorin?, Chem. Eur. J., 13, 5982-5993 (DOI: 10.1002/chem.200700046)

[20] Belcher W. J., Hodgson M. C., Sumida K., Torvisco A., Ruhlandt-Senge K., Ware D. C., Boyd P. D. W., Brothers P. J. (2008), Porphyrin complexes containing coordinated BOB groups: synthesis, chemical reactivity and the structure of [BOB(tpClpp)]2+, Dalton Trans., 2008, 1602-1614 (DOI: 10.1039/b716189a)

[21] Brothers P. J. (2008), Boron complexes of porphyrins and related polypyrrole ligands: unexpected chemistry for both boron and the porphyrin, Chem. Commun., 2008, 2090-2102 (DOI: 10.1039/b714894a)

[22] Kumawat R. L., Garg P., Kumar S., Pathak B. (2019), Electronic Transport through DNA Nucleotides in Atomically Thin Phosphorene Electrodes for Rapid DNA Sequencing, ACS Appl. Mater. Interfaces, 11, 219-225 (DOI: 10.1021/acsami.8b17239)

[23] Brandbyge M., Mozos J. L., Ordejón P., Taylor J., Stokbro K. (2002), Density-Functional Method for Nonequilibrium Electron

Transport, Phys. Rev. B, 65, 165401 (1-17) (DOI: 10.1103/PhysRevB.65.165401)

[24] Pathak B., Löfås H., Prasongkit J., Grigoriev A., Ahuja R., Scheicher, R. H. (2012), Double-Functionalized Nanopore-Embedded gold Electrodes for Rapid DNA Sequencing, Appl. Phys. Lett., 100, 023701 (1-3) (DOI: 10.1063/1.3673335)

[25] Prasongkit J., Grigoriev A., Pathak B., Ahuja R., Scheicher R. H. (2013), Theoretical Study of Electronic Transport through DNA Nucleotides in a Double-Functionalized Graphene Nanogap, J. Phys. Chem. C, 117, 15421-15428 (DOI: 10.1021/jp4048743)

[26] Kratzer P., Tawfik S. A., Cui X. Y., Stampfl C. (2017), Detection of adsorbed transition-metal porphyrins by spin-dependent conductance of graphene nanoribbon, RSC Adv., 7, 29112-29121 (DOI: 10.1039/c7ra04594h)

[27] Li F., Huang J., Hub Y., Li Q. (2019), Transport property of ligand-driven light-induced spin-change Fe-based spin crossover complexes, RSC Adv., 9, 12339-12345 (DOI: 10.1039/c9ra01420a)

[28] Blöchl P.E. (1994), Projector augmented-wave method, Phys. Rev. B, 50, 17953-17979 (DOI: 10.1103/PhysRevB.50.17953)

[29] Kresse G., Joubert D. (1999), From ultrasoft pseudopotentials to the projector augmented-wave method, Phys. Rev. B, 59, 1758-1775 (DOI: 10.1103/PhysRevB.59.1758)

[30] Perdew J. P., Burke K., Ernzerhof M. (1996), Generalized Gradient Approximation Made Simple, Phys. Rev. Lett., 77, 3865-3868 (DOI: 10.1103/PhysRevLett.77.3865)

[31] Perdew J. P., Chevary J. A., Vosko S. H., Jackson K. A., Pederson M. R., Singh D. J., Fiolhais C. (1992), Atoms, molecules, solids, and surfaces: Applications of the generalized gradient approximation for exchange and correlation, Phys. Rev. B, 46, 6671-6687 (DOI: 10.1103/PhysRevB.46.6671)

[32] Gorjizadeh N., Kawazoe Y. (2010), Chemical Functionalization of Graphene Nanoribbons, J. Nanomater., 2010, 513501 (7pp) (DOI: 10.1155/2010/513501)

[33] Bhandary S., Penazzi G., Fransson J., Frauenheim T., Eriksson Olle., Sanyal B. (2015), Controlling Electronic Structure and Transport Properties of Zigzag Graphene Nanoribbons by Edge Functionalization with Fluorine, J. Phys. Chem. C, 119, 21227−21233 (DOI: 10.1021/acs.jpcc.5b06469)

[34] Monshi M. M., Aghaeia S. M., Calizo I. (2017), Edge functionalized germanene nanoribbons: impact on electronic and magnetic properties, RSC Adv., 7, 18900-18908 (DOI: 10.1039/c6ra25083a)

[35] Bader R. F. W. (1991), A quantum theory of molecular structure and its applications, Chem. Rev., 91, 893-928 (DOI: 10.1021/cr00005a013)

[36] Henkelman G., Arnaldsson A., Jo´nsson H. (2006), A fast and robust algorithm for Bader decomposition of charge density, Comput. Mater. Sci., 36, 354-360 (DOI: 10.1016/j.commatsci.2005.04.010)

[37] Sanville E., Kenny S. D., Smith R., Henkelman G. J. (2007), Improved grid-based algorithm for Bader charge allocation, Comput. Chem., 28, 899-908 (DOI: 10.1002/jcc.20575)

[38] Tang W., Sanville E., Henkelman G. J. (2009), A grid-based Bader analysis algorithm without lattice bias, J. Phys.: Condens. Matter., 21, 084204 (7pp) (DOI: 10.1088/0953-8984/21/8/084204)

[39] Schöttke H. (1983), The Electronic Band Structure of α-Rhombohedral Boron, J. Less Common Met., 91, 159-165 (DOI: 10.1016/0022-5088(83)90104-2)

[40] Witt W. (1967), Absolute Präzisionsbestimmung von Gitterkonstanten an Germanium- und Aluminium-Einkristallen mit Elektroneninterferenzen, Z. Naturforsch. A, 22A, 92 (DOI: 10.1515/zna-1967-0115)

[41] Choudhuri I., Patra N., Mahata A., Ahuja R., Pathak B. (2015), B−N@Graphene: Highly Sensitive and Selective Gas Sensor, J. Phys. Chem. C, 119, 24827-24836 (DOI: 10.1021/acs.jpcc.5b07359)

[42] Sun Y., Zhuo Z., Wu X., Yang J. (2017), Room-Temperature Ferromagnetism in Two-Dimensional Fe_2Si Nanosheet with Enhanced

Spin-Polarization Ratio, Nano Lett., 17, 2771-2777 (DOI: 10.1021/acs.nanolett.6b04884)

[43] Schweiger A., Jeschke G. (2001), Principles of Pulse Electron Paramagnetic Resonance, Oxford University Press, Oxford, England, ISBN: 9780198506348.

[44] Baroni S., Giannozzi P., Testa A. (1987), Green's-function approach to linear response in solids, Phys. Rev. Lett., 58, 1861-1864 (DOI: 10.1103/PhysRevLett.58.1861)

[45] Togo A., Oba F., Tanaka I. (2008), First-principles calculations of the ferroelastic transition between rutile-type and $CaCl_2$-type SiO_2 at high pressures, Phys. Rev. B, 78, 134106 (1-9) (DOI: 10.1103/PhysRevB.78.134106)

[46] Nose S. (1984), A unified formulation of the constant temperature molecular dynamics methods, J. Chem. Phys., 81, 511-519 (DOI: https://doi.org/10.1063/1.447334)

[47] Troullier N., Martins J. L. (1991), Efficient Pseudopotentials for Plane-Wave Calculations, Phys. Rev. B, 43, 1993-2006 (DOI: 10.1103/physrevb.43.1993)

[48] Büttiker M., Imry Y., Landauer R., Pinhas S. (1985), Generalized Many-Channel Conductance Formula with Application to Small Rings, Phys. Rev. B, 31, 6207-6215 (DOI: 10.1103/physrevb.31.6207)

[49] Martin T., Landauer R. (1992), Wave-Packet Approach to Noise in Multichannel Mesoscopic System, Phys. Rev. B, 45, 1742-1755 (DOI: 10.1103/PhysRevB.45.1742)

[50] Barreiro A., Börrnert F., Rümmeli M. H., Büchner B., Vandersypen L. M. K. (2012), Graphene at High Bias: Cracking, Layer by Layer Sublimation and Fusing, Nano Lett., 12, 1873-1878 (DOI: 10.1021/nl204236u)

[51] Rocha A. R., García-Suárez V. M., Bailey S., Lambert C., Ferrer J., Sanvito S. (2006), Spin and Molecular Electronics in Atomically Generated Orbital Landscapes, Phys. Rev. B, 73, 085414 (DOI: 10.1103/PhysRevB.73.085414)

[52] Heyd J., Scuseria G. E., Ernzerhof M. (2003), Hybrid functional based on a screened Coulomb potential, J. Chem. Phys., 118, 8207-8215 (DOI: https://doi.org/10.1063/1.1564060)

[53] Agnoli S., Favaro M. (2016), Doping graphene with boron: a review of synthesis methods, physicochemical characterization, and emerging applications, J. Mater. Chem. A, 4, 5002-5025 (DOI: 10.1039/c5ta10599d)

[54] He B., Shen J., Ma D., Lu Z., Yang Z. (2018), Boron-Doped C_3N Monolayer as a Promising Metal-Free Oxygen Reduction Reaction Catalyst: A Theoretical Insight, J. Phys. Chem. C, 122, 20312-20322 (DOI: 10.1021/acs.jpcc.8b05171)

[55] Jung S. M., Lee E. K., Choi M., Shin D., Jeon I. Y., Seo J. M., Jeong H. Y., Park N., Oh J. H., Baek J. B. (2014), Direct Solvothermal Synthesis of B/N-Doped Graphene, Angew. Chem., Int. Ed., 53, 2398-2401 (DOI: 10.1002/anie.201310260)

[56] Bhattacharyya G., Mahata A., Choudhuri I., Pathak B. (2017), Semiconducting Phase in Borophene: Role of Defect & Strain, J. Phys. D: Appl. Phys., 50, 405103 (13pp) (DOI: 10.1088/1361-6463/aa81b8)

[57] Kim Y. A., Fujisawa K., Muramatsu H., Hayashi T., Endo M., Fujimori T., Kaneko K., Terrones M., Behrends J., Eckmann A., Casiraghi C., Novoselov K. S., Saito R., Dresselhaus M. S. (2012), Raman Spectroscopy of Boron-Doped Single-Layer Graphene, ACS Nano, 6, 6293-6300 (DOI: 10.1021/nn301728j)

[58] Endo M., Hayashi T., Hong S. H., Enoki T., Dresselhaus M. S. J. (2001), Scanning tunneling microscope study of boron-doped highly oriented pyrolytic graphite, J. Appl. Phys., 90, 5670-5674 (DOI: https://doi.org/10.1063/1.1409581)

[59] Kawai S., Saito S., Osumi S., Yamaguchi S., Foster A. S., Spijker P., Meyer E. (2015), Atomically controlled substitutional boron-doping of graphene nanoribbons, Nat. Comm., 6, 8098 (DOI: 10.1038/ncomms9098)

[60] Xing M., Fang W., Yang X., Tian B., Zhang J. (2014), Highly-dispersed boron-doped graphene nanoribbons with enhanced

conductibility and photocatalysis, Chem. Commun., 50, 6637-6640 (DOI: 10.1039/c4cc01341g)

[61] Brothers, P. J. (2008), Boron complexes of porphyrins and related polypyrrole ligands: unexpected chemistry for both boron and the porphyrin, Chem. Commun., 2008, 2090-2102 (DOI: 10.1039/b714894a)

[62] Santiago1 J. M., Huang C. L., Morosan E. (2017), Itinerant magnetic metals, J. Phys. Condens. Matter., 29, 373002 (21pp) (DOI: 10.1088/1361-648X/aa7889)

[63] Stoner E. C. (1939), Collective electron ferromagnetism, Proc. R. Soc. Lond. A, 165, 372–414 (DOI: 10.1098/rspa.1939.0003)

[64] Mohn P. (2003), Magnetism in the Solid State: an Introduction, 134, ISBN: 978-3-540-30981-9 (Publisher: Springer-Verlag Berlin Heidelberg) (DOI: 10.1007/3-540-30981-0)

[65] Choi J., Kim Y. H., Chang K. J., Toma´nek D. (2003), Itinerant ferromagnetism in heterostructured C/BN nanotubes, Phys. Rev. B, 67, 125421 (1-5) (DOI: 10.1103/PhysRevB.67.125421)

[66] Zhang S. H., Liu B. G. (2018), Hole-doping-induced half-metallic ferromagnetism in a highly-air-stable $PdSe_2$ monolayer under uniaxial stress, J. Mater. Chem. C, 6, 6792-6798 (DOI: 10.1039/c8tc01450g)

[67] Kumawat R. L., Pathak B. (2019), Individual Identification of DNA Nucleobases on Atomically Thin Black Phosphorene Nanoribbons: van der Waals Corrected Density Functional Theory Calculations, J. Phys. Chem. C, 123, 22377-22383 (DOI: 10.1021/acs.jpcc.9b06239)

[68] Lin J., Ma D. (2008), Origin of negative differential resistance and memory characteristics in organic devices based on tris (8-hydroxyquinoline) aluminium, J. Appl. Phys., 103, 124505 (DOI: 10.1063/1.2942396)

[69] Pati R., McClain M., Bandyopadhyay A. (2008), Origin of Negative Differential Resistance in a Strongly Coupled Single Molecule-Metal Junction Device, Phys. Rev. Lett., 100, 246801 (DOI: 10.1103/PhysRevLett.100.246801).

Chapter 6

Scope of Future Work

6.1. Scope of Future Work

This present doctoral thesis deals with designing of main group based low dimensional (2D and 1D) half-metallic materials for spintronics applications. Moreover, it explains the effect of hole doping (both defect and doping induced) on magnetism and half-metallicity. In addition to that, a detailed investigation has been carried out to find out magnetic ground state and magnetic anisotropy of such low dimensional materials. Calculation of Curie temperature of these ferromagnetic systems has been investigated using Heisenberg model, Ising model and XY model depending on the strength of magnetic anisotropy energy. Moreover, strong itinerant magnetism has been examined in porphyrin array based systems and Curie temperature is also calculated for such systems. Spin-filtering efficiency has been calculated also for porphyrin based molecular spintronics device. This thesis also includes stability analysis for all the ferromagnetic half-metallic low dimensional systems.

Throughout our investigation, it is observed that the stability of such half-metallic materials is very important for practical realization. In many cases, realization of freestanding monolayer is found to be very challenging. Moreover, during the fabrication process, the monolayer is placed on top of a substrate material. Hence, it is very important to choose a proper substrate such that stability as well as the half-metallic properties can be sustained. In future, study of several substrate materials can be done to enlighten in this aspect.

Besides, various new spintronic materials and device can be designed based on several other 1D systems such as nanotubes, nanowires and nanoribbons. Additionally, another new class of materials can be investigated for spintronics application. The introduction section of this thesis already discusses about topological insulator which can provide two counter-propagating dissipation less spin current for electrons with two different orientations (spin-up and spin-down). Therefore, designing of topological insulating materials can be very promising for spintronics domain.